Numerical methods for eigenvalue problems in the description of drift instabilities in the plasma edge

Inaugural-Dissertation

zur Erlangung des Doktorgrades der
Mathematisch-Naturwissenschaftlichen Fakultät
der Heinrich-Heine-Universität Düsseldorf

vorgelegt von

Dominik Löchel

aus Solingen

Düsseldorf, März 2009

Aus dem Institut für Mathematik
der Heinrich-Heine Universität Düsseldorf

Gedruckt mit der Genehmigung der
Mathematisch-Naturwissenschaftlichen Fakultät der
Heinrich-Heine-Universität Düsseldorf

Referent: Prof. Marlis Hochbruck
Koreferenten: Prof. apl. Mikhail Tokar
Prof. Kristian Witsch

Tag der mündlichen Prüfung: 27. März 2009

Acknowledgment

I would like to express my thanks to my supervisor Prof. Dr. Marlis Hochbruck for permitting me to accomplish this work, for her advice and guidance, and in particular for her encouragements and suggestions.

I thank my second supervisor Prof. apl. Dr. Mikhail Tokar who has provided me with the necessary assistance for the physical part of this work.

I want to thank Prof. Dr. Kristian Witsch who helped me to find this Ph.D. position and supported me with his great knowledge in many discussions.

I would like to thank Dr. Dirk Reiser who helped me to understand the physical model and provided the equations for the elongated and triangulated magnetic geometry.

I am pleased to thank Dr. Timo Betcke for his talk on eigenvalue problems that inspired the stopping criteria via the forward error estimate and to use the pseudo spectral method in approximating the derivatives.

I wish to acknowledge Dr. Julia Schweitzer for her careful reading of this thesis and her helpful suggestions. Further I want to thank all the other members of the institute for the discussions we had.

I am grateful to Corinna Alber for her preliminary work on quadratic eigenvalue problems within her diploma thesis which provides a great overview on the topic and helped me to become familiar with the topic. Further I want to mention Ammar Aljammaz who wrote his master thesis on polynomial eigenvalue problems and with whom I had many discussions on the topic.

In conclusion I want to thank my parents for pointing my way in life, for their support and understanding.

Last but not least I thank the Deutsche Forschungsgemeinschaft (DFG) for the financial support to undertake this thesis through the research training group 1203 “Dynamics of hot plasmas”.

Zusammenfassung

Der Menschheit steht ein Energiemangel bevor, da die fossilen Brennstroffe wie Öl und Gas zur Neige gehen. Kernspaltungskraftwerke sind aufgrund ihrer Gefahr und der ungeklärten Endlagerung keine geeignete Alternative. Erneuerbare Energien sind ein recht teurer Ausweg. Auf der anderen Seite bietet die Fusion von Wasserstoff zu Helium ein riesiges Energiereservoir. Wenige Gramm dieses Brennstoffes liefern die Energie wie Tonnen von Kohle und das Abgas Helium verursacht keinen Treibhauseffekt.

Aus diesen Gründen wird schon seit Jahrzehnten versucht eine kontrollierte Kernfusion unter Laborbedingungen zu erreichen. Zum Auslösen der Fusion ist eine genügend hohe Temperatur und Dichte für eine ausreichend lange Zeit – die Einschlusszeit – notwendig. Dabei befindet sich das Gas im sogenannten „Plasmazustand“, d.h. Atome sind vollständig ionisiert. Eine vielversprechende Möglichkeit dieses Plasma zu handhaben ist der magnetische Einschluss mit dem Tokamak, einem Torusförmigen Gefäß. Der Tokamak ist Hauptgegenstand dieser Arbeit.

Im Tokamak wird durch Überlagerung äußerer Magnetfelder mit dem des Plasmastroms eine magnetische Geometrie gebildet, bei der die Bahn jeder Magnetfeldlinie in einer torusförmigen Oberfläche liegt. Geladene Teilchen mit einer Geschwindigkeitskomponente senkrecht zur Feldlinie erfahren im Magnetfeld die Lorentzkraft und gyrieren (kreisen) um die Feldlinie. Der Radius dieser Kreisbahn heißt Larmorradius und ist winzig gegenüber der Größe der Maschine. Der Kreismittelpunkt – das Gyrationszentrum – bewegt sich mit der parallelen Geschwindigkeitskomponente entlang der Magnetfeldlinie und ist damit in der Oberfläche gefangen.

Die klassischen und neoklassischen Transportprozesse in dieser Geometrie sind bereits gut verstanden. Letztere berücksichtigen, dass durch die Krümmung des Plasmazylinders das Magnetfeld auf der Innenseite stärker ist, als außen. Es hat sich allerdings herausgestellt, dass es zusätzlichen Transport senkrecht zu diesen Flussoberflächen, den sogenannten „anomalen Transport“, gibt. Dieser kommt durch Mikroinstabilitäten zustande und ist aktueller Gegenstand der Forschung. Der Anomaltransport verursacht, dass Energie und geladene Teilchen aus der Flussoberfläche nach außen diffundieren wodurch störende Verluste auftreten.

Um diese Prozesse besser zu verstehen und im Endeffekt durch geschickte Bauweise zu reduzieren, ist ein Model zur Beschreibung des anomalen Transports entwickelt worden. Die Komplexität der Gleichungen ist durch verschiedene Vereinfachungen reduziert worden, unter anderem indem sich auf die stärkste Störungsmode konzentriert wird. Aber selbst damit verbleibt eine komplizierte partielle Differential-Eigenwertgleichung zu lösen.

In einem ersten Ansatz wurde das Modell noch weiter vereinfacht, bis es die Form der Mathieu Gleichung erreicht. Damit können allerdings nur gemittelte Plasmagrößen in die Berechnung eingehen. Aber gerade bei einem interessanten Phänomen, dem sogenannten MARFE, treten extreme poloidale Inhomogenitäten auf, deren Betrachtung von großem Interesse ist. MARFE, die vielfältige asymmetrische Strahlung aus der Randzone, tritt toroidal symmetrisch, aber poloidal lokal an Positionen hoher Dichte auf und entzieht dem Plasma einen erheblichen Anteil an Energie, die durch Photonen bei der Rekombination der Ionen und Elektronen zu Atomen

abgestrahlt wird, wodurch sich dieses Phänomen selbst verstärkt.

Ebenfalls von Interesse ist die Untersuchung in elongierter und triangulierter magnetischer Geometrie. Es hat sich gezeigt, dass sich die Plasmastabilität verbessert, wenn die Flussoberflächen in die Höhe gezogen und 'D'-förmig werden. Das dafür notwendige Koordinatensystem bringt stark inhomogene metrische Koeffizienten in die Eigenwertgleichung ein, welche mit der Mathieu-Gleichung nicht mehr zu handhaben sind.

In dieser Arbeit wird die Eigenwertgleichung in ihrer komplizierten Form betrachtet und ein effizienter numerischer Löser entwickelt: das Mehrgitter-Jacobi-Davidson-Verfahren. Da die für die Physik interessante Eigenfunktion mit stärkster zeitlicher Anwachsrate sehr glatt ist, kann eine grobe Approximation mit geringem Zeitaufwand auf sehr grobmaschigem Gitter erreicht werden. Diese wird dann auf geschickte Weise mit dem Mehrgitter-Jacobi-Davidson-Verfahren auf schrittweise feineren Gittern verbessert.

Der effiziente Eigenwertlöser ermöglicht das System der hochgradig nicht-linearen Anomaltransport-Gleichungen in akzeptabler Zeit iterativ zu lösen. Für diese gedämpfte Fixpunktiteration wird eine problemangepasste Dämpfungssteuerung entwickelt.

Mit den entwickelten numerischen Werkzeugen werden Untersuchungen zur Auswirkung der magnetischen Geometrie, zur Plasmapositionierung und dem Einfluss der Einblasstelle des Fusionstreibstoffes durchgeführt und mit den Erkenntnissen aus Experimenten verglichen.

Abstract

The fossil fuels like oil and gas are on the decline and thus a shortage of the available energy is unavoidable in the near future. Power plants of nuclear fission are no good alternatives because of their enormous danger and the unsolved question of the final disposal. Renewable energy sources are an expensive resort. On the other hand the fusion of hydrogen (H) to helium (He) supplies a huge amount of energy. A few grams of such fueling gas offer as much energy as tons of coal do, but without any green house gases.

Due to these reasons, scientists try to realize controllable burn conditions under laboratory surrounding for several decades. For ignition of the fusion process the temperature, the density and the confinement time must reach a certain limit such that many nuclei get close together, overcome the Coulomb barrier and undergo fusion. Under this condition the gas is in state of "plasma", which means that the atoms are fully ionized. One promising possibility to enclose the plasma is the magnetic confinement in a Tokamak—a torus shaped device. This work will focus on the Tokamak device.

The superposition of two magnetic fields, one from the external poloidal field coils and the other one arising from the plasma current, ends up in a magnetic geometry where the trajectory of each field line lies on the surface of a toroidal enclosed flux tube. Charged particles with a velocity component perpendicular to the magnetic field lines feel the Lorentz force and gyrate in the plane perpendicular to the field line. The distance between the charged particle and the gyration center, the larmor radius, is tiny compared to the dimension of the machine. The center of rotation moves along the field line with the parallel component of the velocity and therefore the charged particle is confined in the flux surface.

Classical and neoclassical processes of transport are already well understood within this geometry. The latter one concerns inhomogeneities of the magnetic field strength due to different lengths of the circumference at the inner and the outer side. However, experiments showed the existence of an additional transport of particles and energy perpendicular to the flux surfaces, the so called "anomalous transport". It is driven by micro instabilities and of current research interest. The anomalous transport causes a strong diffusion of energy and charged particles throughout the flux surfaces. These losses make the machine inefficient.

For a better understanding of the anomalous transport and to improve the design of the machine, a model has been developed to describe the process. The complexity of the original equations has been reduced by several simplifications. One idea is to solely concentrate on the perturbation mode with the strongest growth rate in time. This simplified model leads to partial differential eigenvalue problem. In previous approaches the eigenvalue equation has been further simplified to a Mathieu equation with the disadvantage to be restricted to averaged plasma parameters. However, in the most interesting case of the so called MARFE and also with triangulated magnetic geometry, strong poloidal inhomogeneities arise. Their study is of huge research interest.

In this work we consider the eigenvalue equation in its most complicated form and we develop an

efficient numerical solver, the multilevel Jacobi-Davidson algorithm. The eigenmode of physical interest—the one of strongest growth rate in time—is smooth and hence, can be approximated on a coarse grid with low computational cost. This approximation is subsequently improved on finer grids by a new variant of the Jacobi-Davidson method.

Once an efficient solver is available, the system of highly nonlinear anomalous transport equations can be solved iteratively in reasonable computational time. The damped fix point iteration includes an adaptive damping strategy.

The numerical tool is used to simulate the impact of the magnetic geometry, shifts of the plasma column, such that the injection of neutrals occurs at different positions and the influence of the position of puffing in fueling gas.

Contents

Preface

The fossil fuels like oil and gas are on the decline and thus a shortage of the available energy is unavoidable in near future. Power plants of nuclear fission are not good alternatives because of their enormous danger and the unsolved question of the final disposal. Renewable energy sources are an expensive resort. On the other hand the fusion of hydrogen (H) to helium (He) supplies a huge amount of energy. A few grams of such fueling gas offer as much energy as tons of coal do, but without any green house gases.

Due to these reasons, scientists tried to realize a controllable burn condition under laboratory surrounding for several decades. For ignition of the fusion process the temperature and the density must reach a certain limit for some time such that many nuclei get close together, overcome the Coulomb barrier and undergo fusion. Under this condition the gas is in the state of "plasma", which means that the atoms are fully ionized, i.e., electrons and ions move around independently at microscopic level. Macroscopically the plasma is neutral. If the charged particles inside the plasma touch matter they radiate away their ionization energy while they recombine to neutral particles. Therefore the plasma must be confined in a chamber without touching the wall.

One promising possibility to confine the plasma is the magnetic confinement. In a magnetic field, charged particles are affected by the Lorentz force and gyrate around the field lines. The center of gyration is fixed to a field line and a parallel movement results. Hence the idea is to close up the field lines. This is realized in the torus shaped device called Tokamak.

In a Tokamak, the superposition of two magnetic fields, one from the external poloidal field coils and the other one arising from the toroidal plasma current, ends up in a magnetic geometry where the trajectory of each field line lies on the surface of a toroidal enclosed flux tube. The center of gyration moves along the field line with the parallel component of the velocity and therefore it is confined in the flux surface.

Classical and neoclassical processes of transport are already well understood within this geometry. The neoclassical theory concerns the inhomogeneities of the magnetic field strength due to a different lengths of the circumference at the inner and the outer side. However, experiments revealed the existence of additional transport of particles and energy perpendicular to the flux surfaces, which is called the "anomalous transport". The anomalous transport is assumed to be driven by micro instabilities. It is of current research interest because these losses make the system inefficient and have to be reduced by better configurations.

In order to build an efficient fusion device, the physics has to be really well understood and controlled. It is a fact that small fusion devices cannot be efficient. The size of nowadays Tokamaks causes them to be expensive and modifications to take years. Therefore physicists build up models that describe the experimental observations. With these models different configurations can be simulated and the most promising design is can be used experimentally.

This is the point where numerics can help. Numerical methods are required since for most problems the physical model equations are too complicated to be solved analytically. Numerical

solutions are used to study experimental setups, which cannot yet be realized. In addition, very expensive experimental setups can be optimized theoretically beforehand, phenomena can often be analyzed more clearly by numerical solutions than by measurements or they can be used as prediction tools for the experimentalist to know where to look at.

Therefore, numerics is an essential part of physical research and thus there is a lot of interest in having efficient, robust and reliable methods. It is indispensable to minimize computational time and storage requirements, since realistic problems are typically huge.

A major part of this work results from the close collaboration between numerical mathematics and theoretical physics. For a lot of achievements in the implementation of such methods for real world problems, we use physical properties of the solution. Moreover, the results have to fit the needs of the physicists, who use the codes. Thus the communication was essential in many ways. In this thesis, we will present numerical methods to efficiently simulate the anomalous transport process. a long way from a theoretically well understood numerical scheme to an implementation, which is efficient for a particular application.

This thesis is organized as follows: in Chapter 1 we outline the physical background of the fusion process and the basics of the magnetic confinement in the Tokamak device together with its problems, the drift instabilities. This chapter is especially targeted to the mathematician who is not familiar with the physics.

In the second chapter we introduce the basics of the numerical solution of eigenvalue problems. This is intended to the physicians and classifies the different types of eigenvalue problems and the numerical methods from literature. Methods to solve small and medium sized eigenvalue problems are described and the Jacobi-Davidson method to solve large problems is explained.

In the third chapter the anomalous transport model is introduced and simplification, which leads to a partial differential eigenvalue problem, is described shortly.

The fourth chapter deals with the numerical treatment of the eigenvalue equation. It starts with the spatial discretization and develops step by step the strategy of the multilevel Jacobi-Davidson technique that becomes highly efficient. This approach calculates an approximation of the desired eigenpairs on a very coarse grid and uses the eigenvector as the initial search space in the Jacobi-Davidson method that improves the accuracy of the eigenpair on subsequently finer grids. Methods to determine the right Ritz pair of the projected eigenvalue problem and an efficient method to solve the correction equation are deduced. Further a strategy to trace the eigenpairs in respect to a parameter within the eigenvalue equation is developed.

The fifth chapter uses the eigenvalue solver to perform simulations on the impact of the magnetic geometry of the edge layer.

The self consistent treatment of the model equations is deduced in chapter six. The anomalous particle flux determined by the solution of the eigenvalue equation is fed back into the initial plasma parameters by the heat balance equation. By an adaptive damped fixed point trust region iteration simulations on the impact of the position of neutral particle injection are carried out.

The last chapter sums up the results and gives perspectives on aspects to concern in future investigation.

This thesis was supported by the Deutsche Forschungsgemeinschaft through the Research Training Group 1203, “Dynamics of hot plasmas”.

Chapter 1

Introduction to plasma physics

In the first chapter we recall the motivation for the fusion research, the different approaches to realize a self sustaining fusion process on earth and in particular the basic principles of the Tokamak as it is communicated in lectures of U. Samm, G. Pretzler and M. Tokar.

1.1 Energy

The fossil fuels like oil and gas are on the decline and thus a shortage of the available energy is unavoidable in the near future. Power plants of nuclear fission are not good alternatives because of their enormous danger and the unsolved question of the final disposal. Renewable energy sources are an expensive resort. On the other hand the fusion of hydrogen (H) to helium (He) supplies a huge amount of energy. A few grams of such fueling gas offer as much energy as tons of coal do, but without any green house gases. There is plenty of fusion resources available on earth for at least the next century and the problem to solve is the realization of a fusion power plant.

1.1.1 Nuclear energy

In this section we give an overview where the nuclear energy comes from and how the process of fusion works.

If atomic nuclei undergo nuclear fission or fusion the sum m_s of mass of the separated atoms differs from mass m_b of the bound nuclei. This phenomenon is called *mass deficit*. Einsteins well known formula

$$E = mc^2 \qquad \text{(Einstein)}$$

says, that this mass deficit $\Delta m = m_\mathrm{s} - m_\mathrm{b}$ is proportional to the difference of the binding energy

$$\Delta E = \Delta m c^2 = (m_\mathrm{s} - m_\mathrm{b})c^2 = (Z m_\mathrm{p} + N m_\mathrm{n} - m_\mathrm{b})c^2 \tag{1.1}$$

where Z and N denote the number of protons and neutrons respectively, m_p and m_n denote their masses and c the speed of light in vacuum.

These binding energies of all common isotopes are shown in Figure 1.1. In the periodic table of elements the binding energy of the series of light elements from hydrogen (H) generally increases up to iron (Fe). It has a maximum in the range of iron-56 to nickel-62 and decreases for heavier elements. The peak of binding energy is caused by two contrary forces, the attractive *strong*

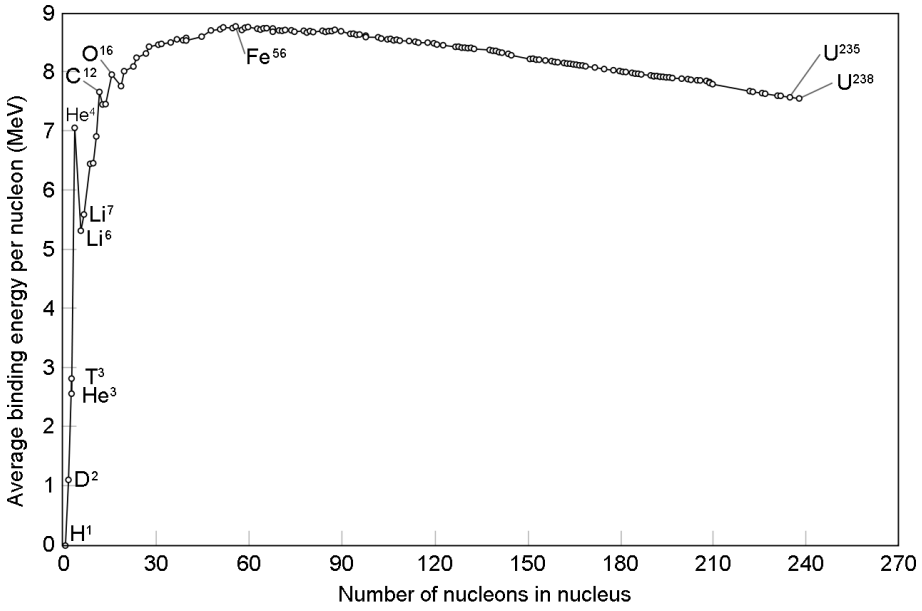

Figure 1.1: Binding energy per nucleon for all common isotopes offered by [45].

nuclear force and the repelling *Coulomb force*

$$F_{\mathrm{C}} = \frac{1}{4\pi\varepsilon_0}\frac{q_1 q_2}{r^2}, \qquad \text{(Coulomb force)}$$

where q_1 and q_2 denotes the electric charge of each particle, r their distance and ε_0 the *dielectric constant*. The *strong nuclear force* has an exponential decay on distance while the Coulomb force is proportional to the inverse squared distance. For light elements the strong nuclear force overwhelms the repellent Coulomb force due to the small distance of the nuclear particles. In heavy isotopes the diameter of the nucleus is several times as large as the diameter of a single proton or neutron and therefore the attractive strong nuclear force of oppositely placed particles decays rapidly, so that the repulsive Coulomb force dominates. Further, this explains why stability of heavy isotopes like uran (U) depends on the number of neutrons.

Nuclear binding energies are several orders of magnitude larger than chemical ones, which depend on the electron sheath. This explains, why nuclear fusion or fission releases much more energy than chemical reactions in relation to the fuel mass. Indeed mass deficit due to chemical reactions is beyond measurement, but theoretically it exists, too.

Furthermore, Figure 1.1 shows, that fusion of hydrogen (H) to helium (He) releases much more energy compared to fission of uran (U). Let the isotopes have a binding energy of $\Delta E_{\mathrm{initial}}$ before and $\Delta E_{\mathrm{outcome}}$ after fusion or fission. Then the energy gained is

$$E_{\mathrm{gain}} = \Delta E_{\mathrm{outcome}} - \Delta E_{\mathrm{initial}}.$$

E_{gain} is positive with exothermic reactions and negative with endothermic ones.

The reaction of currently greatest interest is the fusion of deuterium (^{2}D hydrogen with one proton (p) and one neutron (n)) and tritium (^{3}T hydrogen with one proton (p) and two neutrons (n)). The reaction equation is

$$^2\mathrm{D} + {}^3\mathrm{T} \longrightarrow {}^4\mathrm{He}\ (3.5\,\mathrm{MeV}) + {}^1\mathrm{n}\ (14.1\,\mathrm{MeV}), \qquad \text{(D-T reaction)}$$

where the energies in the brackets denote the kinetic energy ($1\mathrm{eV} = 1.6 \cdot 10^{-19}\mathrm{J}$) released with the particle. ^{4}He denotes an α-particle which is the nucleus of helium with two protons and two

neutrons. The advantage of this reaction is the high energetic output that makes the process very economical. The disadvantage is that the fast neutrons carry most of the energy and these make the surrounding radioactive. However the neutrons can be used to breed new tritium from lithium as tritium is a very rare isotope in the nature.

Other reactions like ${}^2\mathrm{D} + {}^2\mathrm{D}$ and ${}^2\mathrm{D} + {}^3\mathrm{He}$ have a much smaller cross section at temperatures around 10^8 K and therefore are less economical nowadays.

Nuclear fission is already realized in economical power plants. Researchers try to find a way to do this with nuclear fusion as well, because there is much more fuel available and it is less dangerous, due to the fact that fusion stops immediately if conditions are not optimal. The fusion reactor is fueled constantly, so there are only some grams of fuel inside it. Indeed fusion of $\mathrm{p} + {}^{11}\mathrm{B} + 3{}^4\mathrm{He}$ does not produce any neutrons. Also, nuclear reactions do not produce any *green house gases*.

The problem research suffers from is the ignition of fusion fuel in a controllable fusion device with an output energy above the required input. For example, realization of an hydrogen bomb is no problem, but this energy cannot be converted to electric power. It is the same problem with thunderbolts: a huge amount of energy is released in a very short time.

1.1.2 Ignition of nuclear fusion

In order to actuate nuclear fusion one needs to overcome the substantial energy barrier of the repellent electric force (*Coulomb barrier*) before attractive nuclear force preponderates and fusion occurs.

There are several ways to achieve this:

1. *beam-target* fusion
2. *beam-beam* fusion
3. *thermonuclear* fusion
4. *gravitational* fusion
5. *inertial* fusion
6. *magnetic* fusion

In *beam-target* fusion one nuclei is accelerated and collides with a second one. If both nuclei are accelerated it is called *beam-beam* fusion. These methods are highly inefficient because most particles shun each other due to their electric charge.

To explain the other methods the following definitions are introduced.

Definition 1.1. In physics, a *plasma* is an ionized gas. By heating and ionizing a gas, electrons are stripped away from atoms, so that positively charged nuclei and negatively charged electrons move around more freely. The free electric charges make the plasma electrically conductive so that it responds strongly to electromagnetic fields. Without external fields a plasma is *quasi neutral*, i.e. the sum of positive and negative charge is macroscopically equal.

Definition 1.2. The *fusion energy gain factor* Q is the ratio of fusion power produced in a nuclear fusion reactor compared to the power required to maintain the plasma in steady state:

$$Q = \frac{E_{\text{produced}}}{E_{\text{required}}}.$$

The ratio of $Q = 1$ is called *break even*. Above break even ($Q > 1$) there is a net gain of energy.

Definition 1.3. The duration the plasma exists until it is destroyed by touching matter or cooling is called *confinement time*.

Definition 1.4. The *Lawson criterion*, first derived by John D. Lawson in 1955 [22], is fulfilled by a fusion reactor if after the ignition the fusion process is kept up only by the output energy of itself and without further external energy sources. This condition is expressed in a lower bound for the *triple product* $n\tau T$ of the density n, the confinement time τ, and the plasma temperature T. If the Lawson criterion is fulfilled, then the fusion energy gain factor satisfies $Q \geq 1$.

The temperature is a statistical measure of the average kinetic energy of atoms or molecules, so heating the fusion fuel produces fast particles that collide. Especially nuclei in the high energy tail of *Maxwell's temperature distribution* overcome the Coulomb barrier and fuse. Another effect that lowers the required temperature is *quantum tunneling*. This means, that nuclei without enough energy to overcome the Coulomb barrier tunnel through the barrier with a certain probability. If nuclei are part of a plasma close to thermal equilibrium, it is called *thermonuclear* fusion and the Lawson criterion is fulfilled.

Now we offer an overview on several ways to trigger the fusion process until we consider the magnetic fusion in detail.

Gravitational fusion is realized in the sun and other stars. Via gravitation the huge masses of stars lead to such high densities that the Lawson criterion is satisfied. But this requires a minimum mass of a brown dwarf.

Inertial fusion is achieved when the temperature is raised so fast that matter cannot expand before fusion has occurred. This effect is applied in *laser fusion*. A pulse of energy is applied to the surface of a pellet of fusion fuel. This pulse is realized by a coherent *laser* (light amplification by stimulated emission of radiation) beam, that is split and amplified before it hits the target from all sides. The outer part of the particle expands and compresses the inner part to such a high pressure and temperature, that fusion arises. Due to inertia the fuel is burned before the pellet starts to explode. These tiny hydrogen bombs have a diameter of 1mm, only, to prevent the target chamber from damage. The gained energy comes out with fast neutrons, that get thermalized in the target chambers wall.

In *magnetic* fusion one confines plasma by magnetic fields. This will be explained in detail in the next section.

1.2 Magnetic confined plasma

In a plasma, electrons are stripped off from the nuclei. There are mainly two species of particles: positive charged nuclei and negative charged electrons. If particles hit a material surface they neutralize and ionization energy is lost for the plasma. Therefore, a technique of confinement is needed to separate the plasma from the reactors wall.

Definition 1.5. For better readability we introduce the following notation to distinguish scalars and vectors. Vectors are printed bold, e.g., $\boldsymbol{B}$ is the vector of the magnetic field. The same symbol not printed bold denotes the norm of the quantity, e.g., $B := \|\boldsymbol{B}\|_2$.

Imposing a magnetic field $\boldsymbol{B}$, particles with mass m, charge q and velocity $\boldsymbol{v}$ experience the *Lorentz force*

$$\boldsymbol{F}_{\mathrm{L}} = q\, \boldsymbol{v} \times \boldsymbol{B}. \qquad \text{(Lorentz force)}$$

This force is always perpendicular to the magnetic field line and the direction of motion. It causes *gyration* around a magnetic field line and the *centripetal force*

$$\boldsymbol{F}_{\mathrm{Z}} = \frac{mv}{\rho}\frac{\boldsymbol{B}\times\boldsymbol{v}}{B} \qquad \text{(centripetal force)}$$

arises. It is directed to the gyration center. Thus Lorentz and centripetal force are anti parallel and the *larmor radius* ρ of the gyration is obtained by the relation

$$\boldsymbol{F}_{\mathrm{Z}} + \boldsymbol{F}_{\mathrm{L}} = 0 \Leftrightarrow \frac{mv_{\perp}^2}{\rho} = q\, v_{\perp} B \Leftrightarrow \rho = \frac{mv_{\perp}}{qB}$$

and the *larmor frequency* is

$$\Omega_{\mathrm{L}} = \frac{v_{\perp}}{\rho} = \frac{qB}{m}.$$

Total motion of particle is an endless helical trajectory with its gyration center confined on the magnetic field line.

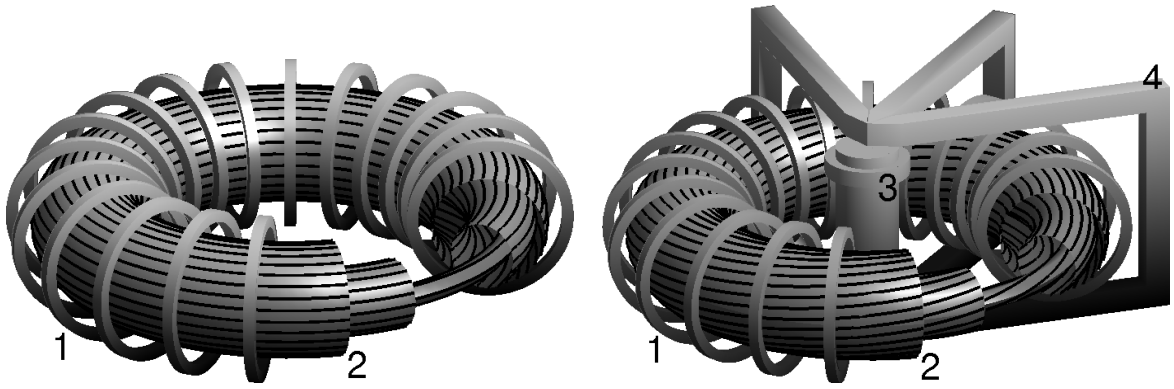

(a) toroidal coils only

(b) Tokamak with transformer, safety factor $q = 2$

Figure 1.2: Essential parts of Tokamak device for magnetic confinement: toroidal field coils (1), magnetic field lines and flux surface (2), primary coil (3) and iron core (4). *Shafranov shift* shifts magnetic flux surfaces to the outer side. In (b) a transformer is added. An increasing continuous current is driven through the primary coil. In the secondary coil—the plasma—a toroidal current is induced and a poloidal field arises. Superposition of the initial toroidal field and the induced poloidal field screws up the magnetic field lines. The minimal number of toroidal turns until a magnetic field line finishes one poloidal turn is called safety factor, $q = 2$ in this Figure.

In order to keep the plasma in the fusion device magnetic field lines have to stay inside it without penetrating matter. One possibility is the *magnetic bottle*: charged particles are trapped between two *magnetic mirrors*.

Definition 1.6. A *magnetic mirror* is a nearly static magnetic field, but in the coils the magnetic field lines run together and there the magnetic field strength increases. Charged particles gyrate on a field line and move along with $v_{\parallel}$. Its perpendicular velocity is $v_{\perp}$. If $\frac{v_{\parallel}}{v_{\perp}}$ is greater then a specific number, depending on field gradient, the particle feels a repellent force driven by the Lorentz force of other field lines that have a component perpendicular to $v_{\parallel}$.

The magnetic bottle was examined for fusion devices in the past, but suffered from too high loss due to fast particles escaping. The concept is mentioned here, because in the device introduced next there are mirroring effects, too, the so called *neoclassical transport*. It arises due to inhomogeneous field strength.

Definition 1.7. A *torus* is a geometric object, that is enclosed by

$$\partial T(R_0, r_0) := \left\{ \begin{pmatrix} x \\ y \\ z \end{pmatrix} \in \mathbb{R}^3 \;\middle|\; \begin{pmatrix} x \\ y \\ z \end{pmatrix} = \begin{pmatrix} (R_0 + r_0\cos(\theta))\cos(\varphi) \\ (R_0 + r_0\cos(\theta))\sin(\varphi) \\ r_0\sin(\theta) \end{pmatrix},\ \varphi, \theta \in [0, 2\pi[\right\}.$$

R_0 is called *major radius*, r_0 minor radius, φ toroidal angle and θ poloidal angle.

The other idea of magnetic confinement is closing up magnetic field lines inside a vessel. Figure 1.2 shows several coils arranged in a torus shaped design. In the poloidal coils there is a direct current. The magnetic field lines are perpendicular to the winding direction, i.e. toroidal coils cause a toroidal magnetic field. Due to the different circumference at the inner and the outer mid plane, the toroidal magnetic field is stronger at the inner side compared to the outer one. Let H_φ be the magnetizing field in toroidal direction, I the current and n the number of windings in all toroidal coils together. By Amperes law

$$\oint_{[0,2\pi]} \boldsymbol{H}\, d\boldsymbol{e}_\varphi = 2\pi R H_\varphi(R) = nI \quad \Rightarrow \quad H_\varphi(R) = \frac{nI}{2\pi R}$$

the $1/R$ dependence is revealed.

The larmor radius varies within one gyration turn around the field line and causes the ∇B *drift*. This is discussed in detail in the next section.

1.2.1 Drift motion of charged particles

Due to several forces beside the Lorentz force ($\boldsymbol{F}_\mathrm{L}$), drift motion of charged particles arises. Before introducing the physical effects, a general formula of drift motion is deduced. Let here be $\boldsymbol{B} = B\boldsymbol{e}_z$ the static and homogeneous magnetic field, $\boldsymbol{v}$ the velocity of the particle, q its charge, m its mass and $\boldsymbol{F} = F\boldsymbol{e}_y$ an arbitrary force. The equation of motion is

$$m\frac{d}{dt}\begin{bmatrix} v_x \\ v_y \end{bmatrix} = m\frac{d\boldsymbol{v}}{dt} = \boldsymbol{F} + \boldsymbol{F}_\mathrm{L} = \boldsymbol{F} + q\boldsymbol{v}\times\boldsymbol{B} = \begin{bmatrix} qv_yB \\ F - qv_xB \end{bmatrix}$$

$$\frac{d^2}{dt^2}v_x = \frac{qB}{m}\frac{d}{dt}v_y = -\left(\frac{qB}{m}\right)^2\left(v_x - \frac{F}{qB}\right) = -\Omega_\mathrm{L}^2(v_x - v_\mathrm{D})$$

and a general solution is

$$v_x(t) = v_0\sin\left(\Omega_\mathrm{L}t + \varphi_0\right) + v_\mathrm{D}, \qquad v_\mathrm{D} := \frac{F}{qB}.$$

The direction of the drift is perpendicular to $\boldsymbol{F}$ and $\boldsymbol{B}$ and the vectored drift velocity is

$$\boldsymbol{v}_\mathrm{D} = \frac{\boldsymbol{F}\times\boldsymbol{B}}{qB^2}. \tag{1.2}$$

The drift velocity $\boldsymbol{v}_\mathrm{D}$ is independent of the particle mass m and therefore equal, except for the sign, for electrons and protons.

Let the magnetic field be directed anticlockwise inside of the torus for further investigation.

In the tokamak the radial gradient of the magnetic field causes additional effects. Particles gyrating on a field line move around this line and fly through regions of stronger and weaker magnetic field strength. The larmor radius ρ depends on magnetic field strength and thus it varies. More precisely, charged particles have a *magnetic moment*

$$\mu = \frac{mv_\perp^2}{2B}. \qquad \text{(magnetic moment)}$$

In an inhomogeneous magnetic field the force

$$\boldsymbol{F}_{\nabla B} = -\mu \nabla B$$

arises and causes a drift velocity

$$\boldsymbol{v}_{\nabla B} = \frac{m v_\perp^2}{2qB^3} \boldsymbol{B} \times \nabla B. \qquad (\nabla B \text{ drift})$$

The magnetic field lines are circularly shaped and their curvature causes a *centrifugal force*

$$\boldsymbol{F}_{\mathrm{Z}} = \frac{m v_\parallel^2}{R} \boldsymbol{e}_R \qquad \text{(centrifugal force)}$$

and the drift velocity

$$\boldsymbol{v}_{\mathrm{Z}} = \frac{m v_\parallel^2}{qB^2 R} \boldsymbol{e}_R \times \boldsymbol{B}$$

arises.

In the presence of an electric field E, there is an *electric force*

$$\boldsymbol{F}_{\mathrm{E}} = q\boldsymbol{E}$$

and a drift velocity

$$\boldsymbol{v}_{E\times B} = \frac{\boldsymbol{E} \times \boldsymbol{B}}{B^2} = \frac{\boldsymbol{B} \times \nabla \phi}{B^2} \qquad (E \times B \text{ drift})$$

which is independent of the charge q.

Temporal variations of the electric field strength cause the drift velocity $\boldsymbol{v}_{E\times B}$ to vary in time. This leads to a *polarization force*

$$\boldsymbol{F}_{\mathrm{P}} = m \frac{\partial}{\partial t} \boldsymbol{v}_{E\times B}$$

and to a *polarization drift velocity*

$$\boldsymbol{v}_{\mathrm{P}} = -\frac{m}{qB^2} \frac{\partial}{\partial t} \boldsymbol{E}.$$

If the density n or the temperature T varies, there is a pressure gradient ∇p, a force

$$\boldsymbol{F}_* = -\frac{\nabla p}{n}$$

and a drift velocity

$$\boldsymbol{v}_{\nabla p} = \frac{\boldsymbol{B} \times \boldsymbol{\nabla} p}{qnB^2}.$$

$\boldsymbol{v}_{\nabla B}$ and $\boldsymbol{v}_{\mathrm{Z}}$ pull protons to the top of the vessel and electrons to the bottom. To prevent losses of the plasma, the basic idea is to twist the torus and switch top and bottom while particles follow its field lines. Then protons drift out at the upper half and back inside in the lower half of the pipe. There are two possibilities to achieve the twisting. One is realized in *stellarators* by deformation of toroidal coils and the other one in *Tokamak* by adding a transformer (see Figure 1.2). In this work the focus is on Tokamaks.

1.2.2 Tokamak

∇B and drifts caused by the curvature create a charge separation in vertical direction and an electric field $\boldsymbol{E}$ arises. $\boldsymbol{E}$ and $\boldsymbol{B}$ together generate the $\boldsymbol{E} \times \boldsymbol{B}$ drift, directed outwards for electrons and ions. Thus the confinement is bad. To counteract this phenomena, the idea is to torque the magnetic field lines and switch inside and outside within the toroidal turn.

In a Tokamak reactor a transformer is added, cf. Figure 1.2. An increasing continuous current is driven through the primary coil. In the transformers secondary coil—the plasma itself—a toroidal current is induced and a poloidal field arises. The superposition of the initial toroidal field and the induced poloidal field twists the magnetic field lines. The minimal number of toroidal turns until a magnetic field line completes one poloidal turn is called *safety factor* and depends on the toroidal and poloidal field strengths B_φ and B_θ, respectively and the major and minor radii R and r, respectively.

$$q = \frac{rB_\varphi}{RB_\theta} \qquad \text{(safety factor)}$$

The transformer is useful for *ohmic heating*, as well. A disadvantage is the magnetic saturation of the iron core, that demands an interruption of work in the range from several minutes up to one hour, depending on the specific device.

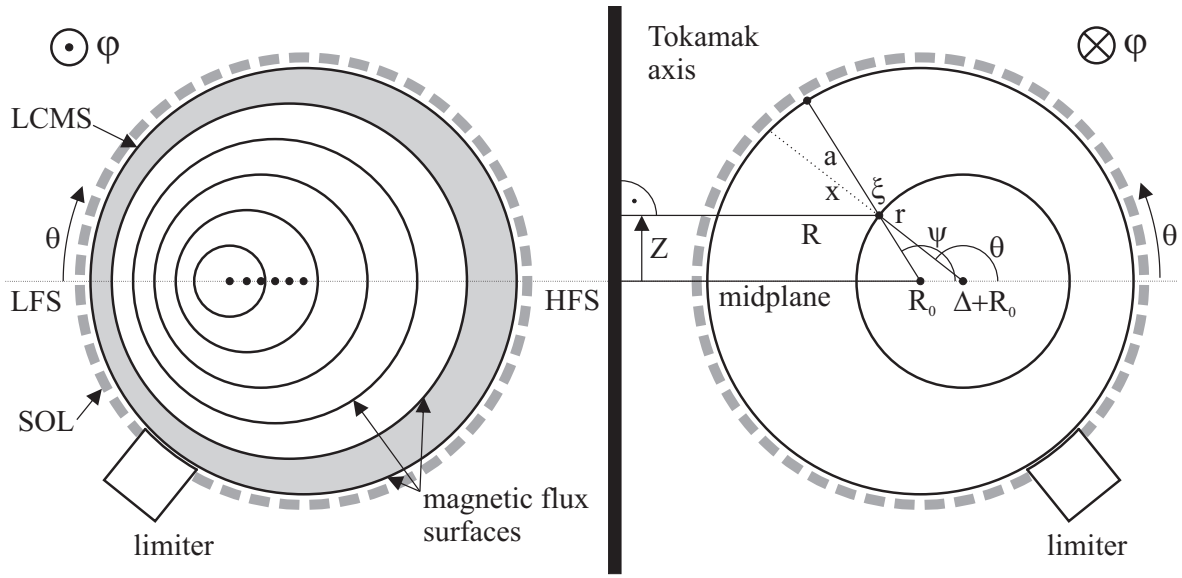

Figure 1.3: Centers (dots) of magnetic flux surfaces (circles) are shifted outwards by Shafranov shift. Particles in the scrape-off (SOL) layer hit the limiter. The gray zone is the edge layer. Right: there are two coordinate systems (ξ, ψ) for neutral particles and (x, θ) for charged ones. a is the radius of the last closed magnetic surface (LCMS), ξ the distance to the point of interest, r the radius of the flux surface and Δ the Shafranov shift.

The temperature T of the plasma is highest at the core and decreases radially to the edge. The density n depends on the radial position, too, and hence a pressure gradient $\boldsymbol{\nabla} p = \boldsymbol{\nabla}(Tn)$ arises, pressing flux surfaces outwards. Additionally, there is the antagonistic *Ampere force* $\boldsymbol{j} \times \boldsymbol{B}$ directed inwards. The balance of these forces results in the *Grad-Shafranov* equation

$$\boldsymbol{j} \times \boldsymbol{B} = \boldsymbol{\nabla} p \qquad \text{(Grad-Shafranov)}$$

and, due to the r dependence of the safety factor q in shifted magnetic surfaces, which are illustrated in Figure 1.3.

In this figure another essential part of the Tokamak is visualized: the *limiter*. The limiter is an obstacle that limits the extension of the plasma tube to a specific size. It works like the mechanism that creates wooden objects on a lathe. The limiter prevents the poloidal coils and the wall to get touched and destroyed by the plasma. Although the plasma edge is much colder than the plasma in the core, the limiter circulates the whole toroidal circumference in order to distribute the heat load intensity on a large surface.

When ions or electrons touch the limiter they recombine to atoms. On the one hand energy E_i is lost by radiation from recombination, but on the other hand neutralization allows to pump out the fusion ash, i.e. helium (He). The ratio of particles that get lost by recombination at the limiter, rather than flying back immediately into the plasma, is expressed by the recycling coefficient R_rec.

Definition 1.8. The *last closed magnetic surface* (LCMS) is the out most magnetic surface that is located before the limiter. The *scrape-off layer* (SOL) is the region of the plasma column where the particles hit the limiter and get scraped off. Due to the different magnetic field strength in radial direction, the inwards side of the plasma column is called *high field side* (HFS) and the outwards one *low field side* (LFS), cf. Figure 1.3.

1.2.2.1 Adequate coordinate system

For neutral particles the coordinate system $(\boldsymbol{e}_r, \boldsymbol{e}_\theta, \boldsymbol{e}_\varphi)$ of the torus is a good choice, where the unit vectors denote the radial, poloidal and toroidal direction, respectively. However, for charged particles a suitable coordinate system takes the magnetic configuration into account, i.e. the pitch angle due to the toroidal plasma current. Therefore, coordinates aligned to the magnetic field lines $(\boldsymbol{e}_r, \boldsymbol{e}_y, \boldsymbol{e}_\parallel)$ are introduced. $\boldsymbol{e}_\parallel$ is defined parallel to the magnetic field line and $\boldsymbol{e}_y$ is perpendicular to $\boldsymbol{e}_r$ and $\boldsymbol{e}_\parallel$, i.e. $\boldsymbol{e}_y$ is tangential to the magnetic flux surface and perpendicular to the magnetic field line. With the magnetic field $\boldsymbol{B} = B_\varphi \boldsymbol{e}_\varphi + B_\theta \boldsymbol{e}_\theta$, the relation between the two coordinate systems is

$$\begin{aligned} \boldsymbol{e}_\parallel &= \frac{B_\theta}{B}\boldsymbol{e}_\theta + \frac{B_\varphi}{B}\boldsymbol{e}_\varphi \\ \boldsymbol{e}_y &= \frac{B_\varphi}{B}\boldsymbol{e}_\theta - \frac{B_\theta}{B}\boldsymbol{e}_\varphi \end{aligned} \quad \Longleftrightarrow \quad \begin{aligned} \boldsymbol{e}_\theta &= \frac{B_\varphi}{B}\boldsymbol{e}_y + \frac{B_\theta}{B}\boldsymbol{e}_\parallel \\ \boldsymbol{e}_\varphi &= -\frac{B_\theta}{B}\boldsymbol{e}_y + \frac{B_\varphi}{B}\boldsymbol{e}_\parallel \end{aligned} \tag{1.3}$$

In a circular Tokamak like TEXTOR (**T**okamak **ex**periment for **t**echnology **o**rientated **r**esearch in Jülich, Germany) the coordinate system introduced above is fine. However, there are elongated devices like MAST (**M**ega-**A**mpere **s**pherical **T**okamak in Culham, United Kingdom), where the magnetic flux surfaces are 'D'-shaped (cf. Figure 1.4). The following definition generalizes the coordinate system for different magnetic geometries.

Definition 1.9. The *poloidal cut* through the flux surfaces of a 'D'-shaped Tokamak MAST is illustrated by the enclosed lines in Figure 1.4 (b), which is a generalization of the poloidal direction. The direction perpendicular to each flux surface, which is the generalized radial direction, is plotted by the lines from the center to the edge and named $\boldsymbol{e}_\chi$. χ is the flux label coordinate and constant on each flux surface, hence, $\nabla\chi$ is perpendicular to each flux surface. $\boldsymbol{e}_\eta$ is the unit vector perpendicular to $\boldsymbol{e}_\chi$ and direction of magnetic field line $\boldsymbol{e}_\parallel$. The projection of the η direction into poloidal plane are the 'D'-shaped lines.

Remark 1.10. It holds

$$\nabla\chi \parallel \boldsymbol{e}_\chi, \qquad \nabla\eta \parallel \boldsymbol{e}_\eta$$

and

$$\boldsymbol{e}_\chi \perp \boldsymbol{e}_\eta \perp \boldsymbol{e}_\parallel \perp \boldsymbol{e}_\chi.$$

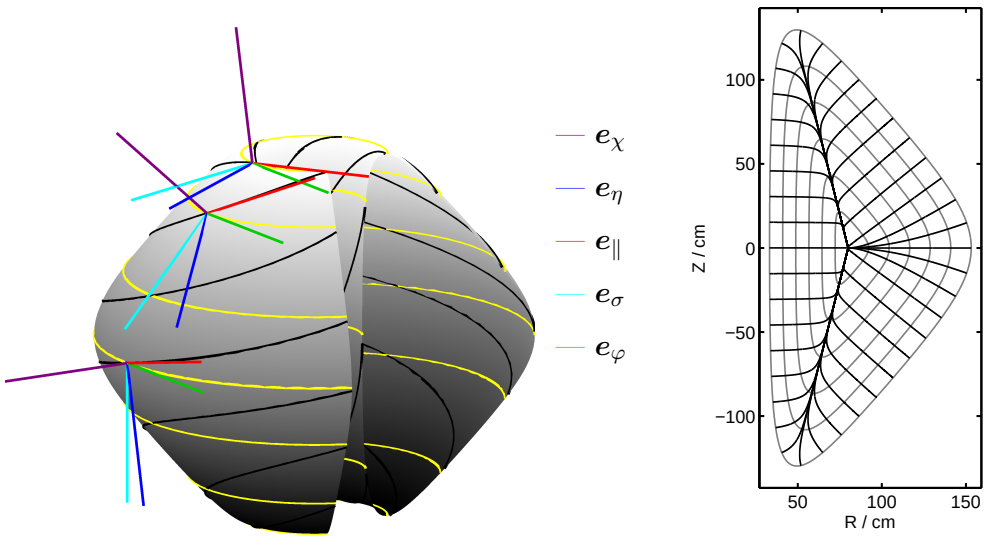

(a) Magnetic surface of Tokamak MAST

(b) Poloidal cut

Figure 1.4: (a) Magnetic flux surface of Tokamak MAST. The yellow lines are magnetic field lines without plasma current and the black lines are magnetic field lines with plasma current and a safety factor $q = 2$. At several positions the unit vectors $(\boldsymbol{e}_\chi, \boldsymbol{e}_\eta, \boldsymbol{e}_\parallel)$ and the directions $\boldsymbol{e}_\sigma$ and $\boldsymbol{e}_\varphi$ are drawn. (b) Poloidal plane of elongated and triangulated magnetic geometry with MAST parameters. The lines from the center to the edge are $(R, Z)(\chi, \sigma_i)$ and the circular lines are $(R, Z)(\chi_i, \sigma)$ where the value with sub index is plotted discretely and the one without is plotted continuously. The lines cross each other right-angled.

Definition 1.11. Within the poloidal cut, σ generalizes the poloidal angle and denotes the circumference coordinate of a specific flux surface normalized to the interval $[0, 2\pi]$ (cf. Figure 1.4 (b)). It holds $\sigma = 0$ is the LFS and $\sigma = \pi$ is the HFS.

1.3 Drift instabilities at the edge

The magnetic confinement is a nice concept to confine the electric charged particles of the plasma. However, unavoidable inhomogeneities in the plasma parameters, like the density, the temperature or the magnetic field strength cause drift instabilities where a flux of charged particles moves perpendicular to the magnetic field lines. The losses due to the drift current are an essential problem and methods reducing it are desired.

We start to describe the way drift waves create, the general features of instabilities and the problem of resonant perturbations. A similar description is in [19] and the references therein.

1.3.1 Model of drift waves in plain geometry

The anomalous transport model in chapter 3 is based on the concept of drift waves. We introduce the simplest case of a drift wave in the plain geometry. We assume the configuration with an homogeneous magnetic field which is illustrated by the three vertical lines in Figure 1.5(a). The electrons and the ions gyrate around the field lines. The positively charged ions and the negatively charged electrons are distributed electrically balanced and there is not space charge.

We increase the density in the center of Figure 1.5(b). Nevertheless the density doubles in the drawing, the change of the density is assumed to be very small. The density gradient accelerates

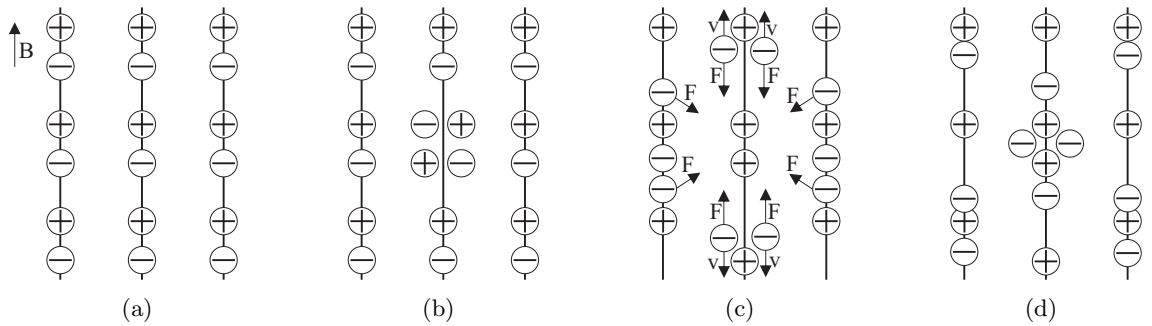

Figure 1.5: (a) displays 3 magnetic field lines with the positive charged ions and the negative charged electrons in a quasi neutral condition. The increased density in the center of (b) is illustrated exaggeratedly. The pressure departs the lighter electrons from the center with a velocity v and the Coulomb force F arises and pulls apart these electrons. The electrons of the adjacent field lines are affected, too. The electrons on the field line in the middle turn back and pull away the electrons of the adjacent field lines. The local peak of pressure recreates.

the light electrons away from the dense region while the heavier ions remain. The electrons follow their field line to the top or bottom of the figure. (c) A charge separation arises and creates the Coulomb force F that decelerates the electrons, but additionally pulls apart the electrons of the adjacent field lines.

The velocity v of the electrons on the field line in the middle decreases and the electrons return to the center. Finally the density peak is recreated and the whole process starts to repeat. The perturbation propagates wavelike in the plane perpendicular to the magnetic field lines.

The mere oscillation of the electrons is not the essential problem. The essential problem arises if there is a macroscopical density gradient that is perpendicular to the magnetic field lines which is visualized in Figure 1.6 where the oscillation of Figure 1.5 proceeds perpendicular to the plain of projection. For a proper description we assume the homogeneous magnetic field to be directed in the z direction and the macroscopical density gradient to be directed in the x direction, i.e., $\boldsymbol{B} = B\boldsymbol{e}_z$ and $\nabla n_0 = -\frac{\partial n_0}{\partial x}\boldsymbol{e}_x$, respectively.

Further, we neglect the movement of the ions due to their huge inertia in comparison to the light electrons and assume that the temperature to remain constant ($\nabla T = 0$) within a small density perturbation $\widetilde{n}$. Thus, a perturbation of the pressure is expressed by a perturbation of the density. The total density is $n = n_0 + \widetilde{n}$.

The electric potential perturbation $\widetilde{\phi}$ is connected to the electric field by the relation

$$\widetilde{\boldsymbol{E}} = -\nabla\widetilde{\phi}$$

and the electric field is related to the Coulomb force as

$$\boldsymbol{F}_\mathrm{C} = q\boldsymbol{E},$$

where q denotes the charge of the affected particle.

The density perturbation and the electric field perturbation are coupled by the *Boltzmann relation*

$$n = n_0 \exp\left(\frac{e\widetilde{\phi}}{k_\mathrm{B}T_\mathrm{e}}\right), \qquad \text{(Boltzmann relation)}$$

where e denotes the electric charge of an electron, k_B the Boltzmann constant and T_e the temperature of the electrons

The linearization of this equation yields

$$\frac{\widetilde{n}}{n_0} = \frac{e\widetilde{\phi}}{k_\mathrm{B} T_\mathrm{e}}, \tag{1.4}$$

which in turn offers a relation between the density perturbation $\widetilde{n}$ and the perturbation of the electric potential $\widetilde{\phi}$. Both perturbations have the same sign and are therefore in-phase. Due to the oscillation and the linear dependence we describe the process by one Fourier mode

$$\begin{aligned} \widetilde{\phi} &= \exp\big(\mathrm{i}(k_x x + k_y y - \omega t)\big) \\ \widetilde{n} &= \frac{n_0 e\widetilde{\phi}}{k_\mathrm{B} T_\mathrm{e}} \exp\big(\mathrm{i}(k_x x + k_y y - \omega t)\big). \end{aligned} \tag{1.5}$$

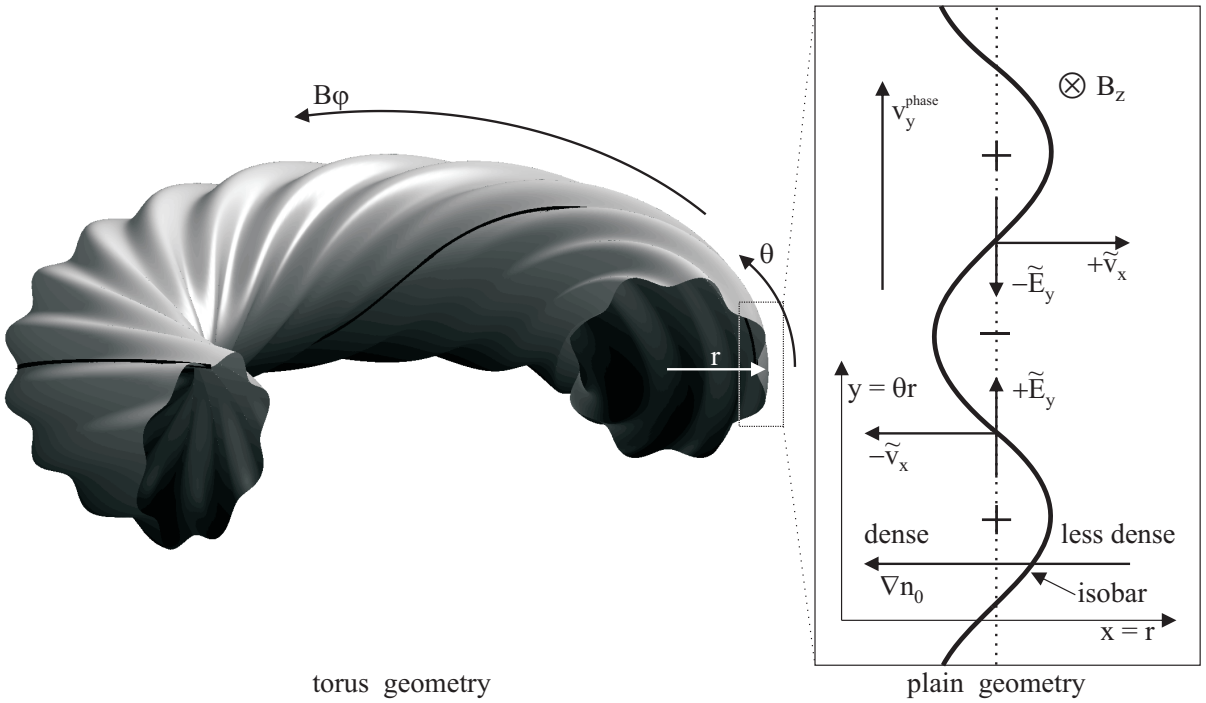

Figure 1.6: k_η drift wave in plain geometry. Details are given in the text below.

In the next step we concern the density gradient

$$\nabla n_0 = -\frac{\partial n_0}{\partial x} \mathrm{e}_x.$$

Due to (1.2), the electric field $\widetilde{E}_y$ in the y-direction creates a drift velocity

$$\widetilde{v}_x = \frac{\widetilde{F}_y}{eB_z} = \frac{\widetilde{E}_y}{B_z} = \frac{-\frac{\partial \widetilde{\phi}}{\partial y}}{B_z} = -\frac{ik_y\widetilde{\phi}}{B_z} \tag{1.6}$$

and the continuity equation reads

$$-i\omega\widetilde{n} = \frac{\partial \widetilde{n}}{\partial t} = \frac{\partial n}{\partial t} = \widetilde{v}_x \frac{\partial n_0}{\partial x} \tag{1.7}$$

where we assume $\frac{\partial n_0}{\partial t} = 0$ within a short period of time.

Inserting (1.4) and (1.6) into (1.7) leads to the *dispersion relation*

$$\omega = k_y v_{D_\mathrm{e}} \tag{1.8}$$

with the phase velocity

$$v_y^{\mathrm{phase}} = \frac{\omega}{k_y} = v_{D_\mathrm{e}} = \frac{k_\mathrm{B} T_\mathrm{e}}{eB_z} \frac{1}{n_0} \frac{\partial n_0}{\partial x}$$

equal to the *diamagnetic electron drift velocity* v_{D_e}.

The magnetic field was initially introduced to confine the charged particles on the field lines. However, the drift velocity v_x is perpendicular to the magnetic field lines. As long as $\omega \in \mathbb{R}$ (1.7) yields v_x to be merely imaginary and thus there is no net flux. But if there is some kind of resistivity ω becomes complex and a net flux arises. Within the drift current charged particles escape from their field line. The drift current reduces the density gradient within a long period of time. If we think of the Tokamak as it is displayed in Figure 1.6 the drift current is directed radially outwards and transports the charged particles perpendicular to the magnetic field lines.

1.3.2 Instability and fluctuation

Definition 1.12. A system, initially in the state of equilibrium, is called *unstable*, if it does not compensate a small perturbation, but reinforces disturbances and departs from the initial state. An illustrative example is a ball resting on a spike. A closed system contains a finite amount of energy only and therefore the increase of perturbation is bounded. The perturbation satiates and either reaches a new, more stable position (ball lies in a valley) or oscillations arise if the kinetic energy is not dissipated rapidly enough.

In the magnetic confined plasma inside a Tokamak the toroidal geometry causes periodic boundary conditions and *unstable modes* arise on resonant surfaces. A magnetic flux surface is called *resonant* if the safety factor q is rational. A turbulent mode is a short-range wavelike disturbance, e.g. the plasma pressure, with a discrete number of modes, that depends on the geometry, i.e. the path length of the magnetic field line until it closes up. Generally, many modes of different growth rate are excited simultaneously.

The perturbations are triggered by some inhomogeneity like a density gradient. If the amplitude of the perturbation reaches the magnitude of the initial cause (e.g. density gradient) it reacts on its origin and becomes nonlinear. The feedback can rise to the level where the mode either destroys itself or interferes with another one or saturates. The mode can become *turbulent* and its amplitude fluctuates.

Such modes have a strong impact on the performance of the magnetic confinement. A full understanding and technical manipulation of these modes make the radial particle and energy flux controllable.

1.3.3 Universal drift instability

The drift equilibrium given by the Grad-Shafranov equation is unstable against perturbations of the pressure. A small perturbation of pressure affects the plasma current $\boldsymbol{j}$ and the modified current in turn causes a change of pressure. A *drift wave* with increasing amplitude arises. Essentially, this happens in laboratory plasmas at the maximum of $|\boldsymbol{\nabla} p|$ or $|\boldsymbol{v}_\mathrm{e} - \boldsymbol{v}_i|$, respectively, and is called *universal drift wave*.

Drift waves propagate primarily in the poloidal direction. Due to the periodic boundary conditions, the wave length λ_θ of each mode is a multiple of the poloidal circumference $2\pi r$

$$2\pi r = m_\theta \lambda_\theta, \qquad m_\theta \in \mathbb{N}.$$

There is also a poloidal screwing of the drift wave with a mode number $m_\varphi \ll m_\theta$ due to the high parallel conductivity.

Definition 1.13. $\lambda_{a,b}$ is the *mean free path* of particle of species a to collisions with particles of species b, $a, b \in \{e, i, n\}$, where e, i, n denote electrons, ions and neutrals, respectively. If the second index is missing, the mean free path to all other species is meant.

Due to the mass ratio of electrons and ions, the electrons react much quicker on perturbations, than ions. Thus a drift wave is called *collision free drift*, when $\lambda_e \gg \lambda_\theta$ and *drift resistive* if $\lambda_e \ll \lambda_\theta$.

1.3.4 Resistive effects in Tokamak

As it is mentioned above, inhomogeneities in the Tokamak plasma create drift waves. Without resistive effects the density and the potential perturbations are in-phase ($\Im(\omega) = 0$) and the amplitude is constant in time. Further, the continuity equation (1.7) yields the drift current to by mere imaginary and there is no net flux perpendicular to the magnetic field lines.

A resistive effect leads to a phase shift between the density perturbation and the electric field perturbation and ω becomes complex. The imaginary part $\Im(\omega)$ determines the temporal behavior of the potential perturbation amplitude. By equation (1.5) it is obvious, that the amplitude of modes with a positive growth rate $\Im(\omega)$ increases (unstable) and the amplitude of modes with a negative growth rate decreases (stable) in time.

An illustrative example of how the energy transport depends on the phase shift is the excited pendulum. It depends on the phase position of nudge whether the pendulum gains energy or emits energy.

The model is highly simplified. Collisions of electrons and other species lead to resistive effects and make the drift waves non-linear. Moreover the amplitude can vary spatially in regions of different collisionality. In toroidal geometry, effects like a centrifugal force, a poloidal change in the ratio of the plasma pressure and the magnetic field pressure and other aspects that cause drifts—some have already been mentioned—come along. We postpone the discussion of these effects to chapter 3 and now introduce the two most important resistive effects that are present in the edge layer, the *Drift Alvèn* and the *Drift Resistive Ballooning* instability.

1.3.4.1 Drift Alfvén

In the plasma core, the pressure is much higher than at the edge, thus a radial pressure gradient exists. Charged particles gyrate around the field lines. Their trajectories are helical curves, hence the distance to the plasma core varies within each turn. The force of the pressure gradient is directed radially outwards and the charged particles are accelerated in poloidal direction, where the sign of direction depends on the electric charge. The plasma column starts to rotate. When rotation speed differs with respect to poloidal position, there is resistivity and a drift current in perpendicular direction arises, which is called *drift Alfvén*.

1.3.4.2 Drift Resistive Ballooning

Drift resistive ballooning modes are unstable modes triggered by resistivity. Its name denotes the fact that the amplitude of the perturbation wave and the corresponding transport depends on the poloidal angle such that the maximum is at the outer side (LFS) and the minimum at the inner side (HFS). The accumulation at LFS causes the ballooning character.

The physical background is the $1/R$ dependence of the magnetic field, such that the plasma pressure

$$\beta \propto \frac{nT}{B^2}$$

is smaller at LFS than at HFS. In [23] and references therein it is shown that the poloidal dependence of the magnetic field strength increases the resistivity at the LFS and thus makes the mode more unstable there.

1.3.5 MARFE

As mentioned earlier, high densities are required to achieve the thermonuclear burn conditions for a self sustaining Tokamak plasma. However, experiments revealed a limit on the maximal achievable density, the so called *Greenwald limit*, at the edge. When this limit is exceeded, a degradation of the plasma confinement or a disruption of the plasma discharge generally occurs.

One phenomena preceding the disruption at the density limit is *multi faceted asymmetric radiation from the edge* (MARFE). It is a zone of high radiation causing a huge loss of energy. Generally, it develops at the HFS, where heating power from the core is smaller due to the shifted flux surfaces. When temperature drops, density rises, while the pressure $p = n(\theta)T(\theta)$ is (nearly) constant.

The radiative power density q_{rad} is determined by the electron density n_{e}, the impurity density n_{Z} and the cooling rate L_{Z}, which is the radiation rate for the impurity. The relation $q_{\mathrm{rad}} = n_{\mathrm{e}} n_{\mathrm{Z}} L_{\mathrm{Z}}$ holds. Increasing density enhances the radiation power and consequently further cools down the edge layer of the plasma, causing the density to increase even further. This self reinforcing process is called radiation instability.

MARFE occurs in the whole toroidal direction. Depending on the heating and heat transport, MARFE can be localized at one poloidal position (generally the HFS) or affects the whole edge layer causing a detachment of the plasma from the SOL. Density limit can be increased by additional heating.

A mechanism triggering the MARFE, is localized recycling of particles between the plasma edge and the first wall. Energy losses are caused by charge exchange, ionization and heating processes of the neutral influx. In a later chapter this is stated more precisely by equations and some simulations on the poloidal position of neutral influx are done.

Chapter 2

Introduction to eigenvalue problems

In this chapter we collect some basic definitions and propositions associated with the numerical solution of eigenvalue problems. It is the knowledge which is required in the subsequent chapters and is usually taught in lectures of linear algebra and numerical mathematics. [4] offers a very comprehensive survey on the topic.

2.1 Definitions from linear algebra

Definition 2.1. The complex space $\mathbb{C}$ augmented by infinity ∞ is denoted by

$$\overline{\mathbb{C}} := \mathbb{C} \cup \{z\infty \mid z \in \mathbb{C},\ |z| = 1\}$$

Definition 2.2. Let be $M_j \in \mathbb{C}^{N\times N}$, $j = 1, \ldots, d$, $N \in \mathbb{N}$. The function

$$P : \overline{\mathbb{C}} \to \overline{\mathbb{C}}^{N\times N}, \qquad P(\lambda) := \sum_{j=0}^{d} \lambda^j M_j \qquad \text{(matrix polynomial)}$$

is called *matrix polynomial* of *degree* $\deg(P) = d$.

It is called *singular*, if $\det(P) \equiv 0$ and otherwise *regular*.

Definition 2.3. Let $P : \overline{\mathbb{C}} \to \overline{\mathbb{C}}^{N\times N}$ be a matrix polynomial. The pair (λ, x) with $\lambda \in \overline{\mathbb{C}}$ and $x \in \mathbb{C}^N \setminus \{0\}$ is called an *eigenpair* of P if and only if

$$P(\lambda)x = 0. \qquad \text{(polynomial eigenvalue problem)}$$

The scalar λ is called *eigenvalue* and the vector x is called *eigenvector*. The aim to find such an eigenpair is called *polynomial eigenvalue problem*.

Definition 2.4. One speaks of an *eigenfunction* instead of an eigenvector, if the eigenvector approximates a function in function space.

Remark 2.5. If $M_0 = A$ and $M_1 = -I$, the polynomial eigenvalue problem is the *standard eigenvalue problem*

$$Ax = \lambda x \qquad \text{(standard eigenvalue problem)}$$

and it is a *generalized eigenvalue problem*

$$Ax = \lambda Bx \qquad \text{(generalized eigenvalue problem)}$$

if $M_0 = A$ and $M_1 = -B$.

Lemma 2.6. *A generalized eigenvalue problem*

$$Ax = \lambda Bx$$

can be reduced to a standard eigenvalue problem if and only if A or B are regular.

Proof. If B is regular, B^{-1} exists and

$$(B^{-1}A)x = \lambda x$$

is a standard eigenvalue problem.

If A is regular, A^{-1} exists and

$$x = \lambda A^{-1}Bx \quad \Leftrightarrow \quad \mu x = \frac{1}{\lambda}x = (A^{-1}B)x$$

is a standard eigenvalue problem on the inverse eigenvalue. □

Lemma 2.7. *Polynomial eigenvalue problems $P(\lambda)x = 0$ of dimension $N \times N$ with $\deg P =: d \geq 2$ can be reduced to a generalized eigenvalue problem of size $dN \times dN$. It has dN eigenpairs (including multiplicities).*

Proof. The proof is done by two out of many possible *linearizations*. I is the identity matrix with ones on the diagonal and zero else. Then one has

$$\begin{aligned} P(\lambda)x &= \sum_{j=0}^{d} \lambda^j M_j x = 0 \\ &\Longleftrightarrow \left(\lambda \begin{bmatrix} M_1 & M_2 & M_3 & \dots & M_d \\ I & & & & \\ & I & & & \\ & & \ddots & & \\ & & & I & \end{bmatrix} + \begin{bmatrix} M_0 & & & & \\ & -I & & & \\ & & -I & & \\ & & & \ddots & \\ & & & & -I \end{bmatrix} \right) \begin{pmatrix} x \\ \lambda x \\ \lambda^2 x \\ \vdots \\ \lambda^{d-1} x \end{pmatrix} = 0, \end{aligned}$$

Another linearization, called companion form, is given by

$$\left(\lambda \begin{bmatrix} M_d & & & \\ & I & & \\ & & I & \\ & & & \ddots \\ & & & & I \end{bmatrix} + \begin{bmatrix} M_{d-1} & M_{d-2} & M_{d-3} & \dots & M_0 \\ -I & & & & \\ & -I & & & \\ & & \ddots & & \\ & & & -I & \end{bmatrix} \right) \begin{pmatrix} \lambda^{d-1} x \\ \lambda^{d-2} x \\ \lambda^{d-3} x \\ \vdots \\ x \end{pmatrix} = 0.$$

□

Remark 2.8. Both linearizations are equivalent, but the numerical stability and efficiency of numerical algorithms might be different. It is possible to replace the identity matrices in each block row by any regular matrix. If M_d is regular with a small condition number, the second linearization allows to reduce the generalized eigenvalue problem to a standard one. There are other possibilities to arrange the blocks in the linearization, however a diagonal matrix and an upper block Hessenberg seem to be the best structures for a generalized eigenvalue equation. This becomes more clear after the QZ algorithm, the state of the art technique to solve generalized eigenvalue problems, is analyzed in section 2.2.2 on page 27.

Remark 2.9. If the matrix polynomial contains structure, that specifies its eigenvalues, for example it is symmetric, skew symmetric, Hermitian or skew Hermitian, then it is a good idea to choose the linearization wisely and preserve these features by permutation of rows and columns. The eigenvalue problem concerned in this thesis is complex symmetric, which does not offer any information about its eigenvalues. Therefore the linearization is not considered here, further.

Remark 2.10. The eigenvectors of polynomial eigenvalue problems of $\deg p > 1$ are linearly dependent.

Definition 2.11. Let be $M \in \mathbb{C}^{N\times N}$. The *null space* of M is

$$\mathcal{N}(M) := \left\{x \in \mathbb{C}^N \mid Mx = 0\right\}$$

and the *range* is defined by

$$\mathcal{R}(M) := \left\{z \in \mathbb{C}^N \mid z = Mx,\ x \in \mathbb{C}^N\right\}.$$

Definition 2.12. The *characteristic polynomial* p_P of a matrix polynomial P is defined by

$$p_P(\lambda) := \det\left(P(\lambda)\right)$$

Lemma 2.13. *Polynomial eigenvalue problems $P(\lambda)x = 0$ can have infinite eigenvalues. The degree $g := \deg p_P$ of the characteristic polynomial p_P is at most dN and the missing $dN - g$ roots are defined as infinite eigenvalues. The generalized eigenvalue equation*

$$Ax = \lambda Bx$$

with $\mathcal{N}(A) = \{0\}$ has $\dim\mathcal{N}(B) = N - \operatorname{rank}(B)$ infinite eigenvalues.

Proof. Each polynomial eigenvalue problem of $\deg P > 1$ is equivalent to a generalized eigenvalue problem. Let $0 \neq y \in \mathcal{N}(B)$, then it holds $y \notin \mathcal{N}(A)$ and

$$\mu \underbrace{Ay}_{\neq 0} = By = 0 \quad \Rightarrow \quad 0 = \mu = \frac{1}{\lambda} \quad \Rightarrow \quad \lambda = \infty$$

To proof the number of infinite eigenvalues, we take a similarity transformation $YBY^{-1} = J$ to Jordan canonical form. The $N - \operatorname{rank}(B)$ last rows of J are zero and thus the degree of

$$p_P(\lambda) = \det(A - \lambda B) = \det(YAY^{-1} - \lambda YBY^{-1}) = \det(YAY^{-1} - \lambda J)$$

is $g = \operatorname{rank}(B)$. □

Remark 2.14. In case $\mathcal{N}(A) \cap \mathcal{N}(B) \neq \{0\}$ the undefined eigenvalues are called infinite, too.

Remark 2.15. Standard eigenvalue problems have no infinite eigenvalues because the "B" matrix is the identity I and $\mathcal{N}(I) = \{0\}$.

Definition 2.16. For $A \in \mathbb{C}^{N\times N}$, $x \in \mathbb{C}^N$, the *Rayleigh quotient* is defined by

$$\rho_A(x) := \frac{x^H Ax}{x^H x}.$$

Lemma 2.17. *Let be $x \in \mathbb{C}^N$ the eigenvector of $A \in \mathbb{C}^{N\times N}$ with the eigenvalue $\lambda \in \mathbb{C}$. It holds*

$$\lambda = \rho_A(x) = \frac{x^H Ax}{x^H x}.$$

Subsequent definitions and propositions are given that deal with the eigenvalue enclosure.

Definition 2.18. Let $A \in \mathbb{C}^{N\times N}$ be a matrix. The set

$$\mathcal{F}(A) := \left\{\rho_A(x) \mid x \in \mathbb{C}^N \setminus \{0\}\right\}$$

of all Rayleigh quotients is denoted as the *field of values* [14, 17] of A.

The relation of the field of values to the set of the eigenvalues yields the following lemma.

Lemma 2.19. *Let $A \in \mathbb{C}^{N\times N}$ be a matrix and $\lambda(A)$ be the set of all eigenvalues, then*

$$\lambda(A) \subseteq \mathcal{F}(A).$$

If A is normal, i.e. $A^H A = AA^H$, it holds

$$\operatorname{conv}\big(\lambda(A)\big) = \mathcal{F}(A),$$

where conv *denotes the convex hull.*

Now, the concept of the field of values is extended for polynomial eigenvalue equations (cf. [21]).

Definition 2.20. Let $P : \overline{\mathbb{C}} \to \overline{\mathbb{C}}^{N\times N}$ be a matrix polynomial. The field of values of the matrix polynomial eigenvalue equation is defined as

$$\mathcal{F}(P) := \left\{\operatorname{roots}(x^H P x) \mid x \in \mathbb{C}^N \setminus \{0\}\right\},$$

where

$$\operatorname{roots}(x^H P x) := \left\{\lambda \in \mathbb{C} \mid x^H P(\lambda) x = 0\right\}.$$

Remark 2.21. Let $A \in \mathbb{C}^{N\times N}$ be a matrix. For the matrix polynomial $P(\lambda) = A - \lambda I$ definition 2.20 implies 2.18.

Definition 2.22. [25] Let $P : \overline{\mathbb{C}} \to \overline{\mathbb{C}}^{N\times N}$ be a matrix polynomial. P is called *weakly normal* if there is a unitary matrix $U \in \mathbb{C}^{N\times N}$ such that $U^H P(\lambda) U$ is diagonal for all $\lambda \in \mathbb{C}$.
If, in addition, every diagonal entry of $U^* P(\lambda) U$ is a polynomial with exactly $N \deg(P)$ distinct zeros, or equivalently, all the eigenvalues of P are semisimple (i.e., for each eigenvalue the algebraic and the geometric multiplicity are equal), then P is called *normal*.

Remark 2.23. Let P be a weakly normal matrix polynomial. The left and the right eigenvector of each eigenvalue λ of P are equal.

The relation between the field of values of an eigenvalue polynomial and its projection onto a subspace $\mathcal{R}(V)$ offers the next lemma.

Lemma 2.24. *Let $P : \overline{\mathbb{C}} \to \overline{\mathbb{C}}^{N\times N}$ be a matrix polynomial and $V \in \mathbb{C}^{N\times k}$ a matrix. It holds*

$$\mathcal{F}(V^H P V) \subseteq \mathcal{F}(P)$$

Proof.

$$\begin{aligned}\mathcal{F}(V^H P V) = \left\{\operatorname{roots}(y^H V^H P V y) \mid y \in \mathbb{C}^k \setminus \{0\}\right\} &= \left\{\operatorname{roots}(x^H P x) \mid x = Vy,\ y \in \mathbb{C}^k \setminus \{0\}\right\} \\ &\subseteq \left\{\operatorname{roots}(x^H P x) \mid x \in \mathbb{C}^N \setminus \{0\}\right\} = \mathcal{F}(P)\end{aligned}$$

□

Remark 2.25. $\mathcal{F}(P)$ is still a colsed set, but it needs not to be connected or bounded [21]. The field of values of a normal matrix polynomial is not the convex hull of the eigenvalues in general.

2.2 Numerical methods for eigenvalue problems

In linear algebra, eigenvalues of linear eigenvalue equations are roots of the characteristic polynomial p_P. However, there is no analytic formula to obtain the roots of polynomials larger than degree 4 ($\deg p_P > 4$) explicitly and something like Newton iteration is necessary. Additionally, determining the eigenvalues from the coefficients of the characteristic polynomial is numerically unstable. Tiny errors in the coefficients often lead to huge loss of precision of the roots. Evaluating the characteristic polynomial directly is more stable at the one hand, but cost-intensive on the other hand. The effort to calculate a determinant of a matrix rises exponentially with its dimension. Hence, the characteristic polynomial is only appropriate for very small problems and theoretical considerations.

In numerical mathematics several different techniques to calculate the eigenpairs have been developed. These techniques can be divided into two main groups. First, the algorithms for medium sized problems, that calculate one up to all eigenvalues and secondly the methods for huge eigenvalue equations, that calculate only a few eigenpairs projecting the huge problem onto a much smaller search space, which is build up within the algorithm. The projected system is small enough to be solved by techniques of the former group.

We start to recapitulate the basic algorithms for small eigenvalue equations up to the state of art techniques which are the QR and QZ algorithm. A more complete survey is [4]. Afterwards we introduce the Jacobi-Davidson method for large problems.

2.2.1 Standard algorithms

2.2.1.1 Power method

In order to solve the standard eigenvalue problem $Ax = \lambda x$ where $A \in \mathbb{C}^{N\times N}$, $\|x\| = 1$, the simplest algorithm is the *power method*. Let $(\lambda_j, x_j)_{j=1,\dots,N}$ be the exact eigenpairs ordered by modulus: $|\lambda_1| \geq |\lambda_2| \geq \ldots \geq |\lambda_N|$.

We assume $|\lambda_1| > |\lambda_2|$. A vector $y_0 \in \mathbb{C}^N$ satisfying $y_0^H x_1 \neq 0$ and $\|y_0\|_2 = 1$ can be written as a linear combination of the eigenvectors x_j

$$y_0 = \sum_{j=1}^{N} \beta_j x_j.$$

The idea of the *power method* is to apply A on y_0

$$Ay_0 = \sum_{j=1}^{N} \beta_j A x_j = \sum_{j=1}^{N} \beta_j \lambda_j x_j$$

several times

$$A^k y_0 = \sum_{j=1}^{N} \beta_j \lambda_j^k x_j = \beta_1 \lambda_1^k x_1 + \mathcal{O}\left(\left|\frac{\lambda_2}{\lambda_1}\right|^k\right)$$

until the direction of x_1 strongly dominates. This idea leads to Algorithm 1.

The power method only works, if the modulus of the largest eigenvalue is simple and y_0 is not perpendicular to x_1. When $|\lambda_1| = |\lambda_2| > |\lambda_3|$ is not simple, this method only works, if $y_0^H x_1 \neq 0$ and $y_0^H x_2 = 0$. However, this is numerical highly unstable. Summing up the basic features of this method:

- convergence if $\eta := \left|\frac{\lambda_2}{\lambda_1}\right| < 1$ and $x_1^H y_0 \neq 0$.
- approximation $\rho(y_k) = \lambda_1 + \mathcal{O}(\eta^k)$, slow if $\eta \approx 1$.
- finds λ_1 only.

Algorithm 1 Power method

Initial guess $\|y_0\|_2 = 1$.
for $k = 0, 1, \ldots, l$ **do**
  $z_{k+1} = Ay_k$ // power
  $\rho_k = y_k^H z_{k+1}$ // Rayleigh quotient $\frac{y_k^H A y_k}{y_k^H y_k}$
  $y_{k+1} = \frac{z_{k+1}}{\|z_{k+1}\|_2}$ // avoid over and underflow
end for
(ρ_l, y_l) is approximation of eigenpair (λ_1, x_1).

Definition 2.26. Let be $A \in \mathbb{C}^{N\times N}$, a *shift* $\mu \in \mathbb{C}$ is a multiple of the identity matrix subtracted to A:

$$\widetilde{A} = A - \mu I$$

2.2.1.2 Inverse power method with shift

A method, that can find interior eigenvalues as well as exterior ones, is the *inverse power method with shift*. The idea of this method is to apply the power method on A^{-1} or on the inverse of the shifted matrix $(A - \mu_0 I)^{-1}$. The eigenvalues of A^{-1} are the inverse eigenvalues of A. Thus, the inverse power method finds the eigenvalue closest to zero. The smallest eigenvalue of the shifted matrix $A - \mu_0 I$ is the eigenvalue of A closest to μ_0. Therefore this method can find any simple eigenvalue, when an appropriate guess μ_0 is available.

The numerical effort in calculating the inverse matrix is in $\mathcal{O}(N^3)$. However it is not necessary to know the inverse. It is sufficient to be able to solve the linear equation systems. The following definitions offer a method to do this with less effort.

Definition 2.27. For a regular matrix $A \in \mathbb{C}^{N\times N}$ the *LU decomposition*

$$LU = A$$

consists of a lower triangular matrix L and an upper triangular matrix U. All the diagonal entries of L are equal to one. The factors L and U are obtained by Gaussian elimination, if necessary with row interchanges collected in a permutation matrix $\mathcal{P}$:

$$LU = \mathcal{P}A$$

Remark 2.28. Systems of linear equation $Ax = b$ ($A \in \mathbb{C}^{N\times N}$, $b \in \mathbb{C}^N$) can be solved by backward and forward elimination from the LU decomposition as follows

$$LUx = Ax = b \qquad \Longleftrightarrow \qquad \left\{\begin{array}{l} Ly = b \\ Ux = y \end{array}\right\}.$$

The equation $Ly = b$ is solved by forward elimination and afterwards $Ux = y$ is solved by backward elimination. Calculating the inverse A^{-1} of A has a computational cost of solving N linear systems by one LU decomposition.

The inverse power method with shift is described in Algorithm 2. Its basic features are

- it converges if $\eta := \max_{m \neq j} \left| \frac{\lambda_j - \mu_0}{\lambda_m - \mu_0} \right| < 1$ and $x_j^H y_0 \neq 0$
- it finds the eigenvalue λ_j closest to μ_0
- its approximation $\rho(y_k) = \lambda_j + \mathcal{O}(\eta^k)$ is slow, if $\eta \approx 1$

Algorithm 2 Inverse power method with shift

Initial guess $\|y_0\|_2 = 1$.
μ_0 initial guess for desired eigenvalue.
Calculate LU decomposition of $A - \mu_0 I$.
for $k = 0, 1, \ldots$ **do**
  Solve $(A - \mu_0 I) z_{k+1} = y_k$ with LU decomposition.
  $y_{k+1} = \frac{z_{k+1}}{\|z_{k+1}\|_2}$ // avoid over and underflow
  $\rho_k = \rho_A(y_{k+1}) = y_{k+1}^H A y_{k+1}$ // Rayleigh quotient
end for

An improvement of the inverse power method with shift is the *Rayleigh quotient iteration* (Algorithm 3). The shift μ_0 is applied in first iteration and in subsequent iteration, A is shifted by the Rayleigh quotient, which is the best known approximation of the desired eigenvalue. The convergence rate is squared, but the LU decomposition has to be recalculated in each loop.

Summing up, the Rayleigh quotient iteration

- converges if $\eta_0 := \max_{m \neq j} \left| \frac{\lambda_j - \mu_0}{\lambda_m - \mu_0} \right| < 1$ and $x_j^H y_0 \neq 0$.
- finds an eigenvalue λ_j close to μ_0.
- if $\eta_0 < 1$: $\eta_k := \max_{m \neq j} \left| \frac{\lambda_j - \mu_k}{\lambda_m - \mu_k} \right| \ll 1, \quad \lim_{k \to \infty} \eta_k = 0.$
- approximation $\rho(y_k) = \lambda_j + \mathcal{O}(\eta_0^{2k})$.
- recalculation of LU decomposition in each step is expensive
- converges quadratic

A possible variant of the Rayleigh quotient iteration is to update the shift and recalculate the LU decomposition not in each cycle, but after a few ones.

Algorithm 3 Rayleigh quotient iteration

Initial guess $\|y_0\|_2 = 1$.
μ_0 initial guess for desired eigenvalue.
for $k = 0, 1, \ldots$ **do**
  Calculate LU decomposition of $(A - \mu_k I)$.
  Solve $(A - \mu_k I) z_{k+1} = y_k$ with LU decomposition.
  $y_{k+1} = \frac{z_{k+1}}{\|z_{k+1}\|_2}$ // avoid over and underflow
  $\rho_k = \rho_A(y_{k+1}) = y_{k+1}^H A y_{k+1}$ // Rayleigh quotient
  $\mu_k := \rho_k$ // set shift to Rayleigh quotient
end for

2.2.1.3 QR algorithm

State of art in calculating all eigenvalues of a matrix $A \in \mathbb{C}^{N\times N}$, where N is not too large, is the QR *algorithm with shift* (Algorithm 5).

Definition 2.29. The QR *decomposition* of a matrix $A \in \mathbb{C}^{N\times N}$ is

$$A = QR$$

where $Q \in \mathbb{C}^{N\times N}$ is unitary and $R \in \mathbb{C}^{N\times N}$ an upper triangular matrix. The decomposition can be calculated by *Householder transformations* or *Givens rotations*. R is unique except for unitary diagonal transformations.

Within the QR algorithm

$$A_{k+1} := R_k Q_k = Q_k^H A_k Q_k = (Q_{k-1}Q_k)^H A_{k-1}(Q_{k-1}Q_k) = \widehat{Q}_k^H A_0 \widehat{Q}_k$$

is a unitary similarity transformation. In the end the approximations to the eigenvalues of A are on the diagonal of A_k, that is an upper triangular matrix [4].

Definition 2.30. A matrix H is *upper Hessenberg* if all elements below the first sub-diagonal are zero.

$$H = \begin{bmatrix} * & \cdots & \cdots & * \\ * & \ddots & \ddots & \vdots \\ & \ddots & \ddots & \vdots \\ & & * & * \end{bmatrix}$$

The variant of the QR algorithm without shift often converges very slowly. A clever choice of the shifts accelerates the convergence. Before the choice of shifts can be explained, some numerical details on the QR algorithm have to be given. The computational effort of the QR decomposition is generally in $\mathcal{O}(N^3)$. However, it is in $\mathcal{O}(N^2)$ for upper Hessenberg matrices, because there are non-zeros only on the first sub-diagonal.

In the QR algorithm, A is unitary transformed to an upper Hessenberg matrix H at first. The QR algorithm is applied to H, which has the same eigenvalues as A. Within the QR algorithm, H remains upper Hessenberg.

If H is upper Hessenberg and if the entry $h_{N,N-1}$ is eliminated, one eigenvalue is equal to the entry in the lower right corner and the problem can be reduced to $H := (h_{i,j})_{i,j=1,\ldots,N-1}$. This is achieved applying the *Wilkinson shift*: the two eigenvalues of the 2×2 block in the lower right corner

$$\begin{bmatrix} h_{N-1,N-1} & h_{N-1,N} \\ h_{N,N-1} & h_{N,N} \end{bmatrix}$$

are calculated analytically and the eigenvalue closer to $h_{N,N}$ is chosen as shift.

Algorithm 4 QR algorithm

```
A_0 := A
for k = 0, 1, ... do
    Calculate QR decomposition A_k = Q_k R_k.
    A_{k+1} := R_k Q_k
end for
```

Algorithm 5 QR algorithm with shift

$A_0 := A$
for $k = 0, 1, \ldots$ **do**
  Choose a shift μ_k. // e.g. Wilkinson shift
  Calculate QR decomposition $A_k - \mu_k I = Q_k R_k$.
  $A_{k+1} := R_k Q_k + \mu_k I$ // undo shift
end for

2.2.2 Solving generalized eigenvalue problem

For the generalized eigenvalue problems

$$Ax = \lambda Bx$$

the power method is not applicable. However, the inverse power method with shift is realizable in the way that the shift μI is replaced by μB, where μ is some guess for the desired eigenvalue of

$$(A - \lambda B)x = 0.$$

The Rayleigh quotient variant works as well.

2.2.2.1 The QZ algorithm

The QZ algorithm plays the role of the QR algorithm for generalized eigenvalue equations and calculates all the eigenvalues.

Definition 2.31. For two matrices $A, B \in \mathbb{C}^{N\times N}$ the QZ *decomposition* (also named *generalized Schur decomposition*) consists of two different unitary matrices Q and $Z \in \mathbb{C}^{N\times N}$, such that $\widehat{A} := QAZ$ is upper Hessenberg and $\widehat{B} := QBZ$ is upper triangular.

For unitary matrices Q, Z the similarity transformations

$$\begin{aligned} & Ax = \lambda x \\ \Leftrightarrow\ & QAQ^H y = \lambda QQ^H y = \lambda y, \quad y = Qx \end{aligned}$$

and

$$\begin{aligned} & Ax = \lambda x \\ \Leftrightarrow\ & Z^H AZy = \lambda Z^H Zy = \lambda y, \quad y = Z^H x \end{aligned}$$

do not change the eigenvalues. Analogously the pre- and post-multiplication of unitary matrices

$$\begin{aligned} & Ax = \lambda Bx \\ \Leftrightarrow\ & QAZy = \lambda QBZy, \quad y = Z^H x \\ \Leftrightarrow\ & \widehat{A}y = \lambda \widehat{B}y, \quad y = Z^H x \end{aligned}$$

do not change the eigenvalues. When $\widehat{A}$ and $\widehat{B}$ are upper triangular, the eigenvalues can be picked from the diagonal elements

$$\lambda_j = \frac{\widehat{a}_{j,j}}{\widehat{b}_{j,j}}, \qquad j = 1, \ldots, N.$$

In order to calculate the QZ decomposition for the generalized eigenvalue equation $\widetilde{A}x = \lambda\widetilde{B}x$, first $\widetilde{B}$ is transformed to an upper triangular matrix B by QR decomposition $\widetilde{B} = \widetilde{Q}B$

$$\begin{aligned} & \widetilde{A}x = \lambda\widetilde{B}x \\ \Leftrightarrow\ & Ax = \lambda Bx, \qquad A = \widetilde{Q}^H\widetilde{A} \\ \Leftrightarrow\ & \begin{bmatrix} a_{11} & a_{12} & \cdots & a_{1N} \\ a_{21} & a_{22} & \cdots & a_{2N} \\ \vdots & \vdots & \ddots & \vdots \\ a_{N1} & a_{N2} & \cdots & a_{NN} \end{bmatrix} \begin{bmatrix} x_1 \\ x_2 \\ \vdots \\ x_N \end{bmatrix} = \lambda \begin{bmatrix} b_{11} & b_{12} & \cdots & b_{1N} \\ 0 & b_{22} & \cdots & b_{2N} \\ \vdots & \ddots & \ddots & \vdots \\ 0 & \cdots & 0 & b_{NN} \end{bmatrix} \begin{bmatrix} x_1 \\ x_2 \\ \vdots \\ x_N \end{bmatrix} \end{aligned}$$

Now the Givens rotation $Q_{N-1,N}$ is applied from the left to eliminate $a_{N,1}$

$$Q_{N-1,N}A = \begin{bmatrix} a_{11} & a_{12} & \cdots & a_{1N} \\ \vdots & \vdots & \ddots & \vdots \\ a_{N-2,1} & a_{N-2,2} & \cdots & a_{N-2,N} \\ a'_{N-1,1} & a'_{N-1,2} & \cdots & a'_{N-1,N} \\ 0 & a'_{N2} & \cdots & a'_{NN} \end{bmatrix}.$$

However, fill-in occurs below the diagonal of B at position $(N, N-1)$:

$$Q_{N-1,N}B = \begin{bmatrix} b_{11} & b_{12} & \cdots & b_{1,N-1} & b_{1N} \\ 0 & b_{22} & \cdots & b_{2,N-1} & b_{2N} \\ \vdots & \ddots & \ddots & \vdots & \vdots \\ 0 & \cdots & 0 & b_{N-2,N-1} & b_{N-2,N} \\ 0 & \cdots & 0 & b'_{N-1,N-1} & b'_{N-1,N} \\ 0 & \cdots & 0 & b'_{N,N-1} & b'_{N,N} \end{bmatrix}.$$

To remove the fill-in, another rotation $Z_{N-1,N}$ is applied from the right. Fortunately, $Z_{N-1,N}$ does not remove any of the produced zeros in left lower corner of A. The Givens rotations can be applied by this procedure until A is upper Hessenberg. From there on, further rotations will destroy zeros again.

$QAZ =: H$ is upper Hessenberg and $QBZ =: U$ is still upper triangular and the generalized eigenvalue problem

$$Hy = \lambda Uy$$

remains. If U is not invertible, there is at least one infinite eigenvalue. It can be obtained from the null-space of U and it can be eliminated. Hence, without loss of generality we assume, that B is invertible and end up with the standard eigenvalue problem

$$HU^{-1}z = \lambda z$$

Note that the inverse U^{-1} is upper triangular, since U is.

To apply one step of the QR algorithm

$$HU^{-1} = QR = Q\widetilde{R}U^{-1},$$

requires a QR decomposition of H only, which is less expensive since H is upper Hessenberg. However, to obtain the Wilkinson shift, one needs to know the bottom right 2×2 block of HU^{-1}. This block can be generated from the bottom right 2×3 block of H and the 3×2 block of U^{-1}. Due to the upper triangular shape, the latter one is obtained by Gaussian elimination of the bottom right 3×2 block of U. The remaining part is analogous to the QR algorithm.

2.2.3 Solving polynomial eigenvalue problems

Algorithms to solve standard and generalized eigenvalue problems are listed above. The polynomial eigenvalue equation P, with $\deg P \geq 2$, can be solved by standard eigenvalue problem solvers by linearization. The inverse power method and Rayleigh quotient iteration are applicable directly.

2.2.4 Classification

According to [4] we define the following classification of algorithms:

Definition 2.32. We denote the QR and QZ algorithms as *direct solvers* in contrast to the algorithms for large eigenvalue problems which are introduced in the next section and denoted as *iterative solvers*.

Remark 2.33. A direct algorithm must still iterate, since finding eigenvalues is mathematically equivalent to finding zeros of polynomials, for which no noniterative methods can exist beyond the dimension 4. We call a method direct if experience show that it (nearly) never fails to converge in a fixed number of iterations.

2.3 Numerical methods for large eigenvalue problems

Theoretically, the numerical algorithms mentioned above are applicable for arbitrary dimensions. But practically, they are limited by memory restrictions and computational time. The effort of the QR algorithm is in $\mathcal{O}(N^4)$ and cannot be handled for large N on current computers. In this section numerical methods are introduced, that calculate a few eigenvalues with less computational cost.

Huge eigenvalue problems often arise from discretized partial differential equations. One common feature of discretizing derivatives by finite differences (cf. section 4.2.1 on page 49) is the fact, that the matrices are sparse. One idea to reduce memory requirement and computational effort of matrix vector products is to save non-zero entries, only.

Definition 2.34. A matrix $S \in \mathbb{C}^{N\times N}$ is called *sparse*, if there are only $\mathcal{O}(N)$ entries non-zero. It is called *dense* or *full*, if $\mathcal{O}(N^2)$ elements are non-zero.
The positioning of zero and non-zero entries is called *sparsity pattern*.

Remark 2.35. Let $A, S \in \mathbb{C}^{N\times N}$, A full, S sparse, $v \in \mathbb{C}^N$. The computational cost of the matrix vector product Av is in $\mathcal{O}(N^2)$ and Sv in $\mathcal{O}(N)$.

Definition 2.36. Let $V \in \mathbb{C}^{N\times k}$, $(k < N)$ be a basis of a k-dimensional subspace of $\mathbb{C}^{N\times N}$ and let P be a matrix polynomial. The pair (ν, y), $\nu \in \mathbb{C}$, $0 \neq y \in \mathcal{R}(V)$ is called *Ritz pair* if and only if

$$P(\nu)y \perp \mathcal{R}(V)$$

holds. In particular, y is called *Ritz vector* and ν a *Ritz value*.

2.3.1 Jacobi-Davidson method

The Jacobi-Davidson method was initially proposed as a solution technique for standard eigenvalue problems [10], but it works with polynomial eigenvalue problems as well [32]. Here, the

polynomial case is described, which can be easily restricted to the special case of a standard eigenvalue problem.

The idea of Davidson is to approximate the initial problem

$$P(\lambda)x = 0$$

by a projection onto a low-dimensional search space, spanned by the orthonormal columns of the matrix V:

$$V^H P(\nu)Vy = 0.$$

Due to much lower dimension, the projected system can be solved by a direct solver, i.e., linearization and applying QZ algorithm on the generalized eigenvalue equation. The solution of the projected system is linked to an approximation of the original one by the *Galerkin condition*

$$u = Vy, \qquad P(\nu)u =: r \perp \mathcal{R}(V),$$

thus (ν, u) is a Ritz pair.

This method is efficient, if the dimension of search space V remains small. On the other hand, the accuracy of the approximation Vy depends on the angle between the desired eigenvector x and the search space $\mathcal{R}(V)$. This angle must be small for a proper approximation. Therefore, the search space needs to be expanded carefully.

The idea to expand the search space V by the *residual* r is formally equivalent to the *Arnoldi process*. In the original algorithm, Davidson expanded the search space by

$$t = -\Big(\operatorname{diag}\big(P(\nu)\big)\Big)^{-1} r,$$

which works well with strongly diagonal dominant matrices. To take $t = P(\nu)^{-1}r$ is equivalent to the inverse power method with shift. The inversion is expensive and the result is dense in general.

At this point, the idea of Jacobi comes into play. The current Ritz pair (ν, u) is improved by an update (η, v) such that

$$P(\nu + \eta)(u + v) = 0.$$

This is a nonlinear equation that cannot be solved directly, but a Newton step can be applied on the system

$$f(\lambda, x) := \begin{pmatrix} P(\lambda)x \\ x^H x - 1 \end{pmatrix} = 0. \tag{2.1}$$

The first block line is the original eigenvalue equation and the bottom row is a normalization of the eigenvector, such that $\|x\|_2 = 1$. The latter one cures the rank deficiency.

The Newton iteration requires the derivative

$$Df(\lambda, x) = \begin{pmatrix} P'(\lambda)x & P(\lambda) \\ 0 & 2x^H \end{pmatrix}. \tag{2.2}$$

Let (ν, u) be a Ritz pair of P with respect to the search space $\mathcal{R}(V)$. It holds $u \in \mathcal{R}(V)$ and therefore

$$P(\nu)u = r \perp u. \tag{2.3}$$

Now f is linearized at the Ritz pair (ν, u) and a correction step (η, v) is added to find an improved eigenvector $x = u + v$ and an eigenvalue $\lambda = \nu + \eta$ such that

$$Df(\nu, u)\begin{pmatrix} \eta \\ v \end{pmatrix} = -f(\nu, u) \quad \Leftrightarrow \quad \begin{pmatrix} P'(\nu)u & P(\nu) \\ 0 & 2u^H \end{pmatrix}\begin{pmatrix} \eta \\ v \end{pmatrix} = \begin{pmatrix} -r \\ 0 \end{pmatrix} \tag{2.4}$$

We multiply the first block line by u^H from the left and get

$$\eta u^H P'(\nu)u + u^H P(\nu)v = -u^H r = 0 \quad \Leftrightarrow \quad \eta = -\frac{u^H P(\nu)v}{u^H P'(\nu)u}. \tag{2.5}$$

The second block line demands

$$v \perp u \quad \Leftrightarrow \quad \left(I - \frac{uu^H}{u^H u}\right) v = v \tag{2.6}$$

an orthogonal projection onto $u^\perp$.

Finally, equation (2.5) and (2.6) are linked to the *correction equation*

$$\left(I - \frac{P'(\nu)uu^H}{u^H P'(\nu)u}\right) P(\nu) \left(I - \frac{uu^H}{u^H u}\right) v = -r. \tag{2.7}$$

The new direction v is then orthonormalized to the search space V and added to V:

$$V := \mathrm{orth}(V, v).$$

The correction equation enlarges the search space until the approximation is sufficiently accurate. In order to keep $k \ll N$ it might be necessary to apply *restarts* or *deflation*. At a restart the search space is set to the current eigenvalue approximation ($V = u$), while the deflation skips certain columns of V, but not all. A possible deflation strategy is to keep the last l columns where $l \ll N$.

Algorithm 6 Jacobi-Davidson algorithm

Require: matrix polynomial $P_l(\nu) = \sum_{j=0}^{l} \nu^l M_j$, $M_j \in \mathbb{C}^{N\times N}$.
  choose an initial search space $V = [v^1, \ldots, v^k] \in \mathbb{C}^{N\times k}$, $1 \le k \ll N$.
  loop
    orthonormalize V.
    calculate $W_j := M_j V$ and $H_j := V^H W_j$ for $j = 0, \ldots, l$.
    calculate desired eigenpair(s) of projected equation $\widetilde{P}_l(\nu) := \sum_{j=0}^{l} \nu^j H_j y = 0$, $\|y\| = 1$.
    calculate Ritz value in original space $u := Vy$.
    calculate $w := P_l'(\nu)u = \sum_{j=1}^{l} \nu^{j-1} M_j u$
    calculate residual $r := P_l(\nu)u$.
    if $\|r\| <$ tolerance **then**
      stop
    end if
    solve correction equation (approximately) $\left(I - \frac{wu^H}{u^H w}\right) P_l(\nu)(I - uu^H)t = -r$
    expand search space $V := [V, t]$.
  end loop

2.3.2 Solving the correction equation

The correction equation (2.7) is derived from one Newton step. Therefore, it is not necessary to solve it exactly, but approximately. However, the convergence speed of the outer Jacobi-Davidson algorithm depends on the level of the precision. Therefore one has to find the optimal balance.

The generic form of the correction equation (2.7) is

$$XPYv = -r, \quad \text{where} \quad X := \left(I - \frac{P'(\nu)uu^H}{u^H P'(\nu)u}\right), \quad Y := \left(I - \frac{uu^H}{u^H u}\right) \text{ and } P := P(\nu). \tag{2.8}$$

The projections X and Y are sparse matrices and in many applications P is sparse too. In the following considerations we assume P to be sparse. Although X, Y and P are sparse, the product XPY is dense in general. To make use of the sparsity iterative solver have to be applied on (2.8). This class of solvers works with matrix vector multiplications that can be realized as $XPYv = X(P(Yv))$. The iterative solvers require preconditioners specified as approximations K for XPY such that the equation $Kt = r$ can be solved relatively easily. The simplest idea is to chose K as the diagonal or the upper or lower triangular part of XPY.

2.3.2.1 Inverse projection

The iterative solvers for (2.8) require a suitable preconditioner K. The standard ideas like taking the diagonal or the upper or lower triangular part of the matrix XPY are not efficient and cannot make use of the particular structure of the equation.

In [32] Sleijpen et al. considered to take the projections into account. We assume to have an approximation Q such that $QP \approx I$ holds and define the preconditioner

$$K := XQ^{-1}Y.$$

The inverse K^{-1} of the preconditioner is required in order to apply it as $K^{-1}XPYv = -K^{-1}r$. The projections cause K to be singular with null space spanned by u. We are only interested in the solution perpendicular to u. Therefore the *pseudo inverse*

$$K^{-1} = YQX$$

is taken. We call K^{-1} pseudo inverse because

$$K^{-1}(Kv) = v \qquad \forall v : v^H u = 0$$

A projection applied once has the same effect as applying it twice and due to $u \perp r$, $Xr = r$ the preconditioned correction equation reads

$$YQXPYv = -YQr. \tag{2.9}$$

Now iterative solvers like *generalized minimal residual* (GMRES) [30] or the *biconjugate gradients stabilized method* (BiCGstab) [41] can be applied to (2.9).

2.3.2.2 One step approximation

Sleijpen et. al [34] suggested the *one step approximation* as a method to solve the correction equation (2.7) without additional iterative solver if a good approximation $Q(\nu)$ of $P(\nu)$ is available.

We deduce the formula. The Newton equation (2.4) is multiplied by an (approximate) inverse $Q(\nu)$ satisfying $Q(\nu)P(\nu) \approx I$

$$\eta Q(\nu)P'(\nu)u + Q(\nu)P(\nu)v = -Q(\nu)r, \qquad u^H v = 0$$

$$\Rightarrow \eta Q(\nu)P'(\nu)u + Q(\nu)r + v \approx 0.$$

The multiplication of u^H from the left leads to

$$\eta u^H Q(\nu)P'(\nu)u + u^H Q(\nu)r + \underbrace{u^H v}_{=0} = 0 \qquad \Rightarrow \qquad \eta = -\frac{u^H Q(\nu)r}{u^H Q(\nu)P'(\nu)u}.$$

Once an expression of η is found, the new direction is

$$v = \frac{u^H Q(\nu) r}{u^H Q(\nu) P'(\nu) u} Q(\nu) P'(\nu) u - Q(\nu) r \tag{2.10}$$

Remark 2.37. When $Q(\nu)$ is an exact inverse, one step approximation is equivalent to the exact Newton step.

Remark 2.38. It is not necessary to calculate the matrix Q. It is sufficient to solve the linear systems

$$P(\nu)x = r \qquad \text{and} \qquad P(\nu)y = P'(\nu)u,$$

where x and y are the unknown variables.

The advantage of the one step approximation compared to apply iterative solver on the correction equation is the fact, that $Q(\nu)$ is related to the original matrix polynomial evaluated at ν and thus the structure remains, while projections destroy it. One method to calculate the approximate inverse $Q(\nu)$ is the *incomplete LU decomposition*. In Chapter 4 we will find a very efficient way to calculate the approximate inverse Q of the anomalous transport eigenvalue equation P which is introduced in the next chapter.

2.4 Error bounds

The Jacobi-Davidson Algorithm 6 stops if the residual is below a threshold. However, this does not give any information about the accuracy of the eigenvalue. From numerical linear algebra it is known [13] that the forward error depends on the residual and the condition number. In this section we describe a practical method to estimate the forward error.

2.4.1 Condition number

The *condition number* associated with the matrix is a measure of that problem's amenability to numerical computation, that is, how numerically well-conditioned the problem is. A problem with a low condition number (close to 1) is said to be well-conditioned, while a problem with a huge condition number is said to be ill-conditioned. Computing the condition number is practically difficult. Hence the *component wise condition number* κ_c [13] is favorable in practical numerics.

The matrix polynomial

$$P(\lambda) = \sum_{k=0}^{d} \lambda^k M_k$$

turns into a matrix when it is evaluated at λ. Here, the condition number with respect to an eigenpair is of interest. Let (λ, x, y) be an eigentriple, where y is an approximate left eigenvector, x an approximate right eigenvector and λ the approximate eigenvalue of P. Then the component wise condition number is defined (Betcke [5]) as

$$\kappa_c(P, \lambda, x, y) := \frac{|y|^H M |x|}{|\lambda||y^H P'(\lambda) x|}, \qquad M := \sum_{k=0}^{d} |\lambda|^k |M_k|, \tag{2.11}$$

where $P' = \frac{\partial P}{\partial \lambda}$ and the absolute values are taken component wise.

2.4.2 Backward error

The backward error measures the size of perturbation of the eigenvalue equation, such that an approximate eigenpair $(\widetilde{\lambda}, \widetilde{x})$ of $P(\lambda)x = 0$ is the exact solution of the perturbed equation

$$(P + \Delta P)(\widetilde{\lambda})\widetilde{x} = 0.$$

The backward error is a mere theoretical tool. In practical calculations the *component wise backward error* (see [5]) is preferred. The explicit expression of the component wise backward error b_c of an approximate eigenpair $(\widetilde{\lambda}, \widetilde{x})$ with respect to the eigenvalue polynomial P is given by

$$b_\mathrm{c}(P, \widetilde{\lambda}, \widetilde{x}) := \max_j \frac{|r_j|}{\left(\widetilde{P}|\widetilde{x}|\right)_j}, \qquad \widetilde{P} := \sum_{k=0}^{d} |\widetilde{\lambda}|^k |M_k|, \quad r = P(\widetilde{\lambda})\widetilde{x}, \tag{2.12}$$

where the modulus is taken component wise.

2.4.3 Forward error estimate

The *forward error* e_f is the absolute difference of exact solution and numerical one. In other words, the forward error is the precision of numerical solution. Practically the exact solution is unknown and an upper bound of forward error is desired. The relation

$$\text{forward error} \leq \text{backward error} \cdot \text{condition number} \tag{2.13}$$

is well known, e.g. [5]. With respect to computational cost the best approximation is the component wise version

$$e_\mathrm{f}(P, \widetilde{\lambda}, \widetilde{x}, \widetilde{y}) \leq b_\mathrm{c}(P, \widetilde{\lambda}, \widetilde{x}) \cdot \kappa_\mathrm{c}(P, \widetilde{\lambda}, \widetilde{x}, \widetilde{y}) \tag{2.14}$$

with the approximate eigentriple $(\widetilde{\lambda}, \widetilde{x}, \widetilde{y})$.

Remark 2.39. With a complex symmetric eigenvalue polynomial P the left eigenvector $\widetilde{y} = \overline{\widetilde{x}}$ can be computed easily.

Now, the Jacobi-Davidson Algorithm 6 can be extended by the following rules. If the residual r is below the tolerance, equation (2.14) is evaluated. If the forward error estimate is below the tolerance, the stopping criterion is fulfilled. Otherwise the search space iteration is continued.

Chapter 3

Anomalous transport model

In this chapter the physical model of the anomalous transport throughout the edge layer of the Tokamak is introduced and a mathematical description is presented. It is a simplified, but still a so called self consistent transport model derived by Tokar, Kelly, Loozen and Reiser [23, 27, 38]. In the following we sum up the basic ideas and equations of this transport model.

3.1 Linearized transport equations

The fundamental principles such as conservation of particles, momentum and energy yield the basic equations, which are the continuity equation, the momentum equation, the zero current divergence, Faraday's, Ampere's and Ohm's law. These equations are very complex and several simplifications are prepared.

3.1.1 Time scale

In a first step, we compare the time scale of the plasma parameter with the perturbation of micro instabilities. Macroscopically, the plasma is close to the equilibrium and the changes are slow in comparison to the fast varying micro instabilities of the plasma parameters. Hence, each quantity $\widehat{f}$ is assumed to be composed of the temporal nearly constant macroscopic part f_0 and the temporally fast varying microscopic part $\widetilde{f}$. We get the decomposition

$$\widehat{f} = f_0 + \widetilde{f},$$

where $\widetilde{f}$ is called *perturbation term*. The model used in this work concentrates on the microscopic part and therefore the macroscopic one is assumed to be constant in time.

3.1.2 Linear approximation

The perturbations of the density $\widetilde{n}$, the electric potential $\widetilde{\phi}$, the electric current $\widetilde{\mathbf{j}}$ and the magnetic field $\widetilde{\mathbf{B}}$ along the magnetic field lines within the magnetic flux surface are assumed to be a Fourier series of plain waves,

$$\widetilde{f}(l,\chi,t) = \sum_{k_\chi,k_\eta,\widetilde{\omega}} f_{k_\chi,k_\eta}(l,\chi)\exp(\mathrm{i}k_\chi\chi + \mathrm{i}k_\eta\eta - \mathrm{i}\widetilde{\omega}t), \tag{3.1}$$

where l is the length along the magnetic field line, k_χ is the wave number in direction of $\mathbf{e}_\chi$ (cf. Figure 1.4 on page 12), k_η the wave number in the direction of $\mathbf{e}_\eta$ (cf. Figure 1.4), $k_\parallel$ the wave

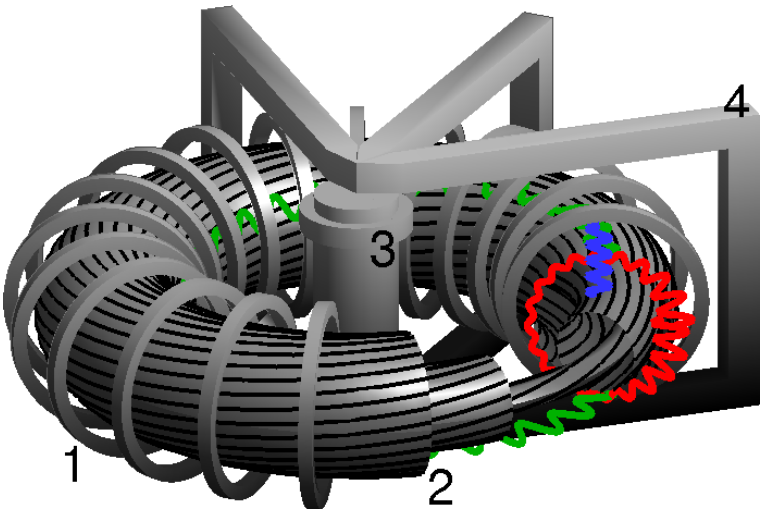

Figure 3.1: The picture 1.2 with the three directions of perturbations illustrated by a sine curve.

number in the direction parallel to the magnetic field line, $\widetilde{\omega}$ is the complex frequency and t the time. The imaginary part of $\widetilde{\omega}$ expresses the temporal amplitude of the perturbation wave $\widetilde{f}$. The special form of $\widetilde{f}$ neglects the perturbation waves parallel to the magnetic field line, because those wave components do not produce transport perpendicular to the magnetic flux surfaces.

In this work the radial direction is averaged and the Fourier series simplifies to

$$\widetilde{f}(l,t) = \sum_{k_\chi,k_\eta,\widetilde{\omega}} f_{k_\chi,k_\eta}(l)\exp(\mathrm{i}k_\chi\chi + \mathrm{i}k_\eta\eta - \mathrm{i}\widetilde{\omega}t).$$

The movement along the magnetic field line l projected onto the poloidal plane corresponds to a movement along the poloidal angle θ and the perturbation synthesis reads

$$\widetilde{f}(\theta,t) = \sum_{k_\chi,k_\eta,\widetilde{\omega}} f_{k_\chi,k_\eta}(\theta)\exp(\mathrm{i}k_\chi\chi + \mathrm{i}k_\eta\eta - \mathrm{i}\widetilde{\omega}t), \tag{3.2}$$

where the length element $\partial_l\theta$ affects the parallel derivative

$$\frac{d\widetilde{f}}{dl} = \frac{d\widetilde{f}}{d\theta}\partial_l\theta.$$

In particular for a Tokamak with circular cross section the length element is given by

$$\partial_l\theta = \frac{1}{qR_0}$$

where q denotes the safety factor and R_0 the major radius of the edge layer.

The time dependent part of the wave equation is $\exp(-\mathrm{i}\widetilde{\omega}t)$. Hence the frequency $\widetilde{\omega}$ with $\Im(\widetilde{\omega})$ the largest imaginary part grows the fastest in time and will dominate all others. Thus, we concentrate solely on the most dominant frequency and assume

$$\widetilde{f}(\theta,t) = f(\theta)\exp(\mathrm{i}k_\chi\chi + \mathrm{i}k_\eta\eta - \mathrm{i}\widetilde{\omega}t), \tag{3.3}$$

where $\Im(\widetilde{\omega})$ is maximal.

3.1.3 Basic model equations

Here, we state the physical equations of the well established anomalous transport model in the version of Dirk Reiser [27]. This version uses an abstract formulation of the occurring operators, which offers the possibility to apply the equations on different magnetic geometries of the Tokamak device. Once the magnetic geometry is chosen, an appropriate coordinate system can be defined and the explicit formulation of the operators can be calculated and applied.

For better readability the vector valued terms are printed bold and the abbreviation

$$\mathcal{K}(f) := \left(\nabla \times \frac{\boldsymbol{B}}{B^2}\right) \cdot \nabla f \tag{3.4}$$

is used for the curvature.

The perturbations are assumed to consist solely of the mode of strongest growth rate in time (3.3). In order to utilize the advantage of the approach

$$\widehat{f}(\theta,t) = f_0(\theta) + \widetilde{f}(\theta,t) = f_0(\theta) + f(\theta)\exp(\mathrm{i}k_\chi\chi + \mathrm{i}k_\eta\eta - \mathrm{i}\widetilde{\omega}t)$$

the physical equations are linearized, i.e., the second order perturbation terms are neglected.

Within the linearized equations it is possible to factor out the exponential function after the operators are applied.

In the following the linearized version of the fundamental equations is given. Here, n denotes the density of the charged particles, v are drift velocities specified by the index, j is the electric current, ϕ is the electric potential, p_s is the pressure of the electrons ($s = \mathrm{e}$) or the ions ($s = \mathrm{i}$), m_s is the mass of the electrons ($s = \mathrm{e}$) or the ions ($s = \mathrm{i}$), $\boldsymbol{A}$ is the vector potential and T_e is the electron temperature. For the ease of presentation the index 0 of the unperturbed quantities is omitted.

Particle continuity

$$\frac{\partial\widetilde{n}}{\partial t} = -\widetilde{\boldsymbol{v}}_\mathrm{E}\cdot\boldsymbol{\nabla}n - \widetilde{\boldsymbol{v}}_\mathrm{E}\cdot\boldsymbol{\nabla}\widetilde{n} - n\mathcal{K}(\widetilde{\phi}) + \frac{1}{e}\mathcal{K}(\widetilde{p}_\mathrm{i}) + \frac{B}{e}\nabla_\parallel\frac{\widetilde{j}_\parallel}{B} \tag{3.5}$$

Momentum balance

$$\boldsymbol{j}_\perp = \boldsymbol{j}_* + \boldsymbol{j}_\mathrm{p} \approx \frac{\boldsymbol{B}\times\boldsymbol{\nabla}p}{B^2} + \frac{m_\mathrm{i}n}{B}\frac{\boldsymbol{B}}{B}\times\frac{d}{dt}(\boldsymbol{v}_\mathrm{E} + \boldsymbol{v}_{*\mathrm{i}}) \tag{3.6}$$

Faraday's law and Ampere's law

Assuming that the perturbed magnetic vector potential $\widetilde{\boldsymbol{A}}$ has only a component $\widetilde{A}_\parallel$ parallel to the magnetic field one obtains

$$\widetilde{E}_\parallel = -\frac{\partial\widetilde{A}_\parallel}{\partial t} - \nabla_\parallel\widetilde{\phi} \tag{3.7}$$

$$\nabla_\perp^2\widetilde{A}_\parallel = -\mu_0\widetilde{j}_\parallel. \tag{3.8}$$

Ohm's law

By neglecting the temperature perturbations and the expression for $\widetilde{E}_\parallel$ above, Ohm's law can be written as

$$\frac{\partial\widetilde{A}_\parallel}{\partial t} + \frac{m_\mathrm{e}}{ne^2}\frac{d\widetilde{j}_\parallel}{dt} = \frac{T_\mathrm{e}}{ne}\nabla_\parallel(n+\widetilde{n}) + \frac{1}{e}\nabla_\parallel T_\mathrm{e} - \nabla_\parallel\widetilde{\phi} - \eta_\parallel\widetilde{j}_\parallel \tag{3.9}$$

Zero current divergence
The quasi neutrality condition $\boldsymbol{\nabla} \cdot \boldsymbol{j} = 0$ gives

$$B\nabla_\parallel \frac{\widetilde{j}_\parallel}{B} = -\mathcal{K}(\widetilde{p}_\mathrm{i} + \widetilde{p}_\mathrm{e}) + \frac{m_\mathrm{i} n}{B^2}\frac{d}{dt}\left(\nabla_\perp^2 \widetilde{\phi} + \frac{\nabla_\perp^2 \widetilde{p}_\mathrm{i}}{en}\right) \tag{3.10}$$

where

$$\frac{d}{dt} = \frac{\partial}{\partial t} + \widetilde{\boldsymbol{v}}_\mathrm{E} \cdot \boldsymbol{\nabla}_\perp = \frac{\partial}{\partial t} + \frac{\boldsymbol{B} \cdot (\boldsymbol{\nabla}_\perp \widetilde{\phi} \times \boldsymbol{\nabla}_\perp)}{B^2}$$

$$\nabla_\parallel = \frac{\boldsymbol{B} \cdot \boldsymbol{\nabla}}{B} - \frac{\boldsymbol{B} \cdot (\boldsymbol{\nabla}_\perp \widetilde{A}_\parallel \times \boldsymbol{\nabla}_\perp)}{B^2}$$

$$\boldsymbol{\nabla}_\perp = \boldsymbol{\nabla} - \boldsymbol{\nabla}_\parallel, \qquad \nabla_\perp^2 = \boldsymbol{\nabla} \cdot \boldsymbol{\nabla}_\perp.$$

3.1.4 Potential perturbation eigenvalue problem

Due to the fact that the problem is analyzed only in one dimension, namely the poloidal direction, the radial derivatives are neglected. The expressions of the operators are transformed into a coordinate system aligned to the magnetic field line and the Fourier mode (3.3) is inserted into the perturbation terms ($\widetilde{n}$, $\widetilde{\phi}$, $\widetilde{j}$, $\widetilde{p}$ and $\widetilde{A}_\parallel$) in the set of equations

$$\begin{aligned}
\frac{\partial \widetilde{n}}{\partial t} &= -\widetilde{\boldsymbol{v}}_\mathrm{E} \cdot \boldsymbol{\nabla} n - \widetilde{\boldsymbol{v}}_\mathrm{E} \cdot \boldsymbol{\nabla} \widetilde{n} - n\mathcal{K}(\widetilde{\phi}) + \frac{1}{e}\mathcal{K}(\widetilde{p}_\mathrm{e}) + \frac{B}{e}\nabla_\parallel \frac{\widetilde{j}_\parallel}{B} \\
\frac{m_\mathrm{i}}{eB}\frac{d}{dt}\left(\nabla_\perp^2 \widetilde{\phi} + \frac{\nabla_\perp^2 \widetilde{p}_\mathrm{i}}{en}\right) &= B\nabla_\parallel \frac{\widetilde{j}_\parallel}{B} + \mathcal{K}(\widetilde{p}_\mathrm{i} + \widetilde{p}_\mathrm{e}) \\
\frac{\partial \widetilde{A}_\parallel}{\partial t} + \frac{m_\mathrm{e}}{ne^2}\frac{d\widetilde{j}_\parallel}{dt} &= \frac{T_\mathrm{e}}{ne}\nabla_\parallel(n + \widetilde{n}) - \nabla_\parallel \widetilde{\phi} - \eta_\parallel \widetilde{j}_\parallel + \frac{1}{e}\nabla_\parallel T_\mathrm{e} \\
\nabla_\perp^2 \widetilde{A}_\parallel &= -\mu_0 \widetilde{j}_\parallel.
\end{aligned} \tag{3.11}$$

This leads to the following Mathieu (cf. (3.14)) like eigenvalue equation for the perturbed electric potential envelope ϕ

$$\frac{\partial^2 \phi}{\partial \theta^2} = \frac{\omega(\widehat{\beta} + z\gamma_3 \widehat{\mu} K_\perp^2) - (1 + \widehat{\lambda})\widehat{\beta} K_\perp + \mathrm{i} z\gamma_3 \widehat{C} K_\perp^2}{\gamma_1^3 z\Big(K_\perp - \omega\big(1 + z\gamma_3(1 + \widehat{\alpha})K_\perp^2\big)\Big)} \left((1 + \widehat{\alpha})\frac{\gamma_2}{\gamma_3}\omega_\mathrm{B}(1 - z\gamma_3 \omega K_\perp) + z\omega(\omega + \widehat{\alpha} K_\perp)\right)\phi, \tag{3.12}$$

where the normalized units are introduced as $K_\perp = k_\eta \rho_\mathrm{i}$, $\omega = \widetilde{\omega}\frac{L_\mathrm{n}}{c_\mathrm{s}}$. The metric coefficients γ_1, γ_2 and γ_3 and the physical quantities are explained subsequently.

The electrons and ions are assumed to have equal densities as well as equal temperature. Thus the ratio is

$$\widehat{\alpha} := \frac{T_\mathrm{i}}{T_\mathrm{e}} = 1.$$

T and n are used without the subscript in the following. Additionally, the e-folding length of the neutrals and of the electron temperature is assumed to be equal and the ratio is

$$\widehat{\lambda} := \frac{L_\mathrm{n}}{L_{T_\mathrm{e}}} = 1.$$

Further abbreviations are

$$\widehat{\epsilon} = \left(\frac{q_0 R_0}{L_\mathrm{n}}\right)^2, \qquad \widehat{\beta} = \widehat{\epsilon}\beta, \qquad \omega_\mathrm{B} = \frac{2L_\mathrm{n}}{R_0}, \qquad \widehat{\mu} = \widehat{\epsilon}\mu, \qquad \widehat{C} = \widehat{\mu}\frac{L_\mathrm{n}}{c_\mathrm{s}}\frac{\nu_\mathrm{e}}{1.96}Z_\mathrm{eff} = \widehat{\epsilon}\sqrt{\mu}\frac{L_\mathrm{n}}{\lambda_\mathrm{e}},$$

where the mass ratio of electrons and ions is

$$\mu = \frac{m_\mathrm{e}}{m_\mathrm{i}},$$

the ratio of the pressure to the magnetic pressure is

$$\beta = \mu_0 \frac{nT}{B_0^2},$$

the sound velocity and larmor radius of ions ($s = \mathrm{i}$) and electrons ($s = \mathrm{e}$) is

$$c_\mathrm{s} = \sqrt{\frac{T}{m_\mathrm{s}}}, \qquad \rho_\mathrm{s} = \frac{c_\mathrm{s} m_\mathrm{s}}{eB_0},$$

the friction coefficient of the electrons is

$$\nu_\mathrm{e} = \frac{e^4 n_\mathrm{e} \Lambda_\mathrm{c}}{3(2\pi)^{3/2}\varepsilon_0^2\sqrt{m_\mathrm{e}}T^{3/2}}$$

and the Coulomb integral is

$$\Lambda_\mathrm{c} = 30.3 - 1.15\log_{10}\left(n\,\mathrm{m}^3\right) + 3.45\log_{10}\left(eT\,\mathrm{eV}^{-1}\right).$$

The physical meaning of the quantities that are not explained here is listed in Table 3.1 and Table 3.2.

The factor z takes into account the magnetic shear

$$\widehat{s} = \frac{d\ln(q)}{d\ln(\chi)}.$$

If the wave vector k_η is large enough, the radial wave vector k_χ is assumed to be equal to k_η (strong turbulence limit). Otherwise k_χ is bounded from below due to *Landau* damping of perturbations with the radial wave length being too large [43]. Additionally this length has to be smaller than L_n. These aspects are considered by the factor $z = 2\gamma$, where

$$\gamma = \frac{k_\chi^2 + k_\eta^2}{2k_\eta^2} = \max\left\{1, \frac{1}{2} + \zeta\left(\frac{\pi}{K_\perp}\max\left\{\frac{\widehat{s}L_\mathrm{n}}{q_0 R_0}, \frac{\rho_\mathrm{i}}{L_\mathrm{n}}\right\}\right)^2\right\}, \qquad \zeta = 2.$$

3.1.4.1 The metric coefficients

The determination of the metric coefficients γ_1, γ_2 and γ_3 requires to consider the variation of the length element on the magnetic flux surfaces.

The coordinates on the magnetic flux surface can be written as

$$x = R\cos(\varphi), \quad y = Z, \quad z = -R\sin(\varphi),$$

where the coordinates in the poloidal plane are described by

$$\begin{aligned} R &= R_0 + r\cos(\theta) + Dr\cos(2\theta) \\ Z &= rE\sin(\theta) - rED\sin(2\theta), \end{aligned}$$

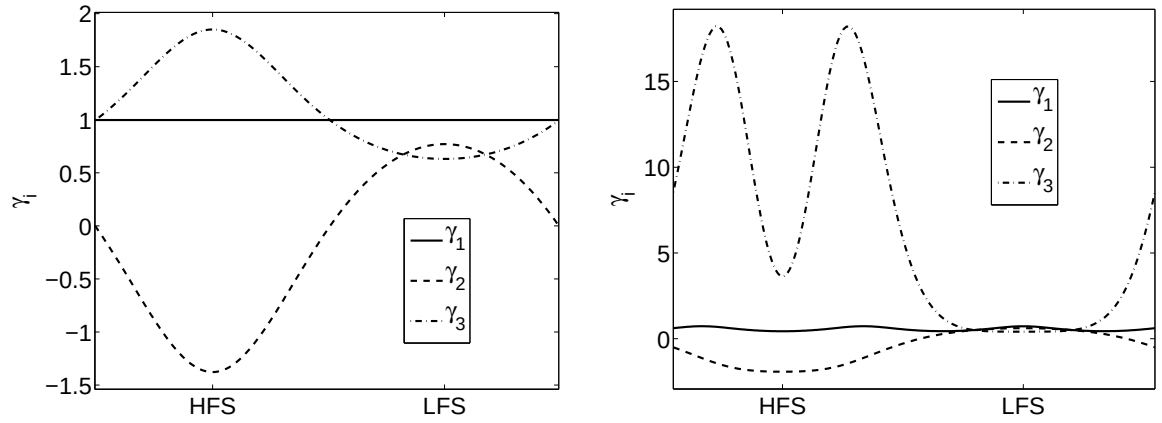

(a) TEXTOR (b) MAST

Figure 3.2: The metric coefficients with (a) TEXTOR parameter $R_0 = 175$ cm, $r_0 = 46$ cm, $E = 1$, $D = 0$, $B = 2.25$ T, $q = 3.5$ and (b) MAST parameter $R_0 = 80$ cm, $r_0 = 60$ cm, $E = 2$, $D = 0.22$, $B = 0.47$ T, $q = 5$.

with the major radius R_0, the minor radius r, the elongation E and the triangulation D.

The magnetic field in the Tokamak is a superposition of the toroidal magnetic field B^φ and the poloidal magnetic field B^θ. In the contravariant basis they are

$$B^\theta = \frac{B_0 r}{qJ}, \qquad B^\varphi = \frac{B_0 R_0}{R^2}.$$

The total field strength is

$$B = \sqrt{g_{\theta\theta} B^\theta B^\theta + g_{\varphi\varphi} B^\varphi B^\varphi},$$

where the covariant metric tensor reads

$$g_{\theta\theta} = \left(\frac{\partial R}{\partial \theta}\right)^2 + \left(\frac{\partial Z}{\partial \theta}\right)^2, \qquad g_{\varphi\varphi} = R^2$$

and an abbreviation for the determinant of the Jacobian is introduced

$$J := R \det\left(\begin{pmatrix} \frac{\partial}{\partial r} \\ \frac{\partial}{\partial \theta} \end{pmatrix} (R, Z)\right) = rRE\big(1 - 2D^2 - D\cos(3\theta)\big).$$

It is used to calculate the inverse of the Jacobian matrix by Cramer's rule which is needed to calculate the contravariant metric tensor

$$g^{\theta\theta} = \left(\frac{\partial \theta}{\partial R}\right)^2 + \left(\frac{\partial \theta}{\partial Z}\right)^2$$

where the derivatives are

$$\frac{\partial \theta}{\partial R} = -\frac{\sin(\theta) - D\sin(2\theta)}{r\big(1 - 2D^2 - D\cos(3\theta)\big)}, \qquad \frac{\partial \theta}{\partial Z} = \frac{\cos(\theta) + D\cos(2\theta)}{rE\big(1 - 2D^2 - D\cos(3\theta)\big)}.$$

A consideration [27] of the underlying physical formulas yields the metric coefficients

$$\gamma_1 = \frac{B^\theta}{B} q R_0, \quad \gamma_2 = \frac{1}{JB^4}\left(\frac{\partial B^2}{\partial \theta} B_r - \frac{\partial B^2}{\partial r}\frac{B^2}{B^\theta}\right)\frac{B_0 R_0 r}{2q}, \quad \gamma_3 = \left(\frac{1}{R^2} + g^{\theta\theta}\left(\frac{B^\varphi}{B^\theta}\right)^2\right)\frac{r^2}{q^2} \tag{3.13}$$

The radial magnetic field B_r is small and thus can be neglected:

$$\gamma_2 \approx \frac{-1}{JB^2B^\theta}\frac{\partial B^2}{\partial r}\frac{B_0R_0r}{2q} = \frac{B_0R_0}{JB^\theta q}\frac{r}{R}\left(\frac{\partial R}{\partial r}\right) - \frac{B^\theta B_0R_0}{JB^2q}\left[\left(\frac{\partial R}{\partial \theta}\right)^2 + \left(\frac{\partial Z}{\partial \theta}\right)^2\right].$$

In γ_3 the factor $1/R^2$ is much smaller than the other term and omitting it simplifies γ_3 to

$$\gamma_3 \approx g^{\theta\theta}\left(\frac{B^\varphi}{B^\theta}\right)^2\frac{r^2}{q^2} = \Big(E^2\big(\sin(\theta) - D\sin(2\theta)\big)^2 + \big(\cos(\theta) + D\cos(2\theta)\big)^2\Big)\frac{R_0^2}{R^2}.$$

For $E = 1$, $D = 0$ and $\frac{r}{R_0} \to 0$ (high aspect ratio limit) the coefficients simplify to $\gamma_1 = 1 = \gamma_3$ and $\gamma_2 = \cos\theta$, which are the values used in [23, 38]. Figure 3.2 displays the profile of the metric coefficients for the Tokamak TEXTOR and MAST.

3.1.4.2 Former approach

In an earlier work, Tokar et al. [23, 38] simplified the eigenvalue equation (3.12) until they could estimate the real and the imaginary part of the eigenvalue ω by the Mathieu equation

$$\frac{\partial^2\phi}{\partial\vartheta^2} + \big(a - 2q\cos(2\vartheta)\big)\phi = 0, \qquad a, q \in \mathbb{R} \tag{3.14}$$

and the eigenfunction ϕ was determined by Loozen with a shooting method. Unfortunately this requires to average all quantities like the plasma parameters temperature, density and the geometric coefficients except for $\gamma_2 = \cos(\theta)$.

Now, the main purpose of this work is to solve the eigenvalue equation (3.12) with the possibility, that any quantity depends on the poloidal angle θ also though the elongation and triangulation of magnetic surfaces expressed through the metric coefficients.

3.1.5 Eigenvalue polynomial

In order to transform the eigenvalue equation (3.12) into a mere eigenvalue polynomial it needs to be multiplied by the denominator containing the eigenvalue ω. To do this, the following abbreviations

$$\begin{aligned}
c_1 &= \widehat{\beta} + z\gamma_3\widehat{\mu}K_\perp^2 & c_2 &= -(1+\widehat{\lambda})\widehat{\beta}K_\perp & c_3 &= z\gamma_3\widehat{C}K_\perp^2 \\
c_4 &= (1+\widehat{\alpha})\frac{\gamma_2}{\gamma_3}\omega_\mathrm{B} & c_5 &= -z(1+\widehat{\alpha})\gamma_2\omega_\mathrm{B}K_\perp & c_6 &= z\widehat{\alpha}K_\perp \\
c_7 &= z & c_8 &= -z\gamma_1^3K_\perp & c_9 &= z\gamma_1^3\big(1 + z(1+\widehat{\alpha})\gamma_3K_\perp^2\big)
\end{aligned} \tag{3.15}$$

are introduced.

Remark 3.1. Although it is not explicitly pointed out, many values c_j depend on the angle θ. Primary it is the temperature T and the density n. Secondary, $\Lambda_\mathrm{c}, \lambda_\mathrm{e}, \beta, L_\mathrm{n}, \gamma$ depend on T or n and therefore on θ, as well. The dependencies are listed in Table 3.2. Thus, $c_j = c_j(\theta)$ holds in general. Further, $c_j(\theta)$ are real valued functions.

Applying the abbreviations, the eigenvalue problem reads

$$0 = \frac{\partial^2\phi}{\partial\theta^2} + \frac{\big(\omega c_1 + c_2 + \mathrm{i}c_3\big)}{(c_8 + \omega c_9)}\big(c_4 + \omega(c_5 + c_6) + \omega^2c_7\big)\phi. \tag{3.16}$$

It is complex symmetric as long as the derivative part is discretized symmetrically, which is true on equidistant spaced grid. Finally, equation (3.16) is multiplied by its denominator, is expanded and sorted by powers of the eigenvalue ω:

$$\begin{aligned} 0 = \Bigg[& c_1 c_7 \omega^3 + \big(c_1(c_5+c_6) + (c_2 + ic_3)c_7\big)\omega^2 \\ & + \left(c_9 \frac{\partial^2 \phi}{\partial \theta^2} + c_1 c_4 + c_2(c_5+c_6) + \mathrm{i}c_3(c_5+c_6) \right) \omega + \left(c_8 \frac{\partial^2 \phi}{\partial \theta^2} + c_4(c_2 + \mathrm{i}c_3) \right) \Bigg] \phi \end{aligned} \tag{3.17}$$

It is no longer complex symmetric, but the left eigenvector

$$\phi_{\text{left}} = \overline{\mathrm{Diag}(c_8 + \omega c_9)^{-1} \phi} \tag{3.18}$$

can be calculated easily when the eigenpair (ω, ϕ) is known.

Remark 3.2. The knowledge of the left eigenvector yields the possibility to calculate the condition number (2.11), which together with the backward error (2.12) allows to estimate the forward error of the calculated eigenvalue.

In the mathematical theory, the eigenvalue problems have many solutions (ω, ϕ), however, consideration of the underlying physical problem points out eigenpairs with a 2π-periodic and smooth eigenfunction ϕ and the eigenvalue with maximal growth rate $\Im(\omega) > 0$ dominates (3.2) in time (see (3.3)).

Definition 3.3. Let (ω, ϕ) be an eigenpair of (3.17), then $(\omega, c\phi)$ solves the equation for any $c \in \mathbb{C} \setminus \{0\}$. Therefore the normalization

$$\frac{1}{2\pi} \int_0^{2\pi} \phi^*(\theta)\phi(\theta) \frac{d\sigma}{d\theta}(\theta)\, d\theta = 1$$

is denoted as the particular eigenfunction, further on.

Remark 3.4. In (3.21), this arbitrary choice of normalization will be adjusted by a calibration factor ϕ_0.

Definition 3.5. If $\phi(0) \neq 0$ the complex phase is normalized by the demand

$$\phi(0) \in \mathbb{R}.$$

Remark 3.6. The complex phase does only affect the plots of eigenfunctions, because the physical formulas that are introduced in the next section use the intensity $|\phi|^2$.

3.2 Anomalous particle flux density

As long as the density perturbation $\widetilde{n}$ is in phase with the electric field perturbation $\widetilde{\phi}$ there is neither a net flux of particles nor of energy. Moreover the relation

$$\widetilde{n} = \iota \widetilde{\phi}$$

holds, with the constant of proportionality ι beeing real. The linear connection is the reason, why only the electric field perturbation was considered before.

The proportionality within the anomalous transport model introduced above is

$$\iota = \frac{K_\perp - 2K_\perp^2 \omega\gamma}{\omega(1 + 2K_\perp^2 \gamma)}. \tag{3.19}$$

However, when the perturbation gets out of phase, ι becomes complex and in turn ω becomes complex, too.

The anomalous particle flux from [43] is

$$\Gamma_\perp = \widetilde{n}\widetilde{v}_\mathrm{e}^* + \widetilde{n}^*\widetilde{v}_\mathrm{e} = \frac{Tn}{eB}\sum_{k_\eta} k_\eta \left[\widetilde{n}\left(-\mathrm{i}\widetilde{\phi}\right)^* + \widetilde{n}^*\left(-\mathrm{i}\widetilde{\phi}\right)\right] = \mathrm{i}\frac{Tn}{eB\rho_\mathrm{i}}\sum_{K_\perp} K_\perp\left(\widetilde{n}\phi^* - \widetilde{n}^*\widetilde{\phi}\right), \quad (3.20)$$

where $\widetilde{v}_\mathrm{e}$ is the perpendicular electron perturbation velocity. The anomalous particle flux $\Gamma_\perp$ is zero if $\widetilde{n}$ and $\widetilde{v}_\mathrm{e}$ are in phase.

A short calculation yields

$$\begin{aligned}\Re(\iota) &= \frac{\Re(\omega) - 2K_\perp|\omega|^2\gamma}{|\omega|^2}\frac{K_\perp}{1+2K_\perp^2\gamma}\\ \Im(\iota) &= -\frac{\Im(\omega)}{|\omega|^2}\frac{K_\perp}{1+2K_\perp^2\gamma}.\end{aligned}$$

This allows to eliminate the density perturbation:

$$\Gamma = -2\frac{Tn}{eB\rho_\mathrm{i}}\sum_{K_\perp} K_\perp\Im(\iota)|\widetilde{\phi}|^2 = 2\frac{Tn}{eB\rho_\mathrm{i}}\sum_{K_\perp}\frac{\Im(\omega)}{|\omega|^2}\frac{K_\perp^2}{1+2K_\perp^2\gamma}|\widetilde{\phi}|^2.$$

In [43], Weiland compares the exponential growth of the perturbation wave (e.g. $\widetilde{\phi}$, $\widetilde{n}$) with the initial linear causer (e.g. $\nabla\phi_0$, ∇n_0). Close to the level where the perturbation reaches a magnitude comparable to the initial causer, the perturbation wave cancels its causing and saturates. Within Weilands mixing-length theory the amplitude of the electric potential perturbation is estimated and here taken into account by the substitution

$$\widetilde{\phi} \leftarrow \frac{\phi_0}{k_\chi\rho_\mathrm{i}}\frac{\Im(\widetilde{\omega})}{k_\eta c_\mathrm{s}}\widetilde{\phi} = \phi_0\frac{\rho_\mathrm{i}}{L_\mathrm{n}}\frac{\Im(\omega)}{K_\perp^2\sqrt{\gamma}}\widetilde{\phi}.$$

The factor $\phi_0 \approx 1$ is a calibration parameter that compensates the normalization in Definition 3.3. It is obtained by a comparison with experimental data, which is described in the next section.

Finally, the anomalous particle flux is

$$\Gamma_\perp = \Gamma_1(n,T)\phi_0^2, \quad (3.21)$$

where

$$\Gamma_1(n,T) = 2\frac{Tn\rho_\mathrm{i}}{eBL_\mathrm{n}^2}\sum_{K_\perp}\frac{\Im(\omega)^3}{K_\perp^2(1+2K_\perp^2\gamma)\gamma}\frac{|\widetilde{\phi}|^2}{|\omega|^2}, \qquad [\Gamma_1] = \mathrm{m}^{-2}\mathrm{s}^{-1}. \quad (3.22)$$

Remark 3.7. Equation (3.22) reveals the particle flux $\Gamma_\perp$ to be related to the intensity of the electric potential perturbation envelope amplitude $\phi(\theta)$. Therefore the complex phase of the eigenfunction does not affect the anomalous particle flux. Tokamak conditions, which are symmetric to the mid plane, lead to a particle flux with distinguished points at the LFS and the HFS, e.g. like the zeroth even Mathieu function (ce_0). Hence, the desired eigenfunction is expected to passes such a feature.

3.3 Determination of plasma parameters

In this section we discuss the balance of the energy in the edge layer due to the inflow of heating power from the plasma core and due to losses from the anomalous particle flux $\Gamma_\perp$. The heat is conducted mainly parallel to the magnetic field lines and, hence, the deformation of the magnetic geometry is subordinate except for the profile g of the heat flow from the core.

In the Tokamak the heat balance in the edge layer due to the heating power from the plasma core and the losses through LCMS is described by the non-linear heat balance equation

$$\frac{\delta_{\text{edge}}}{q^2 R_0^2} \frac{\partial}{\partial \theta} \left(-\kappa_\parallel \big(n(\theta), T(\theta)\big) \frac{\partial T(\theta)}{\partial \theta} \right) = g(\theta) q_{\text{core}} - q_{\text{loss}}\big(T(\theta), \theta\big). \tag{3.23}$$

The right hand side contains the temporal change of energy, on the one hand there is the heating power from the plasma core q_{core} with the poloidal distribution g and on the other hand there are the losses q_{loss} due to charged particles that leave the LCMS and the ionization of neutrals that penetrate into the plasma. The heat flow distribution g concerns the Shafranov shift and [37] obtains the rough approximation

$$g(\theta) = 1 + \Delta_1 \cos(\theta)$$

in case of a circular cross section, where $\Delta_1 \approx 0.5$ expresses the poloidal varying heat gradient, due to the Shafranov shift. The heat flux is largest at the LFS and smallest at the HFS.

The essential part on the left side is the electron parallel heat conductivity

$$\kappa_\parallel = 1.94 \cdot 10^{21} \frac{(eT)^{2.5}}{\Lambda_{\text{c}} Z_{\text{eff}}}$$

that depends on the temperature T and causes the heat balance equation to be non-linear in T. The width δ_{edge} of the edge layer depends on the penetration depth L_{n} of the neutral particles, thus

$$\delta_{\text{edge}} = L_{\text{n}}$$

is assumed.

The intensity of the energy loss q_{loss} is composed at the one hand by the charged particles leaving the plasma and taking their kinetic energy (temperature) out ($3\Gamma_\perp T$) and on the other hand by the required energy to ionize the neutral particles ($E_{\text{i}} J$), which penetrate into the plasma

$$q_{\text{loss}} = 3T\Gamma_\perp + E_{\text{i}} J.$$

The total energy E_{i} lost by exciting and ionizing each neutral particle, that penetrates into the plasma, is approximated [15] as

$$E_{\text{i}} = \left[30\,\text{eV} - 16.4\,\text{eV} \cdot \exp\left(-\frac{5 \cdot 10^{19}}{n} \right) \right] \exp\left[\frac{5.45\,\text{eV}}{eT} \exp\left(\frac{n^{0.26}}{1.72 \cdot 10^5} \right) \right], \tag{3.24}$$

where n is measured in $10^{20}\,\text{m}^{-3}$. $E_{\text{i}} \approx 30$ eV holds for temperatures above 30 eV and it rises exponentially when the temperature approaches zero.

The particles that leave the plasma get neutralized at the wall and reflect back into the plasma by a recycling probability $R_{\text{rec}} = 0.9$. Additional to the reflected particles, a flow Φ_{gas} of fusion fuel is puffed into the plasma at a position θ_{g} and a width δ_{g} with an angular distribution

$$f(\theta) = \exp\left(-\frac{(\theta - \theta_{\text{g}})^2}{\delta_{\text{g}}^2} \right).$$

So the total influx of neutrals is

$$J = \Gamma_\perp R_{\text{rec}} + \Phi_{\text{gas}} f(\theta).$$

The global particle balance in the steady state

$$\int_0^{2\pi} \Gamma_\perp(\theta) \frac{d\sigma}{d\theta}(\theta)\, d\theta = \int_0^{2\pi} J(\theta) \frac{d\sigma}{d\theta}(\theta)\, d\theta \tag{3.25}$$

yields the relation

$$\Phi_{\text{gas}} = (1 - R_{\text{rec}}) \frac{\int_0^{2\pi} \Gamma_1(n, T; \theta) \frac{d\sigma}{d\theta}(\theta)\, d\theta}{\int_0^{2\pi} f(\theta) \frac{d\sigma}{d\theta}(\theta)\, d\theta} \phi_0^2.$$

In state of global heat balance, the input heating power and the losses are equal, thus

$$2\pi q_{\text{core}} = \int_0^{2\pi} q_{\text{core}} \frac{d\sigma}{d\theta} d\theta = \int_0^{2\pi} q_{\text{loss}} \frac{d\sigma}{d\theta} d\theta = \int_0^{2\pi} (3T\Gamma_\perp + E_{\text{i}} J) \frac{d\sigma}{d\theta} d\theta = \phi_0^2 \int_0^{2\pi} (3T + E_{\text{i}}) \Gamma_1 \frac{d\sigma}{d\theta} d\theta$$

holds.

The state of reference is one with a low puffing, i.e., small Φ_{gas}, and an experimentally known poloidal nearly homogeneous profile (T_{exp}, n_{exp}). This leads to the calibration parameters

$$\phi_0^2 = \frac{2\pi q_{\text{core}}}{(3T_{\text{exp}} + E_{\text{i}}) \int_0^{2\pi} \Gamma_1(n_{\text{exp}}, T_{\text{exp}}) \frac{d\sigma}{d\theta}(\theta)\, d\theta}, \qquad [\phi_0] = 1, \tag{3.26}$$

and

$$\Phi_{\text{exp}} = \frac{2\pi(1 - R_{\text{rec}}) q_{\text{core}}}{(3T_{\text{exp}} + E_{\text{i}}) \int_0^{2\pi} f(\theta) \frac{d\sigma}{d\theta}(\theta)\, d\theta}, \qquad [\Phi_{\text{exp}}] = \frac{1}{\text{m}^2\text{s}}. \tag{3.27}$$

Methods to solve the heat balance equation (3.23) are explained in the numerical study in section 6.1 on page 87.

physical background	symbol	TEXTOR value	MAST value
safety factor	q_0	3.5	5
major radius of Tokamak	R_0	1.75 m	0.80 m
minor radius of Tokamak	r_0	0.46 m	0.60 m
atomic number of nuclei in fusion fuel	A_{i}	2 (deuterium)	2
density of particles	n	$4.5 \cdot 10^{19}\,\text{m}^{-3}$	$2 \cdot 10^{19}\,\text{m}^{-3}$
temperature	T	40 eV	50 eV
magnetic field strength	B_0	2.25 T	0.47 T
heating power from plasma core	q_{core}	$3.13 \cdot 10^{23}\,\text{eV}\,\text{m}^{-2}\,\text{s}^{-1}$	$2.13 \cdot 10^{23}\,\text{eV}\,\text{m}^{-2}\,\text{s}^{-1}$
recycling coefficient	$1 \geq R_{\text{rec}}$	0.9	0.9

Table 3.1: The device dependent physical values used in the anomalous transport equations.

physical background	symbol	value and unit
mass ratio of electron and ion	μ	$= \frac{m_\mathrm{e}}{m_\mathrm{i}} = \frac{5.45 \cdot 10^{-4}}{A_\mathrm{i}}$
mass of electron	m_e	$= 9.10938188 \cdot 10^{-31}\,\mathrm{kg}$
mass of deuterium nuclei	m_i	$= 2 \cdot 1.67262158 \cdot 10^{-27}\,\mathrm{kg}$
Coulomb logarithm	Z_eff	$= 1.5$
Coulomb integral	Λ_c	$= 30.3 - 1.15 \log_{10}\left(n\,\mathrm{m}^3\right) + 3.45 \log_{10}\left(eT\,\mathrm{eV}^{-1}\right)$
mean free path length	λ_e	$= 2.88 \cdot 10^{17}\mathrm{eV}^{-2}\,\mathrm{m}^{-2} \cdot \frac{e^2T^2}{n\Lambda_\mathrm{c}Z_\mathrm{eff}}, \quad [\lambda_\mathrm{e}] = \mathrm{m}$
ratio of plasma and magnetic pressure	β	$= \mu_0 \frac{nT}{B^2}, \quad [\beta] = 1$
cross section of charge exchange and ionization	σ_*	$= 10^{-18}\,\mathrm{m}^2 \exp\left(-\frac{6.8\,\mathrm{J\,C}}{eT}\right), \quad [\sigma_*] = \mathrm{m}^2$
penetration depth of neutral particles	L_n	$= \frac{2}{\sigma_* n}, \quad [L_\mathrm{n}] = \mathrm{m}$
ratio of radial k_χ^2 and azimuthal k_η^2 wave numbers	γ	$= \frac{k_\chi^2 + k_\eta^2}{2k_\eta^2} = \max\left\{1, \frac{1}{2} + \zeta\left(\frac{\pi L_\mathrm{n}}{qR_0K_\perp}\right)^2\right\}, \quad \zeta = 2$
larmor frequency	ω_c	$= \frac{eB}{m_i}, \quad [\omega_\mathrm{c}] = \mathrm{s}^{-1}$
ion sound velocity	c_s	$= \sqrt{\frac{T}{m_i}}, \quad [c_\mathrm{s}] = \mathrm{m\,s}^{-1}$
larmor radius	ρ_i	$= \frac{c_\mathrm{s}}{\omega_\mathrm{c}}, \quad [\rho_\mathrm{i}] = \mathrm{m}$
elementary charge	e	$= 1.602176487 \cdot 10^{-19}\,\mathrm{C}$
charge of ion	e_i	$= e$
speed of light in vacuum	c	$= 2.99792458 \cdot 10^{8}\,\mathrm{m\,s}^{-1}$
Boltzmann constant	k_B	$= 1.3806504 \cdot 10^{-23}\,\mathrm{J\,K}^{-1}$
permeability of free space	μ_0	$= 4\pi \cdot 10^{-7}\,\mathrm{N\,A}^{-2}$
permittivity of free space	ε_0	$= 8.8541878176 \cdot 10^{-12}\,\mathrm{F\,m}^{-1}$

Table 3.2: The physical values used in the anomalous transport equations.

1 T	=	10^4 Gauss
1 eV	=	$1.602176462 \cdot 10^{-12}$ erg
1 eV	=	$1.602176462 \cdot 10^{-19}$ J
1 eV	=	$44.5 \cdot 10^{-27}$ kWh
1 K	=	$8.61735 \cdot 10^{-5}$ eV
1 eV	=	$1.16045 \cdot 10^{4}$ K
1 K	=	$1.38066 \cdot 10^{-23}$ J
1 J	=	$7.24290 \cdot 10^{22}$ K
1 J	=	1 Ws
1 C	=	$2.99792458 \cdot 10^{9}$ cgs

Table 3.3: Constants of proportionality between certain units.

Chapter 4

Numerical treatment of the anomalous transport eigenvalue equation

This chapter concentrates on the numerical methods to efficiently solve the eigenvalue equation (3.17) of the anomalous transport model. Additional to mathematicians, the target audience of this work are physicists, that might not be that familiar with the numerical techniques. Therefore we start with the spatial discretization of the derivatives and transform the continuously defined eigenvalue equation into a matrix polynomial eigenvalue equation.

We solve the matrix polynomial eigenvalue equation with a well adopted Jacobi-Davidson method and improve its efficiency by a multilevel approach that offers an initial search space with a small angle to the desired eigenvector with low computational costs. We discuss how the right Ritz pair can be chosen and how the correction equation can be solved efficiently to a suitable accuracy.

4.1 Discretization

In order to solve the eigenvalue problem (3.17) numerically, the functions and the derivative operations have to be approximated by discrete functions, i.e., on grids.

4.1.1 Grids

In the discrete space a function $f : [a, b] \to \mathbb{C}$ on an interval $I := [a, b]$ is represented by its values $f_i = f(x_i)$ in the *grid points* $x_i \in I,\ 0 \leq i < N$.

Definition 4.1. A *grid*

$$G\big(I = [a, b], N\big) := (x_i)_{i=0,\dots,N-1},\ a \leq x_i < x_j \leq b\ \forall\, 0 \leq i < j \leq N - 1$$

is a strictly monotonically sequence of $N \in \mathbb{N}$ increasing grid points $x_i \in I$. For some operations, it is helpful to arrange the grid points into a vector $\vec{x}$, such that $(\vec{x})_i = x_i$.

On an *equidistant* grid

$$G^{\mathrm{u}}\big([a, b], N\big) := (x_i = a + ih)_{i=0,\dots,N-1}, \qquad h := \frac{b - a}{N - 1}$$

the distance of two adjacent grid points x_i, x_{i+1} is a fixed mesh size $h = x_{i+1} - x_i = \frac{b-a}{N-1}$.

A grid is of length $N \in N$ is called 2π-*periodic* if $x_j = x_{j+N} \mod 2\pi$. Further, $G(N)$ denotes a 2π-periodic grid and $G^{\mathrm{u}}(N)$ is additionally equidistantly spaced.

Definition 4.2. A *grid generating function*

$$g(x):\ G^{\mathrm{u}}\big([a,b],N\big) \to G_2\big([a,b],N\big),$$

maps each grid point $x_i \in G^{\mathrm{u}}$ onto a grid point $g(x_i) = z_i \in G_2$. g is strictly monotone and the derivatives are continuous.

Remark 4.3. When a grid is defined by a grid generating function, equivalent grids with a different number of grid points are available.

Definition 4.4. A function f evaluated at a vector $\vec{\theta} = (\theta_1, \theta_2, \ldots, \theta_{N-1}, \theta_N)^T$ defines the vector

$$f(\vec{\theta}) := \begin{pmatrix} f(\theta_1) \\ f(\theta_2) \\ \vdots \\ f(\theta_{N-1}) \\ f(\theta_N) \end{pmatrix}$$

of function values.

The operator Diag places the elements of a vector $\vec{f}$ onto the diagonal of a matrix:

$$\mathrm{Diag}(\vec{f}) := \begin{pmatrix} f_1 & & & & & \\ & f_2 & & & & \\ & & f_2 & & & \\ & & & \ddots & & \\ & & & & f_{N-1} & \\ & & & & & f_N \end{pmatrix}.$$

Remark 4.5. The product of two functions $f(\theta) \cdot g(\theta)$ can be written in matrix operations as follows

$$\mathrm{Diag}\left((f \cdot g)(\vec{\theta})\right) = \mathrm{Diag}\left(f(\vec{\theta})\right) \cdot \mathrm{Diag}\left(g(\vec{\theta})\right)$$

4.2 Spatial discretization

The eigenvalue equation (3.17) of the anomalous transport model contains a second derivative term. The heat-balance equation (3.23) to determine the plasma parameters includes the first and the second derivatives. In discrete space these derivatives have to be approximated by a numerical differentiation technique, because the values of the underlying functions are only available in grid points. In order to write the eigenvalue equation in form of a matrix polynomial eigenvalue problem, it is necessary to write the derivatives as multiplication with a suitable matrix, i.e.,

$$\frac{\partial^k f}{\partial \theta^k}(\vec{\theta}) \approx D_k f(\vec{\theta}),\ k \in \{1,2\}.$$

There are several well known approximations like finite differences or the pseudo spectral methods. The underlying idea of both methods is as follows [39]. A set of functions $(\psi_j)_{j=0,\ldots,d}$, orthonormal in the sense

$$\sum_{i=0}^{d} \psi_j^H(x_i)\psi_k(x_i) = \langle \psi_j, \psi_k \rangle = \delta_{j,k}$$

is chosen, where $\delta_{j,k}$ denotes the *Kronecker delta*, i.e.,

$$\delta_{j,k} = \begin{cases} 0 & \text{if } j \neq k \\ 1 & \text{if } j = k \end{cases}.$$

Then the function f is expanded in terms of the generating system $\Psi := \{\psi_j,\ j = 0, \ldots, d\}$

$$f(x) = \sum_{j=0}^{d} \langle \psi_j, f \rangle \psi_j(x) + f_\perp(x), \qquad f_\perp \perp \operatorname{span}\{\psi_j \mid j = 0, \ldots, d\}.$$

The residual $f_\perp$ is zero if Ψ is a basis of our discrete space $\mathbb{R}^N$ which requires $d = N - 1$. In case that our function f has complex values, we remember $\mathbb{C} = \mathbb{R} + \mathrm{i}\mathbb{R}$ and we can apply the derivative process on real and imaginary part separately.

Now the derivative of f is taken by the derivative of the ψ_j:

$$\frac{\partial^k f}{\partial \theta^k}(x) = \sum_{j=0}^{d} \langle \psi_j, f \rangle \frac{\partial^k \psi_j}{\partial \theta^k}(x) + \frac{\partial^k f_\perp}{\partial \theta^k}(x)$$

The finite differences apply the interpolation through polynomials up to the degree d with the support restricted to the $d+1$ points which are adjacent the point x_c of interest. The derivative of this polynomial approximates the derivative of the interpolated function. Thus, finite differences concern the local behavior of the function values in adjacent grid points.

In contrast to the finite differences the pseudo spectral methods work globally. For 2π-periodic functions a set $\psi_j(\theta) = \exp(\mathrm{i}j\theta)$ up to some frequency is appropriate. In discrete space the frequency is limited by the so called *sampling theorem*. One can restrict to the sine or the cosine function as well, if the underlying function is symmetric. For non-periodic applications there are different bases [39] like the sinc function or the Tschebychev polynomials. For the periodic boundary conditions in the Tokamak application, the complex exponential function is suited best.

4.2.1 Finite difference stencil by polynomial interpolation

In this section the approximation of the derivative at a grid point x_c by local polynomial interpolation of degree $d \in 2\mathbb{N}$ is deduced. This technique uses $d + 1$ adjacent grid points. First the formula is deduced and afterward the error bounds are analyzed.

Let $N \in \mathbb{N}$ and $f : [x_1, x_N] \to \mathbb{C}$ be an analytic function. At the grid points

$$x_1 < x_2 < \ldots < x_{N-1} < x_N$$

the values

$$f_i := f(x_i)$$

are known. One is interested in an approximation of the first and second derivative in an interior grid point x_c. The methods derived here will be applied to periodic functions later and therefore the assumption to have grid points at both sides of x_c is fully justified.

In the case of a periodic boundary condition a polynomial interpolation of degree $d = N - 1$ is not sufficient. Thus the interpolation is restricted to a local subset of grid points, namely taking $b \in \mathbb{N}$ points to the left and the right of x_c. Then the discrete support of the interpolating polynomial is

$$S_c := \{x_j \mid j \in I_c\}, \qquad I_c := \{c - b, \ldots, c, \ldots, c + b\}.$$

Now, a basis of the polynomial space on I_c is needed. To avoid any restriction on the choice of grid points, a basis of *Lagrangian polynomials*

$$L_{i,c}(x) := \prod_{\substack{j=c-b \\ j\neq i}}^{c+b} \frac{x - x_j}{x_i - x_j}, \qquad i \in I_c,$$

the "fundamental polynomials for point wise interpolation" [7], is chosen.

The feature $L_{i,c}(x_l) = \delta_{i,l}$, $i, l \in I_c$ makes the interpolation easy:

$$p_c(x) = \sum_{i=c-b}^{c+b} f_i L_{i,c}(x).$$

For the derivatives holds

$$p_c'(x) = \sum_{i=c-b}^{c+b} f_i L_{i,c}'(x) \quad \text{and} \quad p_c''(x) = \sum_{i=c-b}^{c+b} f_i L_{i,c}''(x)$$

and the approximation is $f'(x_c) \approx p_c'(x_c)$ and $f''(x_c) \approx p_c''(x_c)$.

With the product rule one obtains

$$L_{i,c}'(x) := \frac{d}{dx} L_{i,c}(x) = \sum_{\substack{k=c-b \\ k\neq i}}^{c+b} \left(\frac{1}{x_i - x_k} \prod_{\substack{j=c-b \\ j\neq i \\ j\neq k}}^{b+c} \frac{x - x_j}{x_i - x_j} \right) \tag{4.1}$$

and

$$L_{i,c}''(x) := \frac{d^2}{dx^2} L_{i,c}(x) = \sum_{\substack{k=c-b \\ k\neq i}}^{b+c} \frac{1}{x_i - x_k} \left(\sum_{\substack{l=c-b \\ l\neq i \\ l\neq k}}^{c+b} \frac{1}{x_i - x_l} \left(\prod_{\substack{j=c-b \\ j\neq i \\ j\neq k \\ j\neq l}}^{c+b} \frac{x - x_j}{x_i - x_j} \right) \right). \tag{4.2}$$

At grid points x_q, $q \in I$, the derivative of the Lagrangian polynomial simplifies to

$$L_{i,c}'(x_q) = \begin{cases} \displaystyle\sum_{\substack{k=c-b \\ k\neq i}}^{c+b} \frac{1}{x_i - x_k}, & q = i \\ \displaystyle\frac{1}{x_i - x_q} \prod_{\substack{j=c-b \\ j\neq i \\ j\neq q}}^{c+b} \frac{x_q - x_j}{x_i - x_j}, & q \neq i \end{cases} \tag{4.3}$$

and

$$L''_{i,c}(x_q) = \begin{cases} \sum\limits_{\substack{k=c-b \\ k\neq i}}^{c+b} \frac{1}{x_i - x_k} \left(\sum\limits_{\substack{l=c-b \\ l\neq i \\ l\neq k}}^{c+b} \frac{1}{x_i - x_l} \right), & q = i \\ \frac{2}{x_i - x_q} \left(\sum\limits_{\substack{l=c-b \\ l\neq i \\ l\neq q}}^{c+b} \frac{1}{x_i - x_l} \left(\prod\limits_{\substack{j=c-b \\ j\neq i \\ j\neq q \\ j\neq l}}^{c+b} \frac{x_q - x_j}{x_i - x_j} \right) \right), & q \neq i \end{cases} \tag{4.4}$$

The *stencil* of the finite differences is

$$[L^{(k)}_{c-b,c}(x_c), \ldots, L^{(k)}_{c,c}(x_c), \ldots, L^{(k)}_{c+b,c}(x_c)],$$

where (k) denotes the kth derivative. On equidistant spaced grids, the stencil is independent of the position c.

4.2.1.1 Finite difference operators with periodic boundary condition

Let $f : [0, 2\pi[\to \mathbb{C}$ be a 2π-periodic function and $\vec{f} := f(\vec{\theta})$ a discrete representation on a grid G, $\theta_0 < \theta_1 < \ldots < \theta_N = \theta_0 + 2\pi$.

$$S^{k,\theta_c} := [L^{(k)}_{c-b,c}(\theta_c), \ldots, L^{(k)}_{c,c}(\theta_c), \ldots, L^{(k)}_{c+b,c}(\theta_c)]$$

is the stencil that approximates the kth derivative of f in θ_c. For a three point stencil

$$[S^{k,\theta_c}_{-1}, S^{k,\theta_c}_{0}, S^{k,\theta_c}_{1}]$$

the matrix operation is

$$\frac{\partial^k}{\partial\theta^k} f \begin{pmatrix} \theta_0 \\ \theta_1 \\ \theta_2 \\ \vdots \\ \theta_{N-2} \\ \theta_{N-1} \end{pmatrix} \approx \begin{pmatrix} S^{k,\theta_0}_{0} & S^{k,\theta_0}_{1} & & & & & S^{k,\theta_0}_{-1} \\ S^{k,\theta_1}_{-1} & S^{k,\theta_1}_{0} & S^{k,\theta_1}_{1} & & & & \\ & S^{k,\theta_2}_{-1} & S^{k,\theta_2}_{0} & S^{k,\theta_2}_{1} & & & \\ & & \ddots & \ddots & \ddots & & \\ & & & S^{k,\theta_{N-2}}_{-1} & S^{k,\theta_{N-2}}_{0} & S^{k,\theta_{N-2}}_{1} & \\ S^{k,\theta_{N-1}}_{1} & & & & S^{k,\theta_{N-1}}_{-1} & S^{k,\theta_{N-1}}_{0} & \end{pmatrix} \begin{pmatrix} f_0 \\ f_1 \\ f_2 \\ \vdots \\ f_{N-2} \\ f_{N-1} \end{pmatrix} = D_k \vec{f}$$

In general, the stencil is put onto a row with S_0 on the diagonal. The elements outside the matrix are shifted to the opposite side in the same row, due to the periodic boundary condition. Let the stencil have $2p+1$ entries. The resulting matrix is a band matrix of width p and additionally the upper right and the lower left corner have non-zero entries to a width of p. This sparsity pattern is entitled by the following definition.

Definition 4.6. A band matrix with the band width p and additionally non-zeros on the upper right and the lower left corner to a width of p is called *periodic band matrix* of band width p. The sparsity pattern is illustrated in Figure 4.1.

The matrix which approximates the derivative by the Lagrangian interpolation technique, as defined above, has a periodic band width of $p = b$ and it is sparse because of $b \ll N$.

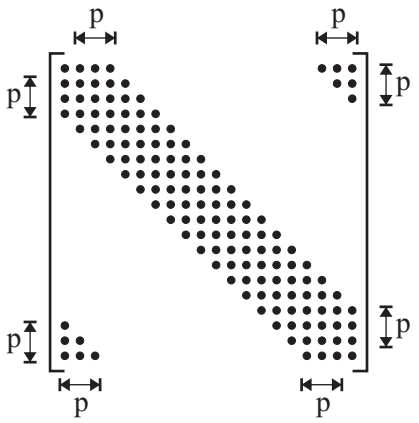

Figure 4.1: A periodic 20×20 band matrix with a band width of $p = 3$. Each dot marks a non-zero entry.

4.2.1.2 Approximation error

The polynomial interpolation technique to obtain the derivative cannot be exact in general. Hence some estimate on the error is of interest, especially how the error reduces if the number of grid points is increased. The following theorem is taken from [35].

Theorem 4.7. *Let $f : [x_0, x_d] \to \mathbb{R}$ be d times differentiable and let be p the interpolating polynomial of degree d through (x_i, f_i), $i = 0, \ldots, d$. For each $x \in [x_0, x_d]$ there is a $\xi = \xi(x) \in]x_0, x_d[$ such that*

$$f(x) - p(x) = (x - x_0)(x - x_1) \ldots (x - x_d) \frac{f^{(d+1)}(\xi)}{(d+1)!}$$

holds.

Definition 4.8. The *order* of the error

$$f(x) - p(x) = \mathcal{O}\left((x_d - x_0)^{d+1}\right)$$

is defined by the power $d + 1$.

The following theorem is possibly not new, but it has not be found in the literature.

Theorem 4.9. *Let $x_i := ih$, $h > 0$, $i = -b, \ldots, b$, $b \in \mathbb{N}$ be an equidistant grid of $2b + 1$ supporting points with its center in $x_0 = 0$. Let f be an analytic function and p, $\deg(p) = d := 2b$, the polynomial that interpolates $f(x_i) = p(x_i)$, $i = -b, \ldots, b$.*

In the center $x_0 = 0$ the accuracy of the derivative approximation is

$$p'(x_0) - f'(x_0) \in \mathcal{O}(h^d)$$
$$p''(x_0) - f''(x_0) \in \mathcal{O}(h^d).$$

Proof. Due to Theorem 4.7 it holds

$$p(x_0) - f(x_0) \in \mathcal{O}(h^{d+1}).$$

Each derivative looses one order and thus

$$p'(x_0) - f'(x_0) \in \mathcal{O}(h^d)$$
$$p''(x_0) - f''(x_0) \in \mathcal{O}(h^{d-1})$$

holds. However, the stencil of the second derivative is symmetric and though the error is symmetric it holds

$$p''(x_0) - f''(x_0) \in \mathcal{O}(h^d).$$

□

In the Appendix A on page 123 there is another variant of this proof by direct computation.

Theorem 4.10. *Let G_1 be an equidistant grid of N grid points. The values $f_j = f(z_j)$ of the analytic function f are known in $z_j \in G_1$ and its derivative is approximated by the Lagrangian interpolation polynomial p of degree $d = 2b$ in $z_0 \in G_1$. We define $G^{\mathrm{u}} := (jh)_{j=-b,\dots,b}$, $h > 0$. Let be $g : G^{\mathrm{u}} \to G_1$ the grid generating function with $g(x_j) = z_j$.*
The accuracy of the approximation $p^{(n)}$ of $f^{(n)}$, $n = 1, 2$ from theorem 4.9 holds for non-equidistant grid G_1, too. However, the constant in the error term depends on the size of the derivatives $g^{(n)}(x_0)$, $n = 1, \dots, d$.

Proof. With the grid generating function g the values $f_i = f(z_i)$, $z_i \in G_1$ can be written $f_i = f(g(x_i))$, where $x_i \in G^{\mathrm{u}}$.

Now, Theorem 4.9 is applicable to $f(g)$ and we derive from its proof

$$p^{(n)}(0) - f^{(n)}\big(g(0)\big) = \sum_{k=d}^{m} c_k f^{(k)}\big(g(0)\big)\frac{h^k}{k!} + \mathcal{O}(h^{m+1}), \qquad n \in \{1, 2\}$$

where

$$c_k = \sum_{j=-b}^{b} j^k L_j^{(n)}(0).$$

The inner derivatives of $f^{(k)}\big(g(0)\big)$ are factors within the error term. □

Remark 4.11. Although the finite difference stencil can be calculated out of the Taylor formula by solving a linear system, the Lagrangian interpolation technique offers the solution directly. The proof of Theorem 4.9 points out that both methods are theoretical equal. Both methods become numerically unstable if d is too large with respect to the floating point precision of the data type *double*. If the knowledge of the derivative of a given vector is sufficient, the *method of divided differences* [35] is more stable.

4.2.2 Spectral methods

In contrast to the finite difference technique, the pseudo spectral methods make use of the whole domain for a global interpolation. "If one wants to solve an ODE or PDE to high accuracy on a simple domain, and if the data defining the problem are smooth, then pseudo spectral methods are usually the best tool. They can often achieve ten digits of accuracy where a finite difference or finite element method would get two or three. At lower accuracies, they demand less computer memory than the alternatives." [39]. Due to numerical stability and the possibility to apply the *fast Fourier transformation* (FFT), the pseudo spectral method is considered for equidistant spaced grids in this thesis only.

The discrete *inverse Fourier transformation* yields coefficients $\alpha_j \in \mathbb{C}$ of a vector $f(\vec{\theta})$ such that

$$f(\theta) = \begin{cases} \displaystyle\sum_{j=-(N-1)/2}^{(N-1)/2} \alpha_j \exp\left(\mathrm{i}j\theta\right), & N \text{ odd} \\ \displaystyle\sum_{j=-(N-2)/2}^{(N-2)/2} \alpha_j \exp\left(\mathrm{i}j\theta\right) + \frac{1}{2}\left(\exp\left(\mathrm{i}\frac{N}{2}\theta\right) + \exp\left(-\mathrm{i}\frac{N}{2}\theta\right)\right), & N \text{ even} \end{cases}$$

holds in each grid point $\theta = (\vec{\theta})_k$. The two cases are necessary in order to take the highest frequency symmetric at both sides. The derivative is

$$\frac{\partial^k f}{\partial \theta^k}(\theta) = \begin{cases} \sum_{j=-(N-1)/2}^{(N-1)/2} \alpha_j \left(\mathrm{i}j\right)^k \exp\left(\mathrm{i}j\theta\right), & N \text{ odd} \\ \sum_{j=-(N-2)/2}^{(N-2)/2} \alpha_j \left(\mathrm{i}j\right)^k \exp\left(\mathrm{i}j\theta\right) + \frac{1}{2}\left(\mathrm{i}\frac{N}{2}\right)^k \left(\exp\left(\mathrm{i}\frac{N}{2}\theta\right) + (-1)^k \exp\left(-\mathrm{i}\frac{N}{2}\theta\right)\right), & N \text{ even.} \end{cases}$$

Definition 4.12. Let be $V \in \mathbb{C}^{N\times l}$ and $\mathcal{F}_N = (\exp(\mathrm{i}j\theta_k))_{k,j=0,\ldots,N}$ the matrix, that applies the Fourier transform on each column of V. $\mathcal{F}_N^{-1}$ denotes the inverse discrete Fourier transform. The matrix notation is for the theoretical discussion. The implementation makes use of the fast Fourier variant. The factors which are obtained when the complex exponential function is derived are arranged within Ξ. We have to take care of the aliasing effect and choose the representative with the smallest $|j|$:

$$\Xi^k := \mathrm{Diag}\left(0, \mathrm{i}^k, (2\mathrm{i})^k, (3\mathrm{i})^k, \ldots, \left(\frac{N-1}{2}\mathrm{i}\right)^k, \left(-\frac{N-1}{2}\mathrm{i}\right)^k, \ldots, (-2\mathrm{i})^k, (-\mathrm{i})^k\right)$$

if N is odd and

$$\Xi^k := \mathrm{Diag}\left(0, \mathrm{i}^k, \ldots, \left(\left(\frac{N}{2}-1\right)\mathrm{i}\right)^k, \left(\frac{N}{2}\mathrm{i}\right)^k + \left(-\frac{N}{2}\mathrm{i}\right)^k, \left(-\left(\frac{N}{2}-1\right)\mathrm{i}\right)^k, \ldots, (-\mathrm{i})^k\right)$$

if N is even.

Remark 4.13. If N is even and k is odd the $\left(\frac{N}{2}+1\right)$th diagonal element in Ξ^k is zero.

Remark 4.14. The computational cost to calculate the Fourier transform is in $\mathcal{O}(N\log(N))$ in case of the fast variant and in $\mathcal{O}(N^2)$ with the matrix product.

The derivative for a given function f is calculated in $\mathcal{O}(N\log(N))$ as follows. The inverse discrete Fourier transform yields the Fourier coefficient α_j of the frequency j. They are weighted by Ξ^k and transformed back by the discrete Fourier transform. This process can be written elegantly as

$$\frac{\partial^k f}{\partial \theta^k}(\vec{\theta}) = \mathcal{F}_N \Xi^k \mathcal{F}_N^{-1} \vec{f}, \quad \vec{f} := f(\vec{\theta}).$$

The matrices $D_k := \mathcal{F}_N \Xi^k \mathcal{F}_N^{-1}$, $k = 1, 2$ can be calculated directly by an approach similar to the Lagrangian interpolation. The *periodic sinc function*

$$\mathrm{sinc}(x) = \frac{h \sin\left(\frac{\pi x}{h}\right)}{2\pi \tan\left(\frac{x}{2}\right)}$$

is one in $x = 0 \mod 2\pi$ and zero in all the other grid points. In [39] it is derived in detail, that

$$\mathrm{sinc}'(x_j) = \begin{cases} 0, & j = 0 \mod N \\ \frac{1}{2}(-1)^j \cot\left(\frac{jh}{2}\right), & j \neq 0 \mod N \end{cases}$$

holds and the matrix of the first derivative is

$$D_1 = \begin{pmatrix} 0 & & & & -\frac{1}{2}\cot\left(\frac{1h}{2}\right) \\ -\frac{1}{2}\cot\left(\frac{1h}{2}\right) & \ddots & \ddots & & \frac{1}{2}\cot\left(\frac{2h}{2}\right) \\ \frac{1}{2}\cot\left(\frac{2h}{2}\right) & \ddots & & & -\frac{1}{2}\cot\left(\frac{3h}{2}\right) \\ -\frac{1}{2}\cot\left(\frac{3h}{2}\right) & & \ddots & & \vdots \\ \vdots & & \ddots & \ddots & \frac{1}{2}\cot\left(\frac{1h}{2}\right) \\ \frac{1}{2}\cot\left(\frac{1h}{2}\right) & & & & 0 \end{pmatrix}.$$

The second derivative of the sinc function is

$$\operatorname{sinc}''(x_j) = \begin{cases} -\frac{\pi^2}{3h^2} - \frac{1}{6} & j = 0 \mod N \\ -\frac{(-1)^j}{2\sin^2\left(\frac{jh}{2}\right)} & j \neq 0 \mod N \end{cases}$$

and the matrix reads

$$D_2 = \begin{pmatrix} \ddots & \vdots & \\ \ddots & -\frac{1}{2}\csc^2\left(\frac{2h}{2}\right) & \\ \ddots & \frac{1}{2}\csc^2\left(\frac{1h}{2}\right) & \\ & -\frac{\pi^2}{3h^2} - \frac{1}{6} & \\ & \frac{1}{2}\csc^2\left(\frac{1h}{2}\right) & \ddots \\ & -\frac{1}{2}\csc^2\left(\frac{2h}{2}\right) & \ddots \\ & \vdots & \ddots \end{pmatrix},$$

where $\csc(x) := \frac{1}{\sin(x)}$.

In special cases, where f is known to be even or odd, the cosine or sine transformation takes the role of the Fourier transformation. This reduces the cost of the calculation and conserves the symmetry to highest accuracy.

4.2.3 Comparison of the polynomial interpolation with the pseudo spectral method

Lagrange interpolation is a local method with an expense in $\mathcal{O}(Nd)$. The derivative matrices are sparse if $d \ll N$ holds and the approximation error of the first and the second derivative is of the order $(x_b - x_{-b})^{d-1}$. It can be applied on non equidistant spaced grids, but the error may increase on strongly irregular grids.

On the other hand the pseudo spectral method acts globally. Therefore the derivative matrices are dense, causing an expense of $\mathcal{O}(N^2)$ operations. However, at equidistant spaced grids, to derive one given vector can be computed by the *fast Fourier transformation* (FFT) , which reduces the derivative costs to $\mathcal{O}(N\log(N))$.

In [3] the Mathieu equation (3.14) is solved by the pseudo spectral method. A linear combination of low frequencies

$$\phi(\vartheta) = \sum_{j=0}^{m} \alpha_j \sin(j\vartheta) + \beta_j \cos(j\vartheta), \qquad \alpha_j, \beta_j \in \mathbb{R}$$

is applied to (3.14) and the coefficients α_j, β_j are determined. Due to a fast decay of the weighting factors, higher frequencies can be truncated.

We will compare both methods in the sections of the eigenvalue solver and the heat balance equation again.

4.3 Solving the cubic eigenvalue problem numerically

The previous section provides the basic numerical techniques to write the continuous eigenvalue problem (3.17) in form of matrices. In compact form (cf. (3.16)) the continuous one looks like

$$P(\omega) = a_3(\theta)\omega^3 + a_2(\theta)\omega^2 + \left(a_1(\theta) + b_1(\theta)\frac{\partial^2}{\partial\theta^2}\right)\omega + a_0(\theta) + b_0(\theta)\frac{\partial^2}{\partial\theta^2}. \tag{4.5}$$

The angular domain $[0, 2\pi[$ is discretized by a periodic grid $\vec{\theta}$ of $N \in \mathbb{N}$ grid points. The terms which depend on the angle θ are represented by diagonal matrices and the second derivative is approximated by the matrix D_2 from the previous section because of the periodic boundary condition

$$P_{\vec{\theta}}(\omega) = \overbrace{\operatorname{Diag}\left(a_3(\vec{\theta})\right)}^{M_3}\omega^3 + \overbrace{\operatorname{Diag}\left(a_2(\vec{\theta})\right)}^{M_2}\omega^2 + \overbrace{\left(\operatorname{Diag}\left(a_1(\vec{\theta})\right) + \operatorname{Diag}\left(b_1(\vec{\theta})\right)D_2\right)}^{M_1}\omega + \underbrace{\left(\operatorname{Diag}\left(a_0(\vec{\theta})\right) + \operatorname{Diag}\left(b_0(\vec{\theta})\right)D_2\right)}_{M_0}. \tag{4.6}$$

$P_{\vec{\theta}}(\omega)$ is a cubic matrix polynomial in $\mathbb{C}^{N\times N}$.

The naive method to find the eigenpairs $(\omega, \vec{\phi})$ such that

$$P_{\vec{\theta}}(\omega)\vec{\phi} = 0$$

is to linearize (cf. (2.1)) the cubic matrix polynomial $P_{\vec{\theta}}$ and apply the QZ algorithm (cf. section 2.2.2.1 on page 27) on the resulting generalized eigenvalue problem of the dimension $3N$.

The calculation with the QZ algorithm and $N = 1024$ on a 2 GHz processor takes one hour. This is too slow because we have to solve one eigenvalue equation for each wave number $K_\perp$ and the self consistent calculation in Chapter 6 requires to repeat it several times which requires to solve a total number of thousands to a million eigenvalue equations. With the QZ algorithm the self consistent simulation would take several years.

We are interested in a fast algorithm that calculates the one or two eigenpairs with the maximal growth rate $\Im(\omega)$.

4.3.1 Jacobi-Davidson method

In Chapter 2, the Jacobi-Davidson method is introduced as a technique to find one or a few eigenpairs by solving smaller eigenvalue problems on (small) subspaces. First we rewrite Algorithm 6 on page 31 for the special structure of the eigenvalue equation (4.6). This is done in Algorithm 7.

The derivative in the eigenvalue equation (3.17) operates on the column vectors of the search space V. This allows to apply the fast Fourier transformation. In the case of the finite differences a divided differences scheme can be applied in order to find the coefficients of the interpolating polynomial and to take its derivative the cost is only $\mathcal{O}(N)$. The numerical stability of the divided difference scheme is better for derivatives of higher order compared to the matrix obtained by the Lagrangian interpolation method.

Beside the derivative matrices, all the other matrices are diagonal. Although the description of Algorithm 7 is written with diagonal matrices, its implementation avoids the indexing process of sparse matrices completely.

The stopping criteria is enhanced by a forward error estimate (cf. section 2.4 on page 33) because a small residual is only a necessary condition but not sufficient in case of badly conditioned eigenvalues ($\kappa(P(\omega)) \gg 1$). To keep the computational costs low, a much smaller residual r can be demanded until the forward error estimate e_f is calculated, i.e., $\varepsilon_\mathrm{r} < \varepsilon_\mathrm{f}$, where the appropriate ratio

$$\frac{\varepsilon_\mathrm{f}}{\varepsilon_\mathrm{r}} \approx \kappa(P(\omega))$$

depends on the condition number, which can be approximated by the component wise condition number (2.11).

Algorithm 7 Jacobi-Davidson algorithm for anomalous transport eigenvalue equation (4.5)

Require: a grid $\vec{\theta}$ of $N \in \mathbb{N}$ grid points.
Require: a k dimensional initial search space $V = [v^1, \ldots, v^k] \in \mathbb{C}^{N \times k}$, $1 \leq k \ll N$.
1: discretize $D_2 \leftarrow \frac{\partial^2}{\partial \theta^2}$ if not the pseudo spectral method is applied.
2: discretize $A_j = \mathrm{Diag}\left(a_j(\vec{\theta})\right)$, $j = 0, 1, 2, 3$.
3: discretize $B_j = \mathrm{Diag}\left(b_j(\vec{\theta})\right)$, $j = 0, 1$.
4: $P(\omega) := A_3\omega^3 + A_2\omega^2 + (A_1 + B_1 D_2)\omega + A_0 + B_0 D_2$.
5: orthonormalize V.
6: **loop**
7: calculate $E = D_2 V$ or $E = \mathrm{FFT}(\Xi^2(\mathrm{IFFT}(V)))$. // derivative
8: calculate $W_j := A_j V + B_j E$, $j = 0, 1$. // projection from the right side
9: calculate $W_j := A_j V$, $j = 2, 3$. // projection from the right side
10: calculate $H_j := V^H W_j$ for $j = 0, \ldots, 3$. // projection from the left side
11: calculate the desired eigenpair(s) of the projected equation $\widetilde{P}(\nu)y = \sum_{j=0}^{3} \nu^j H_j y = 0$, $\|y\| = 1$ by a direct solver (QZ).
12: calculate the Ritz value in the original space $u := Vy$.
13: calculate the residual $r := P(\nu)u = \sum_{j=0}^{3} \nu^j W_j y$.
14: **if** $\|r\|_\infty < \varepsilon_\mathrm{r}$ **then**
15: calculate the component wise backward error b_c as stated in (2.12).
16: calculate the component wise condition number κ_c as stated in (2.11).
17: calculate the forward error estimate $e_\mathrm{f} := b_\mathrm{c}\kappa_\mathrm{c}$.
18: **if** $e_\mathrm{f} < \varepsilon_\mathrm{f}$ **then**
19: stop.
20: **end if**
21: **end if**
22: calculate $w := P'(\nu)u = \sum_{j=1}^{3} \nu^{j-1} W_j y$.
23: solve the correction equation $\left(I - \frac{wu^H}{u^H w}\right) P(\nu)(I - uu^H)t = -r$ approximately.
24: expand the search space $V := [V, t]$.
25: orthonormalize V.
26: **end loop**

These aspects have already been realized in Algorithm 7. We will discuss the choice of the initial search space V, the choice of the right Ritz pair of each projected system and a method to solve the correction equation in the subsequent sections.

The orthonormalization process in line 5 and 25 of Algorithm 7 can be numerically realized mainly in two ways. One possibility is to orthonormalize t against the columns of V. The advantage is in the update process of V. Let

$$\widehat{t} := \left(I - VV^H\right) t$$

be the orthonormal component of t with respect to V. First the search space is expanded as

$$V^{\mathrm{new}} := \begin{bmatrix} V & \widehat{t} \end{bmatrix}$$

and then the projection from the right side is updated as

$$W_j^{\mathrm{new}} := \begin{bmatrix} W_j & M_j\widehat{t} \end{bmatrix}, \qquad j = 0, \ldots, 3.$$

Finally the whole projected eigenvalue equation reads

$$H_j^{\mathrm{new}} := \begin{bmatrix} V^H \\ \widehat{t}^H \end{bmatrix} \begin{bmatrix} W_j & M_j\widehat{t} \end{bmatrix} = \begin{bmatrix} V^H W_j & V^H M_j \widehat{t} \\ \widehat{t}^H W_j & \widehat{t}^H W_j \widehat{t} \end{bmatrix} = \begin{bmatrix} H_j & V^H M_j \widehat{t} \\ \widehat{t}^H W_j & \widehat{t}^H W_j \widehat{t} \end{bmatrix}, \qquad j = 0, \ldots, 3,$$

where the largest block in the upper left corner is already known and the last row and column needs to be calculated. The only problem with this approach is the numerical stability. The angle of t against V might be very small and also with reorthogonalization applied twice it sometimes happens that the columns of V become linearly dependent which causes the algorithm to break down.

This can be avoided by the second possibility, which adds t first $V \leftarrow [V, t]$ and then orthonormalizes the columns of V by QR or *singular value decomposition* (SVD). In general these methods change all the columns of V and therefore W_j and H_j have to be calculated from scratch. When $\dim(V)$ is small this is only a tiny disadvantage, but when the search space is huge it really is computational cost intensive. The computational cost of an SVD also depends strongly on the dimension of the search space.

We do not worry about the computational costs on calculating the projected eigenvalue system, further, because the subsequent ideas will achieve that the search space stays very small, i.e., less than 10.

The selection of the Ritz pair of the maximal growth rate does not guarantee to find the desired eigenpair of the maximal growth rate. If the desired eigenvector is almost orthogonal to the search space V, it might not be found. Further more, the Ritz values can be a very rough approximation of the eigenvalues and so the decision if the gap of the Ritz value of the maximal growth rate to the second most one is very small is unsafe. In this case several Ritz values need to be improved by subsequent Jacobi-Davidson iterations until the accuracy of the Ritz values is sufficient to determine the desired one.

If the angle between the search space and the eigenvector of the desired eigenpair is small, there is at least one Ritz value that is close to the eigenvalue of the desired eigenpair. However, other Ritz values can be approximated badly and thus one of them might attain the greatest imaginary part.

Lemma 2.24 on page 22 says that the field of values $\mathcal{F}(V^H P V)$ of the Ritz pairs is contained in the field of values $\mathcal{F}(P)$ of the matrix polynomial P. However, $\mathcal{F}(P)$ can be much larger than the convex hull of the eigenvalues and thus the growth rate of the Ritz pairs is not bounded by the eigenvalues. Summing up, the decision on the Ritz pair based on the Ritz values is highly risky and cannot guarantee to find the eigenpair of the strongest growth rate.

On to physical reasons, it is not only the maximal growth rate $\Im(\omega)$ but additionally the perturbation amplitude envelope ϕ has to be consistent with the physical surrounding. In a Tokamak of our model, there are two remarkable points: the high field side (HFS) at $\theta = \pi \mod 2\pi$ and the low field side (LFS) at $\theta = 0 \mod 2\pi$. Hence, $|\phi|^2$ is expected to have extremal points at these positions and to be smooth in between.

In the past Tokar et al. [38] solved the simpler eigenvalue equation as described in section 3.1.4.2 on page 41 by the Mathieu equation (3.14) and the suitable solution is the zeroth even Mathieu function ce_0 [3]. ce_0 looks like the real part of the eigenfunction displayed in Figure 4.2(b,c). The aim with the more complex eigenvalue equation is to find the eigenmode that is equivalent to Mathieus ce_0—equivalent in the sense of a homotopy between the averaged and the angular dependent profiles.

Some investigation revealed the fact, that there are eigenpairs similar to ce_0 (cf. Figure 4.2). The eigenvalue equation of the anomalous transport eigenvalue problem (3.17) is evaluated at several values of the wave number $K_\perp \in [0.05, 0.6]$. The plasma parameters we used belong to TEXTOR. The three eigenvalues which have the maximal growth rate $\Im(\omega) > 0$ are plotted in Figure 4.2(a) for each wave number. The circle marks the eigenvalue of the smallest wave number and the x-marks marks the eigenvalue of the largest wave number.

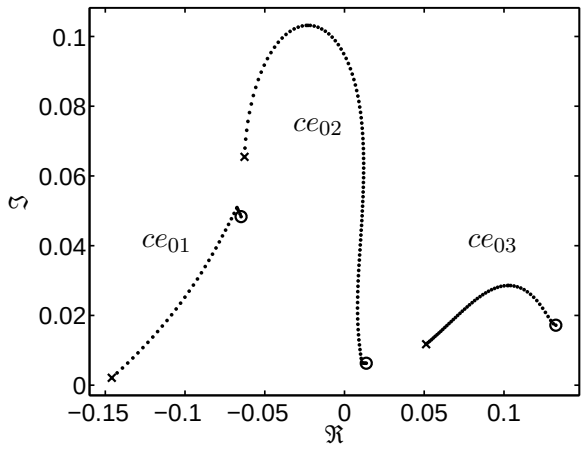

(a) eigenvalues in complex plane

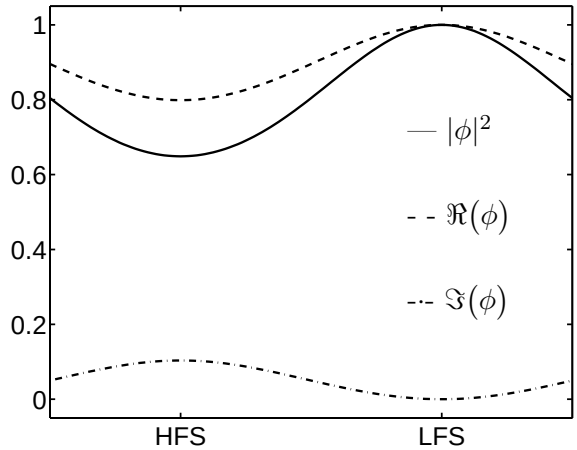

(b) eigenfunction ce_{01} $K_\perp = 0.06$, $\omega = -0.067 + 0.051i$

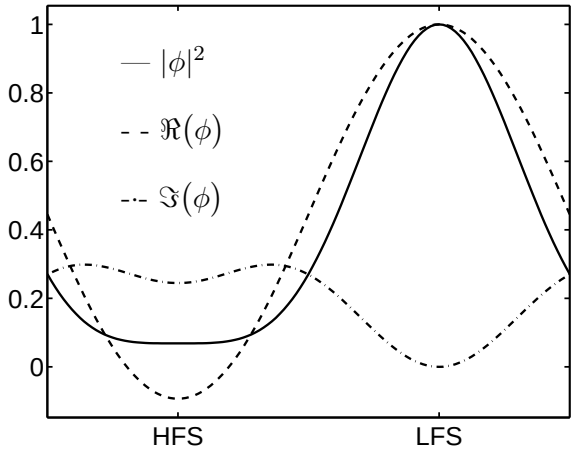

(c) eigenfunction ce_{02} $K_\perp = 0.34$, $\omega = -0.023 + 0.103i$

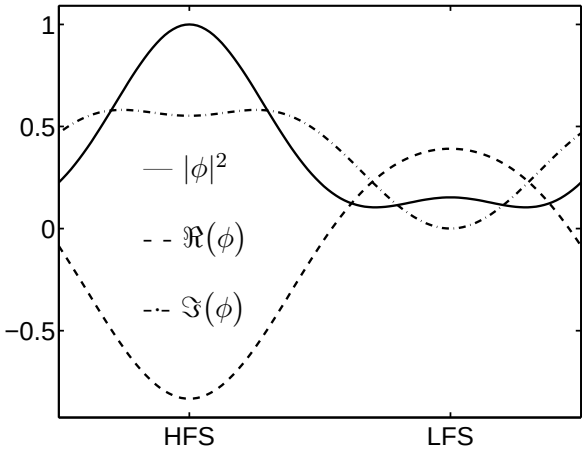

(d) eigenfunction ce_{03} $K_\perp = 0.25$, $\omega = 0.103 + 0.029i$

Figure 4.2: (a) The three eigenvalues of the largest imaginary part for several wave numbers of the anomalous transport eigenvalue problem (3.17) with TEXTOR parameters. The curve of the eigenvalues of ce_{01} has a kink at the wave number where the derivative of the factor γ in the eigenvalue equation is not differentiable. (b-d) Eigenfunction at the wave number where the imaginary part of the three curves in (a) is maximal. Here the eigenfunctions are normalized such that $\max_\theta |\phi(\theta)| = 1$ and the complex phase is normalized such that the imaginary part vanishes at the LFS. The eigenfunctions ce_{01} and ce_{02} have the maximal intensity at the LFS and the minimal intensity at the HFS. The extremal intensity of ce_{03} is located the other way round.

In 4.2(b-d) the eigenfunctions are plotted. Here the eigenfunctions are normalized such that $\max_\theta |\phi(\theta)| = 1$ and the complex phase is normalized due to Definition 3.5 on page 42. The dashed line is the real part of the eigenfunction and the dash-dotted line the imaginary part. The intensity $|\phi|^2$ is plotted by the solid line. This three eigenfunctions are similar to ce_0 and therefore we entitle them by similar names in the Definition 4.15. ce_{01} and ce_{02} have maximal intensity at the LFS and minimal intensity at the HFS. The extremal intensity of ce_{03} is located the other way round. The shape of the real part (dashed line) is similar to the eigenfunction ce_0 of the Mathieu equation (3.14). The curve of the eigenvalues of ce_{01} has a kink at the wave number where the derivative of the factor γ in the eigenvalue equation is not differentiable.

Classification 4.15. Let the eigenfunction ϕ be normalized such that $\max_\theta |\phi(\theta)| = 1$ and the complex phase complies with Definition 3.5 on page 42. The eigenfunction ϕ of equation (3.17) is similar to the eigenfunctions of the Mathieu equation (3.14). Therefore we call the eigenfunction which has the following characteristics ce_{01} (cf. Figure 4.2(b)):

- $|\phi(\text{HFS})|^2 < |\phi(\text{LFS})|^2$
- $|\Im(\phi)| \ll \Re(\phi)$
- $\Re(\phi(\text{HFS})) < \Re(\phi(\text{LFS}))$
- $\Im(\phi(\text{HFS})) > \Im(\phi(\text{LFS}))$
- The shape of the real and the imaginary part is similar to the shape of a sine function.

ce_{02} (cf. Figure 4.2(c)) are called eigenfunctions with the features:

- $|\phi(\text{HFS})|^2 < |\phi(\text{LFS})|^2$
- $|\Im(\phi(\text{LFS}))| < |\Re(\phi(\text{LFS}))|$
- $|\Im(\phi(\text{HFS}))| > |\Re(\phi(\text{HFS}))|$
- $\Re(\phi(\text{HFS})) < \Re(\phi(\text{LFS}))$
- $\Im(\phi(\text{HFS})) > \Im(\phi(\text{LFS}))$
- The shape of the real part is similar to a sine function.

ce_{03} (cf. Figure 4.2(d)) are called eigenfunctions of the characteristics:

- $|\phi(\text{LFS})|^2 < |\phi(\text{HFS})|^2$
- $-\Re(\phi(\text{HFS})) > \Re(\phi(\text{LFS}))$
- $|(\phi)|^2$ has its maxima at the LFS and the HFS.
- The shape of the real part is like the sine function.

Remark 4.16. The classification of the Definition 4.15 is not perfect. There are constellations, where some of the criteria are not fulfilled. However, a precise classification is not possible without concerning all the plasma parameters in the eigenvalue equation which is too complex.

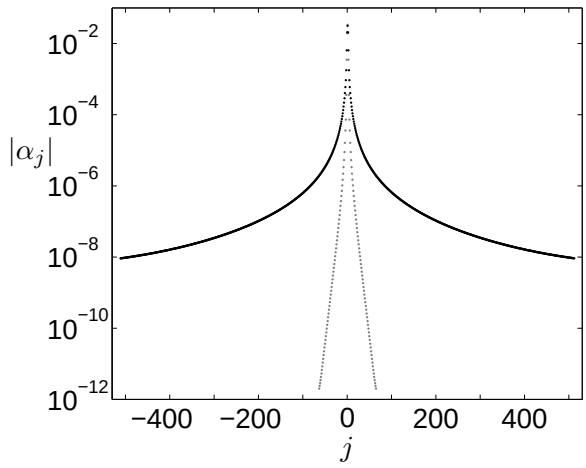

Figure 4.3: The Fourier decomposition of the eigenfunction with an almost constant plasma profile (gray) and a strongly inhomogeneous profile (black). The modulus of the Fourier coefficients α_j in the frequency space is plotted. The amplitude decreases at higher frequencies.

The absolute α_j of the Fourier coefficients of ce_{01}, ce_{02} and ce_{03} decay with an increasing frequency $|j|$. The gray curve of Figure 4.3 shows the modulus of the amplitudes where the frequencies are defined as $\exp(-\mathrm{i}j\theta)$. With this information, the obvious approach is to choose the search space V in the Jacobi-Davidson method as

$$V = \left[\exp(-\mathrm{i}k\vec{\theta}), \exp(-\mathrm{i}(k-1)\vec{\theta}), \ldots, \exp(-\mathrm{i}\vec{\theta}), 1, \exp(\mathrm{i}\vec{\theta}), \ldots, \exp(\mathrm{i}k\vec{\theta})\right]$$

where k is in the range from 3 to 10. If the plasma parameters (temperature, density) are almost constant this method works fine, but when the plasma parameter profiles become steep higher frequencies are necessary. An example is the black curve in Figure 4.3. In such a case search space of the naive method becomes huge and the performance low.

The weights of the frequencies in Figure 4.3 are strictly monotonous decreasing. This is only one special case. In all our simulations for the eigenfunction of physical interest (ce_{01}, ce_{02} or ce_{03}) there has always been observed that there is a $k \in \mathbb{N}$, a strictly monotonous decreasing curve g and a small number $\varepsilon > 0$ such that

$$|\alpha_j - g(|j|)| < \varepsilon \quad \forall |j| > k$$

holds.

4.4 Multilevel Jacobi-Davidson approach

A more sophisticated approach to solve the eigenvalue equation (3.17) is to use a multilevel approach to obtain a suitable initial search space V^{init} by low computational costs. The idea is to solve the eigenvalue equation on a coarse grid first. Due to the smoothness of the desired eigenfunction a solution will exist on a coarse grid that approximates the desired solution on the fine grid.

We will discuss the appropriate alignment of the grid points in the sense to make the coarse grid approximation of the eigenvalue most accurate in section 4.4.3 on page 67. In the following we assume to use a pseudo spectral method on an equidistant spaced grid.

On a grid of $N = 8$ points only, a direct solver can be applied. It allows to approximate the desired eigenpair and to choose the candidate of interest. The eigenvector can be prolonged to

a finer grid of e.g. twice the number of grid points by interpolation. There it is taken as the initial search space V^{init} in the Jacobi-Davidson algorithm that improves the accuracy of the eigenpair approximation on the finer resolution. The result can be prolonged to an even finer grid and improved again.

The Jacobi-Davidson algorithm is applied subsequently on different levels of the discretization. Therefore we call Algorithm 8 the *multilevel Jacobi-Davidson algorithm*.

Algorithm 8 Multilevel Jacobi-Davidson algorithm to calculate m eigenpairs

Require: a full resolution of $N = 2^L c$ grid points, where $c \in \mathbb{N}$ is the number of points on the coarsest grid and $L+1$ the number of levels.
Require: a suitable grid $G_{2^k c}$ for each level $k = 0, 1, \ldots, L$ of resolution.
Require: the number $m \in \mathbb{N}$, $m \leq 3c$ of desired eigenpairs.
Require: a fixed wave number $K_\perp$.
1: discretize and solve the eigenvalue problem (3.17) on G_c by a direct solver.
2: choose the m eigenpairs $\left(\omega_i^{G_c}, \phi_i^{G_c}\right)_{i=1,\ldots,m}$ of interest.
3: **for** $i = 1, \ldots, m$ **do**
4: // for each eigenpair
5: **for** $l = 1, \ldots, L$ **do**
6: // on each level of resolution
7: prolong the eigenvector $\phi_i^{G_{2^{l-1}c}}$ to $\phi_i^{G_{2^l c}}$ by interpolation.
8: discretize the eigenvalue problem on the grid $G_{2^l c}$.
9: improve the prolonged eigenpair $\left(\omega_i^{G_{2^l c}}, \phi_i^{G_{2^l c}}\right)$ by the Jacobi-Davidson Algorithm 7, where the initial search space $V := \phi_i^{G_{2^l c}}$ is the prolonged eigenvector of the next coarser grid.
10: **end for**
11: **end for**
12: the solution is $\left(\omega_i^{G_N}, \phi_i^{G_N}\right)_{i=1,\ldots,m}$.

Now we discuss the essential parts of the multilevel Jacobi-Davidson Algorithm 8: The plasma parameters, like the temperature T and the density n, are restricted to the coarsest grid of c (e.g. $c = 8$) grid points. The matrices of the cubic eigenvalue problem (3.17) are build on this grid and all eigenpairs are calculated by a direct solver. The direct solver linearizes the cubic matrix polynomial and applies the QZ algorithm on the linearization. Due to the low dimension the direct solver is efficient.

Then the $m \in \mathbb{N}$ eigenpairs of physical interest are chosen among the $3c$ ones. For each of the m selected eigenpairs, the following procedure is repeated. The eigenpair is prolonged to the next finer grid G_{2c} of twice the number of points. Now, the matrices of the eigenvalue problem are build on the new grid and the Jacobi-Davidson algorithm is applied to improve the eigenpair. Thereby the initial search space is the prolonged eigenvector. In each Jacobi-Davidson cycle the Ritz pair closest to the prolonged solution of the coarser grid is selected. The definition of the closest Ritz pair and a method to determine it is described in section 4.4.1.

Since the initial search space V is the prolonged eigenvector from the next coarser grid we hope that there is one Ritz pair close to the desired eigenpair. It is close in the sense that the angle between the search space and the desired solution is small. When the Jacobi-Davidson method finishes, we have the improved eigenpair. This eigenpair can be prolonged to an even finer grid and be improved again, until the finest grid $G_{2^L c}$ of $2^L c$ grid points is reached.

Many approaches can be found in the literature which apply multilevel or multigrid methods to eigenvalue problems. The most traditional approach is to treat the eigenvalue problem as a

nonlinear equation and apply the *full approximation scheme* (FAS). See [20] and the references therein. Another approach is to use the multilevel technique on the linear systems in the Rayleigh quotient iteration. It requires special attention because the linear system is nearly singular and a high accuracy of the solution is required. Contrary to these approaches, the multilevel Jacobi-Davidson method developed in this work uses the multilevel technique to build up the initial search space by constructing a good approximation of the desired eigenvector.

4.4.1 Choosing the right Ritz pair

This section deals with the selection of the right Ritz pair in the multilevel Jacobi-Davidson method. We have the prolonged eigenpair (ν_*, u_*) of the next coarser grid and want to use it as the reference.

Consider the case that an approximation (ν_*, u_*) of a desired but yet unknown eigenpair (ω, ϕ) is given. Depending on the accuracy of (ν_*, u_*), the Jacobi-Davidson method is very efficient if one takes u_* as the initial search space $V_1 = u_*$. Within each cycle the Ritz pair closest to (ν_*, u_*) is to choose. In order to know which Ritz pair is the closest one, we define a distance measure of eigenpairs that we derive in the following.

In the Jacobi-Davidson Algorithm 6 on page 31 we set the initial search space $V_1 = u_*$ and in the first cycle we calculate the Ritz pairs of

$$V_1^H P(\lambda) V_1 y = 0, \quad y \in \mathbb{C}^1, \quad \|y\| = 1 \qquad \Leftrightarrow \qquad u_*^H P(\lambda) u_* = 0.$$

Each Ritz pair can be written as $u_j = V_1 y_j = u_*$ (modulo complex phase) for $j = 1, \ldots, \deg(P)$. Thus, all Ritz vectors are equal to u_* and the choice can only rely on the Ritz values ν_j. If there are equal Ritz values, the specific Ritz pairs are equal.

In subsequent iterations the dimension of $\mathcal{R}(V)$ is greater than two and $u_j \neq u_*$ in general. Due to the fact, that the whole set of the eigenvectors of the polynomial eigenvalue equation is linearly dependent and the eigenvalues are not necessarily distinct (see Figure 4.11), it is necessary to consider both, the Ritz value and the vector.

The norm $\|u_* - u_j\|$ is a bad idea to measure the distance because of the freedom to choose the complex phase of the eigenvectors. In [11] the distance of two subspaces is defined by the Eucleadian distance of the associated orthogonal projections. In our case of two one dimensional subspaces $\mathcal{R}(u_*), \mathcal{R}(u_j) \subset \mathbb{C}^N$ ($\|u_*\| = 1$, $\|u_j\| = 1$) it reads

$$\operatorname{dist}\left(\mathcal{R}(u_*), \mathcal{R}(u_j)\right) := \|u_* u_*^H - u_j u_j^H\|_2$$

and the theorem 2.6.1 in [11] says

$$\operatorname{sim}\left(\mathcal{R}(u_*), \mathcal{R}(u_j)\right) = |u_*^H u_j^\perp| = |\sin\left(\angle(u_*, u_j)\right)| = \sqrt{1 - \cos^2\left(\angle(u_*, u_j)\right)} = \sqrt{1 - |u_*^H u_j|^2}.$$

We are interested in a similarity measure $\operatorname{sim}(u_*, u_j)$ such that it provides a value in $[0, 1]$ which depends on the similarity of the vectors such that it is one if both eigenfunctions are equal (modulo complex phase) and zero if they are most unequal. Related to the distance of two subspaces, one possibility to define the similarity of u_* and each Ritz vector u_j is by the angle between them

$$\operatorname{sim}(u_*, u_j) := |u_*^H u_j| = |(u_*^H V) y_j|, \qquad \|u_*\|_2 = 1, \quad \|u_j\|_2 = 1.$$

Because of $\operatorname{sim}(u_*, u_j) = |\cos\left(\angle(u_*, u_j)\right|$, this similarity measure is most sensitive with nearly orthogonal eigenfunctions and most insensitive with almost parallel eigenfunctions.

A natural measure of the distance between the eigenvalue approximation ν_* and each Ritz value ν_j is the Euclidean distance

$$\mathrm{sim}(\nu_*, \nu_j) := |\nu_* - \nu_j|.$$

We transform the Euclidean distance into a similarity measure as

$$\mathrm{sim}_{\alpha,\beta}(\nu_*, \nu_j) := \exp\left(-\alpha\left(\frac{\mathrm{dist}(\nu_*, \nu_j)}{|\nu_*|}\right)^{\beta}\right), \qquad \alpha \in]0, \infty[, \quad \beta \in \{1, 2\}.$$

Of course there are many different possibilities to map $[0, \infty[$ onto $[1, 0]$, but the exponential approach with $\beta = 2$ consists of a suitable sensitivity, such that large distances of eigenvalues have a similarity close to zero and eigenvalues that are close together have a similarity close to one. $\beta = 1$ is preferable to distinguish very tiny distances of eigenvalues. In the multilevel Jacobi-Davidson algorithm the eigenvalue of reference (ν_*) is an approximation and therefore we prefer $\beta = 2$.

We call two eigenpairs (Ritz pairs) similar, if the values and the vectors are similar. We realize this "and" catenation by multiplying both similarity measures

$$\mathrm{sim}_{\alpha,\beta}\left((\nu_*, u_*), (\nu_j, u_j)\right) := \mathrm{sim}_{\alpha,\beta}(\nu_*, \nu_j)\,\mathrm{sim}(u_*, u_j), . \tag{4.7}$$

The parameter α controls the weighting between the similarity of the eigenvalue and the eigenvector. A greater α emphasis the eigenvalues and a smaller α shifts the weight to the eigenvectors. An appropriate choice for the weighting parameter turned out to be $\alpha = 1$.

In each cycle of the multilevel Jacobi-Davidson algorithm the Ritz pair with maximum $\mathrm{sim}_{\alpha,\beta}\left((\nu_*, u_*), (\nu_j, u_j)\right)$, $j = 1, \ldots, \deg P \cdot \dim V$ is chosen.

Another possibility to consider the eigenvector and the eigenvalue is the angle of the eigenvectors of the linearized system

$$\begin{aligned}\mathrm{sim}\left((\nu_*, u_*), (\nu_j, u_j)\right) &= \left|\frac{1}{c_j}\begin{bmatrix} u_* \\ \nu_* u_* \\ \nu_*^2 u_* \end{bmatrix}^H \begin{bmatrix} u_j \\ \nu_j u_j \\ \nu_j^2 u_j \end{bmatrix}\right| = \left|\frac{1}{c_j}\begin{bmatrix} u_* \\ \nu_* u_* \\ \nu_*^2 u_* \end{bmatrix}^H \begin{bmatrix} V y_j \\ \nu_j V y_j \\ \nu_j^2 V y_j \end{bmatrix}\right| \\ &= \left|\frac{u_*^H V y_j}{\|u_*\|\|y_j\|}\,\frac{1 + \bar{\nu}_*\nu_j + \bar{\nu}_*^2\nu_j^2}{\sqrt{(1 + \bar{\nu}_*\nu_* + \bar{\nu}_*^2\nu_*^2)(1 + \bar{\nu}_j\nu_j + \bar{\nu}_j^2\nu_j^2)}}\right|\end{aligned} \tag{4.8}$$

where

$$c_j = \left\|\begin{bmatrix} u_* \\ \nu_* u_* \\ \nu_*^2 u_* \end{bmatrix}\right\| \left\|\begin{bmatrix} u_j \\ \nu_j u_j \\ \nu_j^2 u_j \end{bmatrix}\right\|$$

is the normalization factor. For linear eigenvalue equations, the existence of the Jordan normal form of the linear algebra ensures the eigenvectors (including the generalized eigenvectors) to create a basis. Thus, the eigenvectors of the linearized system are linearly independent and the distance measure above is well posed to detect the right Ritz pair. Problems with numerical instability due to almost linearly dependent vectors have never occurred in the anomalous transport eigenvalue problem. The distance between the desired eigenpair and the other eigenpairs is large enough due to the fact that the eigenfunction of the eigenpairs with similar eigenvalues is different.

Comparing both measures, $\mathrm{dist}_{\alpha,\beta}$ allows to weight between the eigenvector and the eigenvalue. However, this can be a disadvantage as well, if the proper parameters are unknown. The latter measure is parameter free. Equation (4.7) and (4.8) yield the same measure on the eigenvectors, but a different measurement of the eigenvalues. The effect is visualized in Figure 4.4.

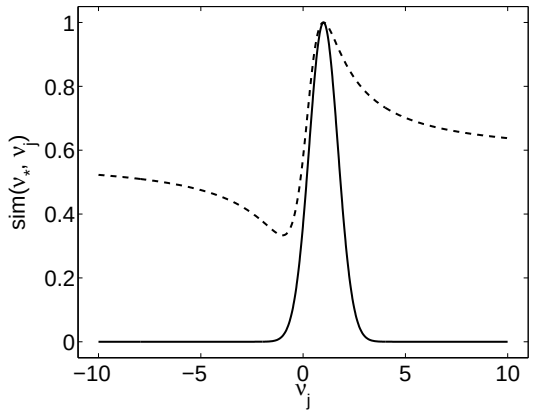

Figure 4.4: A comparison of the similarity measures (4.7) (solid line) and (4.8) (dashed line), where the eigenvectors are equal, $\nu_* = 1$, $\alpha = 1$ and $\beta = 2$.

In a local neighborhood the measurements of the two distance measures are almost equal with $\alpha = 0.5$ but (4.8) has a local minima and does not become zero with an eigenvalue that is far away.

Both techniques work fine, when the approximation (ν_*, u_*) is closer to (ω, ϕ) than to other Ritz pairs. In case of the anomalous transport eigenvalue equation the multilevel Jacobi-Davidson approach fulfills this condition with the eigenpairs of interest.

Example 4.17. The similarity of the Ritz pairs (ν_j, u_j) to the eigenpair of reference (ν_*, u_*) in the Jacobi-Davidson algorithm. The eigenpair of reference is the prolonged coarse grid approximation. Here (4.7) is applied with $\alpha = 1$, $\beta = 2$ and the selected value is printed bold. $\dim V = 1$:

$$\operatorname{sim}\big((\nu_*, u_*), (\nu_j, u_j)\big)_{j=1,\dots,9} = \big(3.64 \cdot 10^{-55}, 1.76 \cdot 10^{-21}, \mathbf{0.9999992}\big)$$

$\dim V = 2$:

$$\operatorname{sim}\big((\nu_*, u_*), (\nu_j, u_j)\big)_{j=1,\dots,9} = \big(0, 8.24 \cdot 10^{-55}, 9.07 \cdot 10^{-22}, \mathbf{0.9999962}, 2.33 \cdot 10^{-3}, 1.57 \cdot 10^{-2}\big)$$

$\dim V = 3$:

$$\operatorname{sim}\big((\nu_*, u_*), (\nu_j, u_j)\big)_{j=1,\dots,9} =$$
$$\big(0, 0, 0, 2.46 \cdot 10^{-58}, 9.89 \cdot 10^{-22}, 2.95 \cdot 10^{-8}, \mathbf{0.9999962}, 0.135, 3.34 \cdot 10^{-2}\big)$$

We will continue the discussion in section 4.5.1 on page 77 where the similarity of the eigenpairs from two eigenvalue equations that differ in the wave number $K_\perp$ are compared.

4.4.2 Solving the correction equation

Hitherto the essential parts of the Jacobi-Davidson method have been discussed except for a suitable method to solve the correction equation (2.7). In section 2.3.2 on page 31 it is mentioned to solve it

- directly by GMRES with a suitable preconditioner
- preconditioned by the inverse projections (2.9)
- by the one step approximation (4.12) with an approximate inverse Q of $P(\nu)$

Remember, that there is no need to solve the correction equation to high accuracy due to the underlying Newton step. A moderate accuracy is sufficient.

The projections within the correction equation (2.7) destroy the sparsity of the original matrix polynomial P. An evaluation of the projected matrix applied to a given vector has still an effort in $\mathcal{O}(N)$ with the finite differences and in $\mathcal{O}(N\log(N))$ with a pseudo spectral method, but the matrix itself loses its structure and becomes dense. This allows to use an iterative solver like GMRES, combined with preconditioning by inverse projections, if necessary.

The inverse projections and the one step approximation require an approximate inverse Q such that $QP(\nu) \approx I$. One step approximation (4.12) with exact inverse is equivalent to solve the correction equation (2.7), but it allows to use the structure of the underlying matrix polynomial. The inverse projection additionally requires an iterative solver. Therefore, one step approximation is preferable.

With the finite differences discretization (denoted by the subscript L), $P_L(\nu)$ is a periodic band matrix and its LU decomposition preserves the sparsity. The sparsity pattern of the LU decomposition of $P_L(\nu)$ without row interchanges is shown in Figure 4.5. The effort is twice as much as with a band matrix of the same band width, but the quality is much better than ignoring the entries at the anti-diagonal corners.

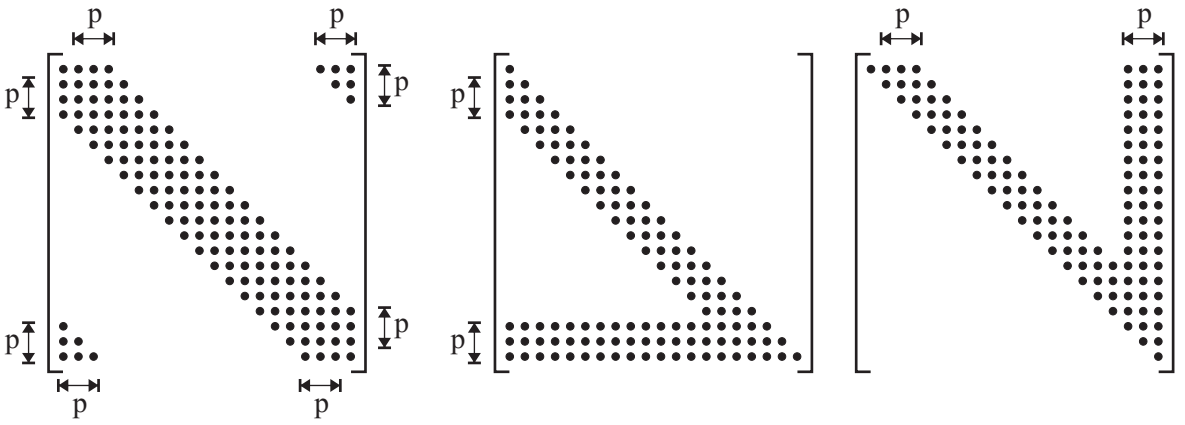

(a) $P_L(\nu) = LU \in \mathbb{C}^{N\times N}$ (b) L (c) U

Figure 4.5: The sparsity pattern of (a) periodic band matrix ($p = 3$), (b) lower and (c) upper triangular factor of the LU decomposition without row interchange. The number of non-zero entries is in $\mathcal{O}(pN)$.

If the derivatives are approximated by a pseudo spectral method (denoted by subscript s), $P_s(\nu)$ is a dense matrix and the inversion is very expensive ($\mathcal{O}(N^3)$ operations). Due to the fact, that the correction equation only needs to be solved approximately, it is possible to apply a finite difference matrix inside of the correction equation although the pseudo spectral method is used otherwise.

In the multilevel Jacobi-Davidson approach, there is a good approximation of the eigenvalue available, namely the solution corresponding to the next coarser resolution. This allows to cache the factors L and U of the LU decomposition and reuse them in subsequent Jacobi-Davidson cycles until the change of the eigenvalue approximation ν becomes too large. Then a new LU decomposition is necessary. Two advantages arise. First, the LU decomposition needs to be updated much more seldom than once per cycle and secondly the expansion of the search space is done by vectors very close to the ones produced in the Rayleigh quotient iteration (cf. Algorithm 3 on page 25). By this strategy the dimension of the search space V stays small and the eigenvectors not of interest have a much smaller component parallel to V, in general.

The one step approximation

$$t = \alpha Q(\nu)P'(\nu)u - Q(\nu)r, \qquad \alpha = \frac{u^H Q(\nu)r}{u^H Q(\nu)P'(\nu)u}$$

is formulated with the approximate inverse $Q(\nu)$. However it is sufficient to solve the linear systems

$$P(\nu)x = r \qquad \text{and} \qquad P(\nu)y = P'(\nu)u.$$

This can be done by backward and forward elimination based on the decomposition $LU = P(\nu)$. So the matrix Q, which is a dense matrix in general, is never calculated.

The multiplication of a vector with $P_s(\nu)$ can be done in $\mathcal{O}(N\log(N))$ operations if FFT is used. This allows to apply GMRES to the linear systems. The required preconditioner can be $(P_L(\nu))^{-1}$, again realized by LU decomposition. However, using finite differences in the correction equation turned out to be sufficient and the effort with the preconditioned GMRES is really dispensable.

If the physical model is extended to two or more dimensions in the future, it may be efficient to solve the correction equation, which for a fixed eigenvalue is some kind of second order partial differential equation boundary value problem, by the algebraic multigrid techniques.

4.4.3 Choice of grid for the multilevel technique

We want to calculate the desired eigenpair with low computational cost, thus the number of grid points on the coarsest grid has to be as small as possible and additionally the accuracy of the coarse grid solution has to be high. Therefore a good assembly of the grid points is essential. Figure 4.6 displays the eigenfunction of interest with MAST parameters. If we discretize the eigenvalue equation by n points equidistantly spaced, the major part of points will be in the area where ϕ is almost constant.

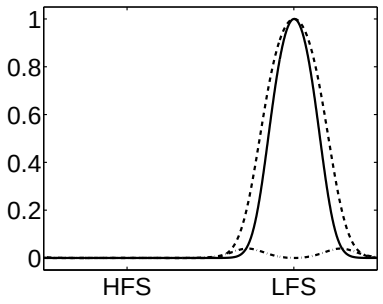

Figure 4.6: The real part $\Re(\phi)$ (dashed curve), the imaginary part $\Im(\phi)$ (dash-dotted curve) and the intensity $|\phi|$ (solid curve) of an eigenfunction ϕ of the anomalous transport eigenvalue equation (3.17). The eigenfunction is almost constant at the HFS.

Let G^{T} be the grid that is adequate to represent the temperature and the density profile. In the case of MARFE at the HFS ($\theta = \pi$), there is a deep and narrow temperature drop at the HFS. Hence, the distance of grid points is taken smaller in this region. Therefore coarsening G^{T} is not qualified to represent the eigenfunction adequately. Thus a different coarse grid G^{C} is required to represent ϕ well. In Figure 4.7(a) we see that the cosine (dashed line) is a suitable function to arrange the grid points.

We are in the paradox situation where we need to know the eigenfunction in order to find the suitable grid to calculate it. Later on we will see that the self consistent calculation of the

plasma parameters requires subsequent evaluations of the eigenvalue equation (3.17) with very small changes in the matrix coefficients. Thus, a good sample for ϕ is the result of a previous evaluation which results in a similar eigenfunction.

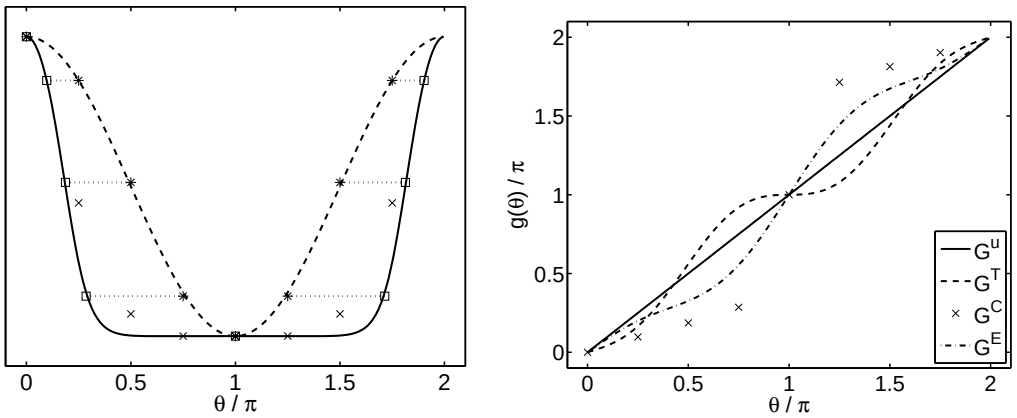

(a) eigenfunction (b) grid generating functions

Figure 4.7: (a) 8 points (squares) are chosen from intensity of eigenfunction $|\phi|^2$ (solid line) to fit to the values of a cosine evaluated on equidistantly spaced grid points (asterisks). The resulting grid generating function g is regularized ($r = 2$) (b) and the eigenvalue solver sees the curve through the x-marks in (a). The grid G^{T} has assembled many grid points close to π where the MARFE develops and temperature and density profiles are very steep. However the eigenfunction is almost constant at this range and a different grid G^{E} is much more sufficient.

Now, we assume to know the shape of the eigenfunction approximately and consider how we can find an adequate grid. We choose a grid

$$G^{\mathrm{C}} = (a_j)_{j=1,\ldots,n}, \qquad 0 = a_1 < a_2 < \ldots < a_n < 2\pi,$$

such that $|\phi|^2$ mapped onto $[-1, 1]$ is equal to the cosine values at the grid points:

$$2\frac{|\phi(a_j)|^2 - \min_\theta |\phi(\theta)|^2}{\max_\theta |\phi(\theta)|^2 - \min_\theta |\phi(\theta)|^2} - 1 = \cos\left(\frac{2\pi j}{n}\right). \tag{4.9}$$

In Figure 4.7 (a), the points from the right hand side of ((4.9)) are marked by asterisks and the corresponding ones on $|\phi|^2$ are marked by squares. The dotted lines illustrates their connection.

Let $g^{\mathrm{C}} : G^{\mathrm{u}} \to G^{\mathrm{C}}$ be the grid generating function from equidistant grid G^{u} to G^{C}. A disadvantage of g^{C} are potentially large derivatives, which strongly reduce the accuracy of the finite differences approximation. In Theorem 4.10 on page 53 it is shown, that a smooth grid generating function from the equidistant spaced grid to the actual one is essential for a high accuracy of the finite difference approximation.

A compromise between the optimal assembly of the grid points and the accuracy of the finite differences derivative approximation is achieved by the following regularization strategy. We arrange the positions a_j of G^{C} in the vector $\vec{a}$ and define the regularized grid generating function

$$g^{\mathrm{E}}(\theta) = \theta + \sum_{j=1}^{r} p_j \sin(j\theta)$$

with a moderate $r \in \mathbb{N}$, e.g., $r = 2$. The optimal coefficients $p_j \in \mathbb{R}$ are defined in the *least squares* sense

$$\left\| \underbrace{g^{\mathrm{C}}(\vec{\theta})}_{=\vec{a}} - \left(\vec{\theta} + \sum_{j=1}^{r} p_j \sin(j\vec{\theta})\right) \right\|_2 \to \min, \qquad \text{e.g. } r = 2 \tag{4.10}$$

which removes the high frequencies that lead to large derivatives. If the parameters p_j are arranged in the vector $\vec{p}$ and

$$S := \left[\sin(\vec{\theta}), \sin(2\vec{\theta}), \ldots, \sin(r\vec{\theta})\right], \qquad \theta_j = \frac{2\pi j}{N}$$

then the least square solution is given by

$$\vec{p} = (S^H S)^{-1} S^H (\vec{a} - \vec{\theta}).$$

The regularized grid $G^{\mathrm{E}} = S\vec{p}$ can be created on each level of resolution by evaluating the sum over the frequencies of the sine (dash-dotted curve in Figure 4.7 (b)). On G^{E} the intensity $|\phi|^2$ does not look like the cosine values any longer, but it still covers the range much more uniform.

Lemma 4.18. *The function*

$$g : G^{\mathrm{u}} \to G^{\mathrm{C}}, \quad g(\theta) = \theta + \sum_{j=1}^{r} p_j \sin(j\theta)$$

is strictly monotone if

$$\left| \sum_{j=1}^{r} j p_j \cos(j\theta) \right| < 1$$

holds.

Proof.

$$g'(\theta) = 1 + \sum_{j=1}^{r} j p_j \cos(j\theta) > 0$$

□

If the solution g^{E} from (4.10) does not fulfill Lemma 4.18, we reduce the coefficients $\vec{p}$ to $c\vec{p}$, where

$$\frac{1}{c} := \varepsilon + \left| \sum_{j=1}^{r} j p_j \cos(j\theta) \right|, \qquad 0 < \varepsilon \ll 1.$$

Then g^{E} becomes a grid generating function.

4.4.4 Multilevel technique on optimized grids

We have already explored the fact that the desired eigenfunction is smooth and therefore the desired eigenpair can be approximated on a coarse grid G^{E}. This decreases the computational effort significantly. In order to be able to start on a very coarse grid with $N = 8$ grid points only, we choose the grid G^{E} via the grid generating function g^{E} suggested in the previous section.

The continuous eigenvalue equation (3.17) is discretized on the grid G^{E}. It can be solved by the multilevel Jacobi-Davidson Algorithm 8 on page 62. From the eigenpair the anomalous particle flux $\Gamma_\perp$ can be calculated. However, the anomalous particle flux needs to be calculated on the grid G^{T} of the other plasma parameters. Therefore the eigenvector is required on the grid G^{T}. The easiest way to transfer the eigenvector from grid G^{E} to G^{T} is interpolation. But this is not the best possibility, because the interpolation may cause a significant loss of accuracy, if both grids differ strongly.

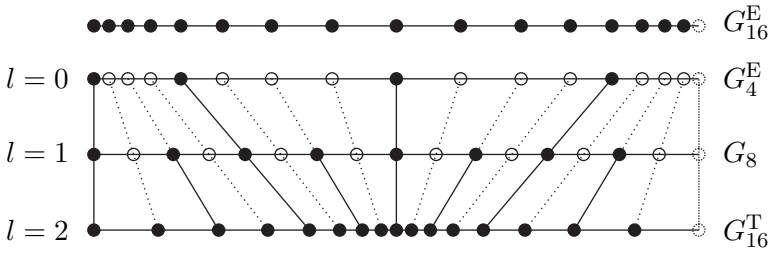

Figure 4.8: There are two grids, G_{16}^{T} optimal for the temperature profile and G_{16}^{E} optimal for the eigenvectors. The filled circles belong to the specific grid and the positions of the open circles are skipped.

Summing up, the optimal grid to calculate the eigenvalue on the coarsest level is G^{E} and the final solution is required on the grid G^{T}. The idea is to discretize the eigenvalue equation of the coarsest level on the coarse grid of G^{E} and the equation of the finest grid on G^{T}. The grid at the intermediate levels of resolution is constructed by a linear transitin from G^{E} to G^{T}. This yields the grid generating function

$$g^{\delta} := (1-\delta)g^{\mathrm{E}} + \delta g^{\mathrm{T}}, \qquad \delta \in [0,1]$$

where δ is zero on the coarsest level of resolution and one on the finest level of resolution. See Figure 4.8 for an example with three levels of resolution.

The filled circles in Figure 4.8 mark the grid points actually available and the open circles are the skipped ones. First the eigenvalue problem is solved on the coarse gird G_4^{E} and the eigenvalue approximation obtained is prolonged to the next finer grid $G_8 = (1-\delta)G_8^{\mathrm{E}} + \delta G_8^{\mathrm{T}}$ ($\delta = 0.5$) and is improved there. The improved eigenfunction is prolonged to G_{16}^{T} and improved again.

The prolongation between each level of resolution requires the interpolation of the eigenfunction approximation, but the final eigenvalue evaluation allows to solve the solution on the required grid G^{T} directly. The difference between the position of grid points from adjacent levels reduces if the number of total levels of resolution is increased.

The idea of the smoothly adopted grid positions can be implemented easily in Algorithm 8 by adding the lines

set $\delta := \frac{l}{L}$.
set grid $G_{2^l c} := (1-\delta)G_{2^l c}^{\mathrm{E}} + \delta G_{2^l c}^{\mathrm{T}}$.

at the beginning of the inner loop.

A direct solver is applied to the eigenvalue equation on the coarsest grid. Therefor a pseudo spectral method with its dense derivative matrix is no disadvantage. With a pseudo spectral method the coarsest grid G^{E} is chosen equidistantly spaced and moves step by step to G^{T} at subsequent levels of resolution as it is described above.

The parameter $\delta \in [0,1]$ of the convex combination can be interpreted as homotopy parameter [46] because g^{δ} is a homotopy.

4.4.5 Complex symmetric eigenvalue equation

The eigenvalue equation (3.12) of the anomalous transport is complex symmetric in its rational formulation (3.16). This feature is lost in the cubic polynomial formulation (3.17). However, if the eigenvalue is known, the expression (3.18) of the left eigenvector allows to preserve this feature.

In the multilevel Jacobi-Davidson Algorithm 8 on page 62 we always have a good approximation ν of the desired eigenvalue ω. The multiplication of the cubic eigenvalue matrix polynomial P from the left with the denominator evaluated at the eigenvalue approximation ν

$$P_\nu(\omega) := \mathrm{Diag}(c_8 + \nu c_9)^{-1} P(\omega)$$

makes P_ν almost complex symmetric, where "almost" means that

$$\left\| P_\nu(\omega) - P_\nu(\omega)^T \right\|$$

is rather small.

The only advantage of the complex symmetric eigenvalue equation is the simple relation between the left and the right eigenvector. In order to exploit this feature we again consider the projected system in the Jacobi-Davidson algorithm. The original aim is to find (ω, ϕ) such that

$$P(\omega)\phi = 0$$

holds.

Let V be the matrix whose columns are a basis of the current search space. In order to handle the system, the dimension of the parameter space is reduced from $\mathbb{C}^N$ to $\mathcal{R}(V)$, but

$$P(\omega)Vy = 0, \qquad y \in \mathbb{C}^k$$

is an overdetermined system. Therefore we require the Galerkin condition

$$P(\omega)Vy \perp \mathcal{R}(S_\nu), \qquad S_\nu \in \mathbb{C}^{N\times k}, \quad y \in \mathbb{C}^k,$$

where $S_\nu = V$ has been used earlier. However with

$$S_\nu := \left(\mathrm{Diag}(c_8 + \nu c_9)^{-1} V\right)$$

the projected system

$$V^T P_\nu(\omega) V = \left(\mathrm{Diag}(c_8 + \nu c_9)^{-1} V\right)^T P(\omega) V = S_\nu^T P(\omega) V$$

is complex symmetric if ν is the exact eigenvalue. Practically, the accuracy of ν is not good enough to apply a complex symmetric solver on the projected eigenvalue problem. However, one advantage still holds for the approximate ν:

$$\mathcal{R}(S_\nu) \perp r_S := P(\omega)Vy \qquad \text{and} \qquad P_\nu(\omega)Vy = y^T S_\nu^T P(\omega) =: r_V \perp \mathcal{R}(V)$$

The residual r_S of the right eigenvector approximation is perpendicular to the left eigenvector approximation, which can be used to increase the accuracy of the Ritz value. An experimental comparison of the complex symmetric approach, is presented in section 4.4.7.

Remark 4.19. The bilinear form $x^T y$, $x, y \in \mathbb{C}^N$ within the complex symmetric approach is not a scalar product because $x^T x = 0 \Rightarrow x = 0$ is not true in general.

In [31] the advantage of complex symmetric equations is explained in detail. Within the correction equation (2.7) some Hermitian expressions change to transposed ones,

$$\left(I - \frac{P'(\nu)uu^T}{u^T P'(\nu) u}\right) P(\nu) \left(I - \frac{uu^H}{u^H u}\right) v = -r \tag{4.11}$$

and the corresponding one step approximation is

$$v = \frac{u^T Q(\nu) r}{u^T Q(\nu) P'(\nu) u} Q(\nu) P'(\nu) u - Q(\nu) r. \tag{4.12}$$

This implies to define $x \perp y \Leftrightarrow x^T y = 0$. However, if $x \perp y \Leftrightarrow x^H y = 0$ is assumed, the one step approximation is (2.7) again.

The version with the transpose runs into problems if *quasi-null vectors*

$$x^T x = 0, \qquad x \neq 0$$

appear in the computation or as solution. The problem arises if $u^T u = 0$ in (4.11).

4.4.6 Prolongation

We discuss the interpolation in the prolongation step. Possible interpolations are linear interpolation, shape preserving cubic Hermite interpolation [8], splines and trigonometric interpolation. Figure 4.9 illustrates the different options. The complex phase is normalized, such that the imaginary part of ϕ vanishes at the LFS:

$$\phi \leftarrow \phi \frac{|\phi(\theta_{\mathrm{LFS}})|}{\phi(\theta_{\mathrm{LFS}})}.$$

The intensity is normalized such that

$$\frac{1}{2\pi} \int_0^{2\pi} |\phi|^2 \, d\theta = 1,$$

where the integral is approximated by the trapezoidal rule on 4 or 8 grid points, respectively.

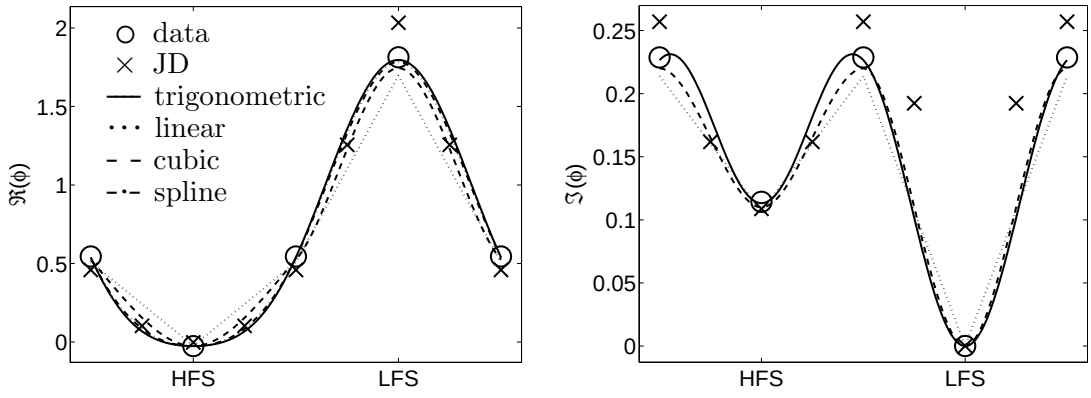

Figure 4.9: The open circles are the values of the eigenpair calculated on a grid of 4 points. The data is interpolated by linear (dotted line), cubic (dash-dotted line), splines (dashed line) and trigonometric (solid line) interpolation. The complex phase is normalized, such that the imaginary part of the eigenvector vanishes at the LFS. The amplitude is normalized with respect to the intensity on an eight point grid. The eigenvector calculated on a grid of 8 points is marked by x-marks.

The linear interpolation is obviously the worst one. Within the other candidates it is not clear which one is the best in general. In order to analyze the impact of the interpolation, a statistical analysis is done. The results are displayed in Figure 4.10. The following section presents further explanations.

4.4.7 Benchmark

In the previous sections several possibilities for the approximation of the derivative, the prolongation of the coarse grid approximation and the complex symmetric approach have been discussed. In order to compare the impact of each variant on the number of Jacobi-Davidson iterations, i.e., the dimension of the final search space V, the eigenvalue equation is evaluated for 15 different magnetic geometries of the Tokamak MAST. The physical background is explained in Chapter 5, but here it is sufficient to know, that each magnetic geometry changes the metric coefficients and therefore the eigenvalue equation.

The statistic is displayed in Figure 4.10. In (a) linear interpolation is applied. In the left diagram there are four groups, each of seven bars. The first group (1) is calculated with fourth order finite differences and the second one (2) is calculated with the pseudo spectral method. The third group (3) again uses finite differences and additionally the complex symmetry from section 4.4.5. The fourth group (4) is calculated with the pseudo spectral method together with the complex symmetry. Each bar displays the minimum, the average and the maximal dimension of the final search space. Within each group the bars from the left to the right contain the values on the resolutions $N = 16$, $N = 32$, $N = 64$, $N = 128$, $N = 256$, $N = 512$ and $N = 1024$.

At each level of resolution, the Jacobi-Davidson cycle is iterated until the forward error estimate e_f (cf. section 2.4.3) of the eigenvalue ω is below 10^{-6}. Let ω^* be the eigenvalue calculated on the finest resolution $N = 1024$. The accuracy of the eigenvalue ω on each level of resolution $N = 8$ to $N = 512$ is displayed in the plot at the right side. The arrangement of the bar groups is the same as on the left side.

Within each Jacobi-Davidson cycle the correction equation is solved by the one step approximation, where the derivative matrix D_2 are finite differences. The LU-decomposition of $P(\omega)$ is recalculated in each cycle.

In (b), (c) and (d) the simulation is recalculated with the specific interpolation method.

For the component wise condition number κ_c of the matrix polynomial P evaluated at the eigenvalue ω^* holds

$$7.9 \cdot 10^3 < \kappa_\mathrm{c} < 4.1 \cdot 10^6, \quad \langle \kappa_\mathrm{c} \rangle = 4.2619 \cdot 10^5, \text{ where the standard deviation is } 5.1474 \cdot 10^4.$$

The component wise condition number strongly depends on the specific magnetic geometry. In turn a condition number $\kappa_\mathrm{c} = 10^6$ requires a backward error $b_\mathrm{c} \leq 10^{-12}$ in order to ensure the forward error to be $e_\mathrm{f} = \kappa_\mathrm{c} b_\mathrm{c} \leq 10^{-6}$. Such a high accuracy is necessary to find the optimal $K_\perp$ value by means of polynomial interpolation prediction technique, which is applied in subsequent simulations.

On a low resolution the accuracy of the eigenvalue is always very small. From $N = 16$ to $N = 128$ it rises and the dimension of the final search space reduces. On the high resolution $N = 512$ and $N = 1024$ it depends on the method, whether the dimension of the final search space reduces further or increases.

With the pseudo spectral method in comparison to the finite differences the accuracy of the eigenvalue approximation is always much better on a medium sized resolution ($N \geq 64$). On the $N = 64$ point grid the accuracy of the pseudo spectral method is better than with the finite differences on $N = 512$. The accuracy is close to the machine precision with respect to the condition number k_c.

The complex symmetric approach reduces the dimension of the search space but it sometimes runs into problems on grids of $N \geq 512$.

The linear interpolation is worst. The shape preserving cubic interpolation and the splines are feasible, but they sometimes are problematic at a high resolution. The best method at all is the

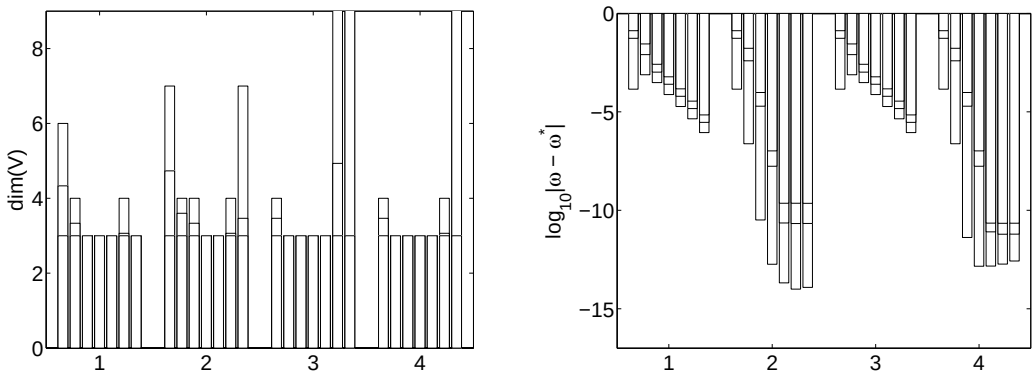

(a) prolongation by linear interpolation

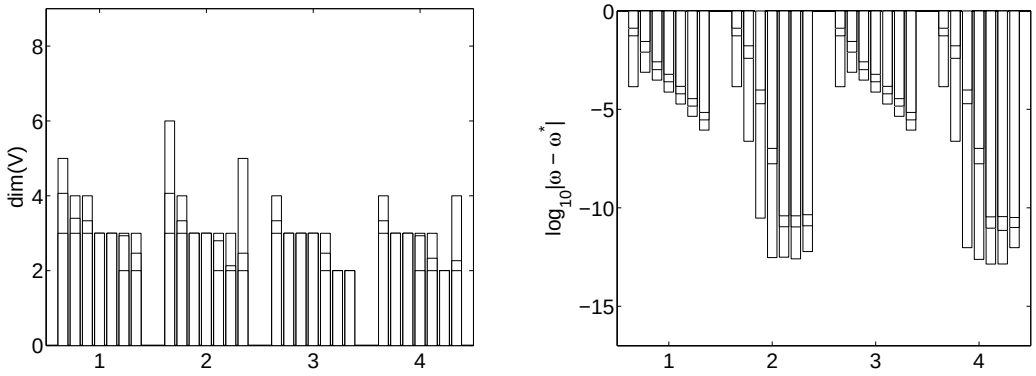

(b) prolongation by shape preserving cubic hermite interpolation

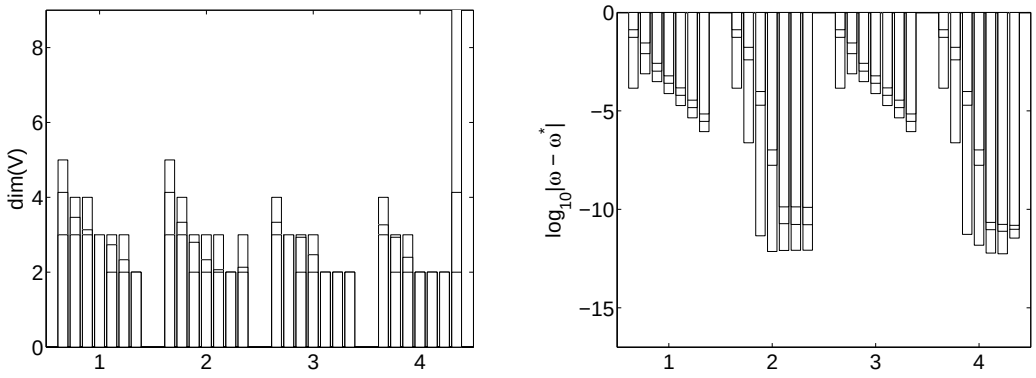

(c) prolongation by splines

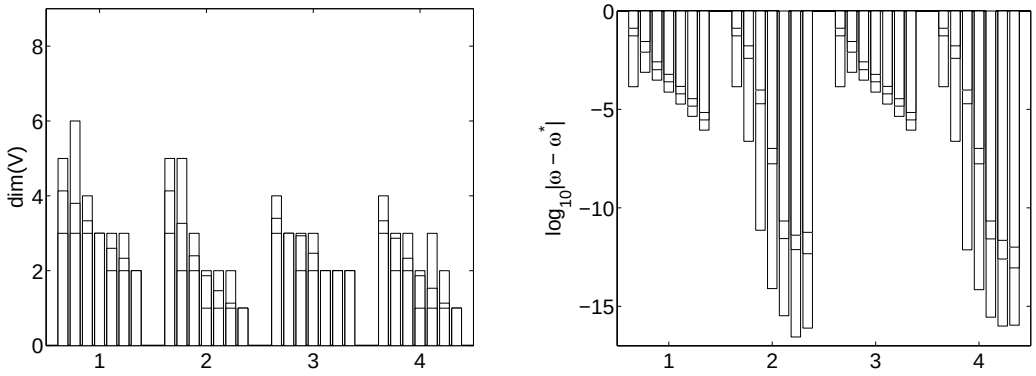

(d) prolongation by trigonometric interpolation

Figure 4.10: First column: Number of Jacobi-Davidson iterations, i.e., dimension of the search space V, improving eigenpair on resolution $N = 16$, 32, 64, 128, 256, 512 and 1024 (left to right) for 15 different magnetic geometries (γ_j) from Figure 5.1. Each bar displays minimum, average and maximum value. Group (1) finite differences, (2) pseudo spectral method, (3) finite differences with complex symmetry (cf. section 4.4.5) and (4) pseudo spectral method with complex symmetry. Second column: Distance of eigenvalue approximation to final solution on each level of resolution ($N = 8, 16, \ldots, 512$).

interpolation by Fourier transform together with the derivative by the pseudo spectral method and the complex symmetry. The FFT is most suitable because of the decreasing weights of higher frequencies as can be seen in Figure 4.3 on page 61.

The efficiency of the multilevel Jacobi-Davidson approach becomes clear because the number of iterations, i.e., the dimension of the final search space is very small in general. With the Fourier interpolation it is below six and on bigger N even less or equal two. The search space dimension on the high resolution is most essential because the computational cost rises at least linear to N. Due to the low dimension of the search space, the linearized eigenvalue equation of the projected system has a dimension $\deg P \cdot \dim V$ that is very small and can be solved efficiently by the QZ algorithm.

4.5 Optimal wave number $K_\perp$

Up to now, the multilevel Jacobi-Davidson approach is developed to calculate the desired eigenpair for a given eigenvalue equation. To be more precise, the wave length parameter $K_\perp$ is fixed while the eigenvalue equation is solved. The original aim is to find the eigenpair $(\omega(K_\perp), \phi(K_\perp))$, such that $\Im(\omega(K_\perp))$ is maximal. Therefore, a maximization process over $K_\perp$ is necessary. The idea is as follows. The eigenvalue equation is solved for a few $K_\perp^j$ values on the physically relevant domain. The growth rate $\Im(\omega(K_\perp^j))$ is determined and a prediction $K_\perp^{\text{pred}}$ on the location of the optimum is calculated by some interpolation technique. At $K_\perp^{\text{pred}}$ the eigenvalue equation is solved and the result is compared to the growth rate of the former evaluated wave numbers.

Some difficulties arise. To describe it in a suitable context the following definition is necessary.

Definition 4.20. Two eigenpairs $(\omega(K_\perp^j), \phi(K_\perp^j))$, $j \in \{1, 2\}$ are said to be the same *mode* or *eigenmode* if and only if

$$f(\alpha) := \Big(\omega\big(\alpha K_\perp^1 + (1-\alpha)K_\perp^2\big), \phi\big(\alpha K_\perp^1 + (1-\alpha)K_\perp^2\big)\Big), \qquad \alpha \in [0,1]$$

is a smooth function, where the eigenvector is modulo its complex phase and normalized. Hence, α is the homotopy parameter and the eigenpairs of one mode at different wave numbers are a homotopy (cf. [46]).

Remark 4.21. Assume $A, B \in \mathbb{C}^{N\times N}$. The eigenvalues λ and the null space of $(A-\lambda B)$ depend continuously on the matrices entries. Therefore, the eigenpairs of the anomalous transport eigenvalue equation (3.16) depend continuously on the wave number parameter $K_\perp$. Thus, the path of the eigenvalues of one mode creates continuous curve in the complex plain. Due to the fact that the factor γ in (3.16) is continuous at each wave number but not differentiable at some specific wave numbers, the path of the eigenvalues with respect to the wave number is continuous but may have discontinuous derivatives. Such a discontinuity is found in ce_{01} in Figure 4.2(a) on page 59. It is not a specific feature of ce_{01} and there are different plasma parameters where it happens with different eigenmodes.

At each wave number one or a few eigenvalues are obtained and it is only reasonable to compare the ones of the same mode. Therefore a method is required which correlates the eigenpairs of the adjacent wave numbers.

In Figure 4.11 the eigenvalues (dots) of eight modes are plotted in the complex plain for 50 wave numbers $K_\perp \in [0.1, 0.5]$ spaced equidistantly. At $K_\perp = 0.3$ the eight eigenpairs ($\circ$) of the maximal growth rate are calculated and tracked for subsequent wave numbers by the method deduced in the subsequent sections. In the plot the eigenvalues of each mode are connected by lines. There is one point, where the paths of at least five eigenvalues cross each other. Thus,

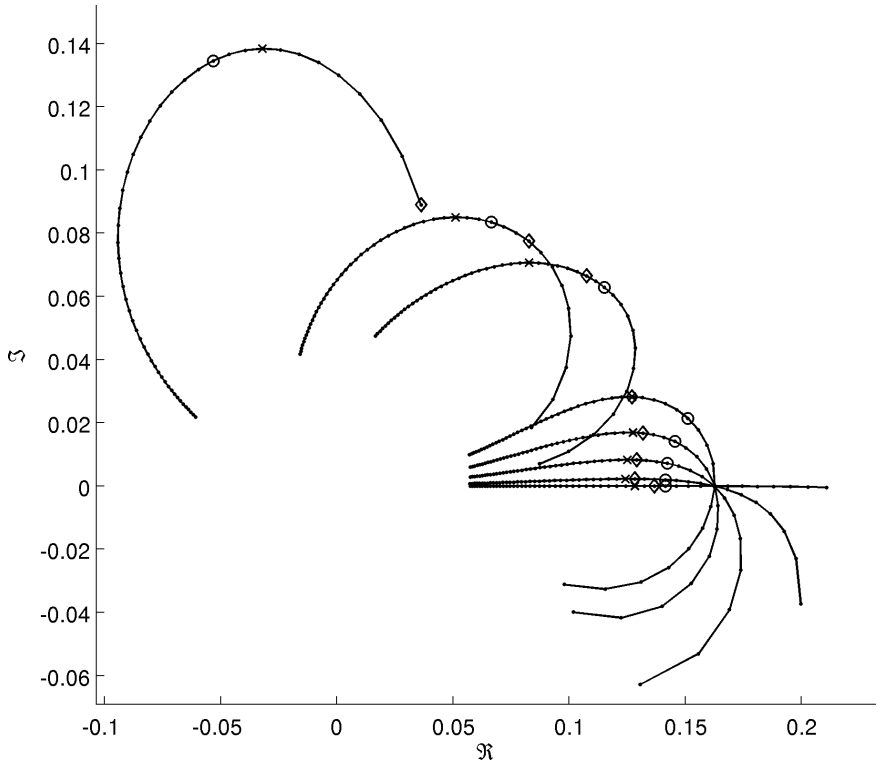

Figure 4.11: The path of the eigenvalues of (3.17) in the complex plane for $K_\perp \in [0.1, 0.5]$. At $K_\perp = 0.3$ the 8 eigenvalues of maximal imaginary part ($\circ$) are calculated. For additionally 49 wave numbers $K_\perp$ equidistantly spaced in $[0.1, 0.5]$ the 8 eigenvalues of the same mode are tracked ($\cdot$) and its path is marked by a line in the plot. There is one point, where the paths of at least 5 eigenvalues cross each other. The position with maximal growth rate is marked by $\times$ and the position where the contribution to the anomalous transport is maximal is marked by $\diamond$.

tracking the modes cannot rely on the eigenvalue itself, but additionally has to concern the eigenvector.

4.5.1 Arranging eigenpairs in modes

For the $k \in \mathbb{N}$ wave numbers $K_\perp^1 < \ldots < K_\perp^k \in [K_\perp^{\min}, K_\perp^{\max}]$ the $m \in \mathbb{N}$ eigenpairs

$$\left(\omega_l^{K_\perp^i}, \phi_l^{K_\perp^i}\right)_{l=1,\ldots,m}$$

are calculated. The eigenpairs of two adjacent wave numbers $K_\perp^i$ and $K_\perp^{i+1}$ are compared in order to find the correlated eigenpairs and arrange them as discrete points of continues modes $(\omega_l(K_\perp), \phi_l(K_\perp))$.

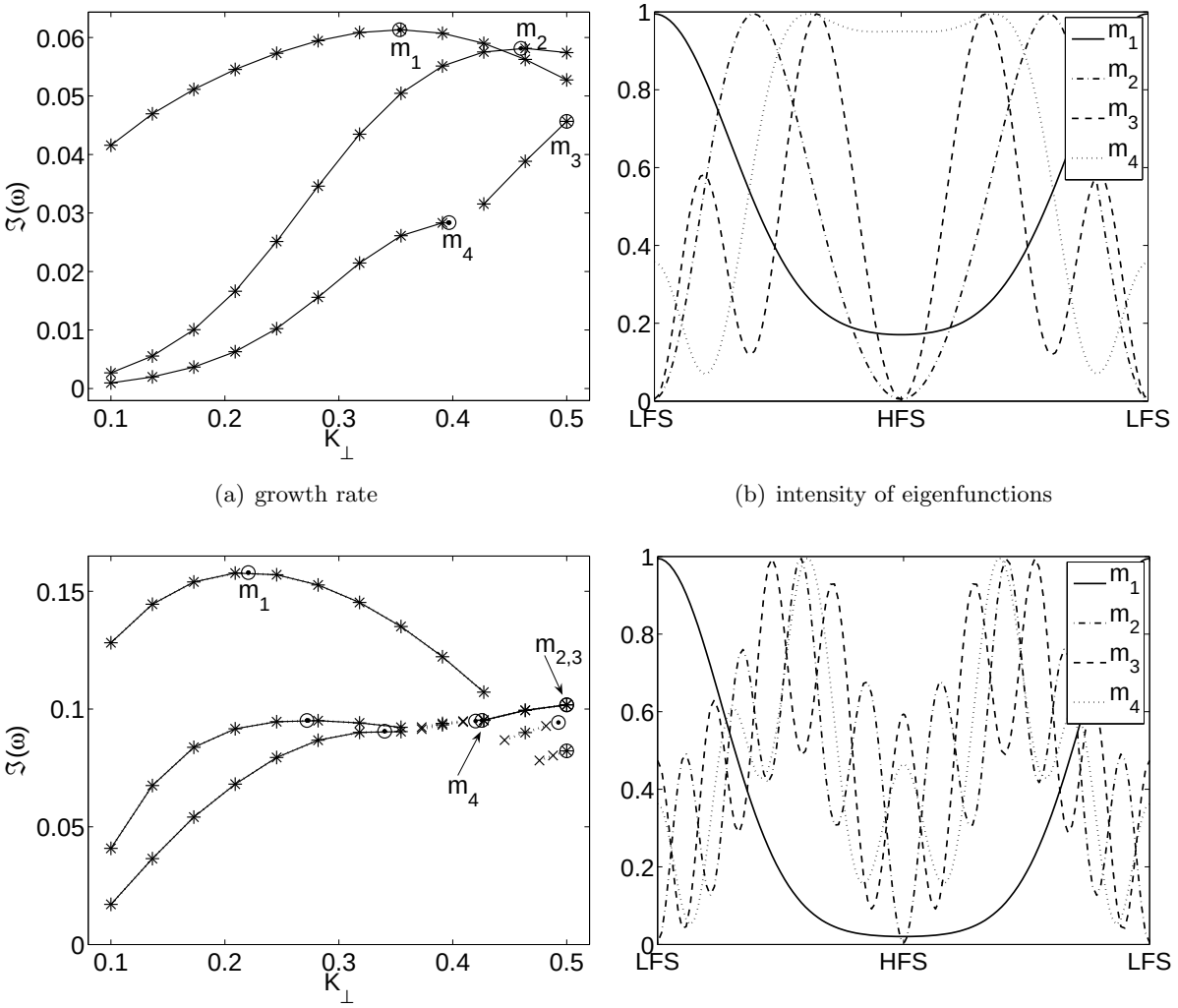

(a) growth rate

(b) intensity of eigenfunctions

(c) growth rate

(d) intensity of eigenfunctions

Figure 4.12: Two examples of the growth rate maximization by Algorithm 10. (a, c) The asterisks mark the three maximal eigenvalues of the twelve discretized wave numbers. The eigenvalues that belong to the same mode are connected by lines. The dots are the additionally evaluated positions within the search procedure and the open circles mark the maximum. The x-marks in (c) mark the additionally required data in order to have three points for the quadratic polynomial interpolation. In (b) and (d) on the right side the intensity shape of the eigenfunctions is plotted.

The eigenvalues depend continuously on the entries of the matrices of the eigenvalue equation and therefore $\omega_j(K_\perp)$ is a continuous trajectory in the complex plane. One might try to trace these trajectories, however, this is highly unstable when the trajectories are close together or cross each other (see Figure 4.11). Then the grid of the wave number range has to be very fine which results in a large number of the evaluations of the eigenvalue equation and thus large computational costs. Even on an infinitely fine grid, the paths of two eigenvalues can be that close there is no chance to distinguish the modes. Additionally the eigenvalue paths of (3.17) have non differentiable points as has been described in Remark 4.21 on page 75.

A different approach to distinguish the modes is the shape of the eigenfunction, in particular the angle. Let ϕ be an eigenfunction at the wave number $K_\perp^1$ and ψ an eigenfunction at the wave number $K_\perp^2$. The angle between the two eigenfunctions is

$$\left|\cos\left(\angle(\phi,\psi)\right)\right| = \left|\frac{\int_0^{2\pi} (\phi(\theta))^H \psi(\theta)\, d\theta}{\sqrt{\int_0^{2\pi} (\phi(\theta))^H \psi(\theta)\, d\theta}\,\sqrt{\int_0^{2\pi} (\phi(\theta))^H \psi(\theta)\, d\theta}}\right| = \frac{1}{2\pi}\left|\int_0^{2\pi} (\phi(\theta))^H \psi(\theta)\, d\theta\right|.$$

The modulus is taken because the complex phase of the eigenfunctions is not defined by the eigenvalue problem. The second equality holds due to the earlier introduced normalization of the eigenfunctions. Since polynomial eigenvalue problems have a number of eigenpairs that is a multiple of the space dimension, the eigenfunctions are linearly dependent and therefore this technique cannot guarantee success.

However, in case of the anomalous transport eigenvalue problem, the eigenmodes of physical interest can be successfully distinguished by a combination of the angular criteria and the distance of the eigenvalues. This comes from the fact, that the eigenfunctions of physical interest differ from the remaining eigenfunctions by the number of maxima and minima and ce_{01} to ce_{03} have well separated eigenvalues (cf. Figure 6.12 on page 112). The criteria to detect the modes is similar to the selection of the right Ritz pair within the multilevel Jacobi-Davidson algorithm in section 4.4.1. Here, the method (4.7) is fine, whereas the method (4.8) requires the adjacent wave numbers to be much closer than the first one.

We assume that n_1 eigenpairs at $K_\perp^1$ and n_2 eigenpairs at $K_\perp^2$ have been calculated. For a better readability we define the abbreviations

$$p_i := \left(\omega_i(K_\perp^1), \phi_i(K_\perp^1)\right) \text{ for } i = 1, \ldots, n_1$$

and

$$q_j := \left(\omega_j(K_\perp^2), \phi_j(K_\perp^2)\right) \text{ for } j = 1, \ldots, n_2.$$

First the similarity distance (cf. section 4.4.1 on page 63) of an eigenpair calculated at $K_\perp^1$ to an eigenpair calculated at $K_\perp^2$ is measured as

$$C_{i,j} := \mathrm{sim}(p_i, q_j),$$

where $C_{i,j} \in [0,1]$ holds and $\mathrm{sim}(p_i, p_i) = 1$ and $\mathrm{sim}(q_j, q_j) = 1$. We call C the *correlation matrix*.

Next we have to detect the eigenpairs that fit. Therefore we detect the maximal element

$$(i_{\mathrm{opt}}, j_{\mathrm{opt}}) = \underset{i=1,\ldots,n_1,\ ,j=1,\ldots,n_2}{\mathrm{argmax}} (C_{i,j})$$

and say that $p_{i_{\mathrm{opt}}}$, $q_{j_{\mathrm{opt}}}$ belong to the same mode if $C_{i_{\mathrm{opt}},j_{\mathrm{opt}}} \geq \varepsilon$. Afterwards these eigenpairs are removed from C by setting

$$C_{i_{\mathrm{opt}},l} := -1 \quad l = 1, \ldots, n_2$$
$$C_{l,j_{\mathrm{opt}}} := -1 \quad l = 1, \ldots, n_1$$

Now we can determine the maximal entry of the modified C and repeat the procedure until all entries of C are below the threshold ε. The remaining eigenpairs belong to distinct modes. The remaining eigenpairs of $K_\perp^1$ are those p_i where an index j exists such that $C_{i,j} \geq 0$ and the q_j where an index i exists such that $C_{i,j} \geq 0$ are the remaining eigenpairs of $K_\perp^2$.

Example 4.22. The correlation matrix from Figure 6.13 on page 113 where $\langle n \rangle = 7 \cdot 10^{19}$ m^{-3} and $K_\perp = 0.2$ is

$$C = \begin{pmatrix} \mathbf{0.999\,930} & 0.327\,491 & 0.434\,935 & 0.354\,636 \\ 0.357\,987 & 0.573\,670 & 0.797\,434 & \mathbf{0.999\,954} \\ 0.436\,660 & 0.897\,339 & \mathbf{0.999\,933} & 0.794\,394 \\ 0.326\,205 & \mathbf{0.999\,924} & 0.894\,890 & 0.570\,867 \end{pmatrix}.$$

The maximal element of each row and column is printed bold and the eigenpairs are related to the modes as (p_1, q_1), (p_2, q_4), (p_3, q_3) and (p_4, q_2).

In a last step, the trajectory of the imaginary part (growth rate) of the eigenvalues is concerned for each mode. The trajectory of the growth rate has a shape of a hill in the anomalous transport eigenvalue problem as can be seen in Figure 4.12. Therefore modes are split at valleys of the growth rate curve.

It is possible to end up with two modes, that are two pieces of one. This causes no essential problem, because the maximization process will find the same maximum twice. The computational effort doubles but since this case occurs very seldom, it can be neglected. Algorithm 9 sums up this process.

In section 4.4.1 on page 63 are derived two different similarity measures. The first similarity measure (4.7) measures the eigenpair and the eigenvalue independently and the second one (4.8) measures the eigenvectors of the linearized system. Within the mode correlation procedure the first similarity measure (4.7) works fine and the second measure (4.8) often fails.

One reason is that a change of the wave number changes the shape of the eigenfunction such that the similarity is of medium-sized value. The eigenvalue comparison of (4.8) is defective with eigenvalues of large distance (cf. Figure 4.4 on page 65) and causes the wrong decision.

4.5.2 Maximization of the growth rate

In the previous section the arrangement of the eigenpairs from several wave numbers $K_\perp^j$ into modes is described. Now, for each of these modes, the wave number $K_\perp^{\text{opt}}$ where the growth rate $\Im(\omega(K_\perp^{\text{opt}}))$ becomes maximal has to be found. We will do this by a polynomial prediction correction technique.

In order to find the maximal growth rate of each mode m_j with respect to the wave number $K_\perp$, a subset of the already calculated data $(K_\perp^i, \Im(\omega(K_\perp^i)))$ is interpolated by a polynomial of low degree (quadratic or cubic) and the position $K_\perp^{\text{pred}}$ of the polynomials maximum is a cheap prediction for the desired maximum of the growth rate.

The quadratic interpolation requires at least three supporting points of data. If there is only one supporting point $(K_\perp^2, \omega_2)$ available, two additional samples are taken at $K_\perp^1 = K_\perp^2 - \Delta K_\perp$ and $K_\perp^3 = K_\perp^2 + \Delta K_\perp$. If there are only two supporting points $(K_\perp^i, \omega_i)_{i=1,2}$ a third one is calculated in the middle of both. Thus we assume that each mode has at least three wave numbers where the data is already calculated.

With the data available at three wave numbers, quadratic polynomial interpolation is feasible. If there are more than three points available, cubic interpolation is applied and the four wave

Algorithm 9 Arranging the eigenpairs in modes

Require: eigenpairs $p_{l,i} = \left(\omega_i^{K_\perp^l}, \phi_i^{K_\perp^l}\right)$, $i = 1, \ldots, n_l$, $l = 1, \ldots, k$

1: **for** $l = 1, \ldots, k-1$ **do**
2: **for** $i = 1, \ldots, n_i$ **do**
3: **for** $j = 1, \ldots, n_{i+1}$ **do**
4: $C_{i,j} := \mathrm{dist}(p_{l,i}, p_{l+1,i})$ // e.g. distance measure (4.8)
5: **end for**
6: **end for**
7: **while** $(i_{\mathrm{opt}}, j_{\mathrm{opt}}) := \mathrm{argmax}_{i=1,\ldots,n_l,\ j=1,\ldots,n_{l+1}}\{C_{i,j} \mid C_{i,j} \geq \varepsilon_{\mathrm{threshold}}\}$ **do**
8: eigenpair $p_{l,i_{\mathrm{opt}}}$ and $p_{l+1,j_{\mathrm{opt}}}$ belong to the same mode.
9: $C_{i_{\mathrm{opt}},r} := -1\ \forall r = 1, \ldots, n_{l+1}$ // deactivate eigenpair $p_{l+1,i_{\mathrm{opt}}}$ for further comparison
10: $C_{r,j_{\mathrm{opt}}} := -1\ \forall r = 1, \ldots, n_l$ // deactivate eigenpair $p_{l,j_{\mathrm{opt}}}$ for further comparison
11: **end while**
12: $I_l := \{i \mid \exists j : C_{i,j} \geq 0\}$ // indices of remaining eigenpairs at $K_\perp^l$
13: $J_l := \{j \mid \exists i : C_{i,j} \geq 0\}$ // indices of remaining eigenpairs at $K_\perp^{l+1}$
14: **end for**
15: Walk through the $K_\perp$ spectra of each mode and split the mode at positions, where the trajectory of $\Im(\omega)$ has a valley.
16: All eigenpairs, that are not arranged in a mode by the procedure above, are a mode of just one single point of data.

numbers closest to

$$K_\perp^{\mathrm{largest}} := \operatorname*{argmax}_{K_\perp} \Im(\omega)$$

are selected to be the supporting points. The position $K_\perp^{\mathrm{pred}}$ of the polynomials maximum is calculated and the eigenvalue equation is evaluated at $K_\perp^{\mathrm{pred}}$ by the multilevel technique where the eigenpair closest to the eigenpair of $K_\perp^{\mathrm{largest}}$ is chosen.

After the eigenvalue equation is solved at the predicted position $K_\perp^{\mathrm{pred}}$, the actual value

$$\Im\big(\omega_{\mathrm{act}}(K_\perp^{\mathrm{pred}})\big)$$

is compared with the predicted

$$\Im\big(\omega_{\mathrm{pred}}(K_\perp^{\mathrm{pred}})\big).$$

The procedure is repeated until the predicted and the actual growth rate are close enough.

There are two possibilities for $K_\perp^{\mathrm{pred}}$. Either it is located inside of the range of the supporting points of the polynomial interpolation (interpolation) or it is outside (extrapolation). In the former case, the distance of the supporting points taken for the polynomial interpolation decreases strictly monotonically and thus the accuracy of the prediction increases (cf. Taylor expansion). In the latter case, the tracking is bounded by the next raster point of $K_\perp$. This limit ensures not to leave the domain $[K_\perp^{\min}, K_\perp^{\max}]$, which prevents to track the eigenpair a long distance through the $K_\perp$ interval into a region, where it has a sub dominant growth rate to another eigenpair. Figure 4.12 illustrates this procedure.

In Figure 4.12 there are two examples of the growth rate maximization by Algorithm 10. In (a) and (c) the twelve values $K_\perp$ are discretized linearly spaced in $[0.1, 0.5]$. For each of these wave numbers the three eigenpairs of the maximal growth rate (asterisks) are calculated of the anomalous transport eigenvalue equation (3.17). In the next step the eigenpairs of adjacent $K_\perp$ values are correlated by the distance of the eigenpairs (solid lines connecting the asterisks). In a last step, the maximum (open circle) of each of the trajectories is searched.

The prediction correction technique by cubic polynomial interpolation finds the maximum at a precision of 10^{-6} by (a) 2 (m_1), 1 (m_2), 0 (m_3) and 3 (m_4) additional evaluations (dots) of the eigenvalue equation. In (c) x-marks mark the additionally required data in order to have three points for the quadratic polynomial interpolation. In (b), (d) the intensity shape of the eigenfunctions is plotted. The example in the first row is the more physical one.

It can happen that the prediction technique converges monotonous from one side to the maximum and the gap between the supporting points of the interpolation on the other side $K_\perp^{\text{afar}}$ hardly decreases. Then the convergence is accelerated by a so called *contraction step*: instead of the predicted $K_\perp^{\text{pred}}$

$$K_\perp^{\text{contract}} := (K_\perp^{\text{pred}} + K_\perp^{\text{afar}})/2$$

is taken.

It is mentioned above, that the eigenvalue problem has to be consecutively evaluated at the predicted wave number. We are interested only in the eigenpair of the current mode. Hence, the Jacobi-Davidson algorithm is a suitable method. The initial search space therein consists of the two eigenvectors of the wave numbers that are adjacent to the predicted one. The eigenvector closest to ϕ_j (j like in Algorithm 10) is selected from the subspace (Ritz values). Again we accelerate the method by the multilevel technique since we start this procedure on a coarser level of resolution.

Algorithm 10 Maximization of the growth rate of a single mode

Require: Mode m of $n \geq 3$ eigenpairs $(\omega_i, \phi_i)_{i=1,\ldots,n}$ at wave numbers $(K_\perp^i)_{i=1,\ldots,n}$.

repeat
  $j := \text{argmax}_{i=1,\ldots,n}\{\Im(\omega_i)\}$
  if $1 < j < n$ **then**
    $k = (j-1, j, j+1)$
  else if $1 < j$ **then**
    $k = (n-2, n-1, n)$
  else
    $k = (1, 2, 3)$
  end if
  if $n \geq 4$ **then**
    Add a fourth neighbor to k, if data at $k_1 - 1$ or $k_3 + 1$ is available. If both are available, choose the $\text{argmax}_{j=k_1-1,k_3+1}\{\Im(\omega_j)\}$
  end if
  Apply quadratic or cubic interpolation on $\left(K_\perp^k, \Im(\omega_k)\right)$ and calculate maximum $(K_\perp^{\text{pred}}, \Im(\omega_{\text{pred}}))$ of polynomial.
  Evaluate eigenvalue problem at $K_\perp = K_\perp^{\text{pred}}$ and obtain actual value $\omega_{\text{act}}(K_\perp^{\text{pred}})$.
  Add $(K_\perp^{\text{pred}}, \omega_{\text{act}})$ to discrete mode data.
until $|\Im(\omega_{\text{act}}) - \Im(\omega_{\text{pred}})| < \text{tol}$

4.6 Summary

Many details on the solution of the eigenvalue equation and the maximization issue are discussed in this chapter. The eigenvalue equation is solved for certain given $K_\perp$ parameter by a direct solver on a very coarse grid. This rough approximation of the eigenpair is subsequently improved on finer grids by a Jacobi-Davidson technique, where the Ritz pair closest to the coarse grid approximation is chosen and the correction equation is solved by the one step approximation.

In general, the derivatives are approximated by the pseudo spectral method, but they are approximated by finite differences in the linear system within the correction equation which leads to a sparse LU decomposition of a periodic band matrix. The stopping criteria of the Jacobi-Davidson iteration relies on a forward error estimate.

The highly efficient multilevel Jacobi-Davdison technique reduces the computational effort from one hour to below one second on a resolution of $N = 1024$ grid points. Thus an evaluation of the eigenvalue problem on many different the wave numbers $K_\perp$ is manageable.

The eigenpairs obtained are arranged for modes by a correlation strategy that concerns the eigenvalue and the eigenvector. For each mode the wave number is optimized by the polynomial interpolation prediction and a correction method which requires further eigenvalue evaluations until the wave number with the eigenpair of maximal growth rate is found. The subsequent eigenvalue equations are solve by the multilevel Jacobi-Davidson algorithm.

Up to here, everything is known to calculate the anomalous particle flux $\Gamma_\perp$ and its normalization factor ϕ_0. In the next chapter some simulations on the geometric shape of the edge layer are accomplished and in the chapter thereafter the influence of the anomalous particle flux on the initial plasma parameters, namely the temperature T, the density n and the pressure p is considered in the self consistent description.

Chapter 5

Effect of magnetic geometry on the edge anomalous transport

5.1 Shape of fusion device

In this chapter we analyze the influence of the magnetic geometry on the growth rate of the perturbations and the impact on the anomalous particle flux. We set the plasma parameters to values of the Tokamaks MAST and TEXTOR and sweep the parameters of the elongation and the triangulation throughout a realistic range. The magnetic geometry of the edge surface for different values of the elongation E and the triangulation D at MAST and TEXTOR is illustrated in Figure 5.1 and 5.2, respectively.

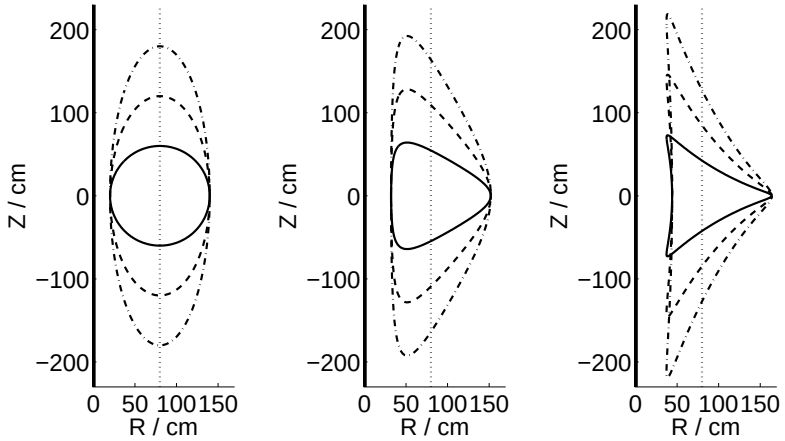

(a) $D = 0$ (b) $D = 0.2$ (c) $D = 0.4$

Figure 5.1: The magnetic geometry of the edge layer in the MAST is projected onto the poloidal plane. The parameters are major radius $R_0 = 80$ cm, minor radius $r_0 = 60$ cm, elongation $E = 1$ (solid line), $E = 2$ (dashed line) and $E = 3$ (dash-dotted line), triangulation D. A common shape corresponds to $E = 2$, $D = 0.2$.

5.2 Elongation and Triangulation

It is commonly known, that the magnetic geometry strongly affects the confinement. A better confinement leads to a decrease of the anomalous particle flux $\Gamma_\perp$. One of the effects of elongation

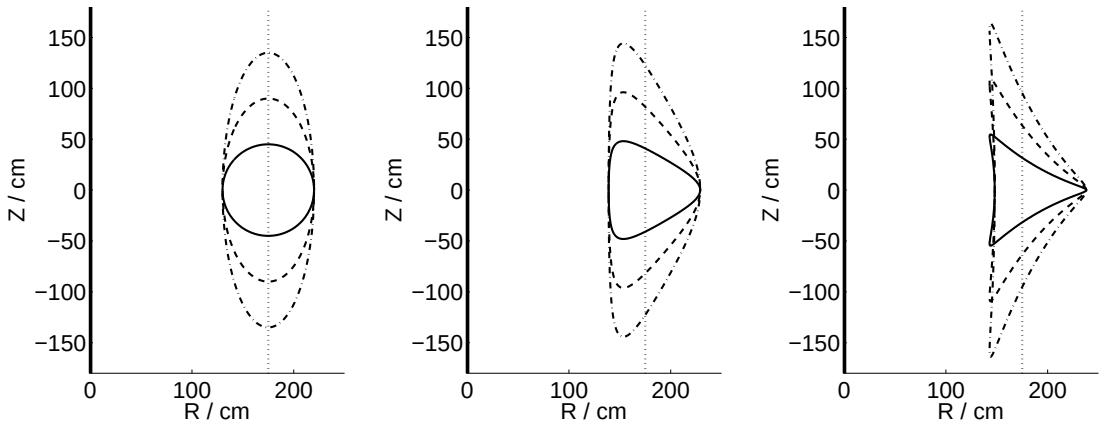

(a) $D = 0$ (b) $D = 0.2$ (c) $D = 0.4$

Figure 5.2: The magnetic geometry of the edge layer in the TEXTOR is projected onto the poloidal plane. The parameters are major radius $R_0 = 175$ cm, minor radius $r_0 = 46$ cm, elongation $E = 1$ (solid line), $E = 2$ (dashed line) and $E = 3$ (dash-dotted line), triangulation D. Usual shape is $E = 1$, $D = 0$.

is to modify the perpendicular space variation and thereby the effective magnetic shear [18]. On drift waves we get an enhanced convective damping due to the magnetic shear. At the same time, however, the mode width is reduced and this tends to reduce the beneficial effect on shear damping. The net effect can even sometimes be destabilizing [44].

In [2] the effect of a non-circular geometry of magnetic surfaces has already been studied in the case of the ion temperature gradient instability. There, a different approach is applied. The drift waves start at a Neumann boundary condition and are damped on their poloidal turns until the envelope vanishes (Dirichlet). In contrast, the model used here uses periodic boundary conditions and considers drift Alvén and drift resistive ballooning instabilities.

In the introduction to Tokamak physics, the charge separation of electrons and ions to the top and the bottom of the vessel is already mentioned. The resulting electric field decreases with the distance. Thus a high value of E is generally preferred. By triangulation the electric field is further reduced at the LFS.

In Figure 5.3 (MAST) and 5.4 (TEXTOR) the result of the calculation on the influence of the magnetic geometry on the growth rate and the anomalous particle flux are shown. The growth rate and the anomalous particle flux $\Gamma_\perp$ increase with the elongation but they decrease by the triangulation. Losses by the anomalous particle flux can be reduced up to a factor of 2.

In Figure 5.3 the result with the MAST parameters is shown. The anomalous particle flux increases with the elongation E but decreases with the triangulation D. This is true with the average anomalous particle flux and the maximal anomalous particle flux. Here, the anomalous flux profile is proportional to $|\widetilde{\phi}|^2$. At a small elongation E the profile is broader and it becomes narrow with a large elongation E. It is just the opposite with the triangulation D. If the triangulation is more pronounced, the anomalous particle flux reduces.

In Figure 5.4 the simulation is repeated with the TEXTOR parameters. Qualitatively, it is the same as with the MAST parameters beside the effect of an increasing anomalous flux average at a small elongation E. The losses by the anomalous particle flux can be reduced up to a factor of 4 with the right choice of the magnetic geometry.

These results comply to the experimental observations [48].

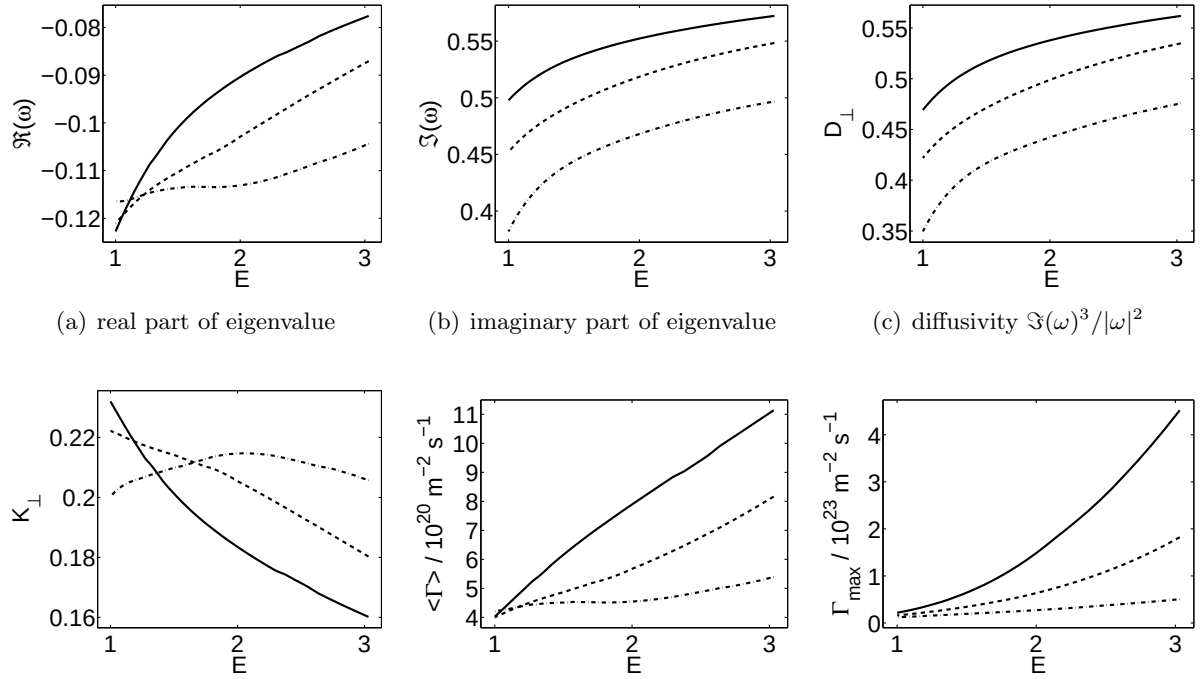

(a) real part of eigenvalue (b) imaginary part of eigenvalue (c) diffusivity $\Im(\omega)^3/|\omega|^2$

(d) $K_\perp$ of maximal growth rate (e) average anomalous particle flux (f) maximal anomalous particle flux

(g) $|\widetilde{\phi}|^2$ at $D = 0.00$ (h) $|\widetilde{\phi}|^2$ at $D = 0.22$ (i) $|\widetilde{\phi}|^2$ at $D = 0.40$

Figure 5.3: The simulation on elongation and triangulation with the MAST parameters ($T = 50$ eV, $n = 2 \cdot 10^{19}$ m^{-3}, $B = 0.47$ T, $\zeta = 2$, $z = 1$) (a-f) $D = 0$ (solid line), $D = 0.22$ (dashed line) and $D = 0.4$ (dash-dotted line). $K_\perp$ is chosen to maximize $\Im(\omega)$. The intensity is plotted in (g-i) proportional to circumference position.

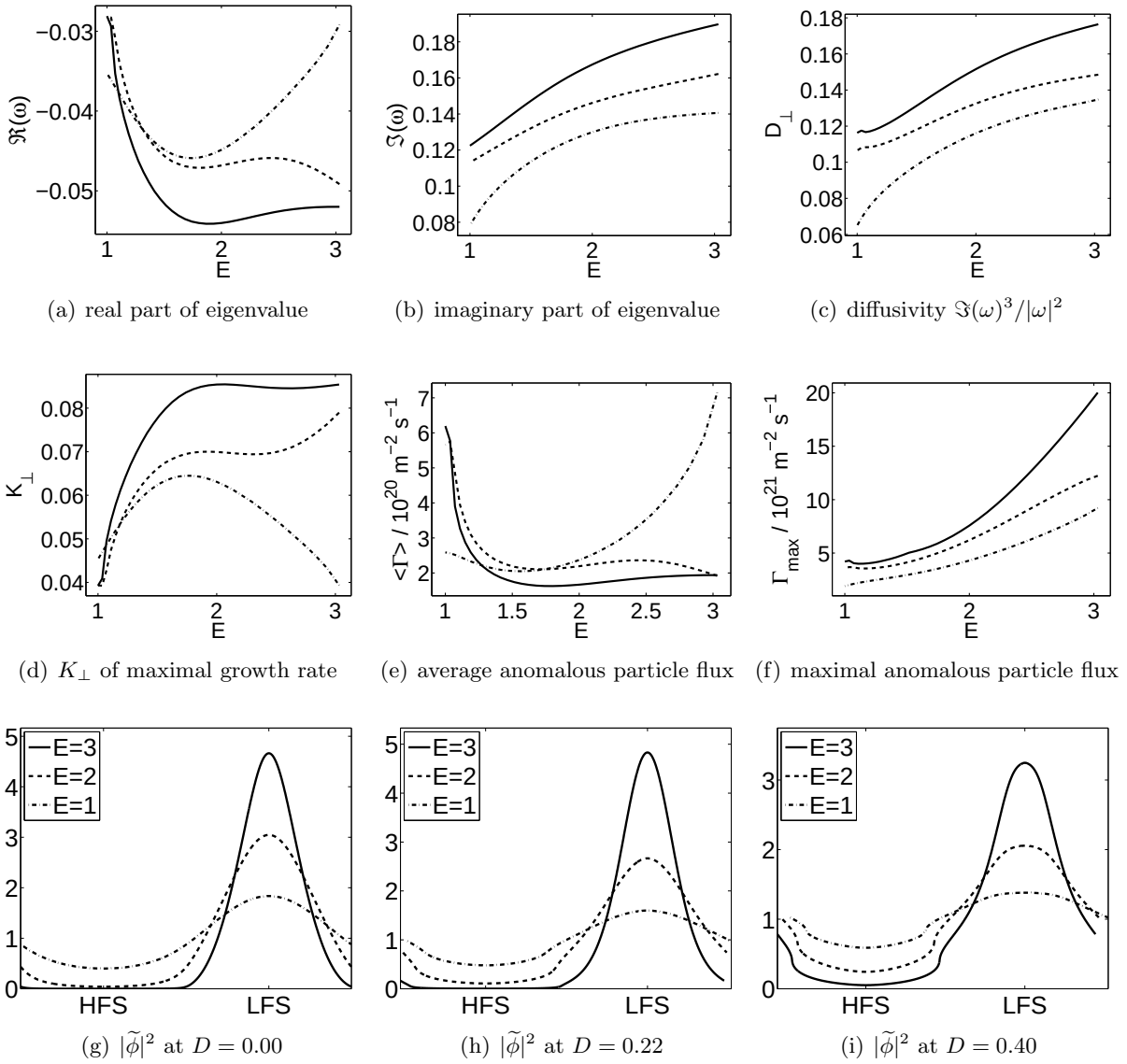

(a) real part of eigenvalue (b) imaginary part of eigenvalue (c) diffusivity $\Im(\omega)^3/|\omega|^2$

(d) $K_\perp$ of maximal growth rate (e) average anomalous particle flux (f) maximal anomalous particle flux

(g) $|\widetilde{\phi}|^2$ at $D = 0.00$ (h) $|\widetilde{\phi}|^2$ at $D = 0.22$ (i) $|\widetilde{\phi}|^2$ at $D = 0.40$

Figure 5.4: The simulation on elongation and triangulation with the TEXTOR parameters ($T = 50$ eV, $n = 3 \cdot 10^{19}$ m^{-3}, $B = 2.25$ T, $\zeta = 2$, $z = 1$) (a-f) $D = 0$ (solid line), $D = 0.22$ (dashed line) and $D = 0.4$ (dash-dotted line). $K_\perp$ is chosen to maximize $\Im(\omega)$. The intensity is plotted in (g-i) proportional to circumference position. (i) the steep curve parts correspond to the acute angles in the magnetic geometry.

Chapter 6

Self-consistent modeling of the anomalous transport and the plasma parameter profiles

In the previous chapters we developed a strategy to solve the anomalous transport eigenvalue equation (3.12) where the plasma parameter profiles like the temperature T and the density n are given. The solution of the eigenvalue equation yields the anomalous particle flux $\Gamma_\perp$. This flux influences the initial plasma parameters. In the introduction of the physical model the *heat balance equation*, the *global particle balance* and the *pressure balance* have been introduced as the means to determine the resulting plasma parameters.

In general, the eigenvalue, the heat balance and the global particle balance equation is one set of highly nonlinear equations to determine the plasma equilibrium. In order to handle the nonlinearity numerically, we solve it iteratively. To become precise, we fix the plasma parameters and solve the eigenvalue equation. Calculate the anomalous particle flux. Fix the anomalous particle flux and obtain the remaining plasma parameters by the heat balance equation and the global particle balance. Repeat this procedure until steady state is reached.

We will concern the heat balance equation and the global particle balance equation at first. Afterward we combine both equations into the profile iteration process.

6.1 Numerical treatment of the heat balance equation

The mathematical form of the heat balance equation (3.23) with the dependencies on the temperature and the poloidal angle stressed is

$$3T(\theta)\Gamma_\perp\big(T(\theta)\big) - \frac{\delta_{\text{edge}}\,1.94\cdot 10^{21}}{q^2R^2Z_{\text{eff}}}\frac{\partial}{\partial\theta}\left(\frac{T^{2.5}(\theta)}{\Lambda_{\text{c}}\big(n(\theta),T(\theta)\big)}\frac{\partial T(\theta)}{\partial\theta}\right) = g(\theta)q_{\text{core}} - E_iJ\big(\Gamma_\perp(T),\theta\big),$$
$$T(\theta) = T(2\pi+\theta), \quad \theta\in[0,2\pi[. \tag{6.1}$$

The first step is to fasten the function $\Gamma_\perp$, such that it becomes independent of the temperature T. Then all quantities on the right hand side are known values. The Coulomb integral Λ_{c} depends weakly on T and n and thus it can be fixed, too. Beside the term $T^{2.5}$ the equation is a linear second order boundary value problem.

Let D_1, D_2 be the matrices that approximate the first and the second derivatives, respectively. A fully linearized variant of the heat balance equation can be written as the linear system

$$\underbrace{\left(3\,\mathrm{Diag}(\Gamma_\perp) - K\,\mathrm{Diag}\left(D_1 \frac{T_j^{2.5}(\vec{\theta})}{\Lambda_\mathrm{c}(n_j,T_j)}\right) D_1 - K\,\mathrm{Diag}\left(\frac{T_j^{2.5}(\vec{\theta})}{\Lambda_\mathrm{c}(n_j,T_j)}\right) D_2\right)}_{=:A} T(\vec{\theta}) = \underbrace{g(\vec{\theta}) q_\mathrm{core} - E_i J_j(\vec{\theta})}_{=:b}. \tag{6.2}$$

The inversion of Λ_c is carried out point wise. T_j, n_j are known approximations in the jth step—the profile used calculating $\Gamma_\perp$ before—and T is the solution of the linear system $AT = b$. Due to the method (D_1, D_2) that approximate the derivatives, A is a periodic band matrix in case of the finite differences and A is a dense matrix with the pseudo spectral method.

By iterating (6.2) on T or with a multiple shooting technique we can solve the original fully nonlinear equation (6.1) except for a given $\Gamma_\perp$. It has been tested. It turned out that the nonlinear solution with a given $\Gamma_\perp$ is insufficient because either the temperature growths to infinity or drops to zero. This depends on the fact if the anomalous particle flux is either to small or to large.

In the anomalous transport problem, a change of the temperature T results in a change of the particle flux $\Gamma_\perp$. The calculation of $\Gamma_\perp$ occurs in a linearized manner of T, too, because the temperature and the density profiles are fixed in the eigenvalue solver. Therefore, it is not feasible to iterate the heat balance equation without adapting $\Gamma_\perp$. A deeper insigth of the process—as mentioned above—points out the necessity to update $\Gamma_\perp$ subsequently and it turned out that only one iteration of the linearized heat-balance equation is adequate before the anomalous particle flux is updated.

However, if the eigenpairs hardly change it is possible to skip the recalculation of the eigenvalue equation for a few times while the last calculated eigenpairs are reused. This has been tested successfully. The maximal number of iterations until the eigenpairs are updated was limited by 16 and predicted by the change of the transport factor

$$\frac{\Im(\omega)^3}{|\omega|^2}|\phi|^2$$

of the actual and the previous set of eigenpairs. This strategy reduces the total effort of the eigenvalue calculation to a tenth. It must be stressed that only the eigenpair is fixed temporarily, but not the anomalous particle flux (3.22).

6.1.1 Reducing the effort in the symmetric case

The linearized heat-balance equation (6.2) is a linear equation system. In case of the pseudo spectral derivatives the matrix A is dense. The computational cost to solve the linear system increases cubically with the dimension N. With finite differences, the sparsity pattern can be used analogously to the one step approximation (cf. Figure 4.5 on page 66). However, the heat balance equation needs to be solved to a high accuracy, at least in the final iterations and therefore we cannot approximate the pseudo spectral matrix by the finite difference matrix as we did it in the correction equation (2.7) in section 4.4.2 on page 65.

In the Tokamak the top half and the bottom half of the torus is symmetric beside boundary effects like the position of the limiter and the puffing position of the fueling gas nozzle. The effects mentioned above determine the influx J of the neutrals. If J is symmetric the whole

problem is symmetric and the boundary condition of the heat-balance equation (6.1) changes from periodic boundary condition on $[0, 2\pi[$ to Neumann boundary condition on $[0, \pi]$. This yields

$$3T(\theta)\Gamma_\perp(\theta) - \frac{\delta_{\text{edge}}\, 1.94 \cdot 10^{21}}{q^2 R^2 Z_{\text{eff}}} \frac{\partial}{\partial\theta}\left(\frac{T^{2.5}(\theta)}{\Lambda_c\big(n(\theta), T(\theta)\big)} \frac{\partial T(\theta)}{\partial\theta}\right) = g(\theta) q_{\text{core}} - E_i J\big(\Gamma_\perp(T), \theta\big),\ \theta \in [0, \pi]$$
$$\frac{\partial T}{\partial\theta}(\theta) = 0,\ \theta \in \{0, \pi\}. \tag{6.3}$$

Beside the advantage, that the discretized problem decreases to half the dimension, the derivative matrices D_1 and D_2 are band matrices with finite differences and so is the whole matrix A. The entries of the finite difference stencil, that are outside of the matrix are mirrored back inside at the outer columns. Solving linear systems with band matrices is more efficient than with periodic band matrices. However, in case of the pseudo spectral derivatives the matrix is still dense, but of half the size and the matrix D_1 and D_2 are created using the discrete cosine transformation [39] analogously to the discrete Fourier transformation in Chapter 4.2.2.

Remark 6.1. In general the advantage of the symmetry is not applicable in the correction equation (2.7) of the Jacobi-Davidson eigenvalue solver because the real and imaginary part of the eigenfunctions can be antisymmetric although the intensity is symmetric. The simplest example of this effect is $\exp(i\theta)$. However, if we restrict the eigenfunctions to the even functions we have an eigenvalue equation with Neumann boundary conditions on half of the domain.

6.2 Global particle balance

The global particle balance from (3.25)

$$\int_0^{2\pi} J \frac{d\sigma}{d\theta}\, d\theta = \int_0^{2\pi} \Gamma_\perp \frac{d\sigma}{d\theta}\, d\theta \tag{6.4}$$

is the second equation to determine the new pressure and the density profile. We analyze the global particle balance equation in the case of the global particle conservation and in case of the gas puff.

6.2.1 Particle conservation

In a scenario with identical inflow and outflow of particles, the number of particles

$$\int_0^{2\pi} n_j \frac{d\sigma}{d\theta}\, d\theta = \widehat{n}_0 := \int_0^{2\pi} n_0 \frac{d\sigma}{d\theta}\, d\theta \tag{6.5}$$

remains constant with each iteration j. Due to the high parallel conductivity, the pressure $p = n(\theta)T(\theta)$ is constant along the poloidal circumference. $\widehat{n}_0$ can be obtained from the initial density distribution $n_0(\theta)$. In order to calculate the new density profile $n_j(\theta)$ out of $T_j(\theta)$, we consider the following: For the hitherto unknown pressure it holds $p_j = n_j(\theta)T_j(\theta)$. Together with the particle conservation (6.13) we have

$$0 = \int_0^{2\pi} n_0(\theta) \frac{d\sigma}{d\theta}\, d\theta - \int_0^{2\pi} n_j(\theta) \frac{d\sigma}{d\theta}\, d\theta = \widehat{n}_0 - \int_0^{2\pi} \frac{p_j}{T_j(\theta)} \frac{d\sigma}{d\theta}\, d\theta = \widehat{n}_0 - p_j \int_0^{2\pi} \frac{1}{T_j(\theta)} \frac{d\sigma}{d\theta}\, d\theta$$
$$\Rightarrow p_j = \widehat{n}_0 \left(\int_0^{2\pi} \frac{1}{T_j(\theta)} \frac{d\sigma}{d\theta}\, d\theta\right)^{-1}$$

$$\Rightarrow n_j(\theta) = \frac{p_j}{T_j(\theta)} = \frac{\widehat{n}_0}{T_j(\theta)} \left(\int_0^{2\pi} \frac{1}{T_j(\theta)} \frac{d\sigma}{d\theta}\, d\theta \right)^{-1} \tag{6.6}$$

We emphasis the fact, that the physical background demands $T(\theta) > 0$. For T close to zero the density is very high.

6.2.2 Gas puff

In the scenario with an external inflow and outflow of neutrals, for example by puffing in fueling gas together with particle losses due to pumping out neutralized dust, the number of particles in the fusion vessel is not necessarily constant. The inflow is known but the outflow strongly depends on the anomalous transport as the pumps can only pump out neutralized particles accumulating in the SOL.

The neutrals in the gas flow Φ_{gas} enter the edge layer with an angular distribution f. The particles of the anomalous particle flux $\Gamma_\perp$ enter the plasma to a specific rate $0 < R_{\text{rec}} < 1$. The influx of neutrals is (cf. section 3.3 on page 44)

$$J(\theta) = R_{\text{rec}} \Gamma_\perp(\theta) + \Phi_{\text{gas}} f(\theta).$$

The remaining neutrals $(1 - R_{\text{rec}})\Gamma_\perp$ are pumped out.

In steady state, the number of particles puffed in equals the number of particles that leave the plasma, thus

$$\int_0^{2\pi} \Gamma_\perp(\theta) \frac{d\sigma}{d\theta}\, d\theta = \int_0^{2\pi} J(\theta) \frac{d\sigma}{d\theta}\, d\theta = \int_0^{2\pi} \big(\Gamma_\perp(\theta) R_{\text{rec}} + \Phi_{\text{gas}} f(\theta) \big) \frac{d\sigma}{d\theta}\, d\theta.$$

Again, the high parallel heat conductivity forces a poloidal homogeneous pressure $p_j = T_j(\theta) n_j(\theta)$. The equation (3.22) of the anomalous particle flux contains the pressure factor, thus the new pressure is

$$p_{\text{new}} := p_j \frac{\Phi_{\text{gas}}}{1 - R_{\text{rec}}} \frac{\int_0^{2\pi} f(\theta) \frac{d\sigma}{d\theta}\, d\theta}{\int_0^{2\pi} \Gamma_\perp(\theta) \frac{d\sigma}{d\theta}\, d\theta}.$$

It depends on the ratio of the inflow and the outflow whether the pressure p increases or decreases. The pressure affects the particle flux linear in the $\Gamma_\perp$ formula (3.22) and additionally nonlinear through the eigenvalue equation (3.12).

6.3 The profile iteration

In the previous sections we suggested numerical methods to solve the eigenvalue equation (3.12), the heat-balance equation (3.23) and the global particle balance (6.4). We summarize this procedure in the function F:

$$(T_{\text{new}}, p_{\text{new}}) = F(T, p),$$

where T is an angular temperature profile and p the scalar valued pressure. F is used iteratively to obtain the plasma equilibrium (T, p), which is a fixed point

$$(T, p) = F(T, p). \tag{6.7}$$

The naive idea of fixed point iteration

$$(T_{j+1}, p_{j+1}) := F(T_j, p_j)$$

does not work because F is not contractive in general. To make the iterative process contractive a damping parameter $\alpha \in]0,1]$ is introduced to define

$$F_\alpha(T_j, p_j) := \alpha F(T_j, p_j) + (1-\alpha)(T_j, p_j).$$

and the fixed point iteration is applied to F_α instead of F

$$(T_{j+1}, p_{j+1}) = F_\alpha(T_j, p_j) \tag{6.8}$$

Before we discuss the choice of the damping parameter α, the profile iteration is interpreted from a different point of view.

6.3.1 Non-linear power method

The damped profile iteration (6.3) can be interpreted as a nonlinear power method for the nonlinear eigenvalue equation

$$F(T,p) = \mu\,(T,p), \tag{6.9}$$

where μ is an eigenvalue and F is the nonlinear counterpart of a matrix vector multiplication. The nonlinear eigenvalue equation is connected to (6.7) in the way, the eigenvalue $\mu = 1$ is assumed to exist for physical reasons. Unfortunately we cannot analyze this analytically due to the complexity of F.

The damped fixed point iteration (6.3) is equivalent to

$$F(T,p) - \beta(T,p) = \widetilde{\mu}\,(T,p), \qquad \beta = -\frac{1-\alpha}{\alpha}, \qquad \widetilde{\mu} = \mu - \beta.$$

We assume that F has real eigenvalues only, because an imaginary temperature is physically nonsens. We consider the scenario where the eigenvalues are $\mu_1 = 1$ and $\mu_2 = -1$, both have the modulus 1. A shift $\beta = -1$ shifts μ_2 on 0 and μ_1 on 2 and the equivalent damping parameter is $\alpha = 0.5$.

6.3.2 Dynamic damping

The appropriate choice of the damping parameter α is essential for a fast and reliable convergence procedure and it is the most difficult part in the profile iteration process. For a better readability the pressure p is skipped in the following.

Let T_j be the temperature profile in the jth iteration. We define

$$\Delta T_j := T_j - F(T_j)$$

and compare the sign

$$s_j(\theta) := \Delta T_{j-1}(\theta)\Delta T_j(\theta)$$

If $s_j(\theta) > 0\ \forall\theta \in [0, 2\pi[$ the profile moves monotonically in one direction. Hence, the damping can be reduced by increasing α:

$$\alpha_j := (1 + c_r)\alpha_{j-1} \qquad \text{(release of damping)}$$

where $c_r \in [0,1]$, e.g. $c_r = 0.1$. c_r is fixed within the whole profile iteration process.

If $s_j(\theta) < 0\ \forall\theta \in [0, 2\pi[$ then the direction of the consecutive profiles is contrary. In order to avoid oscillations, the damping has to be increased:

$$\alpha_j = c_a\alpha_{j-1}. \qquad \text{(attack of damping)}$$

where $c_a \in]0,1[$. An appropriate value is $c_a = 0.5$.

It is necessary to choose c_r and c_a such that the attack of damping is stronger than the release of damping, i.e.,

$$\frac{1}{1+c_r} > c_a.$$

In the remaining case of an indefinite sign, the damping can be increased carefully to accelerate the iteration process,

$$\alpha_j := (1+c_i)\alpha_{j-1}, \qquad c_i \ll c_r.$$

It is necessary to change the damping parameter α smoothly to avoid setting the limit of the profile iteration process through the choice of the $(\alpha_j)_j$ sequence apriori. This is the reason for the small changes described above.

Additionally, the change of the plasma profiles in the subsequent iterations has to be limited. We require the *trust region* [16] condition

$$\max_\theta \left| \frac{T_{j+1}(\theta) - T_j(\theta)}{T_j(\theta)} \right| < c_c, \qquad \text{e.g., } c_c = 0.1 \tag{6.10}$$

which yields

$$\alpha_j \leq \min_\theta \left| \frac{T_j(\theta)}{F(T_j)(\theta) - T_j(\theta)} \right|.$$

We call the strategy of damping *dynamic damping*. It works fine with temperatures above a magnitude of 10 eV. At temperatures close to zero care must be taken to the exponential factor in the penetration depth L_n of the neutral particles. L_n increases exponentially where the temperature T approaches zero. By the dependence $\delta_\mathrm{edge} = L_\mathrm{n}(\theta_g)$ of the edge layer width, the derivative term in the heat balance equation (3.23) is weighted by $T^{3.5}\exp(6.8/T)$ (cf. definition of L_n in Table 3.2 on page 46) where the minimum is at $T = 1.94$ eV and it grows exponentially with lower T.

In order to compensate the exponential growth within the dynamic damping, we add the trust region strategy

$$|L_\mathrm{n}(T_{j+1}) - L_\mathrm{n}(T_j)| < c_\mathrm{L}.$$

on the values of L_n. The condition leads to the Lambert W [47] function and is numerically solved by the Newton method.

Although the output of the linearized heat balance equation (6.2) can consist of poloidal positions with negative values of the temperature, the trust region strategy ensures the temperature output of the damped system to stay positive.

Figure 6.1 shows the convergence $|T_{j+1} - T_j|$ and the associated damping parameter α of two profile iterations. The temperature in the example in the upper row is large enough to result in a moderate L_n. In the example in the lower row, the temperature approaches close to zero and the damping strategy works hard to lead the iteration into convergence.

In the context of the non-linear power method, the dynamic damping is equivalent to applying a dynamical shift μ, such that the influence of adjacent eigenvalues is reduced. It has to be mentioned, that if there are several states of equilibrium in $\mathbb{R}_+ := \{x \in \mathbb{R}, x > 0\}$, the final temperature profile depends on the initial one. A general proposition on the number of possible solutions of an nonlinear equation cannot be given.

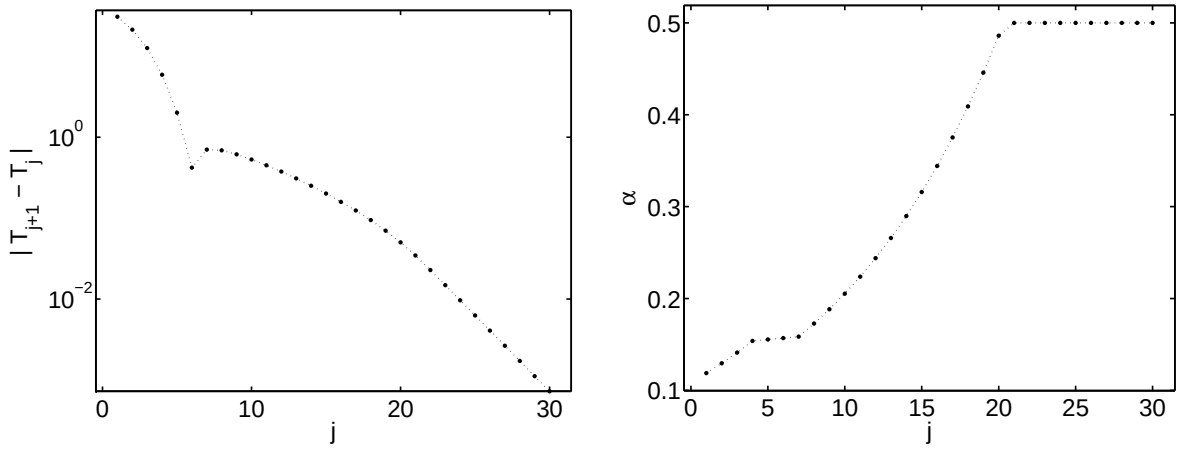

(a) Convergence of temperature profile

(b) dynamic damping of (a)

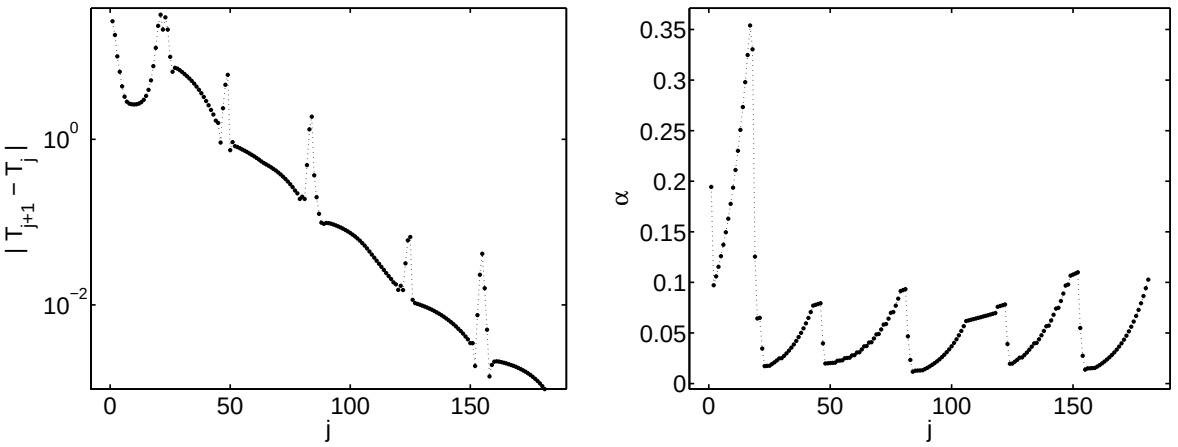

(c) Convergence of temperature profile

(d) dynamic damping of (c)

Figure 6.1: The convergence $|T_{j+1} - T_j|$ and the damping parameter α of two profile iterations that triggered MARFE. The MARFE evolves in the iteration ((a,b) $j = 6$, (c,d) $j = 18$) where the monotonic convergence of the profile is interrupted the first time. In (a) the convergence becomes monotonic again since $j = 7$ and the damping parameter (b) increases to its upper bound of $\alpha = 0.5$. In (c) the monotonic convergence is interrupted consecutively and the dynamic damping strategy (d) reacts with an immediate damping attack. In the piecewise monotonous range the damping is released carefully.

6.3.3 Stopping criterion

Some criteria to stop the profile iteration is required. If the iteration process has converged to a steady state in the jth step it holds

$$(T_{j+k}, p_{j+k}) = F(T_{j+k}, p_{j+k}), \quad \forall k \in \mathbb{N}.$$

Definition 6.2. For a given tolerance $\varepsilon_\mathrm{T}, \varepsilon_\mathrm{p} > 0$ the profile iteration is called *converged* if

$$\|(T_{j+1}, p_{j+1}) - F(T_j, p_j)\|_\infty < (\varepsilon_\mathrm{T}, \varepsilon_\mathrm{p})$$

holds. The temperature T has to fulfill the equation at every angular position.

Remark 6.3. The distance $\|(T_{j+1}, p_{j+1}) - (T_j, p_j)\|_\infty$ is a convergence measure if the damping parameter satisfies $\alpha \approx 1$. We have to ensure that a system is not called converged due to over damping ($\alpha \ll 1$).

An alternative to Definition 6.2 is to use relative distances, which increases the weighting at positions with a small temperature. Another variant is to use the inner product

$$\frac{\int_0^{2\pi} T_j(\theta)\ F(T_j)(\theta)\ d\theta}{\sqrt{\int_0^{2\pi} T_j^2(\theta)\ d\theta\ \int_0^{2\pi} F^2(T_j)(\theta)\ d\theta}}$$

which results in the opposite effect, the weighting of the difference at positions of high temperature is emphasized. Due to the fact that the most interesting effects of F (e.g. MARFE) occur at low temperatures, the latter one is not recommended in the anomalous transport iteration.

6.3.4 Wave length parameter $K_\perp$

The wave number $K_\perp$ is a parameter in the eigenvalue equation (3.12) and for the anomalous particle flux $\Gamma_\perp$. There are at least three possibilities to handle this parameter:

1. A set $\mathcal{K}_\perp$ of appropriate wave numbers is chosen. For each $K_\perp \in \mathcal{K}_\perp$ the eigenvalue equation (3.12) is solved and the eigenpair of maximal growth rate is selected. Afterwards the total anomalous particle flux is calculated as a sum over each $K_\perp$ (see section 3.2 on page 42). The procedure is summarized in Algorithm 11.
2. In each profile iteration, $K_\perp$ is chosen to maximize the growth rate of the mode with the maximal growth rate. The anomalous particle flux of this single eigenpair or the extremal eigenpairs of several modes is calculated. This procedure is listed in Algorithm 12.
3. For a single and fixed value of $K_\perp$ the profile iteration is executed. In an outer loop the values of $K_\perp$ is determined that maximizes the growth rate of the converged profile. Details are given in Algorithm 13.

Each of the three possibilities has some advantages but also some disadvantages.

(1.) is easy to implement, but the result depends on the set $\mathcal{K}_\perp$. The anomalous particle flux $\Gamma_\perp$ increases with the number of elements in $\mathcal{K}_\perp$. If there are many $K_\perp$ values close to the one with the maximal growth rate the anomalous particle flux increases much more than if wave numbers in a region of smaller growth rate are added.

The dependence on the number of $K_\perp$ values is eliminated if the sum is replaced by the integral

$$\Gamma_2 := \int_{K_\perp^{\min}}^{K_\perp^{\max}} \frac{\Im(\omega(K))^3}{K^2(1 + 2K^2\gamma(K))\gamma(K))} \frac{|\phi(K)|^2}{|\omega(K)|^2}\, dK,$$

where $(\omega(K), \phi(K))$ denotes the eigenpair of the maximal growth rate among all the eigenpairs with $K_\perp = K$. Numerically the integral is approximated by a quadrature formula. The dependence on the positions still remains and can be avoided only by taking many values to make the discrete representation smooth. However, the definition of the starting $K_\perp^{\min}$ and the end $K_\perp^{\max}$ of the interval is still an unclarity.

(2.) The implementational aspects to determine the wave number $K_\perp$ which maximizes the growth rate of the dominant mode have been given in section 4.5.2 on page 79 already. The method works fine with the plasma parameters prescribed, as it is done in the experiment on the magnetic geometry in Chapter 5 on page 83. However, the profile iteration to determine the plasma equilibrium self consistently does not converge. Even if the damping parameter α is close to zero the oscillations are huge.

The reason is as follows. The wave number $K_\perp$ is chosen such that the eigenmode with the maximal imaginary part becomes maximal. Very tiny changes in the shape of the temperature profile cause a slightly different $K_\perp$ value to be optimal in the next eigenvalue calculation. This causes the anomalous particle flux $\Gamma_\perp$ to change significantly. Thus the next temperature is strongly different. This problem is so essential, that even a damped Newton iteration on the system

$$F(T,p) - (T,p) = 0$$

does not find a state of plasma equilibrium. The way the damped Newton iteration has been realized is described in the Appendix C.1 on page 131.

(3.) This method has been developed to avoid the problems of (2.). The fixed wave number parameter $K_\perp$ within the profile iteration eliminates the problem of (2.) and the dynamic damping strategy leads to a stable profile iteration. The maximization process in the outer loop needs to take care of the computational cost of a complete profile iteration. Therefore a polynomial interpolation technique that predicts the maximal $K_\perp$ value is applied. This is similar to the one which is used at (2.) in the inner loop. Thus, the overall effort is similar.

The disadvantage of (3.) is the fact that the wave number $K_\perp$ of the maximal growth rate is different to the wave number of the maximal anomalous transport. This leads to jumps in the plasma profiles of consecutive self consistent calculations where one parameter, e.g. the prescribed averaged density or the gas puff intensity, is swept.

Algorithm 11 Averaging the eigenmodes over $K_\perp$

Require: T_0, p_0

1: **for** $j = 1, 2, \ldots$ **do**
2: calculate the l most dominant eigenpairs $\big(\omega_k(K), \phi_k(K)\big)_{k=1,\ldots,l}$.
3: calculate $\Gamma_\perp = C \sum_{k=1}^{l} \frac{\Im(\omega_k)^3}{K_k^2(1+2K_k^2\gamma)\gamma} \frac{|\phi_k|^2}{|\omega_k|^2}$
4: calculate the resulting plasma parameters T_{calc}, p_{calc} by the heat balance equation(3.23) and the global particle balance (3.25).
5: update the plasma profile $T_{j+1} = \alpha T_{\text{calc}} + (1-\alpha)T_j, \quad p_{j+1} = \alpha p_{\text{calc}} + (1-\alpha)p_j$.
6: **end for**

In Algorithm 13 a set $\mathcal{K}_\perp$ of wave numbers to discretize the wave number domain is given. Afterwards the local maxima of $K_\perp$ of the data are determined. Each local maximum is calculated by subsequent profile iterations and the global maximum is determined among the local ones in a last step (see section 6.3.5). For a number $l > 1$ of eigenpairs (2.) and (3.) are different because the most dominant and the second most dominant eigenmode can be taken at different values of $K_\perp$ in (2.) but only at the same wave number in variant (3.).

Algorithm 12 Maximize the growth rate of each mode in the inner loop

Require: T_0, p_0

for $j = 1, 2, \ldots$ **do**
  for $K \in \mathcal{K}$ **do**
    calculate the l most dominant eigenpairs $\big(\omega_k(K), \phi_k(K)\big)_{k=1,\ldots,l}$.
  end for
  arrange the eigenpairs into modes m_k.
  for all mode m_k **do**
    search $K_\perp$ such that the growth rate of the eigenmode becomes maximal.
  end for
  calculate $\Gamma_\perp = C \sum_{m_k} \frac{\Im(\omega_k)^3}{K_k^2(1+2K_k^2\gamma)\gamma)} \frac{|\phi_k|^2}{|\omega_k|^2}$
  calculate the resulting plasma parameters T_{calc}, p_{calc} by the heat balance equation (3.23) and the global particle balance (3.25).
  update the plasma profile $T_{j+1} = \alpha T_{\text{calc}} + (1-\alpha)T_j, \quad p_{j+1} = \alpha p_{\text{calc}} + (1-\alpha)p_j$.
end for

Algorithm 13 Maximize the growth rate in the outer loop

Require: T_0, p_0

for $K_\perp \in \mathcal{K}_\perp$ **do**
  for $j = 1, 2, \ldots$ **do**
    calculate l eigenpairs $\big(\omega_k(K_\perp), \phi_k(K_\perp)\big)_{k=1,\ldots,l}$ such that $\Im(\omega(K_\perp))$ is maximal.
    calculate $\Gamma_\perp = C \frac{1}{K_\perp^2(1+2K_\perp^2\gamma)\gamma)} \sum_{k=1}^{l} \frac{\Im(\omega)^3 |\phi_k|^2}{|\omega_k|^2}$
    calculate the resulting plasma parameters T_{calc}, p_{calc} by the heat balance equation (3.23) and the global particle balance (3.25).
    update the plasma profile $T_{j+1} = \alpha T_{\text{calc}} + (1-\alpha)T_j, \quad p_{j+1} = \alpha p_{\text{calc}} + (1-\alpha)p_j$.
  end for
end for
choose the converged profile of that $K_\perp$ where the growth rate is maximal.

6.3.5 Searching for local maxima

We continue the discussion on variant (3.) of the previous section. The equilibrium plasma profile with the maximal growth rate has to be determined by choosing the optimal wave number parameter $K_\perp$. This can be written abstractly by a function $f: K_\perp \to \Im(\omega)$. The evaluation of f is the complete profile iteration on $F(T, p)$. Thus every evaluation of f is computational expensive.

This aim can be formulated abstractly: Find a local minimum of the smooth function $f : \mathbb{R} \to \mathbb{R}$ in an interval $I = [a, b]$. We consider the case where each evaluation of f is computationally highly expensive. Hence, an algorithm is required that finds the local maximum to a high accuracy by as few function evaluations as possible.

First at arbitrary positions $x_1 < x_2 \in I$, $y_i := f(x_i)$, $i = 1, 2$ is evaluated. Then polynomial interpolation is applied to determine a new position x_{predict} that predicts f to be larger than at y_i. We use quadratic (degree $d = 2$) or cubic (degree $d = 3$) polynomials to be able to calculate their (unique) maximum, thus we use $d+1$ interpolation points. Starting from the $d+2$nd node, we remove an old node. This shall be done wisely. To be more precise, the remaining nodes shall lie close to the maximum of the already tested values ($\max_i\{y_i\}$) and if possible one node right and left of this maximum remains.

The theorem of Taylor says, that each smooth function $f \in C_4(I)$ can be locally expanded by a

cubic polynomial up to an error that depends on the fourth derivative and the distance of the interpolation points to the fourth power:

$$f(x) = f(x_0) + f'(x_0)(x - x_0) + \frac{1}{2}f''(x_0)(x - x_0)^2 + \frac{1}{6}f'''(x_0)(x - x_0)^3 + \mathcal{O}\big((x - x_0)^4\big). \quad (6.11)$$

The derivatives of f are unknown in practical applications. However, from this theorem we can deduce, that the predicted maximum will converge to the actual maximum, if the distance of the interpolation nodes tends to zero. This is equivalent to the maximization of modes within the eigenvalue equation (cf. section 4.5 on page 75) beside the fact, that the domain is not limited, now.

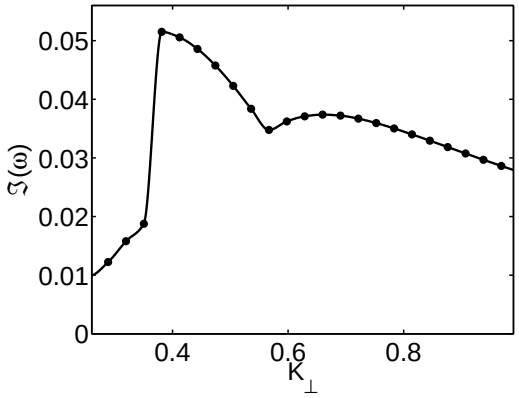

Figure 6.2: The $K_\perp$ spectra curve (dots) of a simulation where the wave number $K_\perp$ is fixed within the profile iteration. The spectra has a maximum at $K_\perp = 0.4$. On the right side, it is very smooth and can be approximated very well by a polynomial of a low degree. However, on the left side of the maximum is a discontinuity.

Some problems arise within the maximization process of the outer loop. For several values $K_\perp \in \mathcal{K}_\perp$ the profile iteration is calculated and the growth rate (dots) of the eigenvalue equation with the final plasma profile is displayed in Figure 6.2. The spectra contains a maximum at $K_\perp = 0.4$. For $K_\perp > 0.55$ the function is smooth and can be well approximated by a polynomial of low degree. However, at $K_\perp = 0.39$ there is a discontinuity.

The growth rate curve in Figure 6.2 consists of two different modes. Below $K_\perp = 0.4$ and above $K_\perp = 0.6$ the dominant mode causes the plasma profiles to be rather homogeneous, while the ballooning mode is triggered with $K_\perp \in [0.4, 0.6]$. The discontinuity at $K_\perp$ arises because the plasma parameter has to reach some state of inhomogeneity to trigger the ballooning mode to become dominant. In the region of $K_\perp = 0.4$ the anomalous transport problem $F_\alpha(T, p) = (T, p)$ consist of two solutions and the outcome of the profile iteration algorithm depends on the degree of inhomogeneity that is accomplished within the iterations.

This discontinuity affects the maximization process as the prediction strategy of the polynomial interpolation approximation will predict the maximum at much smaller $K_\perp$ values without an interpolation point less than $K_\perp = 0.4$. The evaluations are taken at $K_\perp < 0.4$ and subsequent *contraction steps* at the left side occur until the leftmost point reaches a wave number where the ballooning mode is triggered. Then the *extrapolation to the left* is executed again and so on. To prevent the searching mechanism to run into an infinite loop, all the old nodes are cached and the appropriate nodes from the cache are revoked when the extrapolation to the left is predicted. Then the procedure continues as an interval section mechanism.

This is the basic idea behind Algorithm 14, that is a bit more complicated in detail. For a better readability it is split into one main routine and two subroutines. The main routine provides an

estimate of the position of the local maxima by polynomial interpolation. There is either a local maxima in the range of the interpolation points or a careful extrapolation step is executed.

Once a local maxima is in the interior of the range spanned by the outer interpolation points, the width of the range has to be contracted subsequently in order to achieve a high local accuracy of the interpolation (cf. Taylor formula (6.11)). This occurs either automatically when the proposed maxima oscillates around the actual one or it is explicitly forced by *contracting steps*. The contracting steps are taken if one of the outer nodes is strongly separated from the others. This is illustrated in Figure 6.3.

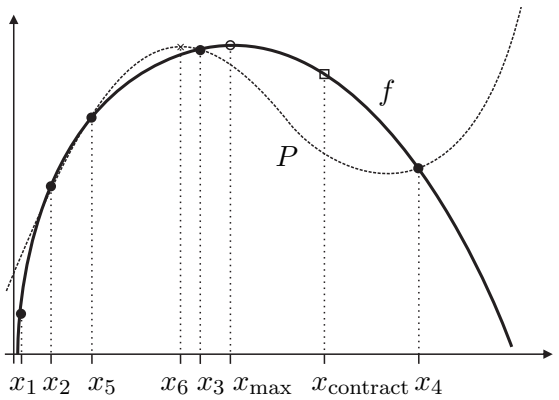

Figure 6.3: The maximum of the function f is to find. The values $\{(x_j, f(x_j)),\ j = 2, \ldots, 5\}$ are interpolated by an polynomial P and the predicted maximum is $(x_6, f(x_6))$. The interpolation points of the next cycle are $\{(x_j, f(x_j)),\ j = 3, \ldots, 6\}$. The three interpolation points $x_j < x_{\max}$ converge to $x_{\max}$ but the only interpolation point greater than $x_{\max}$ remains x_4 which is separated. The convergence is improved by a contracting step that tests x_{contract} and removes x_4.

At a contraction step the old node is removed and the new node becomes the boundary. In all the other scenarios, the new node is added to the set S and the old nodes which is most unqualified for the local maximum is removed. The realization is just a case study (Algorithm 16) and not discussed here in detail.

The nodes removed from S are still cached for cases of a non differentiable curve like in Figure 6.2, where sudden extrapolations occur. Then the next removed node which is available in the cache is added to the polynomial interpolation support and the utmost one on the opposite side is removed. This reduces the number of additional evaluations of f and avoids the search to run into an infinite loop.

Algorithm 14 Detecting local maxima of function f by interpolation

Require: $f : \mathbb{R} \to \mathbb{R}$ (smooth),
Require: $n \in \{2, 3, 4\}$ interpolation points $S_1 = \{(x_i, y_i) \mid y_i = f(x_i),\ i = 1, \ldots, n\}$.
Require: upper bound of interpolating polynomial degree d, e.g. $d = 3$ for cubic polynomials.

for $k = 1, \ldots$ **do**
  $n := |S_k|$
  calculate interpolating polynomial P_k of degree $n-1$, such that $P_k(x_i) = y_i\ \forall (x_i, y_i) \in S_k$.
  $x_{\text{predict}} := \begin{cases} \text{local maximum of } P_k & \text{if exists} \\ x_1 + (x_1 - x_n)/(n-1) & y_1 > y_n \quad // \text{ extrapolate to the left} \\ x_n + (x_n - x_1)/(n-1) & y_1 < y_n \quad // \text{ extrapolate to the right} \end{cases}$
  if x_{predict} is local maximum of P_k **then**
    $x_{\text{predict}} :=$ DecreaseWidthOfNodesDomain$(S_k, P_k, 2, x_{\text{predict}}, y_{\text{predict}})$ // Algorithm 15
  end if
  $y_{\text{predict}} := P_k(x_{\text{predict}})$ // predicted value of f in x_{predict}
  $y_{\text{actual}} := f(x_{\text{predict}})$ // actual value of f in x_{predict}
  if $|y_{\text{predict}} - y_{\text{actual}}| \le \varepsilon$ **then**
    Stop. The local maximum is $(x_{\text{predict}}, y_{\text{actual}})$.
  end if
  if $|S_k| > d$ **then**
    $S_{k+1} :=$ RemoveNodeWisely$(S_k \cup \{(x_{\text{predict}}, y_{\text{actual}})\},\ x_{\text{predict}})$ // Algorithm 16
  else
    $S_{k+1} := S_k \cup \{(x_{\text{predict}}, y_{\text{actual}})\}$.
  end if
end for

Algorithm 15 Decrease width of nodes domain

procedure DecreaseWidthOfNodesDomain(set of nodes S, interpolating polynomial P, ratio parameter of node distance $c > 0$, inner maximum of interpolation polynomial x_m, y_m) // e.g. $c = 2$
$n := |S|$.
if $x_n - x_m > c \cdot \max\{|x_m - x_j|, j = 1, \ldots, n-1\}$ **then**
  // the right node is separated from the others, move it left the half way to x_{n-1}. This is called *contraction on the right.*
  $x_{\text{predict}} := (x_{n-1} + x_n)/2$
else if $x_m - x_1 > c \cdot \max\{|x_m - x_j|, j = 2, \ldots, n\}$ **then**
  // the left node is separated from the others, move it right the half way to x_2. This is called *contraction on the left.*
  $x_{\text{predict}} := (x_1 + x_2)/2$
else
  $x_{\text{predict}} := x_m$ // no modification
end if
return x_{predict}.

Algorithm 16 Remove node wisely

procedure RemoveNodeWisely(set of nodes S, position of last inserted node x_{predict})
$n := |S|$
$i_m := \text{argmax}_{j=1,\dots,n}\{y_j \mid (x_j, y_j) \in S\}$. // the index of largest value yet known
$i_p := \text{argmin}_{j=1,\dots,n}\{|x_j - x_{\text{predict}}| \mid (x_j, y_j) \in S\}$. // the index of the last inserted node
if $x_{\text{predict}} = (x_{n-1} + x_n)/2$ **then**
  $S := S \setminus \{(x_n, y_n)\}$ // last step was contraction on the right
else if $x_{\text{predict}} = (x_1 + x_2)/2$ **then**
  $S := S \setminus \{(x_1, y_1)\}$ // last step was contraction on the left
else if $i_m = i_p$ /* last inserted node is maximal */ **then**
  if $i_m < (n+1)/2$ **then**
    $S := S \setminus \{(x_n, y_n)\}$ // the maximal node is on the left side, so remove the right one
  else if $i_m > (n+1)/2$ **then**
    $S := S \setminus \{(x_1, y_1)\}$ // the maximal node is on the right side, so remove the left one
  else
    // the maximal node is at the center
    if $2x_{i_p} > x_1 + x_n$ **then**
      $S := S \setminus \{(x_1, y_1)\}$ // last inserted one is on the right, so remove at the left
    else
      $S := S \setminus \{(x_n, y_n)\}$ // last inserted one is on the left, so remove at the right
    end if
  end if
else if $i_m > (n+1)/2$ **then**
  // maximum is on the right side, so remove at the left
  if $i_p = 1$ **then**
    $S := S \setminus \{(x_2, y_2)\}$ // the last added node still remains
  else
    $S := S \setminus \{(x_1, y_1)\}$
  end if
else if $i_m < (n+1)/2$ **then**
  // maximum is on the left side, so remove at the right
  if $i_p = n$ **then**
    $S := S \setminus \{(x_{n-1}, y_{n-1})\}$ // the last added node still remains
  else
    $S := S \setminus \{(x_n, y_n)\}$
  end if
else
  // maximal node is in the center
  if $i_p > i_m$ **then**
    $S := S \setminus \{(x_1, y_1)\}$
  else
    $S := S \setminus \{(x_n, y_n)\}$
  end if
end if
return S.

6.4 Effect of plasma shift on density limit

In the Tokamak devices particles inside the scrape-off layer neutralize at the limiter and reenter into the plasma. At the position of reentry, an increase of the density occurs due to the presence of additional particles and a drop of the temperature due to the ionization process. This endangers the development of MARFE that worsens the situation even further. An experimental formula of the density limit was obtained by Greenwald et al. [12]. However TEXTOR experiments [42] revealed the possibility to gain higher densities if the position of the particle reentry is changed. By slight shifts of the plasma column, the plasma either hits the bumper limiter at the HFS or the limiter at the LFS. This is illustrated in Figure 6.4.

The charged particles inside the scrape-off layer (SOL) hit the limiter, recombine to neutrals and reenter the plasma mainly at the same position at a rate R_{rec}. Therefore the plasma shift determines whether the neutrals enter the plasma at the HFS or at the LFS. We want to simulate this experiment and compare the results with experimental observations.

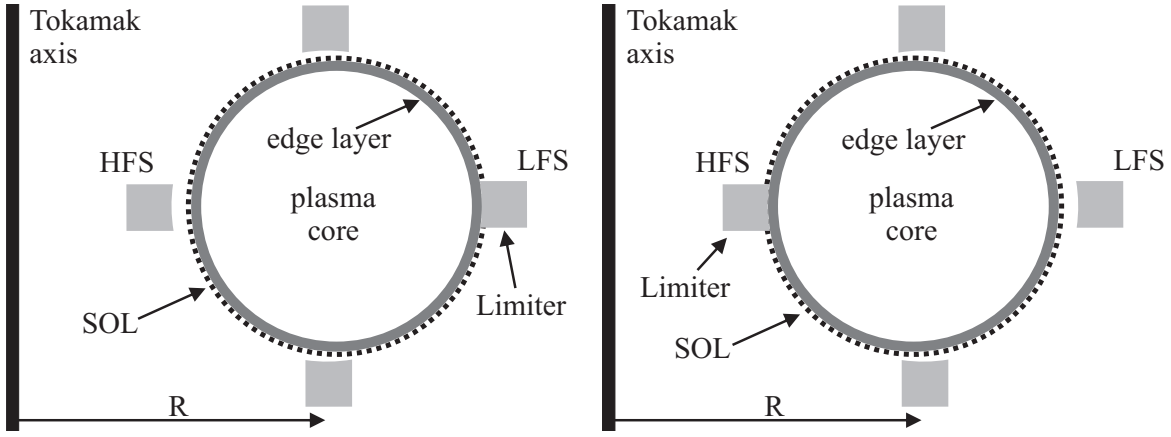

(a) Plasma column shifted to LFS, $\theta_{\mathrm{g}} = 0$

(b) Plasma column shifted to HFS, $\theta_{\mathrm{g}} = \pi$

Figure 6.4: A small shift of the plasma column to the LFS activates the scrape-off at the LFS (a) and vice versa (b). The charged particles inside the scrape-off layer (SOL) hit the limiter either at the HFS or at the LFS.

6.4.1 Modeling the physics

The total number of particles that enter the edge layer is

$$\Gamma_{\mathrm{tot}} = \frac{1}{2\pi} \int_0^{2\pi} \Gamma_{\perp}(\theta) \frac{d\sigma}{d\theta}(\theta)\, d\theta$$

and the position of scrape-off is θ_{g}. The reentry occurs at the same position with a Gaussian distribution of the particle positions

$$f_{\theta_{\mathrm{g}}} := \frac{2\pi \widehat{f}_{\theta_{\mathrm{g}}}}{\int_0^{2\pi} \widehat{f}_{\theta_{\mathrm{g}}} \frac{d\sigma}{d\theta}(\theta)\, d\theta}, \qquad \widehat{f}_{\theta_{\mathrm{g}}} := \exp\left(-\frac{\Big(((\theta - \theta_{\mathrm{g}} + \pi) \mod (2\pi)) - \pi \Big)^2}{\delta_{\mathrm{g}}^2} \right)$$

where δ_{g} is the standard deviation or width of the profile (see Figure 6.5).

The influx of neutrals,

$$J = \Gamma_{\mathrm{tot}} f_{\theta_{\mathrm{g}}},$$

complies to the global particle balance

$$\int_0^{2\pi} \Gamma_\perp \frac{d\sigma}{d\theta}(\theta)\, d\theta = \int_0^{2\pi} J \frac{d\sigma}{d\theta}(\theta)\, d\theta,$$

i.e., the number of particles leaving and entering the plasma is equal.

Using J one step of the linearized heat balance equation (6.2) is solved to obtain the new temperature T_{j+1}. The resulting density n_{j+1} is defined by the poloidal homogeneous pressure

$$p_k = T_k(\theta) n_k(\theta), \quad k \in \{j,\, j+1\} \tag{6.12}$$

and the fact that the total number of particles stays constant

$$\int_0^{2\pi} n_j(\theta) \frac{d\sigma}{d\theta}(\theta)\, d\theta = \int_0^{2\pi} n_{j+1}(\theta) \frac{d\sigma}{d\theta}(\theta)\, d\theta \tag{6.13}$$

without external sources or sinks.

From section 6.2.1 on page 89 the resulting density profile is known to be

$$n_{j+1}(\theta) = \frac{p_{j+1}}{T_{j+1}(\theta)} = \frac{1}{T_{j+1}(\theta)} \left(\int_0^{2\pi} n_j(\theta) \frac{d\sigma}{d\theta}(\theta)\, d\theta \right) \left(\int_0^{2\pi} \frac{1}{T_{j+1}(\theta)} \frac{d\sigma}{d\theta}(\theta)\, d\theta \right)^{-1}. \tag{6.14}$$

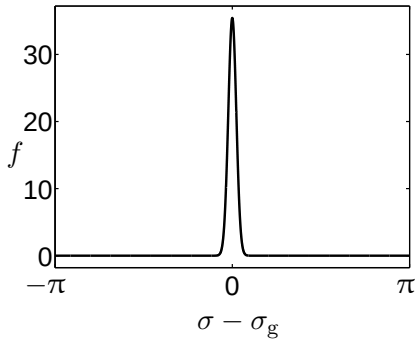

Figure 6.5: Distribution of the entry of neutral particles, $\delta_g = 0.1$.

6.4.2 Results of simulation

As an example, the TEXTOR high density discharges with MARFE have been simulated. The average density $\langle n \rangle$ is prescribed and the resulting profiles are calculated self consistently, one with the injection of neutrals at the LFS and the other one with injection at the HFS. The result is displayed in Figures 6.6 and 6.7. The normalization factor is $\phi_0 = 3.96$ and the method (1.) of section 6.3.4 on page 94 is applied with the integral formula approximated by the trapezoidal rule.

Figure 6.6(a) displays the temperature profile obtained for $\langle n \rangle \in \{4, 5, 6\} \cdot 10^{19}\,\mathrm{m}^{-3}$. With $\langle n \rangle = 4 \cdot 10^{19}\,\mathrm{m}^{-3}$ the temperature is slightly above 50 eV and nearly constant. Increasing the average density to $5 \cdot 10^{19}\,\mathrm{m}^{-3}$ triggers MARFE if the plasma column is shifted outwards to the LFS ($\theta_g = 0$) such that the neutrals enter the plasma at the LFS. However, the same density with the plasma shifted inwards ($\theta_g = \pi$) results in an almost constant profile close to 30 eV. Increasing the density even further to $\langle n \rangle = 6 \cdot 10^{19}\,\mathrm{m}^{-3}$ triggers MARFE for inward shifted plasma, too.

At the position where the temperature is low, there is a narrow spike of huge density as can be seen in Figure 6.6(b). The local increase of the density overcomes the density limit and triggers the MARFE.

The corresponding anomalous particle flux is shown in Figure 6.6(c). An almost constant flux profile in the range of $[1.5, 2] \cdot 10^{21}\,\mathrm{m}^{-2}\mathrm{s}^{-1}$ is obtained for $\langle n \rangle = 4 \cdot 10^{19}\,\mathrm{m}^{-3}$. When the average density increases the minimum of the anomalous particle flux lowers and the maximum rises. A ballooning structure evolves. Due to a temperature close to zero at the LFS the ion larmor radius $\rho_\mathrm{i} \propto \sqrt{T}$ decreases and causes the anomalous particle flux to become a narrow local minimum at this position.

The energy losses due to convection are proportional to the anomalous particle flux which explains the drop of the temperature and the increase of the density at the LFS. Additionally there is the poloidal inhomogeneity of the heat flux from plasma core that causes the heating to be stronger at the LFS than at the HFS. Both effects are contrary and for a quantitative investigation, the profiles of the losses and the heating from core are displayed in Figure 6.7. We will come back to this topic at the end of this section.

In the temporal evolution of the self consistent profile iteration with the outward shifted plasma at $\langle n \rangle = 5 \cdot 10^{19}\,\mathrm{m}^{-3}$, there is a distinct instant where the temperature drops at the LFS and the density strongly increases. At this instant the anomalous transport $\Gamma_\perp$ increases so rapidly, that the profile iteration would run into negative temperatures without a simultaneous damping attack by the dynamic damping strategy due to the trust region approach (cf. Figure 6.1(d)).

The lower temperature reduces the anomalous particle flux until the state of equilibrium is reached. However, the neighborhood of the state of equilibrium is not very stable and the damping mechanism has ensure to neither over damp the system nor to under damp it. Over damping will cause the number of profile iterations to increase and under damping leads to oscillations that can destroy the convergence completely.

The result of our simulation on increasing the average density $\langle n \rangle$ is that MARFE is triggered at lower averaged density $\langle n \rangle$ with outward shifted plasma than with the inward shifted plasma column. This is the converse of what is explored in experiments at TEXTOR [26]. Next, we try to analyze how the result of our simulation is composed.

The reason for the poloidal temperature profiles in the simulation becomes obvious concerning the heat balance in Figure 6.7. The Shafranov shift of $\Delta_1 = 0.5$ cannot compensate the large losses at the LFS due to the ballooning structure (ce_{02}) of the anomalous transport. The losses overcome the heating power from the plasma core and the temperature drops. At the HFS it is the other way round. The losses from the anomalous particle flux are smaller than the heating power. Hence, additional energy losses by ionization of an influx of neutrals is less dangerous for the plasma stability at the HFS than at the LFS.

The simulation has been repeated with a more pronounced Shafranov shift $\Delta_1 = 0.99$, but the result is qualitatively equal to the one with $\Delta_1 = 0.5$. The deduction of this analysis points out the fact, that a better heat flux model is needed in order to obtain realistic results. The simple low order approximation by the cosine shape is not sufficient. The processes in the plasma core that lead to inhomogeneous radial heat transport from the core like the temperature gradient mode have not been considered in our model and might be the reasons for the discrepancy.

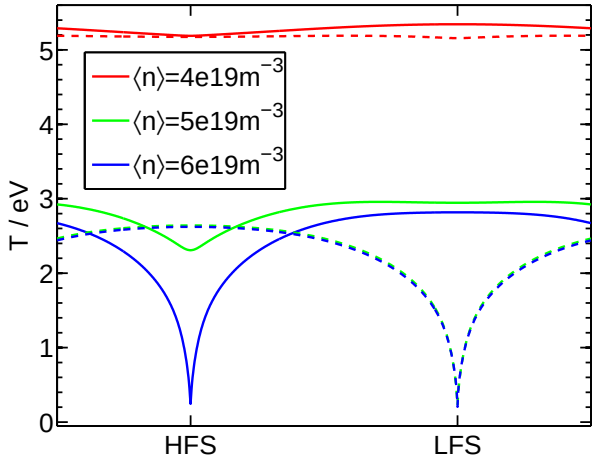

(a) temperature profiles

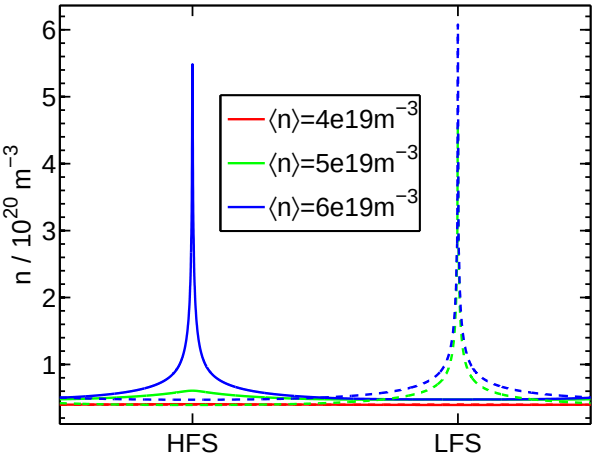

(b) density profiles

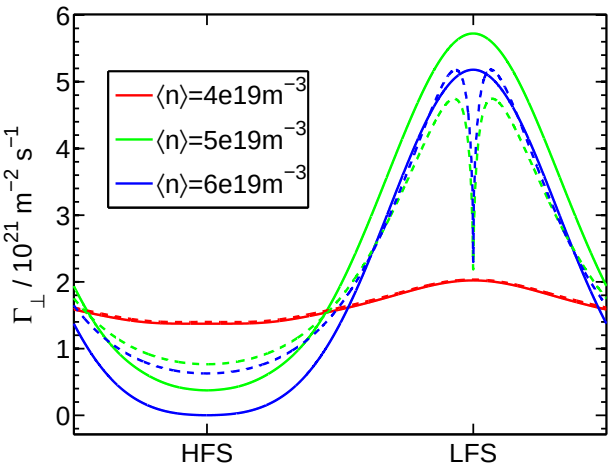

(c) anomalous particle flux profiles

Figure 6.6: The plasma shift simulation with the injection of neutrals at the HFS ($\theta_g = \pi$) (solid line) and the LFS ($\theta_g = 0$) (broken line) for prescribed average density $\langle n \rangle \in \{4, 5, 6\} \cdot 10^{19}\,\mathrm{m}^{-3}$. At $\langle n \rangle = 4{\cdot}10^{19}\,\mathrm{m}^{-3}$ the plasma profiles of temperature and density are almost constant. At $\langle n \rangle = 5{\cdot}10^{19}\,\mathrm{m}^{-3}$ MARFE occurs by the LFS injection, while the profile is still almost constant by the HFS injection. Increasing the average density to $\langle n \rangle = 6 \cdot 10^{19}\,\mathrm{m}^{-3}$ triggers MARFE at the HFS injection, as well.

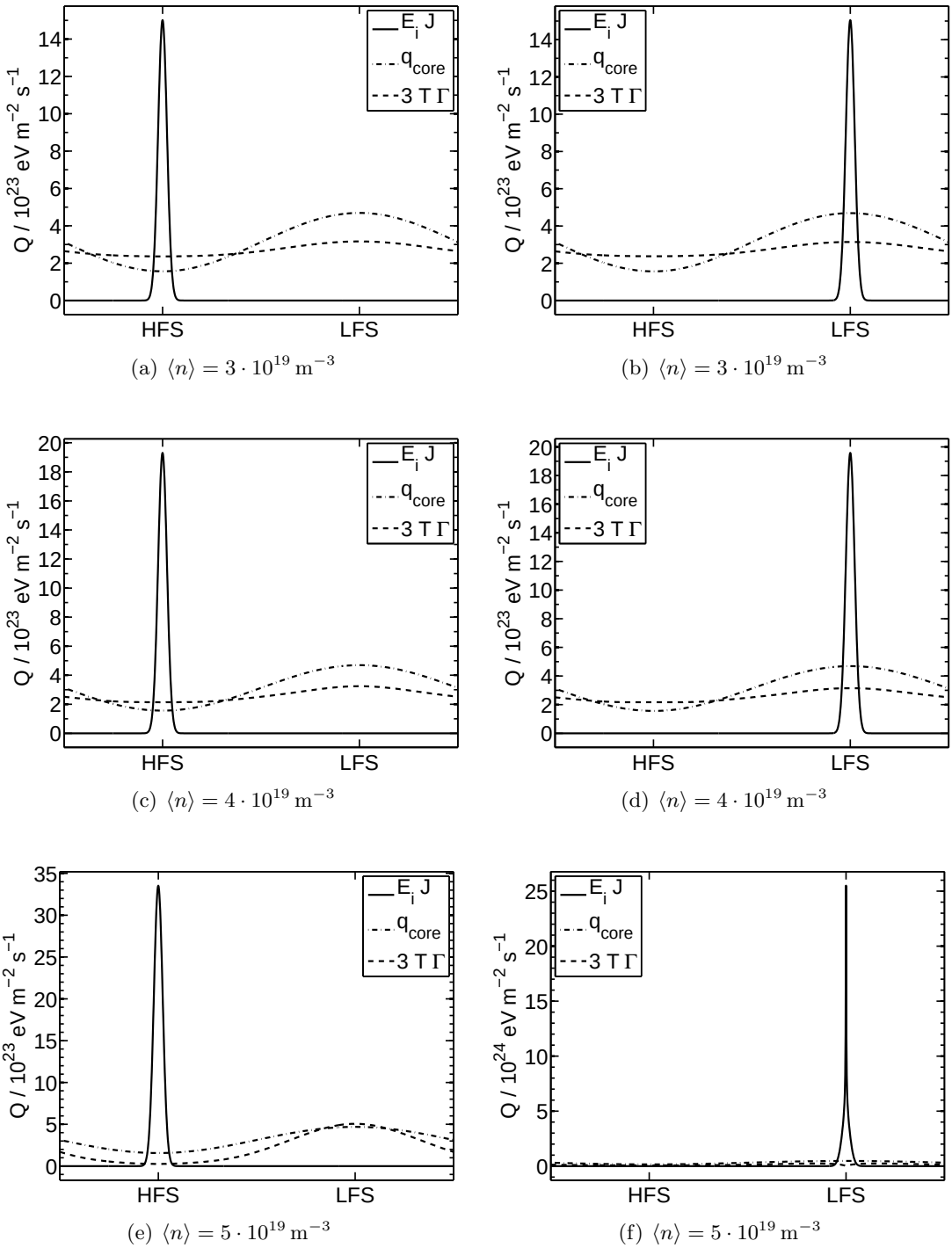

(a) $\langle n \rangle = 3 \cdot 10^{19}\,\mathrm{m}^{-3}$

(b) $\langle n \rangle = 3 \cdot 10^{19}\,\mathrm{m}^{-3}$

(c) $\langle n \rangle = 4 \cdot 10^{19}\,\mathrm{m}^{-3}$

(d) $\langle n \rangle = 4 \cdot 10^{19}\,\mathrm{m}^{-3}$

(e) $\langle n \rangle = 5 \cdot 10^{19}\,\mathrm{m}^{-3}$

(f) $\langle n \rangle = 5 \cdot 10^{19}\,\mathrm{m}^{-3}$

Figure 6.7: The heat balance of the plasma shift simulation with the neutrals entering at the HFS $\theta_\mathrm{g} = \pi$ (left column) or at the LFS $\theta_\mathrm{g} = 0$ (right column).

6.4.3 Influence of plasma inhomogeneity on the growth rate of the perturbation envelope

In addition to the heat balance another effect is revealed. To demonstrate it, we evaluate the eigenvalue equation with three different constellations of the plasma parameter profiles. The first profile is with pronounced MARFE located at the HFS, the second profile is the same but shifted by π such that the MARFE is located at the LFS and the third profile consists of poloidally averaged plasma parameters. These profiles are plotted in Figure 6.8(a).

For each of the three profiles, the eigenvalue equation is solved for several wave numbers and for the pressure $p = 1.7043 \cdot 10^{21}\,\mathrm{eV\,m^{-3}}$. The $K_\perp$ spectra of the growth rate is plotted in Figure 6.8(b). While the profile of averaged plasma parameters and the profile with the MARFE at the HFS have a spectra distributed Maxwellian like and the profile with the MARFE at the LFS results in a strongly localized spectra of twice the maximal growth rate.

The profile of the anomalous particle flux in Figure 6.8(c) is always minimal at the HFS and maximal at the LFS. A local drop occurs at the position of the lowest temperature due to the larmor radius ρ_i in the flux formula ((3.22)) that depends on the square root of the temperature. The total amount of the anomalous particle flux is maximal if the MARFE is located at the LFS and minimal if the MARFE is located at the HFS. The constant temperature profile of average value results in an anomalous particle flux of intermediate size.

These simulations clearly show that the growth rate of the perturbation as well as the resulting anomalous particle flux strongly depend on the position of the MARFE. Therefore, situations with very pronounced inhomogeneities require to calculate the eigenvalue equation with inhomogeneous profiles rather than averaging them as it has been done previously in [38].

The ballooning instability is invoked much stronger if the MARFE evolves at the LFS than at the HFS. This explains the outcome of the plasma shift experiment. The local injection of the neutrals cools down the plasma at the position of injection. If the cooling overcomes the heating from the plasma core and the parallel heat transport, a local drop occurs. If this drop occurs at the LFS the ballooning instability is triggered to become strongly dominant and the losses increase at the LFS and reinforces the drop of temperature until the MARFE is evolved.

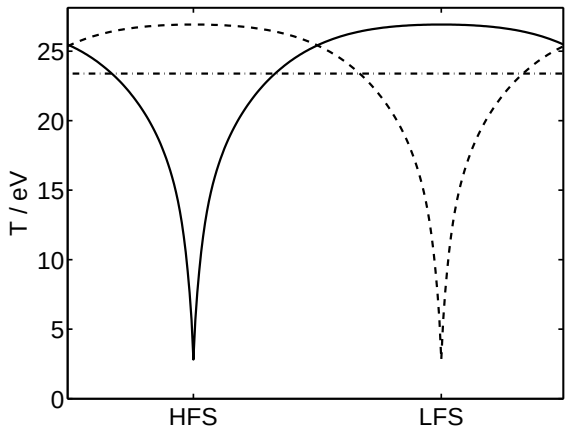

(a) Temperature profile with MARFE at different positions

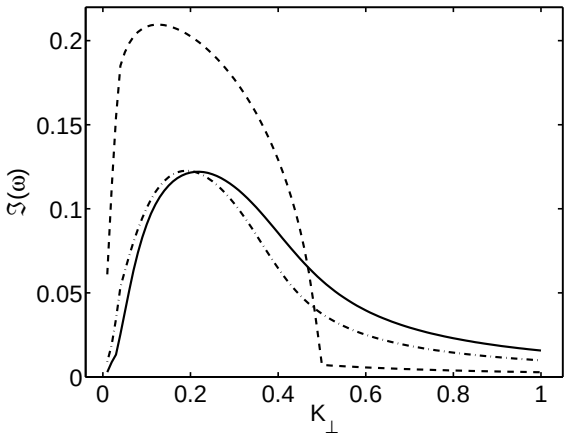

(b) $K_\perp$ spectra of profiles provided in (a)

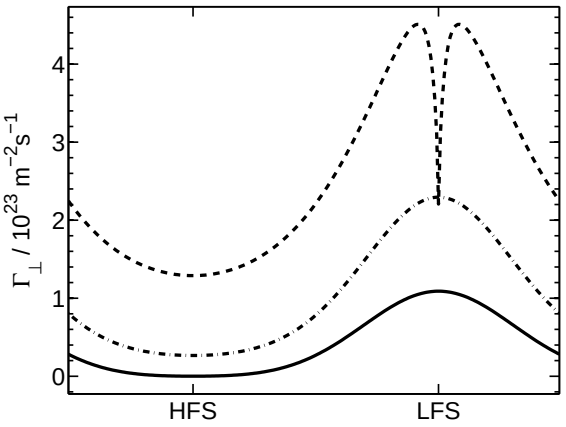

(c) anomalous particle flux

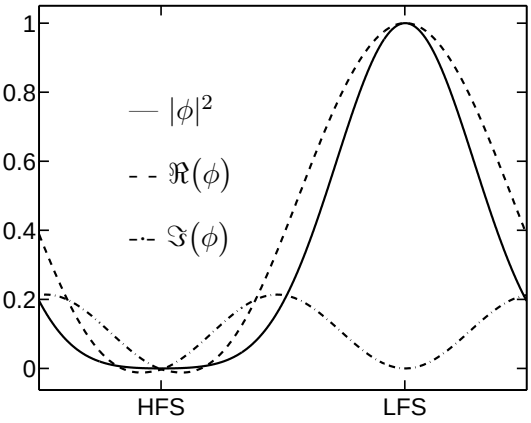

(d) $|\phi|^2$ of MARFE at the HFS

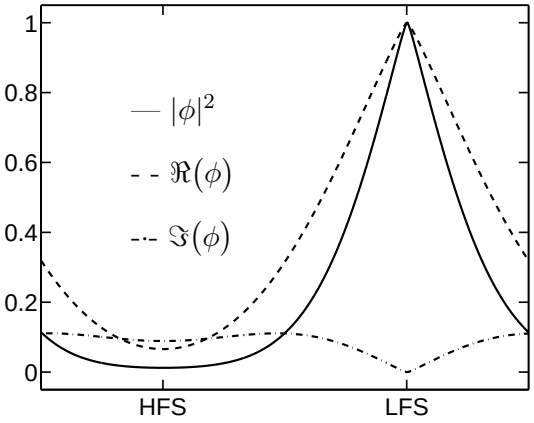

(e) $|\phi|^2$ of MARFE at the LFS

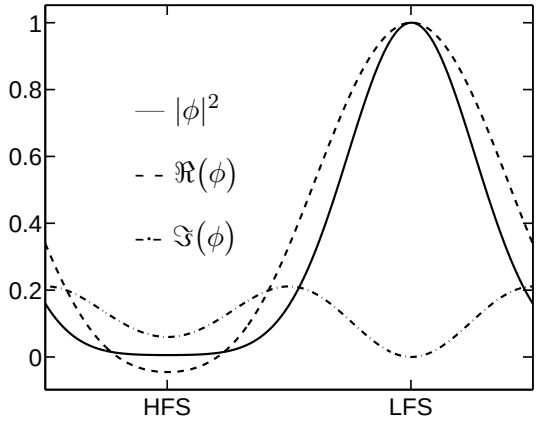

(f) $|\phi|^2$ of average temperature profile

Figure 6.8: Figure (a) shows three temperature profiles. The solid line is MARFE at the HFS and the dashed line is MARFE at the LFS. Both profiles are identical, but shifted poloidal by π. The third profile (dash dotted line) is the average value of the other ones. The eigenvalue equation is solved at several wave numbers with the profiles displayed in (a) where the pressure is $p = 1.7043 \cdot 10^{21}$ eV m^{-3}. The $K_\perp$ spectra is displayed in (b). The spectra of the profile with MARFE at the HFS and the averaged profile are very similar Maxwell distributions. The spectra of the profile with MARFE at the LFS has a growth rate of twice as much and its slope is very steep close to zero and at $K_\perp = 0.5$. (c) The amount of the anomalous particle flux $\Gamma_\perp$. It is smallest at the HFS and largest at the LFS with a local drop at the position where the MARFE is located. The dashed lined profile has the largest total anomalous particle flux and the solid lined profile is of the smallest. (d-f) The associated eigenfunctions (ce_{02}) at the wave number $K_\perp$ with maximal growth rate.

6.4.4 Results with a more realistic core heat profile

In the previous section one simulation has been illustrated that contradicted the experimental observation. Throughout the analysis for the specific behavior, the heat balance turned out to be the reason. The heat flux profile g is $g_1(\theta) = 1 + \Delta_1 \cos(\theta)$ which is a very rough approximation. However, the radial heat flow goes with $\exp(-d^2)$, where d is the distance between the plasma core and the specific position in the edge layer. On the other hand there is a heat flow parallel to the magnetic field lines which lowers the inhomogeneity. Additionally, the temperature gradient modes can cause an inhomogeneous heat flux, too. Since there is no realistic physical model available so far,

$$g(\theta) = a \exp(-d(\theta)^2/b) + c, \qquad a, b, c \in \mathbb{R}, a, b > 0 \tag{6.15}$$

is used in this section. A comparison of several heat flux profiles is displayed in Figure 6.9.

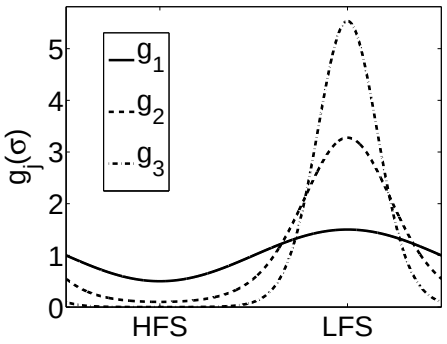

Figure 6.9: Three heat flux distributions from core heating. $g_1(\theta) = 1 + \Delta_1 \cos(\theta)$ is the one proposed in [38]. g_2 and g_3 are derived from the approach $g = a \exp(-d^2/b) + c$, where d is the distance between the plasma core and the edge. $a, b, c \in \mathbb{R}$ with $a, b > 0$. The poloidal average of g is normalized to one.

The simulation is computed with the heat flux profile g_2 again. The plasma profiles are shown in Figure 6.10 and now the MARFE occurs at smaller average density with inward shifted ($\theta_g = \pi$) plasma column. This complies to the experimental observation. The growth rate is still stronger with the MARFE at the LFS (Figure 6.12), but now the heat balance (Figure 6.14) compensates the stronger losses at the LFS. The dependence on the average density can be explored in Figure 6.11. The density limit is slightly higher compared to the experimental values in [38]. This can be explained by the fact, that the impurity sputtering is not included in the model.

At an average density of $\langle n \rangle \leq 4 \cdot 10^{19}\,\mathrm{m}^{-3}$ the eigenfunction ce_{01} is dominant (cf. Figures 6.12 and 6.13) and at higher average density the ballooning eigenfunction ce_{02} becomes dominant.

Figure 6.11 shows that the growth rate and the anomalous diffusivity

$$D_\perp = \frac{\Im(\omega)^3}{|\omega|^2} \propto \Gamma_\perp$$

slightly increase if the MARFE is triggered at the HFS. However, when the MARFE occurs at the LFS these quantities abruptly increase and make the discharge more unstable. This can be explained by the drift resistive ballooning instability that is most unstable at the LFS. By the injection of neutrals at the LFS the ballooning character is enhanced due to the higher density and, hence, the maximum of the density is greater with inward shifted plasma.

Within this simulation, the pseudo spectral method is used to discretize the derivatives. The number of the profile iterations, the evaluations of the eigenvalue equation and the average search space dimension in the multilevel Jacobi-Davidson algorithm are listed in Table 6.1 for the inward shifted plasma and in Table 6.2 for the outward shifted plasma. The average search

space dimension is below 3, which is remarkably good and shows that the multilevel Jacobi-Davidson method is very efficient. The search space dimension reduces at higher resolution, except for the case of a very pronounced density inhomogeneity where very high frequencies are present in the eigenfunction.

Figure 4.3 displays the Fourier decomposition of the eigenfunctions that result with the plasma parameters almost constant (gray) and strongly inhomogeneous (black). The modulus of the Fourier coefficients α_j reduces with increasing $|j|$. This means that the low frequencies are most important and it explains the success of the multilevel Jacobi-Davidson strategy. The eigenfunction of the almost constant plasma parameters mainly consists of frequencies $|j| < 100$ and the eigenfunction of the strongly inhomogeneous profile requires much higher frequencies.

For almost constant plasma profiles, the final dimension of the search space at a higher level of resolution is one. The eigenvalue is improved by solving the projected eigenvalue polynomial, which is a mere cubic polynomial now. Thus the projected eigenvalue problem is equivalent to calculating the roots of this polynomial. The stopping criterion is fulfilled and the eigenvector remains the prolonged coarse grid approximation and the effort with the correction equation is completely avoided.

$\langle n \rangle / \mathrm{m}^{-3}$	$3 \cdot 10^{19}$	$4 \cdot 10^{19}$	$5 \cdot 10^{19}$	$6 \cdot 10^{19}$	$7 \cdot 10^{19}$
number of profile iteration	220	282	36	97	549
evaluations of eigenvalue equation	1881	1980	792	1683	3762
average JD iterations at $N = 1024$	1.00	1.00	1.00	1.00	3.00
average JD iterations at $N = 512$	1.00	1.00	1.00	1.00	3.00
average JD iterations at $N = 256$	1.00	1.00	1.00	1.00	3.00
average JD iterations at $N = 128$	1.00	1.04	1.44	2.00	3.00
average JD iterations at $N = 64$	1.25	1.81	2.00	2.00	3.00
average JD iterations at $N = 32$	1.62	2.00	2.00	2.84	3.00
computation time / minutes:seconds	02:42	03:10	01:16	02:55	16:58

Table 6.1: Plasma shift simulation to the HFS ($\theta_\mathrm{g} = \pi$): The number of the profile iterations, the evaluations of the eigenvalue equation and the average number of The Jacobi-Davidson (JD) iterations on each level of resolution in the multilevel approach. The eigenvalue equation is solved on $N = 16$ grid points by the QZ algorithm. The eigenpair of interest is improved on $N = 32, 64, 128, 256, 512$ and $N = 1024$. The derivatives are approximated by the pseudo spectral method. The precision of the profiles is $|F(T_j) - T_j| < 10^{-3}$.

$\langle n \rangle / \mathrm{m}^{-3}$	$3 \cdot 10^{19}$	$4 \cdot 10^{19}$	$5 \cdot 10^{19}$	$6 \cdot 10^{19}$	$7 \cdot 10^{19}$
number of profile iteration	236	255	37	25	2000
evaluations of eigenvalue equation	1980	1782	693	495	15635
average JD iterations at $N = 1024$	1.00	1.00	1.00	1.00	1.00
average JD iterations at $N = 512$	1.00	1.00	1.00	1.00	1.00
average JD iterations at $N = 256$	1.00	1.00	1.00	1.00	2.00
average JD iterations at $N = 128$	1.00	1.00	1.48	2.00	2.00
average JD iterations at $N = 64$	1.17	1.65	2.00	2.00	2.54
average JD iterations at $N = 32$	1.51	2.00	2.00	2.50	2.65
computation time / minutes:seconds	02:49	02:49	01:10	00:45	40:26

Table 6.2: Plasma shift simulation to the LFS ($\theta_\mathrm{g} = 0$). See Table 6.1 for further explanations.

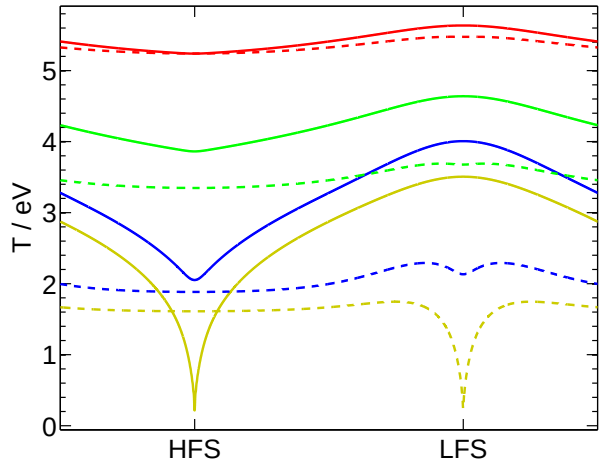

(a) temperature profiles

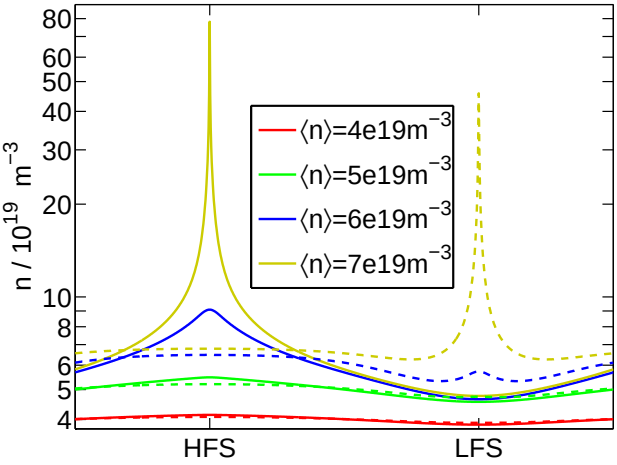

(b) density profiles

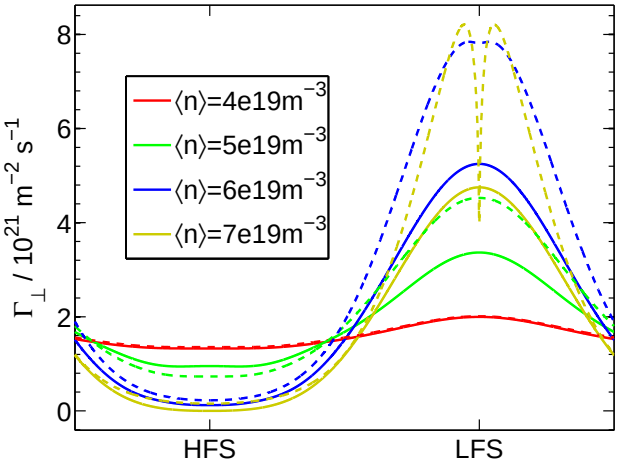

(c) anomalous particle flux profiles

Figure 6.10: Plasma profiles of plasma shift simulation with core heat flux profile g_2. Simulated is inward shifted plasma $\theta_g = \pi$ (HFS) (solid line) and outward shifted one $\theta_g = 0$ (LFS) (broken line). The average densities are $\langle n \rangle \in \{5, 7, 8, 10\} \cdot 10^{19}\,\mathrm{m}^{-3}$. See also Figure 6.11.

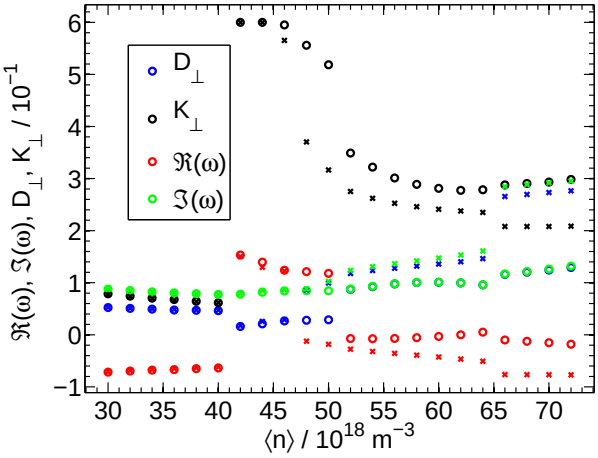

(a) wave number $K_\perp$ and eigenvalue ω

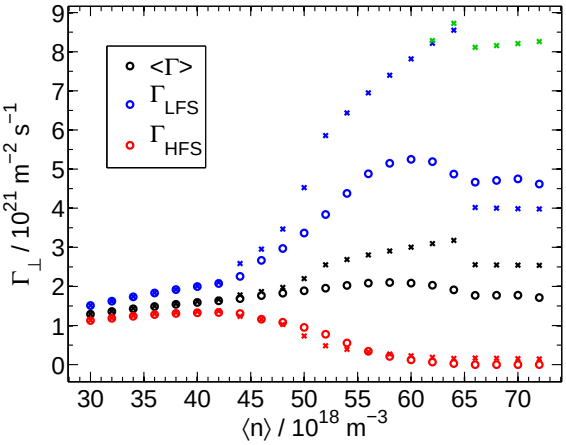

(b) anomalous particle flux $\Gamma_\perp$

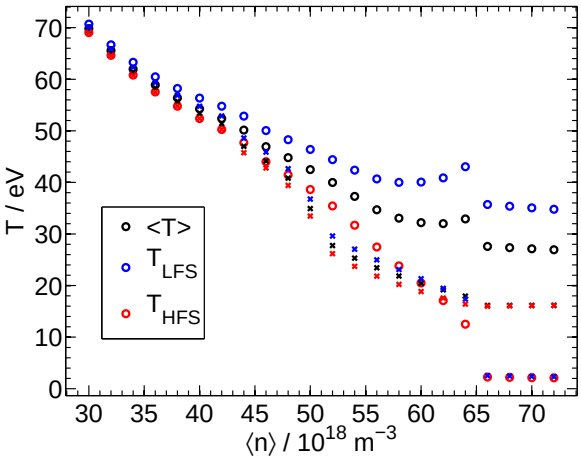

(c) temperature T

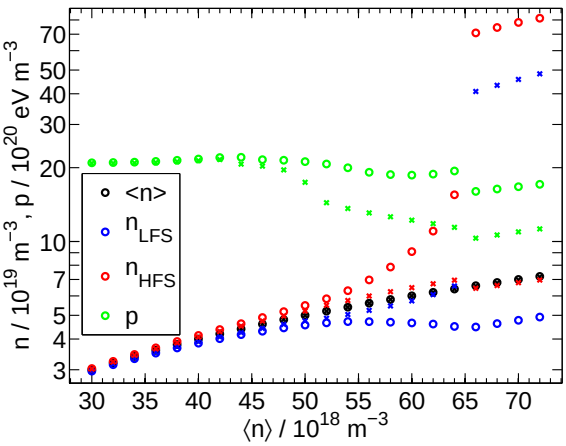

(d) density n and pressure p

Figure 6.11: Plasma shift simulation. Dependency of plasma quantities on the average density with core heat flux profile g_2. Simulated is inward shifted plasma $\theta_g = \pi$ (HFS) (open circles) and outward shifted one $\theta_g = 0$ (LFS) (x-marks). In (a) $K_\perp := \text{argmax}_{K_\perp} \Im(\omega)$ is displayed. The green x-marks in (b) are the maximum of $\Gamma_\perp$ when a local drop occurs at the LFS due to the temperature decline at this position. Angular profiles are shown in Figure 6.10.

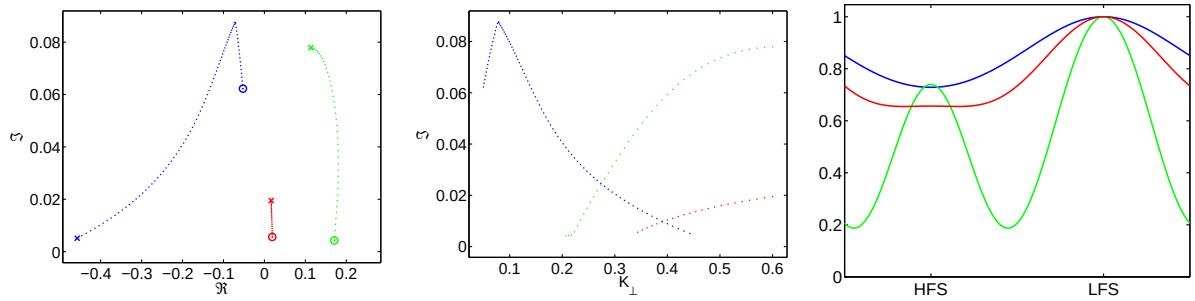

(a) $\langle n \rangle = 3 \cdot 10^{19}\,\mathrm{m}^{-3}$ (b) $\langle n \rangle = 3 \cdot 10^{19}\,\mathrm{m}^{-3}$ (c) $\langle n \rangle = 3 \cdot 10^{19}\,\mathrm{m}^{-3}$

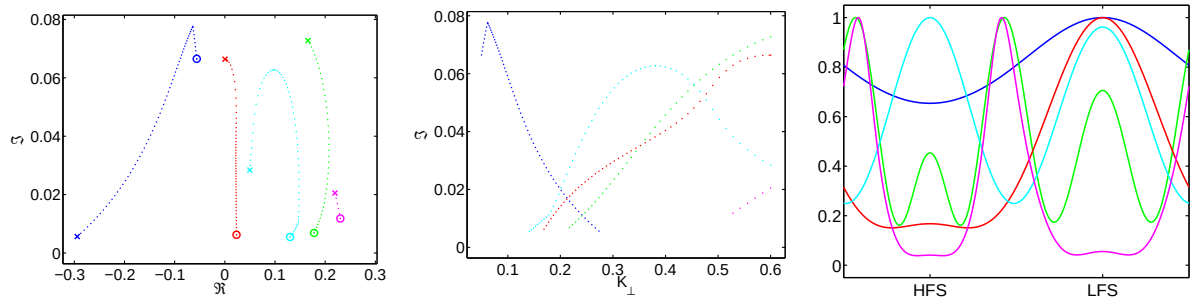

(d) $\langle n \rangle = 4 \cdot 10^{19}\,\mathrm{m}^{-3}$ (e) $\langle n \rangle = 4 \cdot 10^{19}\,\mathrm{m}^{-3}$ (f) $\langle n \rangle = 4 \cdot 10^{19}\,\mathrm{m}^{-3}$

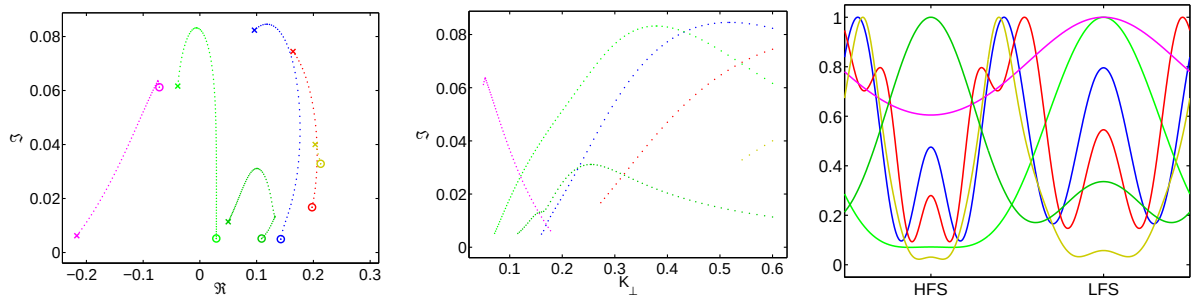

(g) $\langle n \rangle = 5 \cdot 10^{19}\,\mathrm{m}^{-3}$ (h) $\langle n \rangle = 5 \cdot 10^{19}\,\mathrm{m}^{-3}$ (i) $\langle n \rangle = 5 \cdot 10^{19}\,\mathrm{m}^{-3}$

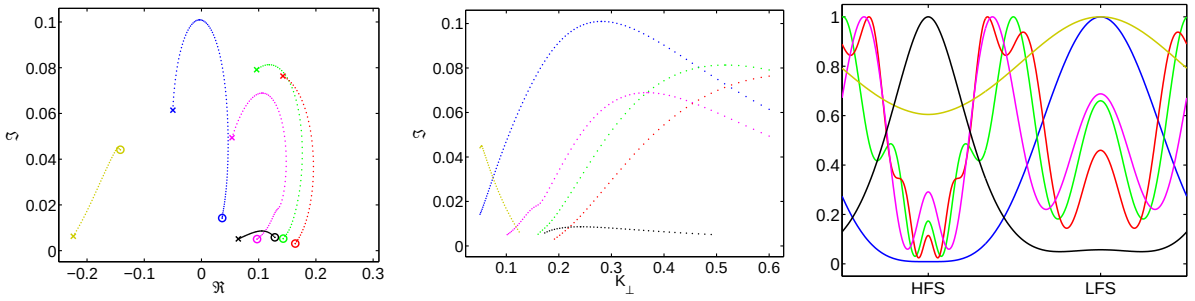

(j) $\langle n \rangle = 6 \cdot 10^{19}\,\mathrm{m}^{-3}$ (k) $\langle n \rangle = 6 \cdot 10^{19}\,\mathrm{m}^{-3}$ (l) $\langle n \rangle = 6 \cdot 10^{19}\,\mathrm{m}^{-3}$

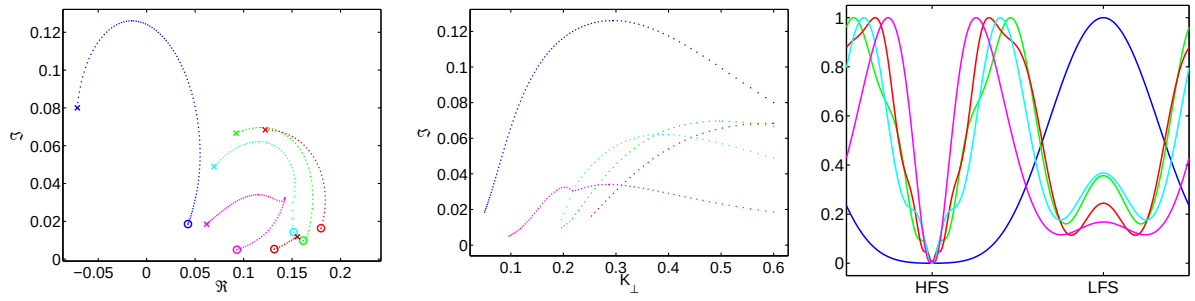

(m) $\langle n \rangle = 7 \cdot 10^{19}\,\mathrm{m}^{-3}$ (n) $\langle n \rangle = 7 \cdot 10^{19}\,\mathrm{m}^{-3}$ (o) $\langle n \rangle = 7 \cdot 10^{19}\,\mathrm{m}^{-3}$

Figure 6.12: The eigenpairs of the plasma shift simulation to the HFS are displayed, where the plasma parameters are taken from the converged profiles. Each row displays the eigenvalues, the $K_\perp$ spectra and the intensity of the eigenfunction for several eigenpairs at the specific prescribed level of the average density $\langle n \rangle$. Within each row the color specifies the mode and the eigenfunction is taken at the wave number, where the growth rate is maximal. The kink in the eigenvalue path corresponds to the non-differential position in the γ factor within the eigenvalue equation. The open circle marks the eigenvalue that belongs to the smallest wave number and the x-mark marks the eigenvalue at the largest wave number.

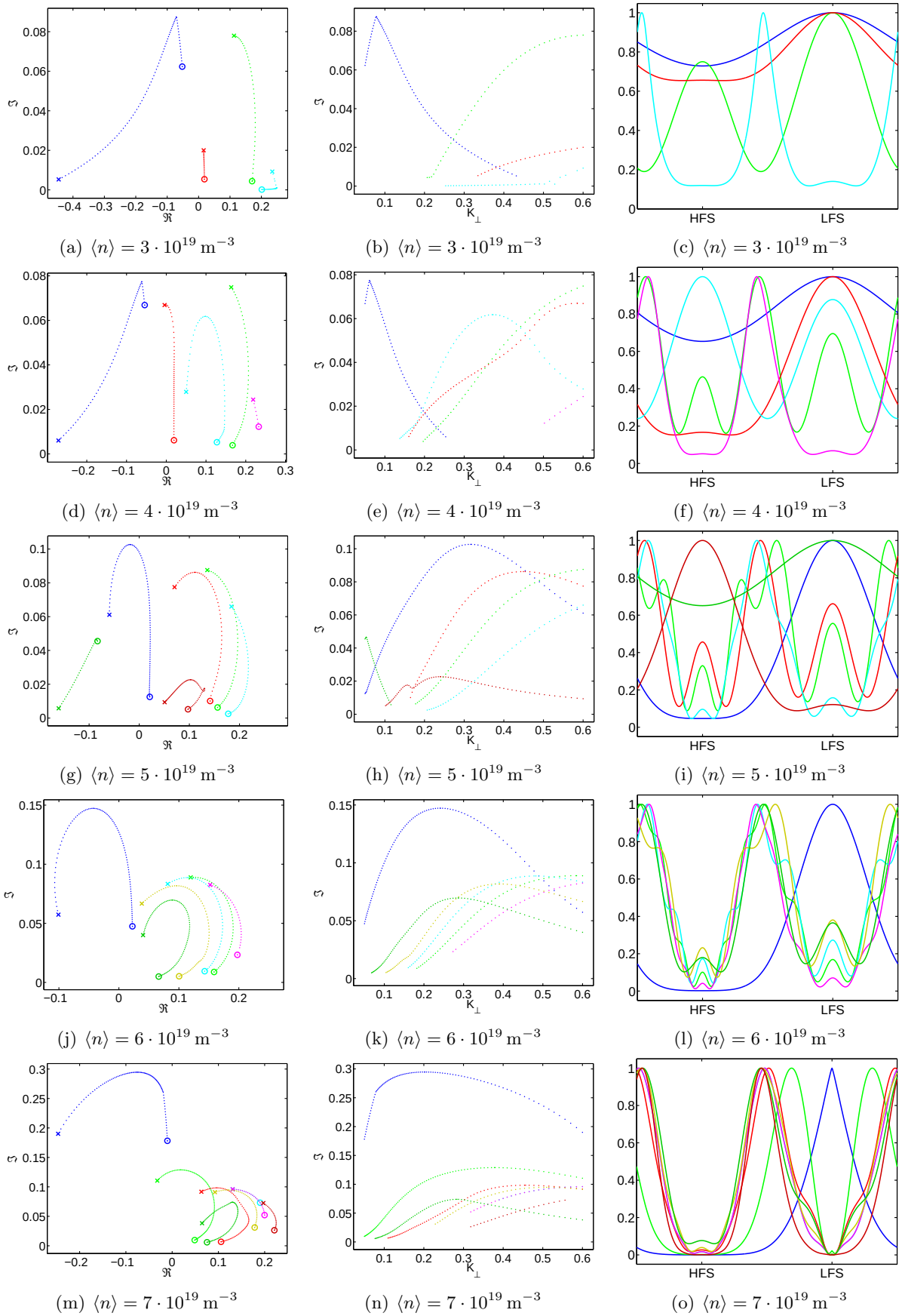

(a) $\langle n \rangle = 3 \cdot 10^{19}\,\mathrm{m}^{-3}$ (b) $\langle n \rangle = 3 \cdot 10^{19}\,\mathrm{m}^{-3}$ (c) $\langle n \rangle = 3 \cdot 10^{19}\,\mathrm{m}^{-3}$

(d) $\langle n \rangle = 4 \cdot 10^{19}\,\mathrm{m}^{-3}$ (e) $\langle n \rangle = 4 \cdot 10^{19}\,\mathrm{m}^{-3}$ (f) $\langle n \rangle = 4 \cdot 10^{19}\,\mathrm{m}^{-3}$

(g) $\langle n \rangle = 5 \cdot 10^{19}\,\mathrm{m}^{-3}$ (h) $\langle n \rangle = 5 \cdot 10^{19}\,\mathrm{m}^{-3}$ (i) $\langle n \rangle = 5 \cdot 10^{19}\,\mathrm{m}^{-3}$

(j) $\langle n \rangle = 6 \cdot 10^{19}\,\mathrm{m}^{-3}$ (k) $\langle n \rangle = 6 \cdot 10^{19}\,\mathrm{m}^{-3}$ (l) $\langle n \rangle = 6 \cdot 10^{19}\,\mathrm{m}^{-3}$

(m) $\langle n \rangle = 7 \cdot 10^{19}\,\mathrm{m}^{-3}$ (n) $\langle n \rangle = 7 \cdot 10^{19}\,\mathrm{m}^{-3}$ (o) $\langle n \rangle = 7 \cdot 10^{19}\,\mathrm{m}^{-3}$

Figure 6.13: The eigenpairs of the plasma shift simulation to the LFS are displayed, where the plasma parameters are taken from the converged profiles. Each row displays the eigenvalues, the $K_\perp$ spectra and the intensity of the eigenfunction for several eigenpairs at the specific prescribed level of the average density $\langle n \rangle$. Within each row the color specifies the mode and the eigenfunction is taken at the wave number, where the growth rate is maximal. The kink in the eigenvalue path corresponds to the non-differential position in the γ factor within the eigenvalue equation. The open circle marks the eigenvalue that belongs to the smallest wave number and the x-mark marks the eigenvalue at the largest wave number.

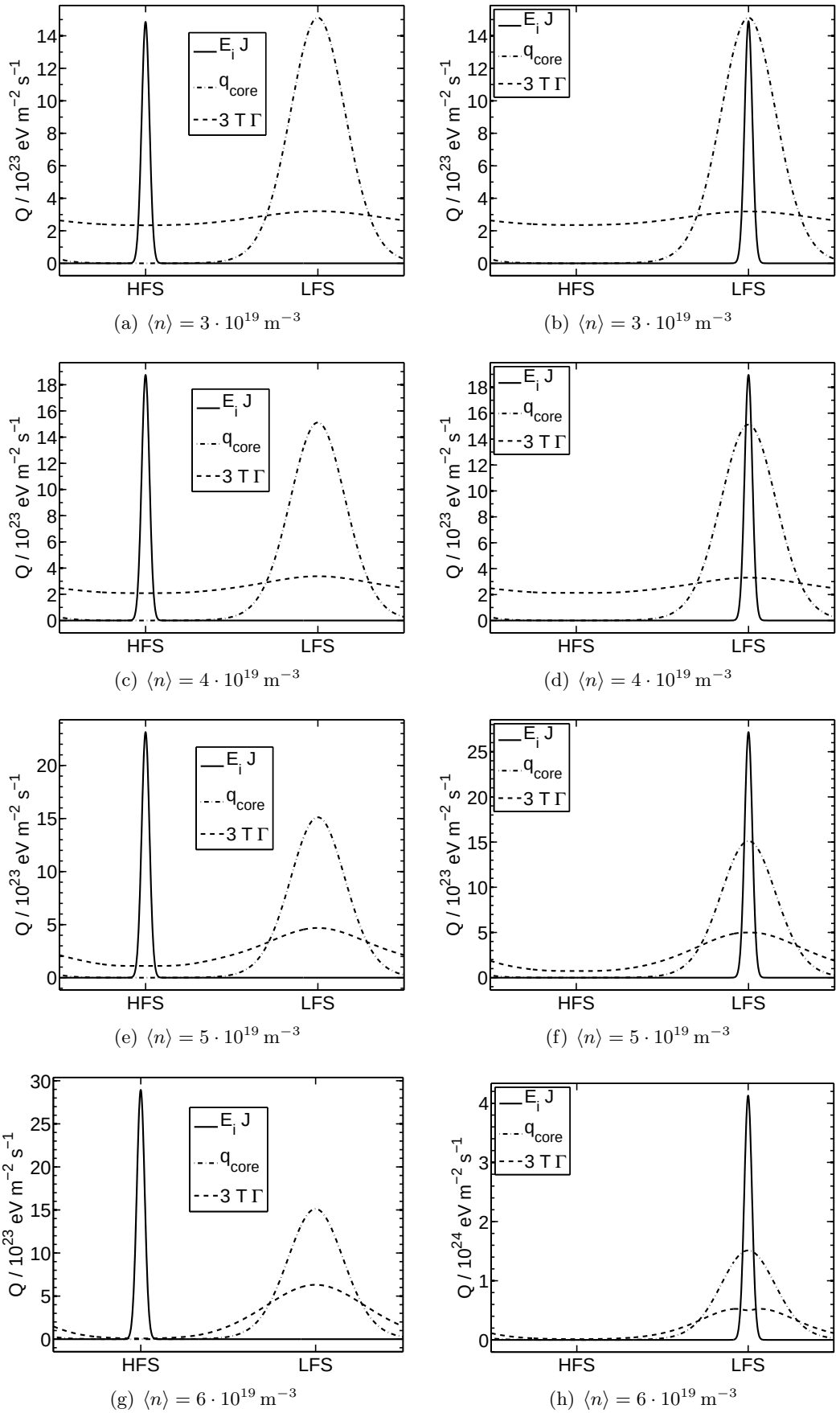

(a) $\langle n \rangle = 3 \cdot 10^{19}\,\mathrm{m}^{-3}$ (b) $\langle n \rangle = 3 \cdot 10^{19}\,\mathrm{m}^{-3}$

(c) $\langle n \rangle = 4 \cdot 10^{19}\,\mathrm{m}^{-3}$ (d) $\langle n \rangle = 4 \cdot 10^{19}\,\mathrm{m}^{-3}$

(e) $\langle n \rangle = 5 \cdot 10^{19}\,\mathrm{m}^{-3}$ (f) $\langle n \rangle = 5 \cdot 10^{19}\,\mathrm{m}^{-3}$

(g) $\langle n \rangle = 6 \cdot 10^{19}\,\mathrm{m}^{-3}$ (h) $\langle n \rangle = 6 \cdot 10^{19}\,\mathrm{m}^{-3}$

Figure 6.14: The heat balance from the plasma shift simulation where the neutrals enter the plasma at the HFS $\theta_\mathrm{g} = \pi$ (left column) and at the LFS $\theta_\mathrm{g} = 0$ (right column). Due to the heat profile g_2 the heat influx at the LFS is much greater than the convective losses $3\Gamma_\perp T$ and hence it can withstand the additional cooling by the ionization $E_\mathrm{i} J$ at the same position with the outward shifted plasma column.

6.5 Gas puffing simulation

Another interesting experiment that we want to simulate is the impact of the position where the fueling gas is puffed into the plasma. The physical modeling has already been done in section 3.3 on page 44. In experiments [6, 9] the influence of poloidal puffing position on the L-H transition in the Tokamak MAST has been investigated. The L mode is a state of the low confinement and the H mode is a state of high confinement. We do not discuss this in detail because a modeling of the H mode requires to include the radial direction within the calculation, but one can remember that improving the confinement, reduces the losses ($\Gamma_\perp$).

Remark 6.4. One comment is necessary: due to the one-dimensional model, the gas puff simulation describes a toroidal symmetric puffing, which is very difficult to realize in experiments. In the experiment a nozzle is build into the vessel and therefore the influx of the gas is distributed by a poloidal and toroidal profile. Nevertheless, the idealized case of a toroidal homogeneous gas puff has been simulated and the results are discussed below.

We start the gas puff simulation with the puffing position at the LFS and at the HFS. The normalization factor is $\phi_0 = 0.37$. In order to take the impact of the plasma parameters in the edge layer on the anomalous transport in the deeper regions into account, the heat flux profile from the plasma core is modeled as

$$g(\theta) = \frac{\Gamma_\perp(\theta) + \xi\langle\Gamma_\perp\rangle}{\langle\Gamma_\perp\rangle(1+\xi)}, \qquad \xi = 0.08.$$

The puffing intensity is set to $\Phi_{\text{gas}} = 1 \cdot 10^{19}\,\text{m}^{-2}\,\text{s}^{-1}$ which is slightly below the reference value $\Phi_{\text{exp}} = 1.2 \cdot 10^{19}\,\text{m}^{-2}\,\text{s}^{-1}$. The self consistent calculation is iterated until $|F(T_j, p_j) - (T_j, p_j)|$ is below 10^{-3}. Then the gas puff intensity is increased and the self consistent iteration is continued with the result of the previous one.

At a low puffing rate $\Phi_{\text{gas}} \in [1, 2] \cdot 10^{19}\,\text{m}^{-2}\,\text{s}^{-1}$ the profiles of the temperature and the density are nearly constant and close to the experimental values in Table 3.1 on page 45. The outflow $\Gamma_\perp$ is about ten times larger than the inflow Φ_{gas},

$$\Gamma_\perp \approx 10\Phi_{\text{gas}}.$$

$R_{\text{Rec}} = 0.9$ particles of the anomalous particle flux return back into the plasma, thus,

$$(1 - R_{\text{Rec}})\Gamma_\perp \approx \Phi_{\text{gas}}$$

holds. However, the outflow is slightly larger than the inflow which causes the pressure to decrease slowly with increasing Φ_{gas}.

The total heating power from the plasma core is assumed to be constant in our simulation and therefore the increase of the neutral particle source due to the gas puff and the return current causes the heat losses to increase and the temperature to decrease.

At a gas puffing intensity $\Phi_{\text{gas}} = 2.4 \cdot 10^{19}\,\text{m}^{-2}\,\text{s}^{-1}$ with the puffing position at the LFS or $\Phi_{\text{gas}} = 2.6 \cdot 10^{19}\,\text{m}^{-2}\,\text{s}^{-1}$ with the puffing position at the HFS, the plasma profiles become more and more inhomogeneous, where the minimum of the temperature is at the position of the gas puff. The maximum of the density is at the puffing position, too. In both cases, the anomalous particle flux is pronounced at the LFS due to the shape of $|\phi|^2$ (cf. Figure 4.6 on page 67). When the plasma profiles become inhomogeneous, the particle flux at the LFS increases even stronger (cf. Figure 6.15(b)).

This causes the density and the anomalous particle flux to grow rapidly and to reinforce the cooling. Thus MARFE evolves.

It is obvious that the strongly localized neutral particle source of the gas puff enhances the heat loss at the specific position. However, a tiny modification of the heat flux profile from the plasma core where $\xi = 0.05$ triggers the MARFE always at the HFS and $\xi = 0.1$ triggers the MARFE at the LFS independently of the puffing position.

The plasma profiles stay almost constant until the parallel heat conduction $\kappa_\parallel$ drops at a temperature around $T = 12\,\mathrm{eV}$. There, the losses from the heat convection $3T\Gamma_\perp$ and the ionization $E_\mathrm{i}J$ of the current cease to be balanced by the parallel heat conduction and thus a local drop of the temperature occurs. Hence, the heat conduction becomes even lower and the process reinforces itself. Additionally the ionization energy E_i (3.24) increases at a low temperature and reinforces the process even further. At a temperature below $2\,\mathrm{eV}$ $\delta_\mathrm{edge} = L_\mathrm{n}$ rises exponentially and increases the weight of the derivative term in (3.23) such that the temperature stays positive.

Figure 6.18 displays the losses due to convection and ionization in comparison to the heating from the plasma core. The puffing at the LFS adds additional loss at the position of strongest loss due to the heat convection $3T\Gamma_\perp$. However, puffing at the HFS adds the loss at the opposite position. Thus the density limit is reached earlier at the LFS puffing such that the HFS position is preferable for a safe discharge.

The heat flux profiles that are used in the plasma shift experiment in the previous section, do not produce realistic results. One reason is the anomalous transport $\Gamma_\perp$ that is strongly localized at the LFS with the MAST parameters. Another very interesting aspect are the growth rates of the eigenvalues. In the simulation of MAST there is always one eigenpair of growth rate $\Im(\omega) \approx 0.4$ and the second largest growth rate is a hundred times smaller. In contrast, in the TEXTOR simulation there are many eigenpairs of similar growth rate as can be seen in Figure 6.12 on page 112 and Figure 6.13 on page 113.

The shear of the radial electric field induced by the toroidal plasma rotation from [9] has been considered by the modification

$$\Im(\omega) \leftarrow \frac{\Im(\omega)}{1 + \left(\frac{\Omega}{\Im(\omega)}\right)^\alpha}, \qquad \Omega = \frac{\rho_i}{2L_n}\left(3 + \frac{0.17}{\left(1 + \frac{r_0}{R_0}\cos(\theta_g)\right)^2}\right), \quad \alpha \in [2,3] \tag{6.16}$$

of the growth rate. It is an estimate to describe the turbulence suppression by the radial electric shear. It turns out that

$$\frac{1}{1 + \left(\frac{\Omega}{\Im(\omega)}\right)^\alpha} \in \begin{cases} [0.98, 0.99], & \theta_g = 0 \qquad \text{puffing at the LFS} \\ [0.93, 0.98], & \theta_g = \pi \qquad \text{puffing at the HFS} \end{cases}$$

so that the simulation changes as follows. The growth rate modification reduces the growth rate and so the anomalous diffusivity especially with the puffing position at the HFS. The growth rate is reduced mainly at angular positions of high temperatures due to the L_n factor that becomes large at lower temperatures. The average anomalous transport $\langle\Gamma_\perp\rangle$ reduces by a factor of 0.0012. However, the anomalous transport increases by a factor 1.1 at the position θ where the temperature is minimal. The wave number of the maximal growth rate reduces by a factor of 0.1. Additionally the average density increases by a factor of 1.3. In our simulation, MARFE is triggered at a lower puffing rate with the modification (6.16) applied.

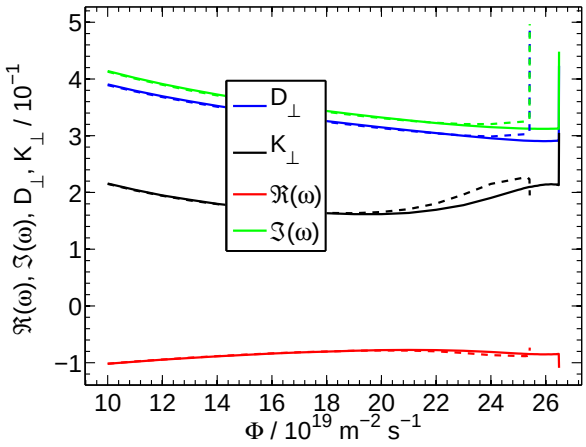

(a) wave number $K_\perp$ and eigenvalue ω

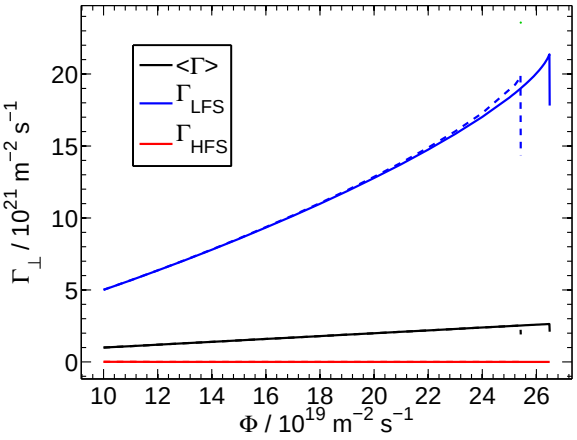

(b) anomalous particle flux $\Gamma_\perp$

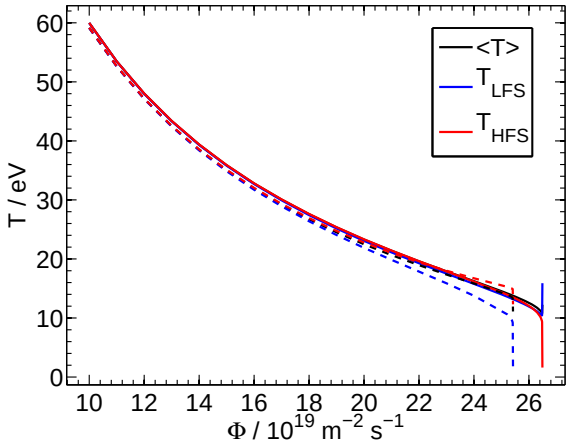

(c) temperature T

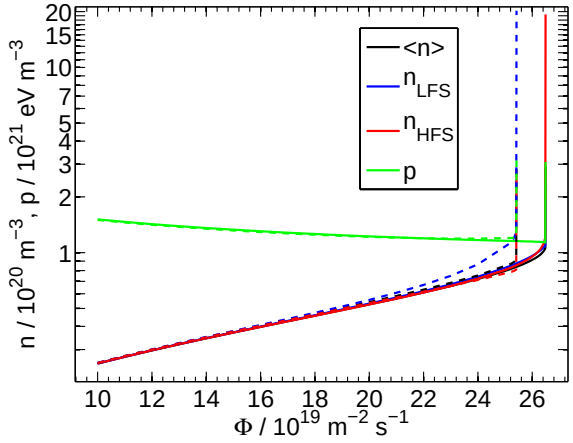

(d) density n and pressure p

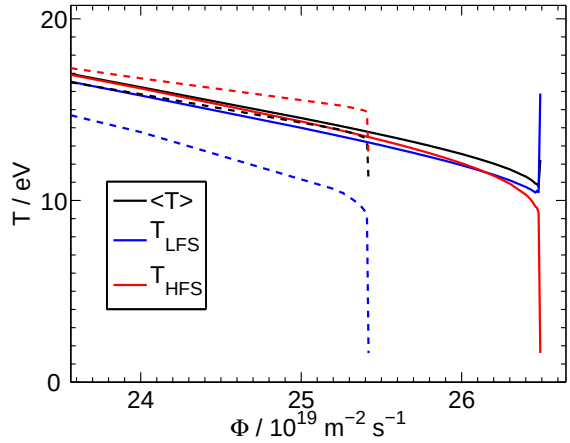

(e) temperature T (scale-up of (c))

Figure 6.15: The gas puff simulation with MAST parameters. The puff position is $\sigma_{\text{gas}} = \pi$ (HFS) (solid line) and $\sigma_{\text{gas}} = 0$ (LFS) (dashed line). The heating power from the plasma core is $q_{\text{core}} = 2.13 \cdot 10^{23}\,\text{eV}\,\text{m}^{-2}\,\text{s}^{-1}$ and the width of the gas puff distribution is $\delta_g = 0.1$. In (a) $K_\perp := \text{argmax}_{K_\perp}\, \Im(\omega)$ is displayed. In (b) the green line is the maximum of $\Gamma_\perp$ when a local drop occurs at the LFS due to a temperature drop at this position.

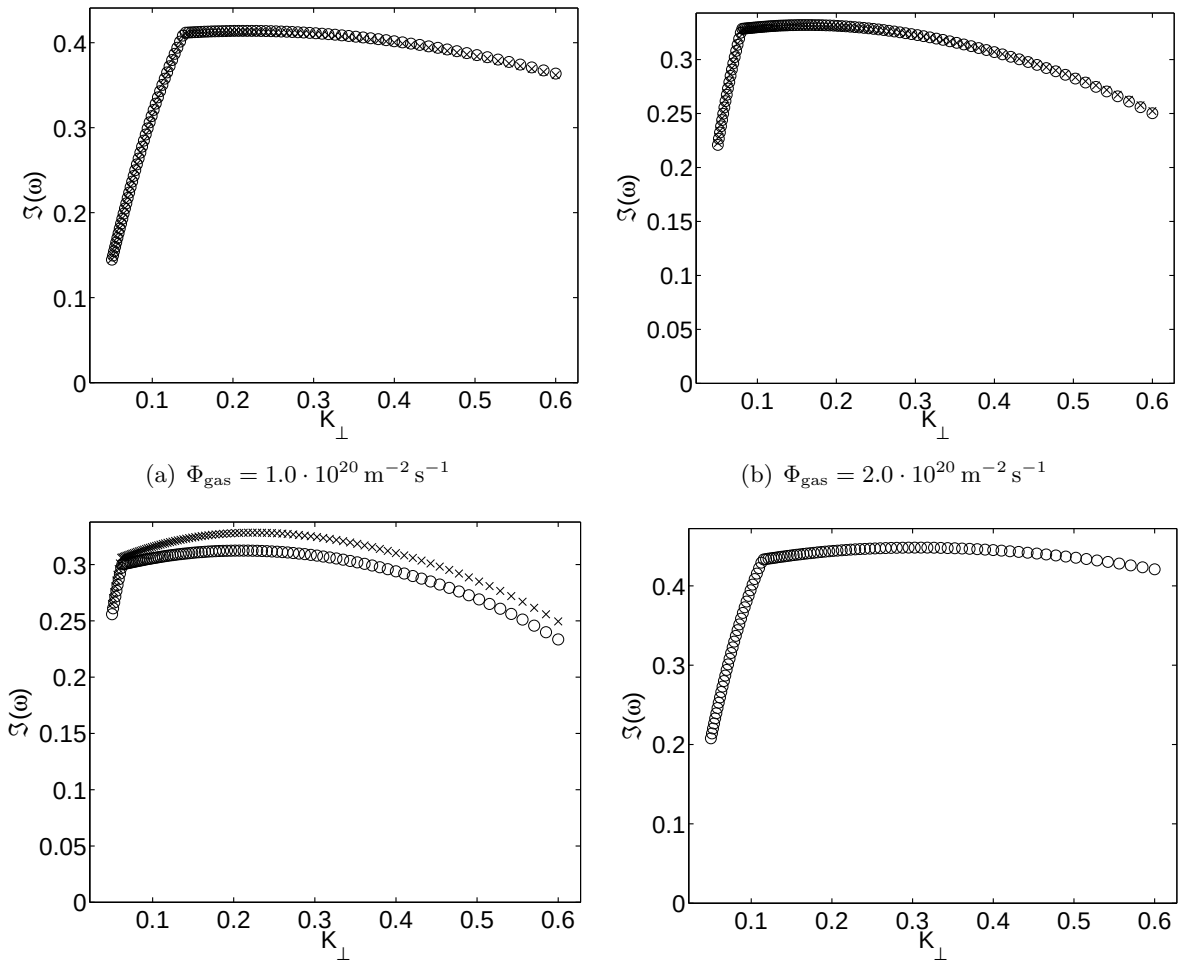

(a) $\Phi_{\mathrm{gas}} = 1.0 \cdot 10^{20}\,\mathrm{m}^{-2}\,\mathrm{s}^{-1}$

(b) $\Phi_{\mathrm{gas}} = 2.0 \cdot 10^{20}\,\mathrm{m}^{-2}\,\mathrm{s}^{-1}$

(c) $\Phi_{\mathrm{gas}} = 2.5 \cdot 10^{20}\,\mathrm{m}^{-2}\,\mathrm{s}^{-1}$

(d) $\Phi_{\mathrm{gas}} = 2.6 \cdot 10^{20}\,\mathrm{m}^{-2}\,\mathrm{s}^{-1}$

Figure 6.16: $K_\perp$ spectra of the gas puff simulation at the HFS $\theta_g = \pi$ (open circles) and the LFS $\theta_g = 0$ (x-marks). The kink corresponds to the non differentiable point in the γ factor of the eigenvalue equation (3.12).

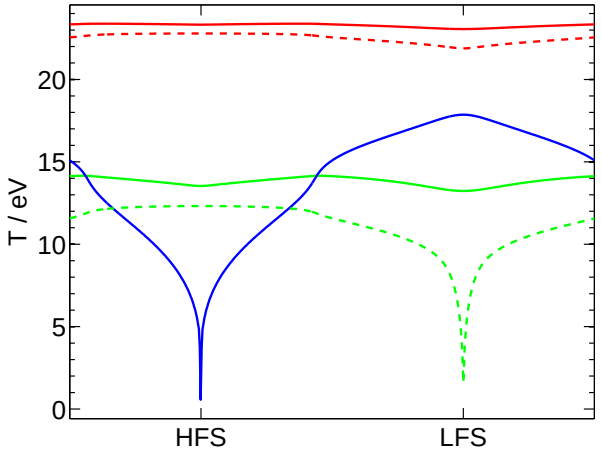

(a) temperature profiles

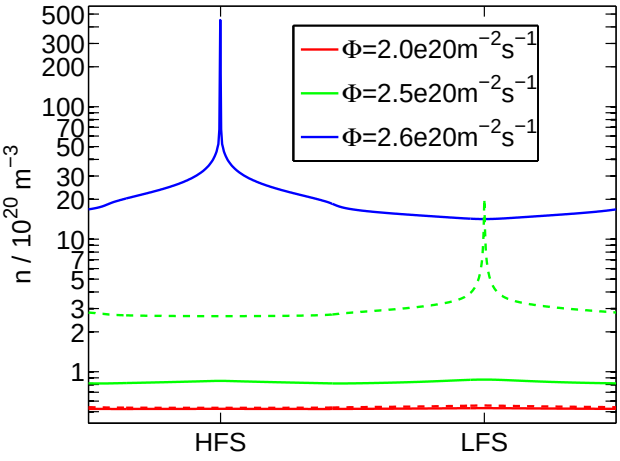

(b) density profiles

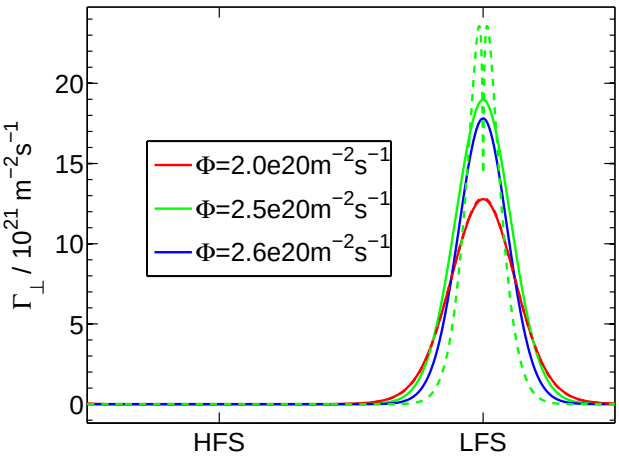

(c) anomalous particle flux profiles

Figure 6.17: The plasma profiles of the gas puff simulation. The puffing position is at $\theta_g = \pi$ (HFS) (solid line) and at $\theta_g = 0$ (LFS) (broken line). The horizontal axis is scaled proportional to the circumference of the edge layer. The kinks at the top and bottom corner of the magnetic triangle correspond to the short range of steep gradients between the HFS and the LFS in the temperature profiles.

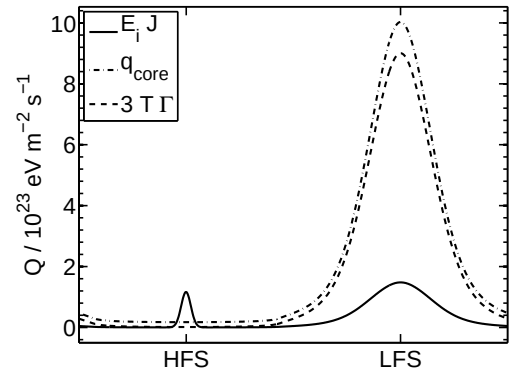

(a) $\Phi_{\mathrm{gas}} = 1.0 \cdot 10^{20}\,\mathrm{m}^{-2}\,\mathrm{s}^{-1}$

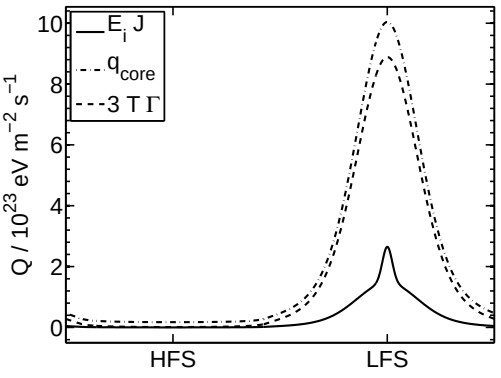

(b) $\Phi_{\mathrm{gas}} = 1.0 \cdot 10^{20}\,\mathrm{m}^{-2}\,\mathrm{s}^{-1}$

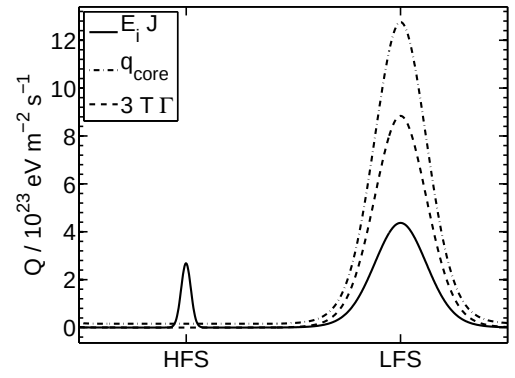

(c) $\Phi_{\mathrm{gas}} = 2.0 \cdot 10^{20}\,\mathrm{m}^{-2}\,\mathrm{s}^{-1}$

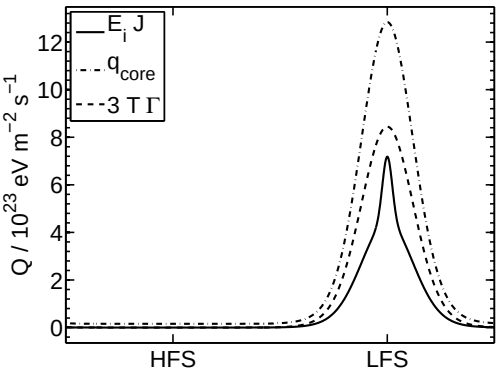

(d) $\Phi_{\mathrm{gas}} = 2.0 \cdot 10^{20}\,\mathrm{m}^{-2}\,\mathrm{s}^{-1}$

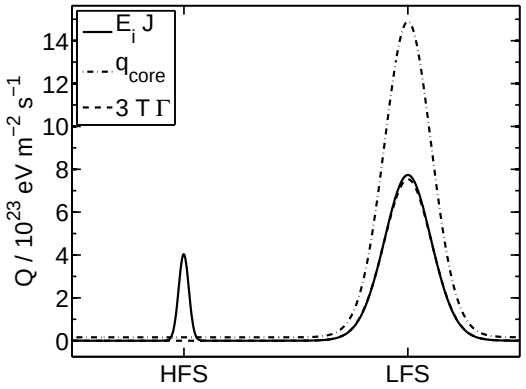

(e) $\Phi_{\mathrm{gas}} = 2.5 \cdot 10^{20}\,\mathrm{m}^{-2}\,\mathrm{s}^{-1}$

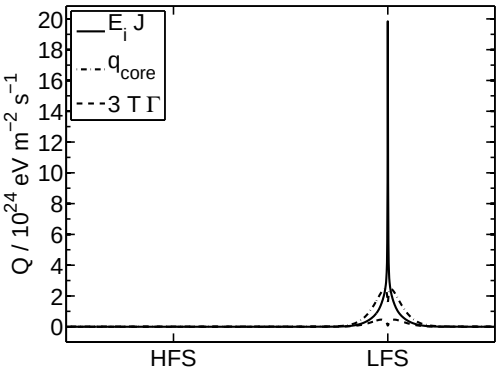

(f) $\Phi_{\mathrm{gas}} = 2.5 \cdot 10^{20}\,\mathrm{m}^{-2}\,\mathrm{s}^{-1}$

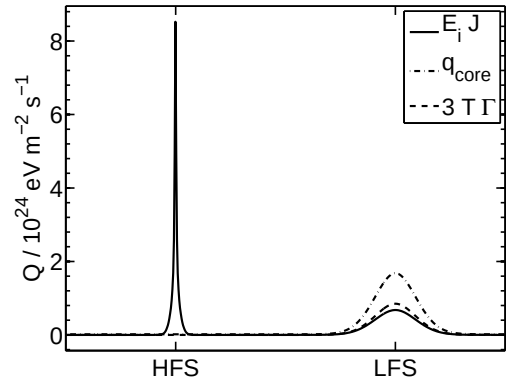

(g) $\Phi_{\mathrm{gas}} = 2.6 \cdot 10^{20}\,\mathrm{m}^{-2}\,\mathrm{s}^{-1}$

Figure 6.18: The heat balance of the gas puff simulation. The gas puff position is at HFS $\theta_g = \pi$ (left column) and LFS $\theta_g = 0$ (right column). The horizontal axis is scaled proportional to the circumference of the edge layer.

Chapter 7

Summary and perspectives

In the present work we developed algorithms to simulate the one-dimensional anomalous transport model of a Tokamak. Our main contribution was an efficient numerical method for solving the eigenvalue equation of the electric potential perturbation envelope. The new multilevel Jacobi-Davidson method can handle strongly inhomogeneous plasma parameters as well as different magnetic geometries.

The algorithm strongly relies on the physical properties of the eigenfunction of interest, namely the spatial smoothness. This motivates to start with a coarse grid approximation, which is then interpolated to a finer grid. The eigenvalue problem on the finer grid is then solved with a Jacobi-Davidson method with initial search space consisting of the interpolated coarse grid approximation, so that only few iterations are required. This process is repeated until the finest grid is reached. In order to improve the efficiency of this multilevel iteration, a number of intermediate steps haven been optimized for our particular application. For instance, we proposed a strategy for the selection of grid points and we investigated the efficient solution of the so-called correction equation. A major difficulty is to follow the correct Ritz pair during the iteration in the case that the eigenvalue with largest imaginary part is not well separated from the others. We proposed a mechanism based on distances between subspaces.

Our new multilevel Jacobi-Davidson algorithm is able to compute the desired eigenpair within one second up to a resolution of 1024 grid points, while the standard solver (QZ) takes about one hour. This allows to investigate the dependence of the anomalous transport of certain parameters such as the magnetic geometries of MAST and of TEXTOR. The simulation results are in good agreement with experimental observations.

We further studied self consistent modeling. The heat balance and the global particle balance equations are considered in order to calculate the impact of the anomalous particle flux on the initial plasma parameters. The system of nonlinear equations is solved iteratively, requiring the solution of a large number of eigenvalue problems. This makes an efficient eigenvalue solver indispensable. We proposed to use fixed point iteration with a well adopted damping strategy coupled with a trust region approach.

Moreover, we simulated the effect of the plasma shift for a prescribed average density. The simulation produced MARFE when the density limit was reached. These simulations showed that this process depends on the position of the injection of neutrals. Close to the density limit the ballooning structure is very pronounced so that the use of averaged plasma parameters is not justified. In addition, we verified that the heat flux distribution from the core has a huge impact on the qualitative result. The simple approximation of the poloidal heat flux distribution due to the Shafranov shift turns out to be insufficient for a realistic simulation. Future models should include instabilities in the plasma core, such as the ion gradient mode that cause the

anomalous heat flux into the plasma edge zone.

The gas puff simulation in the Tokamak MAST reveals the experimentally verified fact that the puffing at the HFS allows a higher puffing intensity before the MARFE is triggered. The L-H transition itself cannot be analyzed using a radially averaged direction. Therefore we plan to consider a two-dimensional model in the future. The idea of the multilevel Jacobi-Davidson method is still applicable but the solution of the correction equation needs special attention.

Finally we would like to mention that our new numerical scheme will also be useful in other applications, where only few eigenpairs corresponding to smooth eigenfunctions are required.

Appendix A

Proof of Theorem 4.9

We prepare the proof of the Theorem 4.9 on page 52 with the following three lemmas. This is possibly not new, but it has not be found in the literature.

Lemma A.1. *For $b \in \mathbb{N}$ it holds*

$$\sum_{i=1}^{b} \prod_{\substack{j=1 \\ j \neq i}}^{b} \frac{j^2}{j^2 - i^2} = 1$$

Proof. We define the supporting points

$$x_k := k^2, \qquad k = 1, \ldots, b$$

and the Lagrange basis polynomials

$$l_i(x) := \prod_{\substack{j=1 \\ j \neq i}}^{b} \frac{x - x_j}{x_i - x_j}.$$

Due to Theorem 4.7 on page 52

$$q_0(x) := \sum_{i=1}^{b} 1 l_i(x)$$

interpolates the function $f(x) := 1$ exactly, i.e., $q_0(0) = 1$ and we have

$$1 = f(0) = q_0(0) = \sum_{i=1}^{b} 1 l_i(0) = \sum_{i=1}^{b} \prod_{\substack{j=1 \\ j \neq i}}^{b} \frac{0 - x_j}{x_i - x_j} = \sum_{i=1}^{b} \prod_{\substack{j=1 \\ j \neq i}}^{b} \frac{j^2}{j^2 - i^2}.$$

□

Lemma A.2. *For $b, k \in \mathbb{N}$, $k < b$ it holds*

$$\sum_{i=1}^{b} i^{2k} \prod_{\substack{j=1 \\ j \neq i}}^{b} \frac{j^2}{j^2 - i^2} = 0$$

Proof. We define the supporting points

$$x_k := k, \qquad k = 1, \ldots, b$$

and the Lagrange basis for even polynomials of degree $2b-2$ is

$$l_i(x) := \prod_{\substack{j=1 \\ j\neq i}}^{b} \frac{x^2 - x_j^2}{x_i^2 - x_j^2}.$$

The polynomial

$$q_k(x) := \sum_{i=1}^{b} x_i^{2k} l_i(x)$$

interpolates the function $f(x) := x^{2k}$ exact for $k \leq b-1$ and thus

$$0 = f(0) = q_k(0) = \sum_{i=1}^{b} x_i^{2k} l_i(0) = \sum_{i=1}^{b} x_i^{2k} \prod_{\substack{j=1 \\ j\neq i}}^{b} \frac{0 - x_j^2}{x_i^2 - x_j^2} = \sum_{i=1}^{b} i^{2k} \prod_{\substack{j=1 \\ j\neq i}}^{b} \frac{j^2}{j^2 - i^2}$$

□

Lemma A.3. *For $b, k \in \mathbb{N}$, $k < b$ holds*

$$\sum_{i=1}^{b} \frac{1}{i^2} \left(\prod_{\substack{j=1 \\ j\neq i}}^{b} \frac{j^2}{j^2 - i^2} - 1 \right) = 0$$

Proof. We proof this theorem by induction. For $b = 1$ the product is empty and thus one. Hence the sum is zero. For $b = 2$ we have

$$\frac{1}{1}\left(\frac{4}{4-1} - 1\right) + \frac{1}{4}\left(\frac{1}{1-4} - 1\right) = \frac{1}{3} - \frac{1}{3} = 0.$$

We assume that the proposition is true for a fixed $b \in \mathbb{N}$

$$\sum_{i=1}^{b} \frac{1}{i^2} = \sum_{i=1}^{b} \frac{1}{i^2} \prod_{\substack{j=1 \\ j\neq i}}^{b} \frac{j^2}{j^2 - i^2} \tag{A.1}$$

and show the induction step to $b+1$:

$$\begin{aligned}
\sum_{i=1}^{b+1} \frac{1}{i^2} \left(\prod_{\substack{j=1 \\ j\neq i}}^{b+1} \frac{j^2}{j^2-i^2} - 1 \right) &= \sum_{i=1}^{b} \frac{1}{i^2} \prod_{\substack{j=1 \\ j\neq i}}^{b+1} \frac{j^2}{j^2-i^2} - \sum_{i=1}^{b} \frac{1}{i^2} + \frac{1}{(b+1)^2} \left(\prod_{j=1}^{b} \frac{j^2}{j^2-(b+1)^2} - 1 \right) \\
&\overset{(A.1)}{=} \sum_{i=1}^{b} \frac{1}{i^2} \left(\frac{(b+1)^2}{(b+1)^2-i^2} - 1 \right) \prod_{\substack{j=1 \\ j\neq i}}^{b} \frac{j^2}{j^2-i^2} + \frac{1}{(b+1)^2} \left(\prod_{j=1}^{b} \frac{j^2}{j^2-(b+1)^2} - 1 \right) \\
&= \sum_{i=1}^{b} \frac{1}{(b+1)^2-i^2} \prod_{\substack{j=1 \\ j\neq i}}^{b} \frac{j^2}{j^2-i^2} + \frac{1}{(b+1)^2} \left(\prod_{j=1}^{b} \frac{j^2}{j^2-(b+1)^2} - 1 \right) \\
&= \frac{1}{(b+1)^2} \left(\sum_{i=1}^{b} \prod_{\substack{j=1 \\ j\neq i}}^{b+1} \frac{j^2}{j^2-i^2} + \prod_{j=1}^{b} \frac{j^2}{j^2-(b+1)^2} - 1 \right) \\
&= \frac{1}{(b+1)^2} \left(\sum_{i=1}^{b+1} \prod_{\substack{j=1 \\ j\neq i}}^{b+1} \frac{j^2}{j^2-i^2} - 1 \right) \overset{\text{Lemma } A.1}{=} 0
\end{aligned}$$

□

We are now able to prove Theorem 4.9 on page 52.

Proof. of Theorem 4.9.

The Lagrangian polynomial is calculated as

$$p(x) = \sum_{i=-b}^{b} f_i L_i(x).$$

The derivative of p in $x_0 = 0$ requires the derivative $L_i'(0)$:

$$L_0'(0) = 0 \tag{A.2}$$

and for $i \neq 0$ holds

$$L_i'(0) = \frac{1}{2hi} \prod_{\substack{j=1 \\ |j|\neq|i|}}^{b} \frac{j^2}{j^2-i^2}, \qquad L_i'(0) = -L_{-i}'(0). \tag{A.3}$$

The Taylor expansion of f_i in $x_0 = 0$ is

$$f_i := f(x_i) = \sum_{k=0}^{m} f^{(k)}(0) \frac{i^k h^k}{k!} + \mathcal{O}(h^{m+1}). \tag{A.4}$$

Now, the first derivative of p is written with the Lagrangian polynomials and the Taylor expansion

$$\begin{aligned}
p'(0) &= \sum_{i=-b}^{b} f_i L_i'(0) = \sum_{i=-b}^{b} \left(\sum_{k=0}^{m} f^{(k)}(0) \frac{i^k h^k}{k!} + \mathcal{O}(h^{m+1}) \right) L_i'(0) \\
&= \sum_{k=0}^{m} \sum_{i=-b}^{b} f^{(k)}(0) \frac{i^k h^k}{k!} L_i'(0) + \mathcal{O}(h^m).
\end{aligned}$$

Due to $L_i'(0) = -L_{-i}'(0)$ it simplifies to

$$\begin{aligned} p'(0) &= \sum_{k=0}^{m} f^{(k)}(0) \left(\frac{0^k h^k}{k!} L_0'(0) + \sum_{i=1}^{b} \frac{\left(i^k - (-i)^k\right) h^k}{k!} L_i'(0) \right) + \mathcal{O}(h^m) \\ &= \sum_{k=0}^{m} f^{(k)}(0) \sum_{i=1}^{b} \frac{\left(i^k - (-i)^k\right) h^k}{k!} L_i'(0) + \mathcal{O}(h^m). \end{aligned}$$

For k even, the numerator is zero. For k odd and with (A.2), (A.3) it holds

$$\begin{aligned} p'(0) &= \sum_{k=0}^{m} f^{(k)}(0) \sum_{i=1}^{b} \frac{\left(i^k - (-i)^k\right) h^k}{k!} \frac{1}{2hi} \prod_{\substack{j=1 \\ j \neq i}}^{b} \frac{j^2}{j^2 - i^2} + \mathcal{O}(h^m) \\ &= \sum_{k=0}^{m} f^{(k)}(0) \frac{h^{k-1}}{k!} \underbrace{\sum_{i=1}^{b} i^{k-1} \prod_{\substack{j=1 \\ j \neq i}}^{b} \frac{j^2}{j^2 - i^2}}_{=:t_k} + \mathcal{O}(h^m). \end{aligned}$$

In case of $k = 1$ it holds

$$t_1 = \sum_{i=1}^{b} \prod_{\substack{j=1 \\ j \neq i}}^{b} \frac{j^2}{j^2 - i^2} \overset{\text{Lemma } A.1}{=} 1.$$

For $1 < k < b$ it holds

$$t_{2k+1} = \sum_{i=1}^{b} i^{2k} \prod_{\substack{j=1 \\ j \neq i}}^{b} \frac{j^2}{j^2 - i^2} \overset{\text{Lemma } A.2}{=} 0.$$

For $k = 2b + 1$ it holds

$$t_{2b+1} = \sum_{i=1}^{b} i^{2b} \prod_{\substack{j=1 \\ j \neq i}}^{b} \frac{j^2}{j^2 - i^2} \neq 0$$

in general.

$$\Rightarrow p'(0) = f'(0) + \mathcal{O}(h^{2b})$$

Now, the accuracy of the second derivative is proofed analogous:

$$\begin{aligned} L_0''(0) &= \frac{1}{h^2} \sum_{\substack{k=-b \\ k \neq 0}}^{b} -\frac{1}{k} \sum_{\substack{l=-b \\ l \neq k \\ l \neq 0}}^{b} -\frac{1}{l} = \frac{1}{h^2} \sum_{\substack{k=-b \\ k \neq 0}}^{b} \frac{1}{k} \sum_{\substack{l=-b \\ l \neq k \\ l \neq 0}}^{b} \frac{1}{l} = \frac{2}{h^2} \sum_{k=1}^{b} \frac{1}{k} \sum_{\substack{l=-b \\ l \neq k \\ l \neq 0}}^{b} \frac{1}{l} \\ &= \frac{2}{h^2} \sum_{k=1}^{b} \frac{-1}{k^2} + \sum_{l=1}^{b} \frac{1}{kl} - \frac{1}{kl} = -\frac{2}{h^2} \sum_{k=1}^{b} \frac{1}{k^2} \end{aligned} \tag{A.5}$$

For $i \neq 0$ holds

$$L_i''(0) = \frac{1}{h^2} \frac{2}{i} \sum_{\substack{l=-b \\ l \neq i \\ l \neq 0}}^{b} \frac{1}{i - l} \prod_{\substack{j=-b \\ j \neq i \\ j \neq l \\ j \neq 0}}^{b} \frac{j}{j - i}$$

The sum is split into the part of negative and positive l and l is replaced by $-l$ for the negative part:

$$L_i''(0) = \frac{1}{h^2}\frac{2}{i}\left(\sum_{\substack{l=1\\ l\neq i}}^{b}\frac{1}{i-l}\prod_{\substack{j=-b\\ j\neq i\\ j\neq l\\ j\neq 0}}^{b}\frac{j}{j-i} + \sum_{\substack{l=1\\ l\neq -i}}^{b}\frac{1}{i+l}\prod_{\substack{j=-b\\ j\neq i\\ j\neq -l\\ j\neq 0}}^{b}\frac{j}{j-i}\right).$$

After a short calculation

$$L_i''(0) = \frac{1}{h^2}\frac{2}{i}\left(\sum_{\substack{l=1\\ l\neq i}}^{b}\frac{1}{i-l}\frac{-l}{-l-i}\prod_{\substack{j=-b\\ j\neq i\\ |j|\neq|l|\\ j\neq 0}}^{b}\frac{j}{j-i} + \sum_{\substack{l=1\\ l\neq -i}}^{b}\frac{1}{i+l}\frac{l}{l-i}\prod_{\substack{j=-b\\ j\neq i\\ |j|\neq|l|\\ j\neq 0}}^{b}\frac{j}{j-i}\right)$$

all summands except the one for $l=-i$ vanish:

$$\begin{aligned} L_i''(0) &= \frac{1}{h^2}\frac{2}{i}\left(\sum_{\substack{l=1\\ l\neq|i|}}^{b}\underbrace{\left(\frac{-l}{l^2-i^2}+\frac{l}{l^2-i^2}\right)}_{=0}\prod_{\substack{j=-b\\ j\neq i\\ |j|\neq|l|\\ j\neq 0}}^{b}\frac{j}{j-i} + \frac{1}{i+i}\prod_{\substack{j=-b\\ |j|\neq|i|\\ j\neq 0}}^{b}\frac{j}{j-i}\right) \\ &= \frac{1}{h^2}\frac{1}{i^2}\prod_{\substack{j=-b\\ |j|\neq|i|\\ j\neq 0}}^{b}\frac{j}{j-i} = \frac{1}{h^2}\frac{1}{i^2}\prod_{\substack{j=1\\ |j|\neq|i|}}^{b}\frac{j}{j-i}\frac{j}{j+i} = \frac{1}{h^2}\frac{1}{i^2}\prod_{\substack{j=1\\ |j|\neq|i|}}^{b}\frac{j^2}{j^2-i^2} \end{aligned} \tag{A.6}$$

and it holds $L_i''(0) = L_{-i}''(0)$.

In the expression of the second derivative of the Lagrangian polynomial p the values f_i are replaced by its Taylor expansion in $x_0 = 0$ (A.4):

$$\begin{aligned} p''(0) &= \sum_{i=-b}^{b} f_i L_i''(0) = \sum_{i=-b}^{b}\left(\sum_{k=0}^{m} f^{(k)}(0)\frac{i^k h^k}{k!} + \mathcal{O}(h^{m+1})\right)L_i''(0) \\ &= \sum_{k=0}^{m}\sum_{i=-b}^{b} f^{(k)}(0)\frac{i^k h^k}{k!}L_i''(0) + \mathcal{O}(h^{m-1}). \end{aligned}$$

Due tp $L_i''(0) = L_{-i}''(0)$ the expression simplifies to

$$p''(0) = \sum_{k=0}^{m}\frac{h^k}{k!}f^{(k)}(0)\left(\underbrace{0^k L_0''(0) + \sum_{i=1}^{b}\left(i^k + (-i)^k\right)L_i''(0)}_{=:s_k}\right) + \mathcal{O}(h^{m-1}). \tag{A.7}$$

To proof the proposition, it must be shown that $s_k = 0$ for $k = 0, 1, 3, 4, \ldots, 2b+1$ and $s_2 = \frac{2}{h^2}$, and $s_{2b+2} \neq 0$.

If $k \in \mathbb{N}$ is odd $s_k = 0$ holds obviously.

If $k = 0$ (A.5), (A) and (A.7) offer

$$\begin{aligned} s_0 &= 1L_0''(0) + 2\sum_{i=1}^{b} L_i''(0) \\ &= \frac{2}{h^2}\left(\sum_{i=1}^{b}\frac{1}{i^2}\left(-1 + \prod_{\substack{j=1\\ j\neq i}}^{b}\frac{j^2}{j^2-i^2}\right)\right) \overset{\text{Lemma } A.3}{=} 0. \end{aligned}$$

For $k \in \mathbb{N}$ and even it holds

$$s_k = 2\sum_{i=1}^{b} i^k L_i''(0) = 2\sum_{i=1}^{b} i^k \frac{1}{h^2}\frac{1}{i^2}\prod_{\substack{j=1\\ j\neq i}}^{b}\frac{j^2}{j^2-i^2} = \frac{2}{h^2}\sum_{i=1}^{b} i^{k-2}\prod_{\substack{j=1\\ j\neq i}}^{b}\frac{j^2}{j^2-i^2}.$$

In case of $k = 2$ with Lemma A.1 on page 123 it holds

$$s_2 = \frac{2}{h^2}\sum_{i=1}^{b}\prod_{\substack{j=1\\ j\neq i}}^{b}\frac{j^2}{j^2-i^2} = \frac{2}{h^2}.$$

If $2 \leq k \leq b$ with Lemma A.2 it holds

$$s_{2k} = \frac{2}{h^2}\sum_{i=1}^{b} i^{2k-2}\prod_{\substack{j=1\\ j\neq i}}^{b}\frac{j^2}{j^2-i^2} = 0.$$

In case of $k = 2b + 2$ it holds

$$s_{2b+2} = \frac{2}{h^2}\sum_{i=1}^{b} i^{2b}\prod_{\substack{j=1\\ j\neq i}}^{b}\frac{j^2}{j^2-i^2} \neq 0$$

in general.

□

Appendix B

Poloidal circumference with triangulated plasma

Several times the average of a quantity $\widehat{f}(\sigma)$ along the poloidal circumference is required. The integral over the circumference with the elongation E and the triangulation D can be transformed into an integral over the poloidal angle θ as follows.

$$\int_0^{2\pi} \widehat{f}(\sigma)\, d\sigma = \int_0^{2\pi} \widehat{f}\big(\sigma(\theta)\big) \frac{d\sigma}{d\theta}(\theta)\, d\theta = \int_0^{2\pi} f(\theta) \frac{d\sigma}{d\theta}(\theta)\, d\theta$$

The arc length element is

$$r\frac{d\sigma}{d\theta} = \sqrt{\left(\frac{\partial R}{\partial \theta}\right)^2 + \left(\frac{\partial Z}{\partial \theta}\right)^2}$$

where

$$R = R_0 + r\cos(\theta) + Dr\cos(2\theta)$$
$$Z = rE\sin(\theta) - rED\sin(2\theta).$$

The integral can be handled numerically by a quadrature formula, e.g., the trapezoidal rule.

Appendix C

The Newton method for the self consistent calculation

Again, we denote the plasma profile iteration that calculates the anomalous particle flux and one step of the linearized heat balance equation (6.2) and the global particle balance (6.4) by $F(T, p)$. We skip the pressure argument for better readability.

C.1 Inverse non-linear power method

Let

$$F(T) = \lambda T \tag{C.1}$$

denote the non-linear eigenvalue problem. The solution of physical interest is an eigenpair with eigenvalue $\lambda = 1$. A Shift -1 is applied on the non-linear eigenvalue problem (C.1):

$$\widehat{F}(T) := F(T) - T. \tag{C.2}$$

The aim is to find $\widetilde{T}$, such that $\widehat{F}(\widetilde{T}) = 0$. In case of linear $\widehat{F}$ this is done by the power method applied on the inverse matrix. Here, in case of the non-linear equation Newtons method is applied:

$$T_{i+1} := T_i - \left(D\widehat{F}(T_i)\right)^{-1} \widehat{F}(T_i). \tag{C.3}$$

The Jacobian $D\widehat{F}(T_i)$ cannot be calculated analytically. Therefore a numerical approximation is required. For any direction ψ_j and a step size $h > 0$ a second order approximation is

$$\begin{aligned} D\widehat{F}(T_i)\psi_j &= \frac{\partial \widehat{F}}{\partial \psi_j}(T_i) \\ &= \frac{\widehat{F}(T_i + h\psi_j) - \widehat{F}(T_i - h\psi_j)}{2h\|\psi_j\|_2} + \mathcal{O}(h^2) \\ &= \frac{F(T_i + h\psi_j) - T_i - h\psi_j - F(T_i - h\psi_j) + T_i - h\psi_j}{2h\|\psi_j\|_2} + \mathcal{O}(h^2) \\ &= \frac{F(T_i + h\psi_j) - F(T_i - h\psi_j)}{2h\|\psi_j\|_2} - \frac{\psi_j}{\|\psi_j\|_2} + \mathcal{O}(h^2). \end{aligned} \tag{C.4}$$

Let $N \in \mathbb{N}$ be the number of grid points. The calculation of $\widehat{F}(T_i)$ requires $2N$ evaluations of F. In order to keep small the computational effort, we assume the following: within a small change of T_i to $T_i \pm h\phi_j$ the $K_\perp$ value of maximal growth rate does not change and the eigenpair is

similar, as well. Therefore the eigenpair $(\omega_i, \widetilde{\phi}_i)$, that produces T_i is improved by the Jacobi-Davidson algorithmat $T = T_i \pm h\psi_j$ to obtain $\Gamma_\perp(T_i \pm h\psi_j)$. "improved" means to choose the initial search space in the Jacobi-Davidson algorithm as $V_{\text{initial}} = \widetilde{\phi}_i$. At last the heat balance equation is solved for $T = T_i \pm h\psi_j$ and $\Gamma_\perp = \Gamma_\perp(T_i \pm h\psi_j)$ to find $F(T_i \pm h\psi_j)$.

C.1.1 Symmetry

If the position of the gas puff position and the limiter is symmetric to the mid plane of the Tokamak vessel, the plasma parameter profiles are symmetric with respect to $\theta = 0$ and $\theta = \pi$. Thus the calculation can be restricted to $[0, \pi]$ and the obtained values are mirrored onto $]\pi, 2\pi[$ afterwards. The eigenvalue problem of the potential perturbation itself cannot be reduced in general, because there are point symmetric complex eigenvectors where the intensity is symmetric (think of $\cos(\theta) + i\sin(\theta)$).

Let $N \in 2\mathbb{N}$ be the number of grid points of a symmetric periodic grid G such that $\theta_0 = 0$ and $\theta_{N/2} = \pi$. Further, we define the series of vectors $(e_j)_{j=0,\dots,N-1}$, $e_j(\theta_i) = \delta_{j,i}\ \forall \theta_i \in G$. The symmetric vectors are combined to

$$\widehat{e_j} := e_j + e_{N-j}, \quad j = 1, \dots, \frac{N}{2} - 1, \qquad \widehat{e_j} := e_j, \quad j = 0, \frac{N}{2}.$$

The effort to calculate the Jacobian of $\widehat{F}$ is reduced to the half:

$$D\widehat{F}(T_i)\widehat{e_j} = \frac{\partial \widehat{F}}{\partial \widehat{e_j}}(T_i) = \frac{F(T_i + h\widehat{e_j}) - F(T_i - h\widehat{e_j})}{2h\|\widehat{e_j}\|_2} - \frac{\widehat{e_j}}{\|\widehat{e_j}\|_2} + \mathcal{O}(h^2), \quad j = 0, \dots, \frac{N}{2}. \tag{C.5}$$

$$D\widehat{F}(T_i) \in \mathbb{R}^{(N/2+1)\times(N/2+1)}$$

Now, we can calculate the first $N/2 + 1$ components of the Newton direction t

$$D\widehat{F}(T_i)t_{0,\dots,N/2} = \left(\widehat{F}(T_i)\right)_{0,\dots,N/2}$$

and mirror it afterwards

$$t_{N/2+1,\dots,N-1} := t_{N/2-1,\dots,1}$$

to obtain the full vector.

The finite difference derivative changes the value of T_i at one grid point or in the symmetric case at two grid points. Another possibility is to change the amplitude of the Fourier frequencies. Here, it does not give the spectral precision, but the advance is a smoother temperature profile compared to the profile with one value modified in one grid point. The disadvantage is the additional computational effort, when the support of the direction function $\widehat{e_j}$ broadens in (C.5) though to $\widehat{e_j} = \exp(ij\vec{\theta})$, which is the set of the basis functions. In the standard symmetric case the Fourier frequencies are the cosine.

C.2 Comparing both methods

Two solvers for non-linear eigenvalue problem have been introduced, the power method and the inverse power method. The convergence is much better with the latter one. However the computational cost in calculating the Jacobian is enormous. The move of the temperature profile between two iterations is much smaller with the inverse power method, i.e., the norm of the Jacobian is mostly 10 or above.

C.3 Accelerating non-linear power method by a non-linear full approximation scheme multigrid approach

In order to accelerate the Newton procedure, the idea arises to apply the *full approximation scheme* (FAS) [28] of the non-linear multigrid technique on (C.2). On coarser grids the calculation of the Jacobian DF requires less evaluations of F. To be more precise, the number of evaluations of F is proportional to the number of grid points. Additionally the computational effort to evaluate F reduces at least linear by the dimension of the discrete space. Thus the computational effort to calculate DF reduces quadratically with the number of grid points.

For a given profile T the *defect* d is defined as

$$d := \widehat{F}(T) := F(T) - T$$

In order to achieve $\widehat{F}(T^{\text{opt}}) = 0$, a correction t is desired such that $\widehat{F}(T+t) = 0$. This correction t can be calculated by the Newton iteration which requires the expensive calculation of the Jacobian $D\widehat{F}(T)$. However, a correction of the lower frequencies of T can be calculated on a coarser grid. The details are summed up in algorithm 17.

Algorithm 17 Non-linear full approximation scheme multigrid approach

Require: Profile T^0 on grid G^0 of $c2^m$ grid points.
Require: Number of pre- and post smoothing Newton cycles: ν_1, ν_2.
1: // The upper index (k) always denotes the grid level of a grid of $c2^{m-k}$ points.
2: apply ν_1 Newton cycles on $\widehat{F^0}(T^0 + t^0_{\nu_1}) = 0$.
3: calculate defect $d^0_0 := \widehat{F^0}(T^0 + t^0_{\nu_1})$.
4: **while** $\|d^0_0\| > \varepsilon$ **do**
5: // multigrid pre smoothing
6: **for** $k = 1, \ldots, m$ **do**
7: restrict defect $d^{k-1}_{k-1} \to d^k_{k-1}$ and $(T^{k-1} + t^{k-1}_{\nu_1}) \to T^k$ to coarser grid G^k of $c2^{m-k}$ points.
8: apply ν_1 Newton cycles on $\widehat{F^k}(T^k + t^k_{\nu_1}) + \widehat{F^k}(T^k) = d^k_{k-1}$.
9: **end for**
10: $t^m_{\text{coarse}} = 0$ // there is no correction of coarser grids
11: // multigrid post smoothing
12: **for** $k = m, \ldots, 1$ **do**
13: apply ν_2 Newton cycles on $\widehat{F^k}(T^k + t^k_{\nu_1} + t^m_{\text{coarse}} + t^k_{\nu_2}) + \widehat{F^k}(T^k) = d^k_{k-1}$.
14: $t^{k-1}_{\text{coarse}} := \text{prolong}(t^k_{\nu_1} + t^k_{\text{coarse}} + t^k_{\nu_2})$
15: **end for**
16: apply ν_2 Newton cycles on $\widehat{F^0}(T^0 + t^0_{\nu_1} + t^0_{\text{coarse}} + t^0_{\nu_2}) = 0$.
17: update $T^0 := T^0 + t^0_{\nu_1} + t^0_{\text{coarse}} + t^0_{\nu_2}$.
18: calculate defect $d^0_0 := \widehat{F^0}(T^0 + t^0_{\nu_1})$.
19: **end while**
20: $T^{\text{opt}} := T^0$.

On a coarse grid of half the size of grid points, the effort to calculate one profile is halved. Furthermore the number of required profiles to calculate the Jacobian $D\widehat{F}$ is half the number, too. In particular, the total effort is almost reduced to a quarter. On the next coarser grid of fourth the number of grid points, the effort is reduced to the sixteenth part and so on.

A practical approved choice for the number of Newton cycles are $\nu_1 = 1$ before the coarse grid correction and $\nu_2 = 2$ after the coarse grid correction. On the full resolution only one Newton cycle is calculated before coarse grid approximations are repeated. The *restriction* is realized by

the weighted average of the point itself and the two neighbors. The *prolongation* is implemented by linear or shape preserving cubic hermite interpolation [8].

The acceleration by the coarse grid correction is enormous. The number of cycles on the full resolution of $N = 512$ is reduced from hundred to less than ten. However the number of evaluations of F due to the Jacobian is much larger than the number gained by the fixed point iteration with a problem adopted damping strategy as it is deduced in section 6.3.2 on page 91.

Statement of originality

Die hier vorgelegte Dissertation habe ich eigenständig und ohne unerlaubte Hilfe angefertigt. Die Dissertation wurde in der vorgelegten oder ähnlichen Form noch bei keiner anderen Institution eingereicht. Ich habe bisher keine erfolglosen Promotionsversuche unternommen.

I do herewith declare that the material contained in this dissertation is an original work performed by me without ilegitimate help. The material in this thesis has not been previously submitted for a degree in any university.

Düsseldorf, den 04.03.2009

Dominik Löchel

List of Figures

List of Tables

List of Algorithms

Bibliography

[1] C. Alber: *Numerische Behandlung quadratischer Eigenwertprobleme*, diploma thesis, University Düsseldorf, Germany (2007)

[2] J. Anderson, H. Nordman and J. Weiland: *Effects of non-circular tokamak geometry on ion-temperature-gradient driven modes*, Plasma Phys. Control. Fusion 42 (2000)

[3] M. Abramowitz and I. Stegun: *Handbook of mathematical functions*, Dover publications (1972)

[4] Z. Bai, J. Demmel, J. Dongarra, A. Ruhe and H. van der Vorst, editors: *Templates for the Solution of algebraic Eigenvalue Problems*, A Practical Guide. SIAM, Philadelphia (2000)

[5] T. Betcke: *Optimal scaling of generalized and polynomial eigenvalue problems*, MIMS EPrint: 2007.120, ISSN 1749-9097 (2007)

[6] P. Catto, T. Fülöp and P. Helander: *Localized Gas Puffing Control of Edge Rotation and Electric Field*, Contrib. Plasma Phys. 44, no. 1–3 (2004) pp. 281–282

[7] P. Davis: *Interpolation and approximation*, Dover publications, Inc.(1975)

[8] F. Fritsch and R. Carlson: *Monotone Piecewise Cubic Interpolation*, SIAM J. Numerical Analysis vol. 17 (1980) 238–246.

[9] T. Fülöp, P. Helander and P. Catto: *Effect of Poloidal Density Variation of Neutral Atoms on the Tokamak Edge*, Physical Review Letters vol. 89, no. 22 (2002)

[10] L. Gerard, G. Sleijpen and H. van der Vorst: *A Jacobi-Davidson Iteration Method for Linear Eigenvalue Problems*, SIAM J. Matrix Anal. Appl. vol. 17, no. 2 (1996) pp. 401–425

[11] G. Golub and C. van Loan: *Matrix Computations*, The Johns Hopkins Univerity Press, third edition, ISBN 0-8018-5413-8 (1996) pp. 76–77

[12] M. Greenwald, Plasma Phys. Nucl. Fusion, 44, R27 (2002)

[13] N. Higham: *Accuracy and Stability of Numerical Algorithms*, Manchester Institute for Mathematical Sciences, ISSN 1749-9097 (2002)

[14] A. Horn and C. Johnson, Topics in Matrix Analysis, Chapter 1, Cambridge University Press, ISBN 0-521-46713-6 (1991)

[15] R. Janev, D. Post, W. Langer *et al.*, J. Nucl. Mater, vol. 121, no. 10 (1984)

[16] F. Jarre, J. Stoer: *Optimierung*. Springer (2004) ISBN 3-540-43575-1

[17] C. Johnson: *Functional Characterizations of the Field of Values and the Convex Hull of the Spectrum*, Proceedings of the American Mathematical Society, vol. 61, no. 2 (1976) pp. 201–204.

[18] D. Jua, Y. Yu and T. Fowler, Physics of Fluids 34 3216 (1992)

[19] S. Klose: *Untersuchung der Driftinstabilität an der rotierenden magnetisierten Plasmasäule des PSI-1 im Falle eines Plamahohlprofils und großer endlicher Ionengyroradieneffekte*, Dissertation, Humboldt-Univerity Berlin, Germany (1969)

[20] A.V. Knyazev and K. Neymeyr: *Efficient solution of summetric eigenvalue problems using multigrid preconditioners in the locally optimal block conjugate gradient method*, Elec. Trans. on Numeric. Anal. vol. 15 (2003) pp. 38–55

[21] C. Li and L. Rodman: *Numerical range of matrix polynomials*, SIAM J. Matrix anal. Appl. vol. 15, no. 4 (1994) pp. 1256–1265

[22] J. D. Lawson: *Some criteria for a Power Producing Thermonuclear Reactor*, Proceedings of the Physical Society B, vol. 70 (1957) p. 6.

[23] X. Loozen: *Modeling of Plasma Response to Magnetic Field Perturbations from the Dynamic Ergodic Divertor (DED) and Comparison with Experiment*, Berichte des Forschungszentrums Jülich, Jül-4251 (2006)

[24] K. Meerbergen and D. Roose: *Matrix transformations for computing rightmost eigenvalues of large sparse non-symmetric eigenvalue problems*, IMA J. of Num. Anal. 16 (1996) pp. 297–346

[25] N. Papathanasiou and P. Psarrakos: *Normal matrix polynomials with nonsingular leading coefficients*, Electronic Journal of Linear Algebra, ISSN 1081-3810, International Linear Algebra Society vol. 17 (2008) pp. 458–472

[26] J. Rapp, P. de Vries, F. Schüller, M. Tokar, W. Biel, R. Jaspers, H. Koslowski, A. Krämer-Flecken, A. Kreter, M. Lehnen, A. Pospieszczyk, D. Reiser, U. Samm, G. Sergienko: *Density limits in TEXTOR-94 auxiliary heated discharges*, Nuclear Fusion, vol. 39, no. 6 (1999) pp. 765–776

[27] D. Reiser: *Turbulence models*, preprint

[28] A. Reusken: *Convergence of the multilevel Full Approximation Scheme including the V-cycle*, Journal Numerische Mathematik, ISSN 0945-3245, vol. 53, no. 6 (1988) pp. 663–686

[29] A. Ruhe: *Algorithms for the Nonlinear Eigenvalue Problem*, SIAM J. Numer. Anal. vol. 10, no. 4 (1973)

[30] Y. Saad and M. Schultz: *GMRES: A generalized minimal residual algorithm for solving nonsymmetric linear systems*, SIAM J. Sci. Stat. Comput., vol. 7, no. 3 (1986) pp. 856-869

[31] K. Schreiber: *Nonlinear Eigenvalue Problems: Newton-type Methods and Nonlinear Rayleigh Functionals*, Dissertation at Technische Universität Berlin, ISBN-13: 9783639062519 (2008)

[32] G. Sleijpen, A. Booten, D. Fokkema and H. van der Vorst: *Jacobi-Davidson Type Methods for Generalized Eigenvproblems and Polynomial Eigenproblems*, BIT vol. 36, no. 3 (1996) pp. 595–633

[33] G. Sleijpen, H. van der Vorst and M. van Gijzen: *Quadratic Eigenproblems Are No Problem*, SIAM News vol. 29, no. 8 (1996) pp. 8–10

[34] G. Sleijpen, H. van der Vorst and E. Meijerink: *Efficient expansion of subspaces in the Jacobi-Davidson method for standard and generalized eigenproblems*, Electron. Trans. Numer. Anal. 7 (1998) pp. 75–89

[35] J. Stoer: *Numerische Mathematik 1*, Springer, 9. edition, ISBN 3-540-21395-3 (2005)

[36] F. Tisseur and K. Meerbergen: *The Quadratic Eigenvalue Problem*, SIAM Rev., vol. 43, no. 2 (2001) pp. 235–286

[37] M. Tokar: *Recent progress toward high performance above the Greenwald density limit in impurity seeded discharges in limiter and divertor tokamaks*, Phys. Plasma, vol. 8, 2866 (2001)

[38] M. Tokar, F. Kelly, and X. Loozen: *Role of thermal instabilities and anomalous transport in threshold of detachment and mulitfacetted asymmetric radiation from the edge (MARFE)*, Phys. Plasmas, vol. 12, 052510 (2005)

[39] L. Trefethen: *Spectral Methods in Matlab*, SIAM (2002) ISBN 0-89871-465-6

[40] M. Valovič, P. Carolan, A. Field, S. Fielding, P. Jones, B. Lloyd, H. Meyer, M. Price, V. Shevchenko, K. Stammers, M. Walsh, S. You and the COMPASS-D and ECRH Teams: *Inboard gas puffing and behaviour of H-mode edge parameters in COMPASS-D*, Plasma Phys. Control. Fusion, vol. 44 (2002) A157–A181

[41] H. van der Vorst: *BI-CGSTAB: A fast and smoothly converging variant of BI-CG for the solution of nonsymmetric linear systems*, SIAM J. Sci. Stat. Comput., vol. 13, no. 2 (1992) pp. 631-644

[42] P. de Vries, J. Rapp, F. Schüller, M. Tokar: *Influence of Recycling on the Density Limit in TEXTOR-94*, Physical Rev. Let., vol. 80, no. 16 (1998) pp. 3519–3522

[43] J. Weiland: *Collective Modes in Inhomogeneous Plasma*, IoP publishing (2000) pp. 45–48

[44] J. Weiland, Private communication

[45] Wikipedia ⟨`http://en.wikipedia.org/wiki/Image:Binding_energy_curve_-_common_isotopes.svg`⟩ (2008)

[46] Wikipedia ⟨`http://en.wikipedia.org/wiki/Homotopy`⟩ (2008)

[47] Wikipedia ⟨`http://en.wikipedia.org/wiki/Lambert's_W_function`⟩ (2008)

[48] P. Yshmanov et. al., Nucl. Fusion 30 1999 (1990)

Index